LiNbO3 films : integration for piezoelectric and pyroelectric energy harvesting.

Giacomo Clementi

THÈSE DE DOCTORAT DE L'ÉTABLISSEMENT UNIVERSITÉ BOURGOGNE FRANCHE-COMTÉ

PRÉPARÉE À L'UNIVERSITÉ DE FRANCHE-COMTÉ

Ecole Doctorale n°37
Sciences Pour l'Ingénieur Microtechniques
Doctorat de Sciences pour l'ingénieur

par

M. Clementi Giacomo

$LiNbO_3$ films: intégration pour la récupération de l'énergie piézoélectrique et pyroélectrique

$LiNbO_3$ films: integration for piezoelectric and pyroelectric energy harvesting

Thèse présentée et soutenue à Besançon, le 25/11/2020

Composition du Jury:

M. Lefeuvre Elie	Professeur des Universités, Paris-Saclay	Président
M. Erturk Alper	Professeur des Universités, GeorgiaTech	Rapporteur
M. Cottone Francesco	Maître de Conférences des Universités, UniPg	Examinateur
M. Muralt Paul	Professeur Emeritus, EPFL	Examinateur
Mme. Bartasyte Ausrine	Professeure des Universités, UBFC	Directeur de thèse
M. Dulmet Bernard	Professeur Emeritus, ENSMM	Codirecteur de thèse
M. Margueron Samuel	Maître de Conférences des Universités, ENSMM	Codirecteur de thèse
M. Lallart Mickaël	Professeur des Universités, INSA Lyon	Invité
M. La Rosa Roberto	Directeur de recherche, STMicroelectronics	Invité

I'd take the awe of understanding over the awe of ignorance any day.
Douglas Adams

Acknowledgments

This PhD was truly a journey! I mean quite literally, given the fact that I traveled a lot during the past three years. Google maps recently reminded me that just in 2018, I visited 7 countries and 32 cities in 3 different continents. Basically I made 47.585 km, equal to a complete tour of the world, and this was just the first year (thank you Covid19). When my friends and colleagues were saying: "You should enlist to this MSCA, you will see the world!", I guess they were right. So one thing that I learned during my PhD it's that I should give them more credit. If I look behind, I can see a long road and still a long one ahead. I was helped by amazing people that were knowledgeable, experienced and supportive. I discovered many things, both scientifically and culturally speaking, and it was very exciting to work on such an interesting and wide project. But power sensors or harvest energy was just a part of this journey, probably the most important things were to understand that if we work hard enough the possibilities are endless, that if we work as a team ideas become realities, that if we share our knowledge we can learn so much more. I can say that these are the biggest achievements of my PhD. I deeply thank all the people that supported me, first of all my supervisors, with whom I had the pleasure to work. Ausrine Bartasyte, that is a great team leader and truly an inspiration, Bernard Dulmet, that patiently supported and always wisely advised me, and Samuel Margueron, that embodies the real spirit of an experimental physicist. Also my first teammates were invaluable on so many levels, and they represented one of the best things about these years: Anthony who was always eager to help and laugh, Sabina that is truly one of the most special and funny person that I know, Vincent that was there anytime for anything. I deeply thank Merieme with whom we worked really hard and we achieved so many things, and all the other friends and colleagues like Antonio, Mihaela, Isha, Sondes, Arthur, Tung, Mario, Alex, Alok, Etienne, Guillaume, Melvin, Franif, Kevin and all the others that were always ready to have fun or chat in the lab. Last but not least, all the people that I had the pleasure to work with during the secondments, like really brilliant Giulia that was always supportive and fun, Quentin that tried to keep things real and always had a plan, Lucho that was playing real hard, and all the other ESRs that were having fun with us between measurements and meetings. Finally, I hope I made my family proud and most of all Emilia, that was patiently there whenever I needed her.

Contents

List of Figures

List of Tables

Preface

This thesis is a part of the Marie Sklodowska-Curie Innovative Training Network (ITN) ENHANCE project (*Piezoelectric Energy Harvesters for Self-Powered Automotive Sensors: from Advanced Lead-Free Materials to Smart Systems*), which is related to energy harvesting for automotive applications, specifically for vibrational and thermal harvesting for self-powered sensors. ENHANCE is primarily designed to maximise the formal training opportunities, knowledge-sharing and professional development of early stage researchers (ESRs), but offers also benefits to the scientific staff at the host institutions and to the EU public. Particular attention has been paid for dealing with all the impacts in terms of protection of environment and energy efficiency by developing new energy harvesters for self-powered car sensors. The outcomes of the project may enable the use of wireless self-powered sensors in the cars and the reduction of maintenance cost of car sensors by 80 %, concurrently reducing weight, space and cost of future automobiles and aircrafts.

The main purpose of the ENHANCE project is to create a multidisciplinary joint research activity, implying chemistry, materials science, physics, mechanics, engineering and electronics, gathering the expertise of universities and industrial partners from 5 counties around Europe (Fig. 1a). Thanks to its multidisciplinary approach, the ambitious work plan of ENHANCE (Fig. 1b) starts with molecular engineering and materials synthesis up to transducers micro-fabrication, the design of hybrid harvesters along with smart electronics, to ensure the integration and application of the developed devices in real working conditions. Moreover, the project acts as an application driven training network, creating a strong relationship between research and industry in order to facilitate technology transfer. In order to implement advanced lead-free materials in the form of films or nanostructures with high piezoelectric figure of merit and quality factor, the first task of ENHANCE project is to determine the correct methodology, compatible with the conventional industrial micro electro-mechanical systems (MEMS) processing of fabrication. The aim is to propose complete and real harvesting solutions for industrial application by taking into account real harvesting working conditions (frequency and amplitude ranges, temperatures, shocks, corrosion, etc.) in cars, considering processing guidelines and constraints for implementation of new technologies at initial stage. During the project, 13 ESRs have been trained in different topics to learn and gain experience in a

(a) *(b)*

Figure 1: ITN-ENHANCE Project: a) consortium of partners and beneficiaries; b) institution roles within the project.

multidisciplinary environment about the energy harvesting subject, collaborating toward the main goal of the project and traveling between the hosting institution (maximum 10 months secondment per ESR) to develop their transferable and research skills. The final aim is to develop systems, that are able to offer stabilized output voltage in 1-3 V range and adapted to specific needs of sensors with high autonomy and working in temperature ranges from room temperature (RT) to 600 °C in vehicles.

My role in the project was to investigate the piezoelectric properties of $LiNbO_3$ for energy harvesting application, individuating a suitable micro-fabrication process for the transducers, and eventually integrating the developed technology along with optimized electronic interface in car environment. The thesis is structured as follows:

- Chapter 1 - General overview of kinetic harvesting methods with special focus on vibrations from vehicles, and comparison of the figure of merits of state of the art materials;
- Chapter 2 - Overview of the fabrication process, techniques involved during the course of the work, and the basic characterization of different $LiNbO_3$ orientations.
- Chapter 3 - Theoretical and experimental investigation of piezoelectric and pyroelectric properties of $LiNbO_3$ films with different orientations;
- Chapter 4 - Finite element simulations to optimize the performances of the prototypes, and introduction of theoretical framework for their electronic configuration;
- Chapter 5 - Results from the experimental characterization of different sets of $LiNbO_3$ energy harvesters, and comparison with the state of the art;
- Chapter 6 - General conclusion for the study and perspectives for future developments of $LiNbO_3$ energy harvesting technology.

1 Introduction

In this chapter, I will introduce the most general concept regarding vibrational energy harvesting, showing what are the most efficient ways for converting kinetic into electric energy. I will devote part of the chapter also to the investigation of frequency and acceleration levels in cars, which has special importance in ENHANCE project framework. Eventually, a brief comparison of different methods of vibrational energy harvesting is presented along with the main examples and their operation modes. In the second part of the chapter, I will discuss the state of the art concerning energy harvesting materials, and I will present the most important examples.

1.1 Energy Sources for Internet of Things Applications

As of today, industrial, commercial and residential buildings need monitoring systems for heating/cooling, telephone service, security and lighting. At the same time, new generation cars have multiple networks to control engine function, safety features, and communications systems. All these devices along with portable electronics, and their embedded sensors, represent the *Internet of Things* [1], or a vast network of devices all connected and able to provide useful information in real time. With the evolution of the network that lies behind them, more features will be added in the near future such as security, analytics, and management capabilities. This will allow IoT to become even more powerful while the number of devices that will be *active* is expected to grow to 22 billion by 2025. Along with the concept of IoT, there is a need to simplify the energy supply and to offer sustainable solutions to power up small sensors, and that is exactly why all these ideas converge in the energy harvesting topic. With energy harvesting, we identify the process for which is possible to recover micro-energies (1-10^3 $\mu W/cm^3$), that are otherwise lost in the environment, and convert it into electric current for instantaneous or later usage. Possible sources are light, heat, vibration, or biochemical processes (Fig. 1.1)[2]. Typically, light has the highest power density available (> 10^3 $\mu W/cm^2$), but indoor or other limiting conditions (night, enclosed systems, etc) represent a severe drawback for its application. Thermal sources are also promising (1-10^3 $\mu W/cm^2$) but often they require the usage of

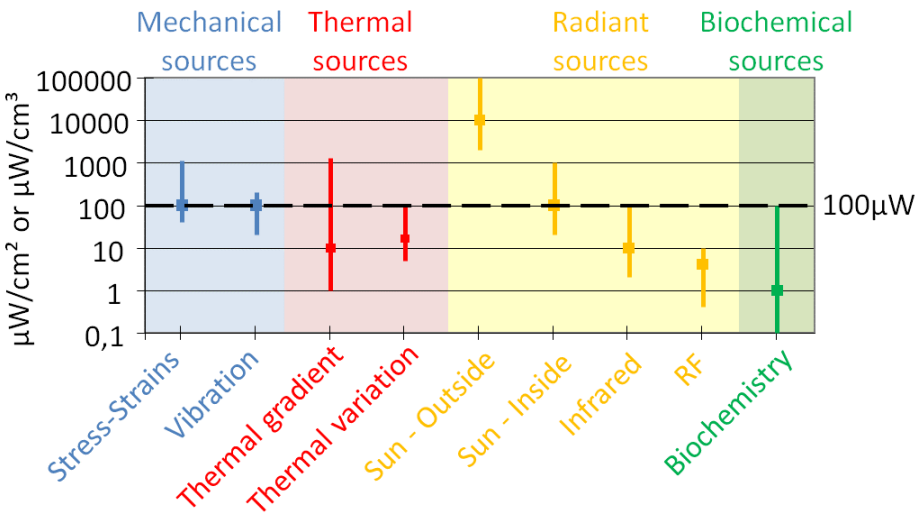

Figure 1.1: Energy density available from different sources [2].

toxic materials (like Bi_2Te_3) and stabilized temperature gradient between heat sink and hot plate, which could be difficult in real environmental conditions. Even though dependent on motion, vibrations look very appealing as a source kinetic energy (human body movements, industrial machinery, cars etc.), which have a considerable power density $100\mu W/cm^{-3}$. In conclusion, a typical energy source does not exist in energy harvesting, and thus its development is application driven. The features for a state of the art harvester are:

- Small scale and maintenance free: for harvesters and packaged electronic interface the target is usually 1 cm^3 of volume, and the protocol is *install and forget*.
- Flexibility: the harvester has to be rather flexible in terms of power output, or energy provided in operation mode to sustain the need of the sensor node.
- Long lasting and low-cost: in principle the device has to last more than a battery, therefore they have to work for more than 10^9 use cycles, and they have to be fabricated with resources which are abundant and not cost intensive.
- Sustainable and environmental friendly: the harvester has to respect worldwide environmental regulation (REACH and RHOS) in terms of toxicity and waste disposal.

Especially for next generation IoT devices, energy harvesting represent an alternative to lithium batteries (Table 1.1). The most used lithium batteries are Li-MnO_2, which can provide a nominal voltage of 3 V and operate between -30°C and 60°C, they show high energy density per volume (280 Wh/Kg), but often contain solvents like monoglyme, which is a substance of very high concern and REACH (Registration, Evaluation, Authorisation and Restriction of Chemicals) candidate. For instance, a lithium button cell (CR2032) has a limited life-span, which can provide 1 mW for about 1 month, or it could last 3 years

for a consumption of 30 µW. Promising batteries for IoT are lithium thionyl chloride (Li-$SOCl_2$), which have the highest power density per volume (500÷700 Wh/Kg), but also high cost and safety concerns, limiting the use in civilian applications. Eventually, deploying batteries for IoT applications could be cost intensive and inefficient, while vibrational harvesters could in principle work for longer time at the same power level [3], or be employed in tandem with rechargeable batteries and super capacitors. Furthermore, for a typical working cycle of a sensor (in terms of communication frequency with the node), often there is no need of continuous energy supply, hence the harvester can accumulate energy and then provide it whenever needed. For instance, ST-Microelectronics provides low power consumption (2 µA @ 1 Hz) capacitive digital sensors for relative humidity and temperature monitoring [4], which need 1.7 to 3.6 V supply. Other than IoT, another important field of application is represented by body implants (peacemaker, health monitoring devices, drug delivery etc.), where most of the time the preference is to avoid expensive or complex surgeries to replace batteries.

Table 1.1: Most common lithium batteries [5].

Type	Voltage (V)	Power density (Wh/Kg)	Temperature
Li-MnO_2	3	280	-30°C ÷ 60°C
Li-FeS_2	1.4÷1.6	297	-20°C ÷ 40°C
Li-$(CF)_x$	3	360÷500	up to 80°C
Li-$SOCl_2$	3.5	500÷700	down to -55°C

For car industry, the *leitmotiv* is to converge towards smart vehicles, where the number of sensors will drastically increase. According to business market studies [6], by 2025 there will be more than 200 million vehicles connected to 5G networks and 100% of the new vehicles will be connected to internet. While vehicles become more connected and advanced, still they are responsible for around 12% of total EU emissions of carbon dioxide. Starting from 2021, the new EU regulation sets a new threshold average emission of 95 g CO_2/km for cars (this emission level corresponds to a fuel consumption of around 4.1 l/100 km of petrol or 3.6 l/100 km of diesel) [7]. Therefore, reducing the weight of the car becomes instrumental regarding fuel consumption and CO_2 emissions. For instance, reducing the vehicle weight by 100 Kg reduce the CO_2 emissions by 4÷6 g/Km. We have to consider the fact that sensors signal transfer and powering in a vehicle introduce a complex network of wires (up to 50 kg, several km in length) and add complexity and costs to installation and maintenance diagnostics. Naturally, the demand of wireless sensors implementation for inaccessible locations or harsh working conditions is now increasing, also because it could have high impact on the mass of cars. Eventually, the objective of ITN ENHANCE project is to develop energy harvesters able to collect and convert the

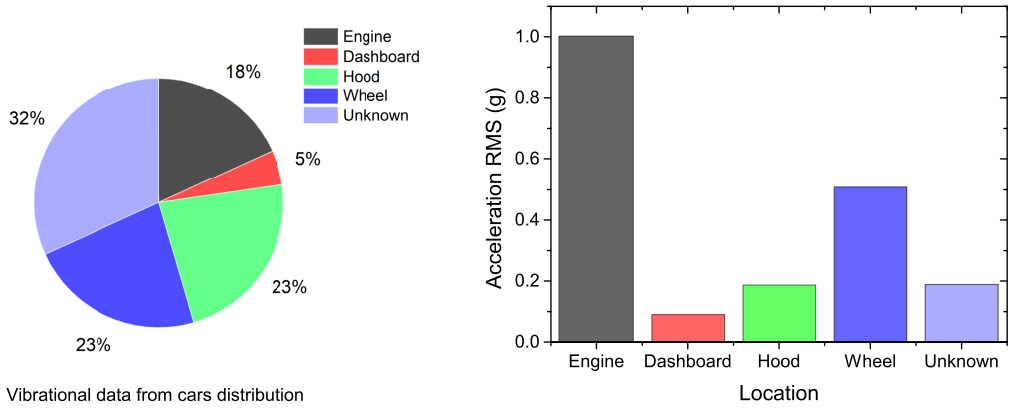

Figure 1.2: Study of data on vibrations available from cars.

abundant energy present in vehicles (vibrations, wasted heat, solar energy), in order to power wireless sensor nodes and reduce complexity, weight and cost. Moreover, the research effort in the project is oriented towards the optimization and implementation of eco-friendly materials which are not containing lead (Pb), such as $LiNbO_3$, $K_{1-x}Na_xNbO_3$ (KNN) and $BiFeO_3$ (BFO). On the other hand, these materials and methods have to be developed along with low power consumption electronics and power management, which represent a further optimization step in wireless sensor node communication networks.

1.2 Available Energy Sources in Cars

In the first part of this study we have to consider the vibrational energy available in the car. For this reason we have studied real acceleration signals from vehicles to understand what are the constraints in terms of signal magnitude or frequency levels, and design harvesters accordingly. This kind of investigation gave us the guidelines needed to implement our prototypes under the right conditions. We have started our study from a database which is currently available online under the project EnABLES [8]. The database contains more than 400 signals from real vibration sources, like animals, machinery, vehicles and human motion. Among the others, signals from cars are part of the database, where they represent the vehicles driven under different conditions. Moreover, also thermal fluctuations near the engine or the exhaust pipe can be used as energy source. In fact, temperature variation in the motor compartment, typically reach more than 50°C in less than 20 s, especially close to radiator support or at the end of the exhaust pipe [9].

In Fig. (1.2a) is presented the batch of data studied. The data were measured with a triaxial accelerometer (sampling frequency 20 kHz) in different car locations (engine, hood, wheel and dashboard) and for different conditions (parking, engine ignition, running on highway etc.). Other signal which are marked as *unknown* locations, were recorded specifically while the car was running in highway or urban roads. The data are typically

represented in terms of acceleration magnitude g (where g = 9.81 m/s^2). In Fig. (1.2b) we calculated the average RMS acceleration magnitude along the principal axis of the accelerometer. The results show that the highest magnitude was observed when the accelerometer was placed on the engine and whenever the car was turned on or off. Otherwise, the acceleration levels were between 0.1÷0.5 g depending on the location. This information gave us an overview of what to expect in real conditions when using an harvester inside the car, and it was later implemented as parameter during simulation phase. The second important aspect is the working frequency of the harvester, because assuming

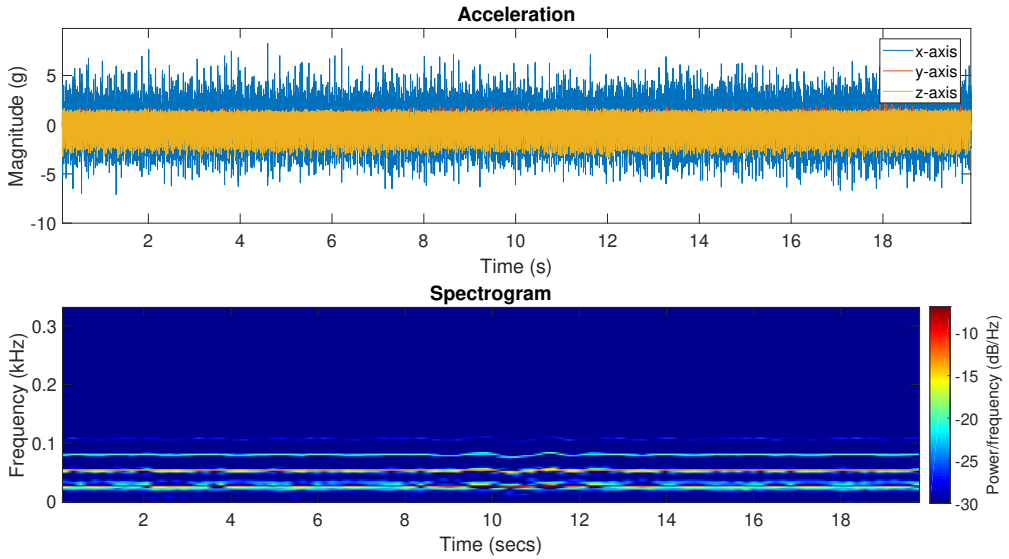

Figure 1.3: Acceleration data from car engine and spectrogram of the signal.

linear behavior, the maximum energy is collected at *resonance* frequency. In principle, the best configuration consists in the device resonance in the excitation frequency range or bandwidth. In order to investigate carefully the system, we needed to represent the data not only in terms of frequency (Fast Fourier Transform - FFT), but also in the time domain using a spectrogram, to see if the frequencies were stationary or dominant in time, and considering their power spectral density. The best case scenario is presented in Fig. (1.3). In the figure above we see the raw acceleration measured with the accelerometer when the engine is turned on and it is kept running continuously. In this case the system is providing an approximately steady excitation for the given time elapsed, and therefore the frequency is stationary. To counter-check this assumption, we have investigated the spectrogram of the signal. We can see that the frequency of 30 Hz, is continuous in time, and the same is for other intense peaks under 100 Hz (harmonics of the first mode). In this case, the 30 Hz frequency from the engine is dominant in time, as well as its higher harmonics, therefore there is the possibility to tune the harvester in a specific range of values and maximize the energy conversion. However, a more realistic example is given in Fig. (1.4). In this case the accelerometer is placed inside the car during a highway cruise.

The signal is strongly varying in the time domain, even because the car is moving and encounters the typical stochastic noise given by the road morphology. Considering the acceleration signal spectrogram, we observe that some frequency levels are stable, even if not as steady as before (30 - 60 Hz). Meanwhile, at higher frequencies, one mode is shifting between 265÷280 Hz, with weak magnitude modulations. In this scenario, we can still use a linear harvester, but we should attain a larger bandwidth in order to capture as much energy as possible, or design structural non-linearities to widen the harvester frequency spectrum.

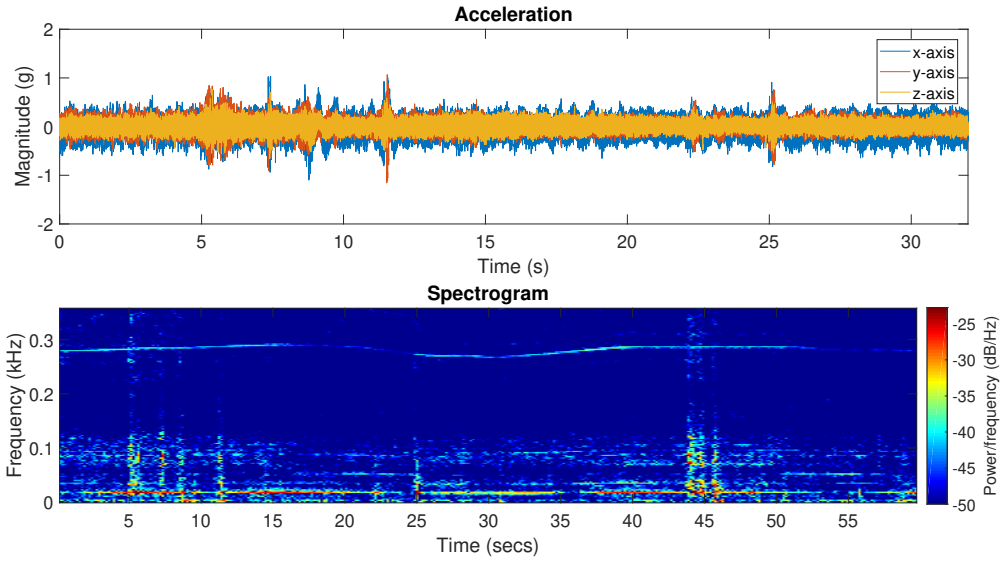

Figure 1.4: Acceleration data from car in highway and spectrogram of the signal.

Finally we can see in Table 1.2 the acceleration and frequency levels encountered in the study. In general we can say that cars generate low frequency vibrations, and the magnitude of acceleration rarely overpasses 0.1 g for $\frac{\omega}{2\pi} > 100$ Hz. The engine vibrations look particularly interesting in terms of acceleration magnitude, but we have to implement materials that can withstand harsh environmental conditions or high temperature.

Table 1.2: Acceleration and frequency levels in cars [8].

Location	Frequency (Hz)	Acceleration RMS (g)	Comments
Engine	30-60	1	Turning on/off
Dashboard	1-10	0.09	Parking
Hood	40-50	0.19	Turning on/off
Wheel	30-100	0.51	Urban road
Unknown	50-90	0.19	On highway

1.3 Vibrational Energy Harvesting

Vibrational energy harvesting, also called inertial harvesting, has become an established focus of interest during the past twenty years. Recent advances permitted to reduce the operating frequencies from several kHz to few Hz, where environmental vibrations are available (human motion, oscillations of bridges, automotive engines, etc.), while maintaining an interesting output power. The size of the systems is highly limited in the case of integrated sensors (volume of sensor < 1 cm^3). The most used methods to harvest energy from vibrations are piezoelectric, electromagnetic and electrostatic. William and Yates [10] have proposed a simple and effective model for kinetic (or vibrational) energy harvesting. In this case, the harvester is approximated to single degree of freedom system and it can be used to explain various approaches in first approximation. The inertial kinetic harvester (Fig. 1.5) is introduced as a mass, M, which is moving with a displacement, x, with respect to the external excitation displacement, y, connected to a spring, K, and a damper, C. The damping term is the sum of the energy dissipated mechanically and the energy harvested. Thus, we can use the following equation to express the dynamic of the system:

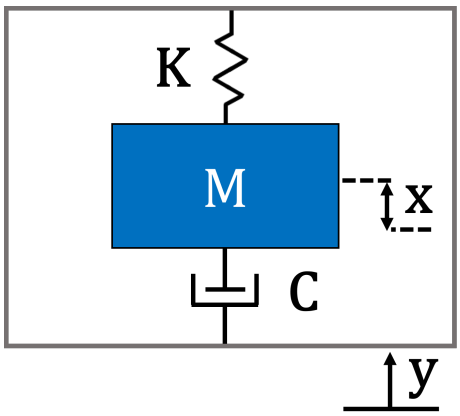

Figure 1.5: Schematic diagram of inertial harvester.

$$-\mathrm{M}\ddot{y} = \mathrm{M}\ddot{x} + \mathrm{C}\dot{x} + \mathrm{K}x \tag{1.1}$$

The system is essentially a second order differential equation, in which we can make the following substitutions:

$$\omega_n^2 = \frac{\mathrm{K}}{\mathrm{M}}$$

$$\frac{\mathrm{C}}{\mathrm{M}} = 2\zeta\omega_n$$

where ω_n is the natural frequency of the harvester and ζ-the dimensionless damping ratio. So we can rewrite the system as:

$$-\ddot{y} = \ddot{x} + 2\dot{x}(\zeta_m + \zeta_e)\omega_n + \omega_n^2 x \tag{1.2}$$

that is typically the equation for an RLC circuit or forced oscillator. Now being the external oscillation harmonic as in $y = \mathrm{Y}\sin\omega t$, and assuming same phase, we can get the magnitude of the response in permanent regime:

$$x_0 = \frac{\Omega^2 y}{\sqrt{(1-\Omega^2)^2 + (2\zeta\Omega)^2}} \tag{1.3}$$

where $\Omega = \frac{\omega}{\omega_n}$ is the ratio between forcing and natural frequency. Eventually the power obtained is given by the equation:

$$\mathrm{P}_{rms} = \frac{\mathrm{M}\zeta_e\Omega^3\mathrm{A}^2}{\omega\left[(1-\Omega^2)^2 + (2\zeta\Omega)^2\right]} \tag{1.4}$$

Therefore we have the maximum power whenever $\Omega = 1$, or matching with the resonance frequency of the system. Another important aspect is that the power is proportional to the mass, M and acceleration magnitude, A, hence we have to optimize the size of the device mass and obviously work at the maximum acceleration levels. From the interface point of view, there is an optimal level of damping which is given from $\zeta_e = \zeta_m$, or whenever electrical and mechanical damping are matching. Therefore, we have to minimize the mechanical damping of the structure while matching it with the electrical load. With the help of this model, we can estimate the maximum power harvested from a kinetic harvester for a given transduction mechanism, expressed through C_e or alternatively ζ_e.

1.3.1 Electromagnetic Transducers

The lumped model applies very well for the theoretical description of electromagnetic harvesters. In this case, the energy is converted using the principle of electromagnetic induction (Fig. 1.6a). Therefore, the voltage is collected from a coil which experiences a variation of the magnetic field, where the movement can derive independently from the coil or the magnet. If we want to express the power in terms of the restoring force produced by the magnet moving through the coil, we can write:

$$\mathrm{P}_{rms} = \frac{1}{2}\frac{(\mathrm{NB}l)^2\,\mathrm{R}_l}{(\mathrm{R}_c + \mathrm{R}_l)^2}\omega^2 x_0^2 \tag{1.5}$$

where R_c and R_l represent coil and external resistive load, N and l the number of turns and length of the coil, and B the magnitude of the magnetic field, respectively. Usually for electromagnetic harvesters, the working frequencies are small (typically below 50 Hz) and therefore the coil inductance can be ignored in first approximation, so the electromechanical force is in phase with the velocity and the lumped model matches correctly the system. If the coil resistance is zero, the power output would match directly the maximum

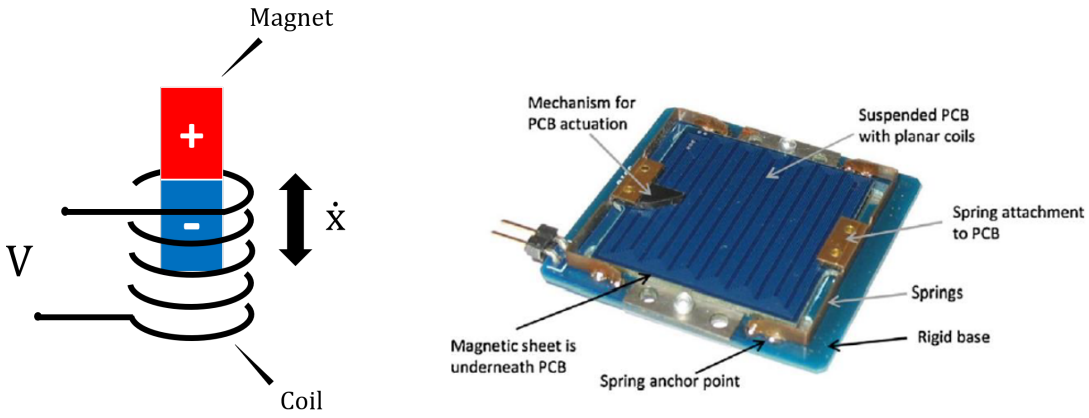

(a) *(b)*

Figure 1.6: Electromagnetic generators: a) electromagnetic induction principle; b) device with suspended planar coils on magnetic sheets[11].

power predicted by the lumped model, but instead we have maximum power whenever $R_c = R_l$. Even if this equations do not hold for more complex geometries like the one in Fig. (1.6b), where planar coils and magnetic sheets are involved [11], this model can still give general insights on design aspects. Electromagnetic harvesters have good efficiency at low frequency but they provide rather small voltages (often in range of 10^{-1} V), and the power output (> 100 $\mu W/cm^3$ for low frequency) is proportional to the coil design and the magnitude of the magnetic field. The advantage is the low cost of such devices as compared to other technologies, even though electromagnetic systems are difficult to miniaturize. They can achieve high coupling (up to 60% [12]) for cm^3 size and above, and they represent the first commercially successful energy harvesters like Perpetuum [13].

1.3.2 Electrostatic Transducers

For the case of electrostatic harvesters, variable capacitance is used to change the charge on a parallel plate capacitor changing their relative distance or electrodes overlapping (Fig. 1.7a). In fact, while changing the distance between the electrodes, the energy stored in the capacitor will change, depending if the energy cycles are either charge- or voltage-constrained. The energy that eventually exceeds in the cycle is the energy that we can harvest. Many geometries can be implemented and usually the device are compatible with MEMS scale processing for miniaturization. The power density is usually small compared to the other technologies, due to the fact that the equivalent mass is limited in size. For instance, whenever the system work in air as a dielectric medium, the power densities become low (< 60 $\mu W/cm^3$ for electret free [2]), unless they operate at high voltages. They require pre-charging or the use of electrets as initial charge on the capacitor. For instance, in Fig. (1.7b) a patterned electret using a high-performance perfluoro polymer material is employed to induce a repulsive electrostatic force [14]. Even though electrets can have similar performances to electromagnetic and piezoelectric harvesters, the fabrication and

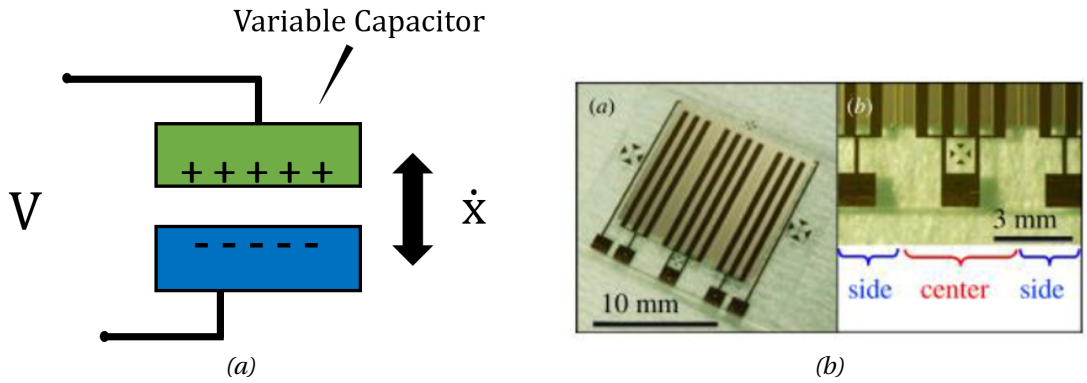

Figure 1.7: Electrostatic generators: a) parallel plate electrode variation generates voltage variation. b) Electret based energy harvester electrode detail[14].

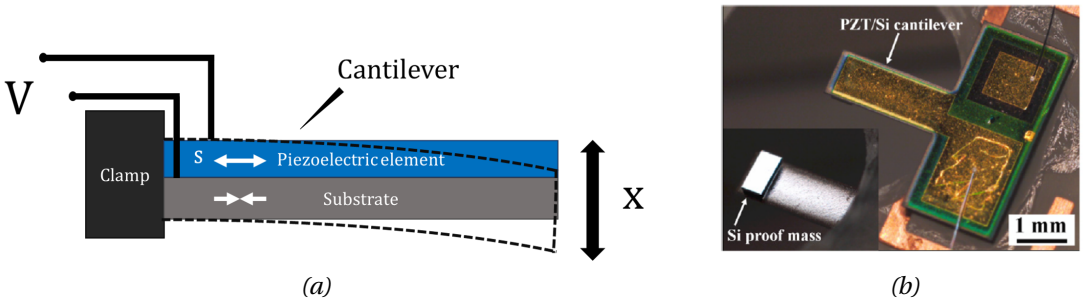

Figure 1.8: Piezoelectric generators: a) displacement of cantilever and strain variation in piezoelectric layer. b) MEMS scale PZT cantilever on Si[15].

conditioning/balancing of electrostatic forces are still challenging.

1.3.3 Piezoelectric Transducers

Piezoelectric materials represent a solid transduction solution for energy harvesting. The most common mechanical structures used for this purpose are cantilevered beams. In this case the material has the capability of converting the transverse mechanical strain provided by the dynamic excitation of the beam, in electric charge displacement. An example of harvester is given in Fig. (1.7a), where the cantilever tip displacement generates a strain in the piezoelectric layer, the voltage is then collected from two parallel plate electrodes. Besides, this devices can be miniaturized down to MEMS scale [15] (Fig. 1.7b). More details regarding material classes and features will be given in the following chapter. Now, if we rewrite the equation of the power in terms of piezoelectric transduction, we have:

$$P_{rms} = \frac{\omega}{4}(\text{FOM})\, v S_i^2 \tag{1.6}$$

Where *FOM* stands for *Figure Of Merit*, and it is related to the electro-mechanical features of the piezoelectric material, v is the active volume, and S_i the strain level on the piezoelectric beam. From this simple formulation we have a better understanding of the

important aspects to take into account:

- We should work at the maximum frequency available of the system, hence tune the cantilever response to ω_n. Therefore, the geometrical parameters have to be optimized for these working conditions;

- We need to optimize the FOM of the piezoelectric material to improve the power output;

- The volume of the piezoelectric layer under strain has to be maximized.

With piezoelectric harvesters we can generate interesting voltage levels (1÷20 V) depending on the size of the harvesters, but the optimal load is usually higher compared to the electromagnetic harvester counterpart (kΩ - MΩ range), developing considerable power densities (> 300 $\mu W/cm^3$). The miniaturization is also possible, even though fabrication results into higher costs.

Table 1.3: Comparison of different transducers technologies.

Type	Advantages	Drawbacks	Power density
Electromagnetic	• Optimized for low frequencies (5-100 Hz) • No external voltage supply • Low impedance (< kΩ)	• Hard to miniaturize • Large mass displacement	• 184 $\mu W/cm^3$ @10 Hz [16] • 306 $\mu W/cm^3$ @52 Hz [17]
Electrostatic	• Miniaturization and MEMS integration • Good output voltage (2-10 V) • Tuning of coupling • Long lasting	• Need of external bias voltage • Low power at small scale	• 58 $\mu W/cm^3$ @50 Hz [18] • 21 $\mu W/cm^3$ @105 Hz [19]
Piezoelectric	• High voltage output (> 10 V) • Miniaturization • High coupling for single crystal • No external voltage supply	• Expensive • Small coupling for thin films • Large optimal load (kΩ-MΩ) • Fatigue effect	• 1.45 mW/cm^3 @18 Hz [20] • 0.39 mW/cm^3 @36 Hz [21]

1.4 Basic Concepts of Electroactive Transduction

In this section several piezoelectric materials, considered for energy harvesting purposes, will be presented. Some of these materials are mainly used for energy harvesting and actuation solutions, some others are more applied in acoustics field. I will discuss about their properties, the general aspects of their fabrication and in particular their suitability the application in energy harvesting.

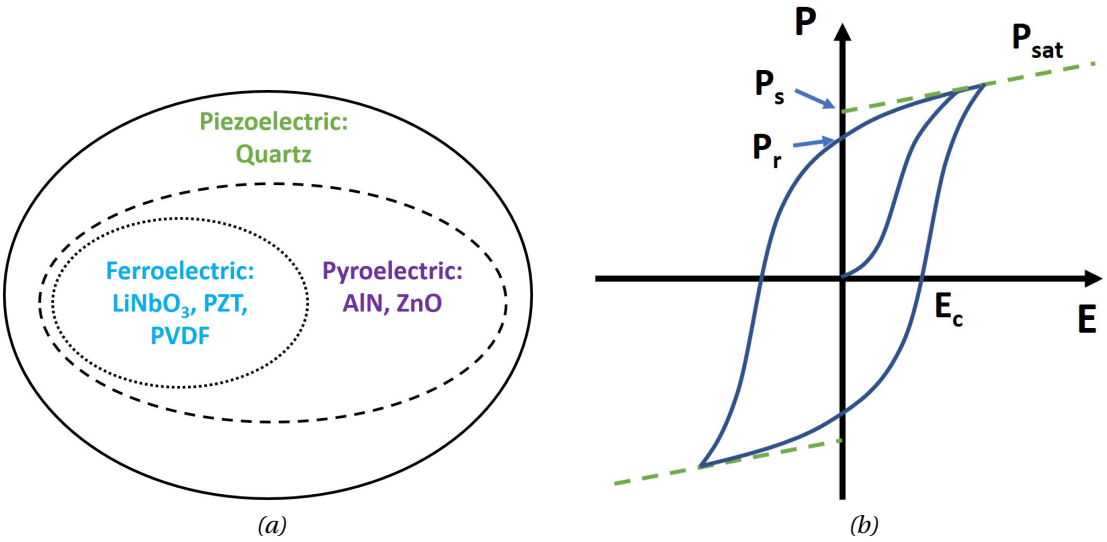

Figure 1.9: Ferroelectric materials as a subclass of piezoelectric materials (a) and polarization change as a function of electric field (b).

1.4.1 Ferroelectricity

The concept of ferroelectricity is similar to the one of *ferromagnetism*. In both cases, a specific class of materials have spontaneous polarization and hysteretic behavior due to local domain arrangements. Ferroelectrics are materials in form of single crystals or polycrystalline solids (made of crystallites). Their main feature is that they show reversible spontaneous polarization (P_S), which can be changed by applying an electric field. Under the same principle, the local crystallites, or the so-called ferroelectric domains, can be aligned under a specific external field condition. If the domains are randomly oriented, then the net response to external mechanical excitation is null. Moreover, ferroelectrics also exhibit *Curie Temperature* (Θ_C), or a temperature above which the spontaneous polarization does not exist anymore, and the material shows para-electric behavior. Ferroelectrics represent a subgroup of piezoelectric and pyroelectric materials (Fig. 1.9a), the former occurs when the crystal structure is non-centrosymmetric and the latter when symmetry allows first rank tensor properties. Notable examples of non-ferroelectrics are AlN and ZnO, which are both piezoelectric and pyroelectric, but they don't present reversible behavior, while $LiNbO_3$ is a ferroelectric along with other ceramics such as $BaTiO_3$ and PZT.

In general, ferroelectric materials can be poled, in order to align the domain orientation, ending up with a net microscopic dipole. For both polycrystalline and single crystal materials, we can reverse the direction of P_S using an electric field in opposite direction, at the condition of being higher than the coercive field. Repeating this process, generates a typical hysteresis loop (Fig. 1.9b). Starting from the origin (polydomain), the polarization increases non-linearly with the electric field, thus the domains start to align. Thereafter,

even if the field is further increased, the polarization reaches a saturation phase (green dotted line in Fig. 1.9b) P_{sat}, which gives us the value of the P_S, when intersecting the P axis. To reverse P_S, the field has to be reduced to zero, and whenever we the polarization axis is intersecting, this value is called *remanent polarization* (P_R). The physical explanation is that even if the value of E is reduced to zero, some domains will still be aligned. The value of the field to bring the polarization to zero, is the *coercive field* (E_C). The second half of the cycle will be the same but for negative values of the field. Eventually the area under the loop will be the energy dissipated during the cycle, due to the losses of the material like thermal dissipation.

1.4.2 Piezoelectricity

Piezoelectricity is a physical phenomenon that occurs when a material has a non-centrosymmetric crystal structure. Just one case of non-centrosymmetric structure is not piezoelectric, namely cubic class 432. Symmetry is an important aspect of piezoelectricity, among the 32 point groups for crystals, only 20 of them are piezoelectric. If the material undergoes mechanical stress or strain, due to the absence of a center of symmetry, the charges inside the crystal will generate a dipole moment and then a voltage. Vice versa, if an electric field is applied on the material, the structure will deform according to the direction of the field. If the relation between the electric field and the mechanical strain is linear, then the phenomenon is called *linear piezoelectric effect*. In the case of *direct* effect, the piezoelectric element acts as a *generator*, thus it can be used for energy harvesting applications. Instead, for *converse* effect the transducer acts as a motor, so the applications are more oriented towards actuators. In case of spontaneous polarization, piezoelectricity goes along with pyroelectricity. For ferroelectric piezoelectrics, high coupling can be attained but also high dielectric losses, and the properties are *non-linear*. In order to mathematically explain piezoelectricity, we may define the direct piezoelectric effect using tensor notation:

$$\mathrm{D}_i = d_{ijk}\mathrm{T}_{jk} \tag{1.7}$$

where D is the dielectric displacement vector, T the applied stress second-rank tensor, and d the strain piezoelectric coefficient third-rank tensor. The following relation is for converse piezoelectric effect:

$$\mathrm{S}_{jk} = d_{ijk}\mathrm{E}_i \tag{1.8}$$

with S the strain second-rank tensor and E the electric field vector. It is important to note that the use of tensors is useful because piezoelectricity is an effect dependant on the orientation of the crystal structure. Both stress and strain tensors are symmetrical, along with the piezoelectric tensors (*i.e.* $T_{ij} = T_{ji}$, $S_{ij} = S_{ji}$ and $d_{ijk} = d_{ikj}$). It is possible then to rewrite the equation using the matrix notation or Voigt notation, where the indexes are reduced in numbers being symmetrical. So the following relations will be valid $T_{ij} = T_l$,

$S_{ij} = S_l$ and $d_{ijk} = d_{im}$. In matrix notation the constitutive equations can be defined in strain-charge form as:

$$\begin{aligned} \mathrm{S}_i &= s^{\mathrm{E}}_{ij}\mathrm{T}_j + d_{ki}\mathrm{E}_k \\ \mathrm{D}_i &= d_{ij}\mathrm{T}_j + \varepsilon^{\mathrm{T}}_{ij}\mathrm{E}_j \end{aligned} \tag{1.9}$$

Where s^{E} is the elastic compliance fourth-rank tensor at constant electric field and ε^{T} the second-rank tensor permittivity at constant stress. The superscript usually takes into account the relative constant electro-mechanical parameter. Whenever we talk about longitudinal excitation (thickness mode) we will consider that the material is activated along its polarization direction, so the coefficient d_{ii} will be used,(with $i = 3$). For transverse excitation (transverse mode) instead the material is excited perpendicularly respect to the polarization, hence the use of d_{ij} coefficient, (with $i = 1,2$, $j = 1,2,3$). Even if not considered in this work, there is also the possibility to excite the material under shear boundary conditions (shear mode), so the relative piezoelectric coefficient is d_{ik}, (with $i = 1,2,3$ and $k = 4,5,6$). Alternatively we can rewrite Eq. (1.9) in terms of the stress T, defining the stress-charge form:

$$\begin{aligned} \mathrm{T}_i &= c^{\mathrm{E}}_{ij}\mathrm{S}_j - e_{ki}\mathrm{E}_k \\ \mathrm{D}_i &= e_{ij}\mathrm{S}_j + \varepsilon^{\mathrm{S}}_{ij}\mathrm{E}_j \end{aligned} \tag{1.10}$$

differently from Eq. (1.9), we have c_{E} that is the elastic stiffness at constant electric field, e is the stress piezoelectric tensor. Both set of Eq. 1.9 and Eq. 1.10 are equally correct, so that theoretically one can use either one. Actually, the specific boundary conditions exerted on a given device must be considered to choose the most suitable equation set for the analysis. As seen, crystal symmetry is a very important aspect, since it gives the exact number of elastic or piezoelectric coefficients which are non-zero or independent. Later on in this chapter, we will see that usually the most popular symmetry classes in energy harvesting are tetragonal (4mm), hexagonal (6mm) and poled ceramic materials (∞ m). The trigonal family (3m) is more rare, and it is the symmetry class for $LiNbO_3$ and $LiTaO_3$.

1.4.3 Pyroelectricity

Pyroelectricity is a physical effect that arises whenever the material undergoes temperature fluctuations over time. It occurs for those piezoelectric materials that possess first rank tensor properties. In fact, whenever the temperature changes, the polarization in a pyroelectric crystal is reduced by the temperature effect, and the charges are relatively free to move. The dipole moment magnitude of the material will lower, therefore the surface charges have to rearrange themselves to balance the different value of spontaneous polarization. To avoid confusion we will keep the notation as in Eq. (1.9), so the stress will be T and the temperature will be Θ. The variational relationship between charge displacement

and temperature effect can be written as:

$$\delta \mathrm{D} = p^{\mathrm{T}} \delta \Theta \tag{1.11}$$

where p is the pyroelectric coefficient ($\mathrm{C.K^{-1}}.m^{-2}$), which is a first-rank tensor. The equation can be rearranged in order to define the coefficient at constant stress as:

$$p^{\mathrm{T}} = \frac{\delta \mathrm{D}}{\delta \Theta} \tag{1.12}$$

If we explicit D in terms of the applied electric field E and the total polarization P then we have:

$$\mathrm{D} = \varepsilon \mathrm{E} + \mathrm{P} = \varepsilon \mathrm{E} + (\mathrm{P}_{in} + \mathrm{P}_s) \tag{1.13}$$

where P_{in} and P_s are the induced and the spontaneous polarization, respectively. Therefore the pyroelectric coefficient can be expressed as:

$$p^{\mathrm{T}} = \frac{\partial \mathrm{P}_s}{\partial \mathrm{T}}\bigg|_{\mathrm{T,E}} \tag{1.14}$$

If we rewrite the constitutive equation in matrix form, by adding thermal effects:

$$\begin{cases} \mathrm{S} = s^{\mathrm{E}} \mathrm{T} + d^t \mathrm{E} + \alpha^{\mathrm{E}} \Delta \Theta \\ \mathrm{D} = d \mathrm{T} + \varepsilon^{\mathrm{T}} \mathrm{E} + p^{\mathrm{T}} \Delta \Theta \end{cases} \tag{1.15}$$

where α is the coefficient of thermal expansion. In condition of constant electric field $\delta E = 0$ and constant strain $\delta S = 0$, from the second constitutive equation we get:

$$\mathrm{D} = \varepsilon^{\mathrm{T}} \left(1 - \frac{d^2}{\varepsilon^{\mathrm{T}} s^{\mathrm{E}}}\right) + \Delta \Theta \left(p^{\mathrm{T}} - \frac{d \alpha^{\mathrm{E,T}}}{s^{\mathrm{E}}}\right) \tag{1.16}$$

In Eq. (1.16), when you deal with d_{33}, then the pyroelectric coefficient is enhanced, because p is negative while α is positive. However, when we deal a negative transverse coefficient, then the pyroelectric coefficient is reduced in the normal case (p negative, α is positive). This is usually the case in thin films where we have $\mathrm{T_3} = 0$, but $\mathrm{S_1} = \mathrm{S_2} = 0$. Moreover, we can define the secondary pyroelectric effect when the crystal is free to react to the thermal variation.

1.4.4 Electro-Mechanical Coupling Factor

The electro-mechanical coupling factor is an important non-dimensional coefficient, that describes the piezoelectric material ability to convert the stored energy into electric or mechanical work. These coefficients are valid in the case of actuators or sensors, and can be specifically defined for the relative excitation mode. They depend on the material elastic, piezoelectric and dielectric properties.

Generally the coupling k^2 is defined as the ratio between two energies:

$$k^2 = \frac{\text{Created mechanical energy}}{\text{Invested electrical energy}} = \frac{\text{Created electrical energy}}{\text{Invested mechanical energy}} \tag{1.17}$$

the first identity of Eq. (1.17) is related to *converse* effect or the case of actuators, while the second identity is used for the *direct* effect or in sensor configuration. For energy harvesters, we usually have an input mechanical energy (in elastic form) that we want to convert into electrical energy, so we have to consider the input mechanical energy as:

$$u_{\mathrm{T}} = \frac{1}{2}\mathrm{ST} = \frac{1}{2}s^{\mathrm{E}}\mathrm{T}^2 \tag{1.18}$$

where we assumed the linear relationship between S and T according to Hooke's law, therefore $\mathrm{S} = s^{\mathrm{E}}\mathrm{T}$. Meanwhile, the electric energy that is generated by the effect of piezoelectric coupling is given by the displacement of charges in the dielectric medium:

$$u_{\mathrm{E}} = \frac{1}{2}\mathrm{DE} = \frac{1}{2\varepsilon^{\mathrm{T}}}\mathrm{D}^2 = \frac{1}{2\varepsilon^{\mathrm{T}}}d^2\mathrm{T}^2 \tag{1.19}$$

If we now consider the ratio between the two, we obtain the electro-mechanical coupling:

$$k_{ij}^2 = \frac{u_{\mathrm{T}}}{u_{\mathrm{E}}} = \frac{d_{ij}^2}{s_{jj}^{\mathrm{E}}\varepsilon_{ii}^{\mathrm{T}}} \tag{1.20}$$

this non-dimensional coefficient can be defined for all piezoelectric materials and can be useful to compare their performance. In this work, I will often address the coupling for transverse mode commonly used in harvesting (k_{31}), but it can be defined also for thickness mode (k_{33}) or shear mode (used mostly in acoustics k_{15})[22]. It has to be noted that this quantity is different from the effective coupling factor, ${k^2}_{\mathrm{eff}}$, which is related to the piezoelectric properties and the particular device design. ${k^2}_{\mathrm{eff}}$ is defined as:

$$k_{\mathrm{eff}}^2 = \frac{f_{\mathrm{oc}}^2 - f_{\mathrm{sc}}^2}{f_{\mathrm{oc}}^2} \tag{1.21}$$

Where f_{oc} and f_{sc} are respectively the open circuit and the short circuit resonance frequencies. The value for ${k^2}_{\mathrm{eff}}$ is usually smaller than k_{ij}, but for a monomorph (or pure piezoelectric bender), they should be the same. It is important to explain that this two coefficients are not representing the efficiency, η, of the harvester. In fact, during a working cycle for the harvester, only part of the input mechanical energy is converted into electrical energy, while the remaining is stored as electrostatic energy in the piezoelectric layer. Eventually η is defined as:

$$\eta = \frac{\text{Created electrical energy}}{\text{Consumed mechanical energy}} \tag{1.22}$$

If the piezoelectric element has low dielectric losses, the stored electric energy will go back to the mechanical source. Typically, PZT ceramic losses are about 1-3%, while single crystals, such as $LiNbO_3$, can go as low as 0.1%. A different approach to efficiency is given analytically by [23] based on a simplified single degree of freedom system. In this case η is defined by the relation:

$$\eta = \frac{k_{eff}^2}{2\left(1-k_{eff}^2\right)}\left(\frac{1}{Q}+\frac{k_{eff}^2}{2\left(1-k_{eff}^2\right)}\right)^{-1} \tag{1.23}$$

It is clear then that η depends on the quality factor, Q, and the coupling of the system, but this definition is valid for a device working at resonance with relative resistive load. It was shown that η can be as high as 90% of the coupling, leading to the relation that $\eta < k^2$. However, this result has to be taken carefully into account, because it applies just for this particular case and it cannot be considered as a general result.

In order to summarize, we sketched in Fig. (1.10) a simple cycle for energy conversion. We start for the environmental energy available, which can be random vibrations or a direct deformation of the piezoelectric transducer. Afterwards, this energy has to be transferred to the harvester, but some energy is either lost due to damping effects or reflected to the source because of mechanical impedance mismatch. Then the transferred energy has to be converted into electrical energy. Here the properties of the transducer are very important (electro-mechanical coupling, effective coupling and efficiency) and dielectric and thermal losses have to be taken into account. Finally, the energy will be extracted by the electronic interface and stored, a small portion of the energy will be lost due to electric leakage or thermal effect.

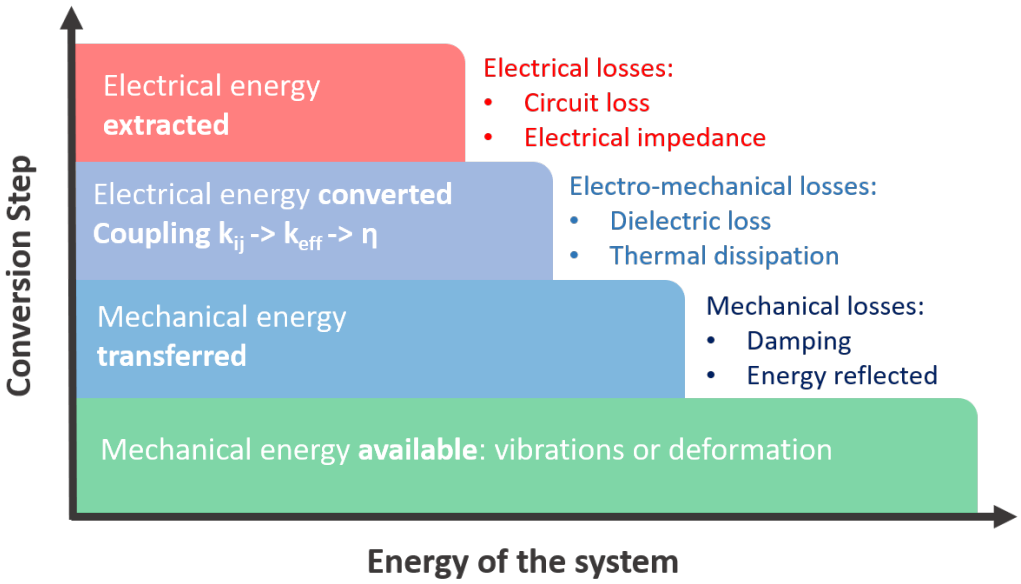

Figure 1.10: Conversion mechanism for energy harvesting cycle.

1.4.5 Figure of Merit

In order to compare different materials that present particular interest for energy harvesting, we may define few figures of merit (FOM). Differently from the coupling, this is a dimensional parameter, and it is strongly related to the energy that the system can generate. Usually, depending on the type of material (*i.e.* bulk or thin films), diverse FOMs are defined. For instance, for thin films the FOM is defined through piezoelectric stress constant and dielectric permittivity, mostly because the elastic properties are not always available, or are difficult to measure. This FOM^f was presented by Muralt in [24] as the electric energy density for a given material from direct investigation of its piezoelectric and dielectric properties. Therefore it is defined as:

$$\mathrm{FOM}^f = \frac{e_{ij}^2}{\varepsilon_{jj}^{\mathrm{T}}} \tag{1.24}$$

FOM^f has the unit of measurement of an energy density, $J.m^{-3}$ or Pa, in this work we will systematically adopt the former one. Other FOMs depend strongly on the transducer design. Bowen et al. [25] defined two kinds of harvesters: inertial (or stress-driven) and kinematic (or strain-driven). In the case of the former harvesters, a mass undergoes an acceleration and its principle relies on the *resistance* of the structure to the applied stress. The latter case instead, is the harvester directly coupled with the source of deformation, which depends on the *compliance* of the material to the applied strain. In order to define the electrical energy density for the stress-driven harvester, we can start from Eq. (1.9) and explicitly resolve in terms of D and E. In this case, we derive the two fields by Eq. (1.19) considering at first $E = 0$ for the short circuit condition, and then $D = 0$ for the open circuit condition. We end up having:

$$\begin{aligned} \mathrm{D}_i &= d_{ij}\mathrm{T}_j \\ \mathrm{E}_i &= -\frac{d_{ij}\mathrm{T}_j}{\varepsilon_{ij}} \end{aligned} \tag{1.25}$$

Then, we can calculate the electric energy density using Eq. (1.19):

$$u_{\mathrm{E}} = \frac{1}{2}\frac{d_{ij}^2}{\varepsilon_{ij}}\mathrm{T}_j^2 \tag{1.26}$$

Finally, we can define for a general excitation direction $\mathrm{FOM}^{\mathrm{T}}$:

$$\mathrm{FOM}^{\mathrm{T}} = \frac{d_{ij}^2}{\varepsilon_{jj}^{\mathrm{T}}} \tag{1.27}$$

This FOM is actually the reciprocal of the energy density, and its units are $m^3.J^{-1}$, we will rather adopt the reciprocal $(\mathrm{FOM}^{\mathrm{T}})^{-1}$ to compare different materials. For strain-driven harvesters, we consider the $\mathrm{FOM}^{\mathrm{S}}$ as defined by [26, 27]. In this case the piezoelectric strain coefficient is divided by the permittivity and two different compliance coefficients. Both s^{D} and s^{E} are considered, typically because these devices are not working mostly in open circuit condition as the stress-driven counterpart. Moreover, the efficiency of strain-driven harvesters does not depend on resonance frequency and quality factor. An example of strain driven harvester is a wearable piezoelectric patch that converts the strain from the deformation into electrical energy. In this case the Eq. [1.9] at open and short circuit becomes:

$$\begin{aligned} \mathrm{D}_i &= \frac{d_{ij}}{s^{\mathrm{E}}}\mathrm{S}_i \\ \mathrm{E}_j &= -\frac{d_{ij}}{\varepsilon_{ij}s^{\mathrm{D}}}\mathrm{S}_i \end{aligned} \tag{1.28}$$

Then, the electrical energy density is:

$$u_{\mathrm{E}} = \frac{1}{2}\frac{d_{ij}^2}{s^{\mathrm{D}}s^{\mathrm{E}}\varepsilon_{ij}}\mathrm{S}_j^2 \tag{1.29}$$

Finally, the definition for the $\mathrm{FOM}^{\mathrm{S}}$ is:

$$\mathrm{FOM}^{\mathrm{S}} = \frac{d_{ij}^2}{s_{ii}^{\mathrm{E}}s_{ii}^{\mathrm{D}}\varepsilon_{jj}^{\mathrm{T}}} \tag{1.30}$$

For the calculation of s^{D}, we used the following relation:

$$s_{ii}^{\mathrm{D}} = s_{ii}^{\mathrm{E}}(1-k_{ij}^2) \tag{1.31}$$

In this case the units of this FOM are $J.m^{-3}$. From Eq. (1.30) it is clear that materials with high stiffness should have better performance if used for strain-driven harvesters. Finally, to attain high energy density, we suggest to use materials with piezoelectric coefficients as high as possible and also dielectric constant as low as possible. In this way, one can increase the coupling factor which is the first parameter to take into account during the design of the harvester, or the FOM^f in the case of devices based on thin films. Thereafter, FOMs can give a good comparison in terms of energy density, for whatever type of harvester, stress- or strain-driven.

Several FOMs for pyroelectric harvesting were proposed, we will illustrate few of them while taking Bowen et al. [28] as a reference. The first one is an electro-thermal coupling

Table 1.4: Coupling and FOMs

Index	Formula	Units
k_{ij}^2	$d_{ij}^2 \big/ s_{ii}^{\mathrm{E}} \varepsilon_{jj}^{\mathrm{T}}$	-
k_{py}^2	$p^2 \Theta_{\mathrm{M}} / c_{\mathrm{E}} \varepsilon_{33}^{\mathrm{T}}$	-
FOM^f	$e_{ij}^2 \big/ \varepsilon_{jj}^{\mathrm{T}}$	$\mathrm{J}.m^{-3}$
$\mathrm{FOM}^{\mathrm{T}}$	$d_{ij}^2 \big/ \varepsilon_{jj}^{\mathrm{T}}$	$m^3.\mathrm{J}^{-1}$
$\mathrm{FOM}^{\mathrm{S}}$	$d_{ij}^2 \big/ s_{ii}^{\mathrm{E}} s_{ii}^{\mathrm{D}} \varepsilon_{jj}^{\mathrm{T}}$	$\mathrm{J}.m^{-3}$
FOM^{py}	$p^2 / \varepsilon_{33}^{\mathrm{T}}$	$\mathrm{J}.m^{-3}\mathrm{K}^{-2}$

factor to estimate the effectiveness of thermal harvesting from Sebald et al. [29]:

$$k_{\mathrm{py}}^2 = \frac{p^2 \Theta_{\mathrm{M}}}{c_{\mathrm{E}} \varepsilon_{33}^{\mathrm{T}}} \tag{1.32}$$

where Θ_{M} is the maximum temperature during the working cycle, and c_{E} the volume specific heat ($\mathrm{J}m^{-3}\mathrm{K}^{-1}$). This nondimensional quantity is also called electrothermal coupling and it has similar meaning to the piezoelectric coupling. Following the coupling, we can define the FOM for energy harvesting case as in [30]:

$$\mathrm{FOM}^{py} = \frac{p^2}{\varepsilon_{33}^{\mathrm{T}}} \tag{1.33}$$

We can see the similarities with piezoelectric FOMs, whereas in this case instead of using the piezoelectric strain coefficient we use the pyroelectric coefficient over the dielectric permittivity. In Table 1.4, the reader can find a summary of the definitions given so far in this section.

1.4.6 Quality Factor

Among the parameters describing resonators or sensors, one of particular interest is the quality factor (Q or *Q-factor*). This quantity indicates the amplitude ratio or sharpness at resonance for the electro-mechanical system, and it is very significant in assessing the amplitude of displacement and strain in such conditions. Experimentally it is extracted from the full width at half maximum of the real part of frequency response :

$$\mathrm{Q} = \frac{f_0}{\Delta f} \tag{1.34}$$

where f_0 is the resonance frequency of the system. Moreover, the Q-factor in general is used to estimate the equivalent damping of the system ζ, defined as $\zeta = 1/2Q$. It is worth to mention that when we deal with electro-mechanical systems, Q is related to both electrical and mechanical losses, and eventually the total quality factor will be ruled by a combination of them. Moreover, the quality factor for a dielectric material is related to $\tan\delta$, or dielectric losses. Usually, this value is considerably small ($\tan\delta < 0.01$) typically leading to a $Q > 100$. This means that for energy harvesters based on high quality factor materials, the dielectric losses are negligible. Otherwise, in terms of mechanical Q-factor, viscous damping can have important consequences in terms of losses for the system, so the choice of materials for substrates have to be carefully considered during design phase. Eventually, for a linear device, it is desirable to keep mechanical damping as low as possible in order to have high output power. But the higher the quality factor the narrower will be the bandwidth of the harvester. In such configuration the resonance of the device will have to match the one from the excitation source, otherwise a significant amount of energy will not be transferred to the system.

1.5 Energy Harvesting Materials

In this section we will discuss briefly about Pb-based and Pb-free piezoelectric materials, analyzing their main characteristics and use in energy harvesting. The electro-mechanical coupling factor and relative FOMs will be presented for each material and compared to the specific case of $LiNbO_3$. A selection of works is also presented with relative references regarding the state of the art of MEMS and mesoscale piezoelectric energy harvesters.

1.5.1 Pb-based Materials

Lead containing materials are commonly known as the best performing materials commercially available. PZT ($PbZr_{1-x}Ti_xO_3$) was discovered in USA during the 1950 and since then it has found various fields of applications, due to its high power output and significant electro-mechanical coupling. In particular, it became the preferred material used as film or bulk in piezoelectric harvesters and in other fields of application [31]. This material has perovskite structure (Fig. 1.11a), in ABO_3 form, where the Pb occupies A position (blue sites) and Zr or Ti occupy the B (violet sites) position in the lattice, while oxygen ions are arranged as an octahedral structure (green sites).

PZT is a ferroelectric ceramic, hence it can be poled with strong DC field at temperature above or close to Curie temperature. In this way the domain walls can rearrange their structure and follow the polarization direction in order to increase the piezoelectric response. For a given temperature and content of Zr, the ferroelectric phase of the material can change, having tetragonal (4mm) structure below 52% Zr, or trigonal (3m) structure above the Zr content threshold. A full representation for the piezoelectric strain tensor anisotropy for the tetragonal case is in Fig. (1.11b). A distinction between the two phases

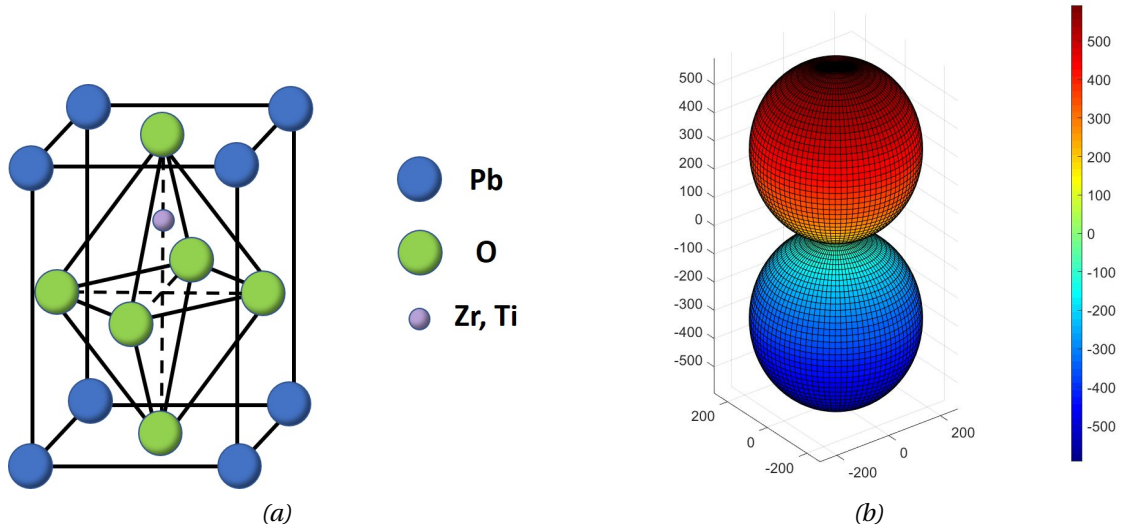

(a) *(b)*

Figure 1.11: PZT-5H properties below Θ_c: (a) tetragonal phase for PZT unit cell, (b) representation of piezoelectric tensor for PZT-5H ceramic in pC/N.

is called morphotropic phase boundary (MPB), which is a mix of the two aforementioned phases (Fig. 1.12). MPB is important because of the optimal piezoelectric and dielectric properties achievable in this composition range.

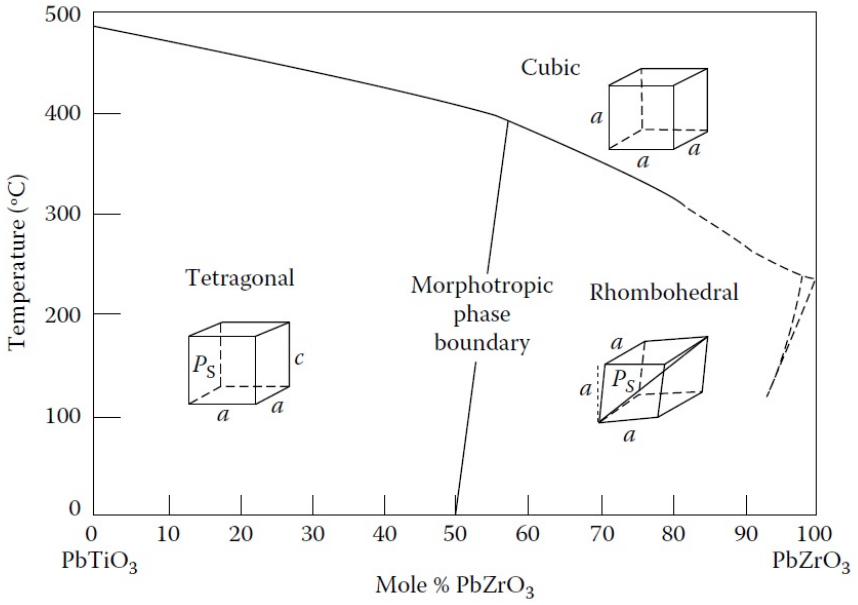

Figure 1.12: Phase diagram of PZT from [32]

There are many kinds of PZT ceramics commercially available, they distinguish themselves by the *hardness* of the bulk ceramic. For *soft* ceramics, as in PZT-5H, the material is doped with Nb or Ta ions, which are improving the domain wall motion. Otherwise, for *hard* ceramics, like PZT-8, Fe or Sc ions are used as dopants to weaken domain wall motion.

Normally, the resulting piezoelectric strain tensor for poled PZT ceramics can be represented as:

$$d = \begin{pmatrix} 0 & 0 & 0 & 0 & d_{15} & 0 \\ 0 & 0 & 0 & d_{15} & 0 & 0 \\ d_{31} & d_{31} & d_{33} & 0 & 0 & 0 \end{pmatrix} \tag{1.35}$$

In this case the piezoelectric coefficients are just three independent values: d_{31}, d_{33}, d_{15}. Regarding other basic properties, the dielectric and elastic properties will be given by:

$$\varepsilon = \begin{pmatrix} \varepsilon_{11} & 0 & 0 \\ 0 & \varepsilon_{11} & 0 \\ 0 & 0 & \varepsilon_{33} \end{pmatrix} \tag{1.36}$$

$$s = \begin{pmatrix} s_{11} & s_{12} & s_{13} & 0 & 0 & 0 \\ s_{12} & s_{11} & s_{13} & 0 & 0 & 0 \\ s_{13} & s_{13} & s_{33} & 0 & 0 & 0 \\ 0 & 0 & 0 & s_{44} & 0 & 0 \\ 0 & 0 & 0 & 0 & s_{44} & 0 \\ 0 & 0 & 0 & 0 & 0 & s_{66} \end{pmatrix} \tag{1.37}$$

Due to the symmetry of these ceramics there are only two independent dielectric coefficients (ε_{11} and ε_{33}) found in a diagonal matrix, while the compliance has just five coefficients, reported in a highly symmetric matrix. The transverse coupling, k_{31}, of PZT is among the highest values, and ranges from 0.3 to 0.5 [33], while the Curie temperature represents an issue, ranging from 150°C to 350°C depending on the composition of the ceramic.

Also PZT thin film deposition is widely studied because of a large span of applications from acoustics, actuation and in the last years also MEMS and meso-scale energy harvesting. The sintering processes involved are usually sol-gel and sputtering [34, 35]. Remarkable example in terms of energy harvesting performances were shown in several papers, starting from Muralt et al. [36], where the implementation of sputtered PZT thin films was firstly presented on Si substrate using inter-digitated electrodes (IDTs) (Fig 1.13a), attaining for a micro device 1.4 µW at 870 Hz for an acceleration of 2 g. Later on, it was shown also the possibility of optimizing IDTs design to enhance the performance of the harvester [37] in thickness mode. More recently, harvesting technology has moved towards metal substrates, in order to improve device performances and robustness. For instance, Lin et al. [38] deposited by areosol a high-quality PZT thick film on stainless steel, and investigated both the harvesting performances of the device in air and vacuum conditions, achieving a maximum of 241.6 µW at 104.4 Hz under 1.5 g acceleration level (0.01 Torr). In a later work done by the same group [39], Wu et al. compared PZT harvesters with identical design fabricated on stainless steel and silicon, showing better performances (power

increased by over 30%) and reliability in the case of metal substrate. Eventually, Kuo et al (2016) [40], fabricated thick PZT films (15 µm) in bimorph configuration (two piezoelectric layers with a central shim) on stainless steel, obtaining 423 µW at 143.5 Hz for 1.5 g acceleration level. More recently, Yeo et al. fabricated PZT films bimorphs on flexible Ni foils by sputtering, obtaining one of the highest power densities for a lead-based MEMS harvester, namely 60 µW at 70 Hz (0.5 g) [41], further optimizing thickness (up to 5.4 µm thick layer) and shape for hybrid configuration with magnet tip mass [42] (Fig. 1.13b).

Significant development was achieved also with PZT ceramics used in quasi-bulk form (thick films > 10 µm). For instance, Aktakka et al. performed AuIn solder and parylene bonding between silicon on insulator (SOI) and PZT-5A wafers [43], and then thinned the active layer down to 20 µm. The fabricated MEMS harvester attained 2.74 µW at 167 Hz for 0.1 g input acceleration [44]. Thereafter, Tang et al. [45] fabricated a 57 µm PZT ceramic film in unimorph configuration, by means of phosphor-bronze bonding and mechanical lapping, achieving 321 µW at 100.8 Hz for high acceleration applications (up to 3 g). More recently, Yi et al. [46] presented a MEMS scale bimorph harvester using thinned PZT (53 µm and 76 µm layers), achieving 0.979 mW at 77.2 Hz with 3.5 g acceleration level. In both cases, the ceramic was bonded using conductive epoxy on metal substrates.

Recently, whenever PZT ceramics are used in bulk form (thickness > 200 µm), the harvesters are designed to work with wider frequency bandwidth and lower acceleration levels for mesoscale and non-linear applications. Dhakar et al. [21], proposed a design with a composite beam formed by a PZT bimorph and a polymer beam, able to resonate at 36 Hz, increasing the power output by 3.12 times compared to a stand alone bimorph at 0.1 g, and with wider bandwidth (from 5 Hz up to 16.4 Hz). In other works, macrofiber composite (MFC) are used, these harvesters are fabricated with piezo-fibers surrounded by an epoxy matrix and covered with a Kapton shell [47]. Tang et al. [48] used piezoelectric MFC bonded to a metal substrate and coupled with magnet to increase the frequency bandwidth, achieving 0.75 mW power output at 18 Hz with 0.1 g acceleration. In a similar approach Arrieta et al. [49], used commercially available PZT bimorphs (QuickPack) to investigate broadband harvesting for cantilevered bi-stable composites, obtaining 7.07 mW at 20 Hz (0.25 g).

Other interesting lead based compounds are PMN-PT ($Pb[Mg_{1/3}Nb_{2/3}]O_3 - PbTiO_3$) or PZN-PT ($Pb[Zn_{1/3}Nb_{2/3}]O_3 - PbTiO_3$). These materials are known also as relaxor ferroelectrics and have the advantage of being available also in single crystal form, grown by modified Brigdman technique [50]. Especially in their MPBs composition, they show low dielectric losses, high coupling ($k_{33} > 0.8$), mono-domain structure, and orientation dependent properties [51]. On the other hand, they are quite brittle, expensive, and have low Curie temperature. Due to their high temperature sensitivity the range of application is mostly room temperature, with Θ_c being around 130-170°C. Their integration is then limited to ultrasonic transducers and actuators (for instance in medical applications), and

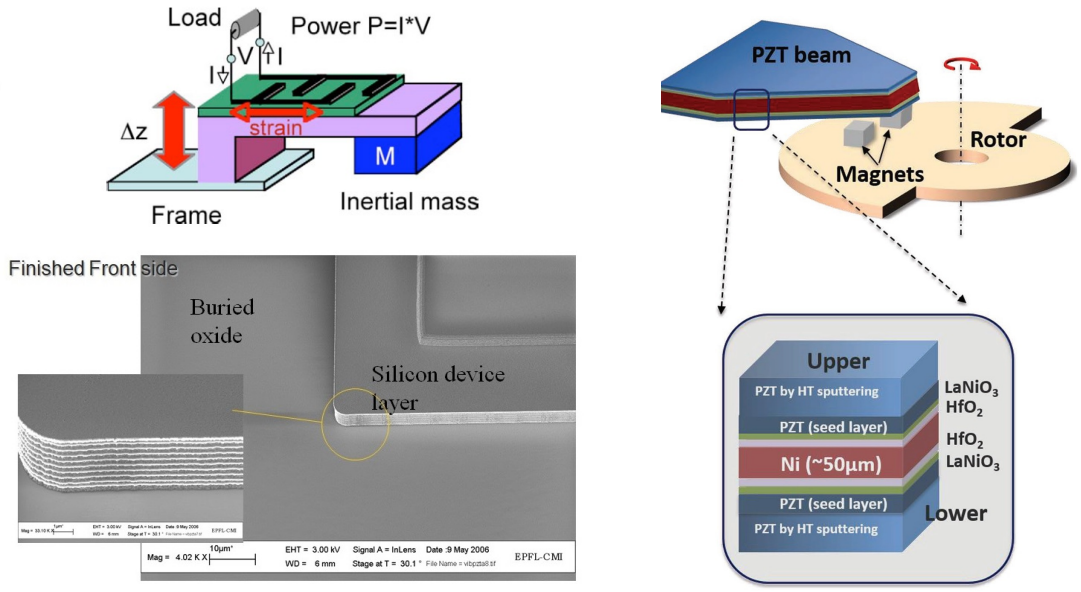

(a) *(b)*

Figure 1.13: Harvesters based on PZT films: (a) exploitation of d_{33} with IDTs on Si cantilever [36]; (b) best recent work on sputtered PZT thick films on metal substrate [41]

PZT is normally preferred for energy harvesting purposes.

In some early works, PMN-PT single crystal harvesters were fabricated bonding with epoxy on aluminum substrates for mesoscale application by Erturk et al., achieving 138 $\mu W.g^2.cm^{-3}$ at 1744 Hz [52], and later by Sun et al. in same configuration obtaining 0.586 mW at 174 Hz for 0.23 g acceleration level [53]. PMN-PT was extensively used also to investigate non-linear electronic interface for piezoelectric harvesting by Lefeuvre and Badel [54, 55], while PZN-PT is used to investigate highly coupled harvesters by Gibus et al. [56]. More recently a comparison of PZT, PMN-PT and PZN-PT was presented in [57], where the experimental results indicated that PMN-PT and PZN-PT single crystals can significantly outperform PZT ceramics energy harvesters, attaining 0.43 mW at 37.5 Hz for 0.3 g acceleration level using PZN-PT transducer.

A summary of the Pb-based energy harvesters state of the art discussed so far, is presented in Table 1.5. Typically, reducing the volume increases the working frequency of the device, and high acceleration levels (> 1 g) are needed to generate considerable power output. Devices based on large volume of PZT and working at low frequency, normally have the highest power densities.

1.5.2 Pb-free Materials

The very first piezoelectric material to find its way in industrial applications was $BaTiO_3$ [58, 59]. This material has tetragonal structure at room temperature, and belongs to Perovskite family (point group 4mm). It has Curie temperature at 120°C, and its properties are in large part dependant on composition and dopants concentration. It was recently

Table 1.5: Comparison of Pb-based piezoelectric harvesters.

Material	Power (μW)	$\vec{a}$ (g)	Frequency (Hz)	Power density ($\mu W.cm^{-3}g^{-2}.Hz^{-1}$)	Ref.
PZT	1.4	2	870	1.57	[36]
PZT-5A	2.74	0.1	167	60.77	[44]
PZT	423	1.5	143.5	26.96	[40]
PZT	241.6	1.5	104.4	79.36	[38]
PZT	9	0.15	72	2576.79	[41]
MFC	1430	0.29	27.8	10366.76	[48]
PZT	7070	0.25	20	11937.53	[49]
PZT	321	3	100.8	9.56	[45]
PZT	979	3.5	77.2	33.39	[46]
PZT-5A	40	0.2	102.08	272.12	[21]
PMN-PT	-	-	1744	0.08	[52]
PMN-PT	586	0.23	174	314.67	[53]
PZN-PT	430	0.3	37.5	4423.87	[57]

used in structures with high porosity in order to increase the piezoelectric response and the energy harvesting figure of merit in thickness mode, $(FOM_{33}^{T})^{-1} = 267$ GJ.m^{-3} [60].

Non-ferroelectric piezoelectric materials such as ZnO and AlN and their derivatives, have much lower k_{31} and k_{33} factor than PZT (by one order of magnitude, typically), but offer compatibility with conventional integrated circuit technology fabrication processes (Complementary Metal Oxide Semiconductor - CMOS). They present hexagonal symmetry and wurtzite structure (point group 6mm) giving as a result similar configuration of the piezoelectric tensor as in PZT.

ZnO is usually sputtered as thin films on several types of substrates, and used especially for shear and bulk acoustic resonators. Regarding energy harvesting, in [61], it was implemented in piezoelectric MEMS vibration energy harvesters with two piezoelectric elements for higher output performance, where the energy harvester was fabricated on a Si wafer by means of standard micro-machining techniques. The resonance frequency was 1300.1 Hz, achieving 1.25 μW for 1 g acceleration level.

Also AlN is compatible with CMOS technology, and several results were promising for AlN films integration in energy harvesting. One of the first successful implementations of the material was by Marzencki et al [62], where AlN was sputtered on a Si beam, achieving 0.8 μW at 1495 HZ for 2 g acceleration level (Fig. 1.15a). Similar results were observed by Elfrink et al [63], where in vacuum conditions an AlN MEMS device was capable to harvest 32 μW at 1 g having a quality factor of 810 [64]. More recently Jia et al. [65] obtained a peak

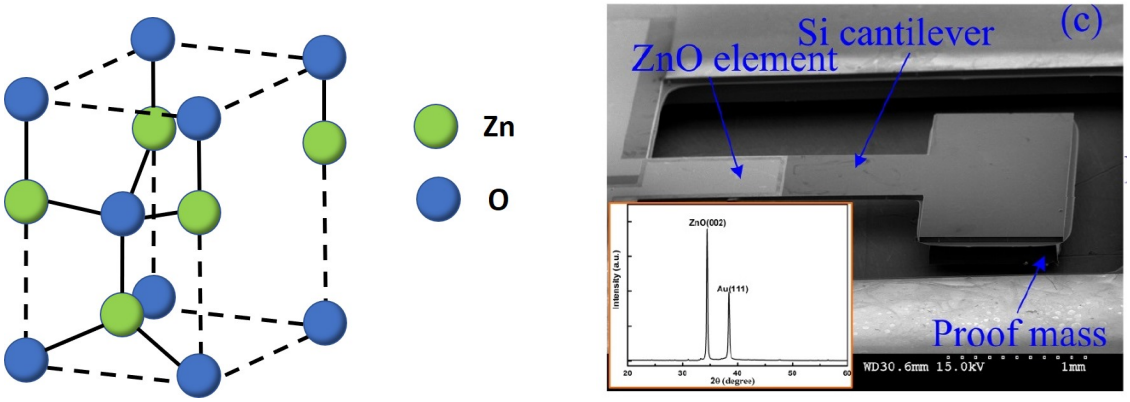

(a) *(b)*

Figure 1.14: Wurtzite material features: (a) Atomic structure for hexagonal unit cell in ZnO; (b) ZnO piezoelectric cantilevers from [61].

power output of 20.5 µW at 0.28 g (@210 Hz) for an AlN-on-SOI cantilever with 70% of its beam dedicated to housing a silicon end mass. Alamin Dow et al. [66] achieved 10 µW at 0.75 g, further reducing the resonance frequency of the cantilever (186 Hz). Andosca et al. [67] proposed an AlN MEMS device capable of working at 58 Hz, that generated 63 µW at 0.7 g. Concerning AlN transducers on metal substrate, Cao et al [68] deposited by sputtering AlN on stainless steel and implemented a copper tip mass, obtaining 5.13 µW at 69.8 Hz for 1 g acceleration. Moreover, it was observed that doping AlN with Sc, increases piezoelectric properties and electro-mechanical coupling [69, 70]. Recently AlScN was considered as transducer for vibrational energy harvesting, but not implemented as such [71, 72]. Le Van Minh et al. doped AlN with MgZr [73], and fabricated a MEMS scale device with 792 Hz resonance frequency, and harvesting 1.3 µW at 0.82 g.

Regarding the potassium and sodium niobate family (KNN), the implementation to energy harvesting resulted promising on silicon substrate. This family of material belongs to the poled ceramics group, so has similar symmetry as PZT. These piezoelectric ceramics are developed using $NaNbO_3$ and $K_{0.5}Na_{0.5}NbO_3$. For instance, Kanno et al. [75] fabricated one of the first prototypes of KNN vibrational energy harvesters by RF-sputtering, achieving 1.1 µW at 1036 Hz (@1 g), and compared the results with similar unimorph devices with PZT, having 1 µW output in same conditions. More recently, Shiraishi et al. deposited KNN by hydrothermal method on metal foils [76], obtaining 126 Hz resonance frequency and 7.7 µW at 1.02 g, while Won et al. used chemical solution deposition, adding small concentration of Mn to enhance the piezoelectric properties of the film [77], obtaining a power output of 3.62 µW at 132 Hz (1 g). Among the highest power densities achieved with KNN there is the work of Le Van Minh et al. [74]. In this work, the device was fabricated on silicon substrate with four tip masses in order to have large frequency bandwidth and high power output (Fig. 1.15b), obtaining 0.73 µW at 1509 Hz (1.02 g). Anyways, due to the challenges of optimization synthesis and processing of

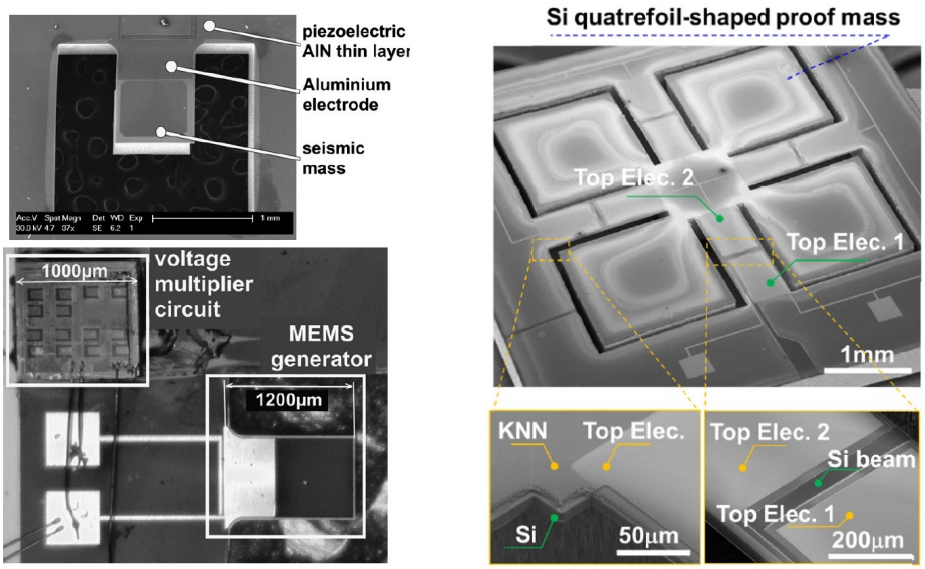

(a) *(b)*

Figure 1.15: Pb-free energy harvesters: (a) AlN based silicon cantilever from [62]; (b) non-linear KNN quad-cantilever harvester [74]

this material, upscaling to industrial level remains one of the most important issues in its implementation.

$BiFeO_3$ represents also an interesting material for energy harvesting. Several works are reporting the epitaxial growth of $BiFeO_3$ on silicon or $SrTiO_3$ single crystals by magnetron sputtering [78, 79] for energy harvesting applications, having 151.2 Hz resonance frequency with 2.4 µW power output at 0.3 g. Otherwise $BiFeO_3$ films can be fabricated with sol-gel process on silicon as in [80, 81], where Yoshimura et al. achieved 98 Hz resonance for 2 nW power output (0.05 g).

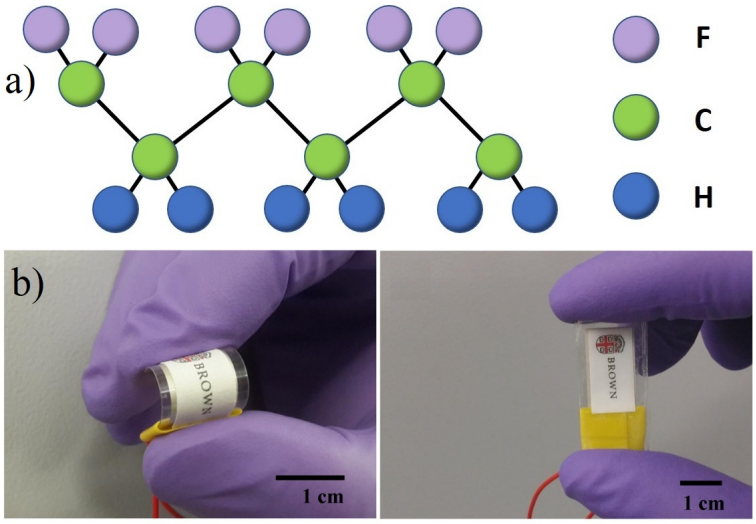

Figure 1.16: PVDF flexible energy harvesting: (a) polymeric chain structure; (b) flexible energy harvester on paper from Won et al [82].

PVDF is a polymer material that has been used in energy harvesting due to its flexibility and robustness. It becomes piezoelectric after stretching during sintering, to induce a polar β-phase. Fig. (1.16a) depicts how carbon atoms are forming a polymeric chain with fluorine and hydrogen atoms. This chain can be poled through electric field as in the case of ceramics. They are used on flexible substrates like plastic polymers or on paper (Fig. (1.16b) [82]. They have small strain piezoelectric coefficient, but due to a small permittivity, the electro-mechanical coupling is comparable to AlN or ZnO. In energy harvesting they can be used in body-motion devices. Due to relatively easy manufacturing process, they can be used with large surface and mass, as in [83], where Song et al. achieved 112.8 μW at 34.4 Hz (0.5 g). However, the drawbacks for PVDF are the low figure of merit and high sensitivity to temperature (maximum 150°C). Rammohan et al. implemented a multilayer and a multistep PVDF harvester, with partial active cover of the beam, obtaining 4.53 μW at 33.3 Hz and 8.59 μW at 30.7 Hz respectively, in same acceleration conditions (0.5 g) [84].

A summary of the Pb-free energy harvesters state of the art is presented in Table 1.6. The more mature Pb-free material so far is AlN, which in terms of power density is showing comparable results to Pb-based MEMS devices, especially when packaged in vacuum conditions.

1.5.3 Lithium Niobate

$LiNbO_3$ single crystals are industrially produced piezoelectric materials easily accessible, rare-earth and toxic-element-free, cheap, available in form of wafers (with diameter up to 6 inches), widely exploited for developments of acoustics and optical devices [85], and presenting similar efficiency in energy harvesting as commonly used PZT. The major advantages of $LiNbO_3$ over PZT are: (i) extremely chemically inert material; (ii) very high Curie temperature (> 1150 °C) thus compatible with EH at high temperatures (PZT limit < 150 °C). However, the $LiNbO_3$ applications in acoustics are limited to 300 °C by the increased losses at high temperatures due to ionic conductivity. It is important to note that the requirements in terms of losses are much lower in the case of energy harvesting applications. $LiNbO_3$ is a ferroelectric material that belongs to 3m point group at room temperature. In Fig. (1.17a), the planar sheets of oxygen are inter-spaced by octahedral interstices of Li or Nb and vacancies, defining P_S along Z-axis. The best quality single crystal wafers commercially available are grown by Czochralski technique [86], and normally present congruent composition. The composition of this type $LiNbO_3$ is non-stoichiometric, and it corresponds to the point where the crystal has 48.38 mol % of Li_2O. In Fig. (1.17b) the phase diagram of $LiNbO_3$ is presented from [87], here the point where the liquid and solid phases are in equilibrium occurs at 1240°C. Above this threshold we have the point where $LiNbO_3$ is stoichiometric (50 mol % of Li_2O), but single crystals with this composition have homogeneity issues due to the non equilibrium of its constituent

Table 1.6: Comparison of Pb-free piezoelectric harvesters.

Material	Power (μW)	$\overrightarrow{a}$ (g)	Frequency (Hz)	Power density ($\mu W.cm^{-3}g^{-2}.Hz^{-1}$)	Ref.
AlN	0.8	2	1495	0.8	[62]
AlN	17	0.64	353	-	[64]
AlN	20.5	0.28	210	249.03	[65]
AlN	10	0.75	186	1.19	[66]
AlN	63	0.7	58	155.85	[67]
AlN	5.13	1	69.8	0.64	[68]
(MgZr)AlN	1.3	0.82	792	10.06	[73]
BFO	2.4	0.3	151.2	-	[79]
BFO	0.002	0.05	98	27.07	[80]
KNN	1.1	1	1036	0.09	[75]
KNN	7.7	1.02	126	14.29	[76]
KNN	3.62	1	132	9.94	[77]
KNN	0.731	1.02	1509	4.43	[77]
PVDF	112.8	0.5	34.4	98.92	[83]
PVDF	8.59	0.5	30.8	-	[84]
ZnO	1.25	1	1300	3.02	[61]

liquid and solid phases. The experimental detail regarding piezoelectric and elastic properties of the material can be found in [88, 89].

$LiNbO_3$ belongs to 3m point group, therefore it has more independent piezoelectric strain coefficients than PZT or AlN. The piezoelectric matrix has the following form:

$$d = \begin{pmatrix} 0 & 0 & 0 & 0 & d_{15} & -2d_{22} \\ -d_{22} & d_{22} & 0 & d_{15} & 0 & 0 \\ d_{31} & d_{31} & d_{33} & 0 & 0 & 0 \end{pmatrix} \tag{1.38}$$

In this case instead of just three coefficients, there are four independent coefficients: d_{22} d_{31}, d_{33}, d_{15}. Especially for the case of d_{15} the value is much higher than others in transverse or thickness mode (d_{31} or d_{22},d_{33}). This means that we can use specific rotations based on our application, in order to optimize the electro-mechanical coupling of our device. In order to investigate k_{ij} we need to take into account both the dielectric and elastic properties of $LiNbO_3$. In terms of permittivity the matrix form is similar to Eq. (1.36), but the compliance matrix is substantially different, having the following form:

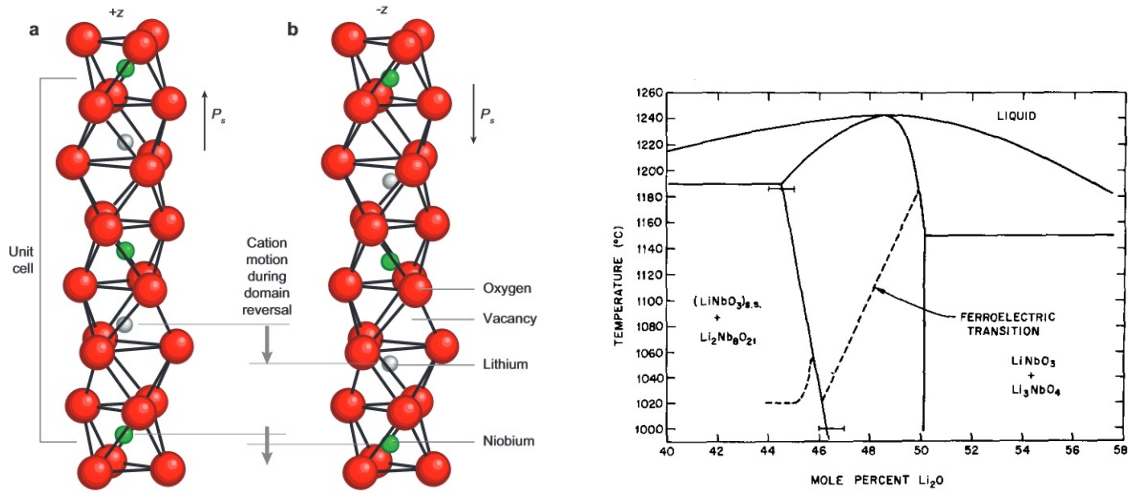

(a) *(b)*

Figure 1.17: $LiNbO_3$ properties: (a) crystal structure of $LiNbO_3$ [90]; (b) phase diagram [87]

$$s = \begin{pmatrix} s_{11} & s_{12} & s_{13} & s_{14} & 0 & 0 \\ s_{12} & s_{11} & s_{13} & -s_{14} & 0 & 0 \\ s_{13} & s_{13} & s_{33} & 0 & 0 & 0 \\ s_{14} & -s_{14} & 0 & s_{44} & 0 & 0 \\ 0 & 0 & 0 & 0 & s_{44} & 2s_{14} \\ 0 & 0 & 0 & 0 & 2s_{14} & 2(s_{11}-s_{12}) \end{pmatrix} \tag{1.39}$$

In this case we have six independent coefficients, where an additional shear term is introduced, s_{14} and $s_{66} = 2(s_{11} - s_{12})$. Even in this case it is important to consider these coefficients, because during the rotation they will have an impact on the relative s'^{E} used to calculate the electro-mechanical coupling. In Table (1.7) the material properties for single crystal $LiNbO_3$ are given [91].

Table 1.7: Physical properties for Z-cut $LiNbO_3$

Compliance	s^E_{11}	s^E_{12}	s^E_{13}	s^E_{14}	s^E_{33}	s^E_{44}
$(10^{-12}\ GPa^{-1})$	5.78	-1.01	-1.47	-1.02	5.02	17
Piezoelectric	d_{22}	d_{31}	d_{33}	d_{15}		
$(pC.N^{-1})$	21	-1	6.2	68		
Permittivity	$\varepsilon^T_{11}/\varepsilon_0$	$\varepsilon^T_{33}/\varepsilon_0$				
	84	30				

In order to investigate $LiNbO_3$ orientations, we have to make a transformation of axis to optimize the piezoelectric response of the material. $LiNbO_3$ piezoelectric tensor is plotted in tri-dimensional representation in figure [1.18]. Both positive and negative values

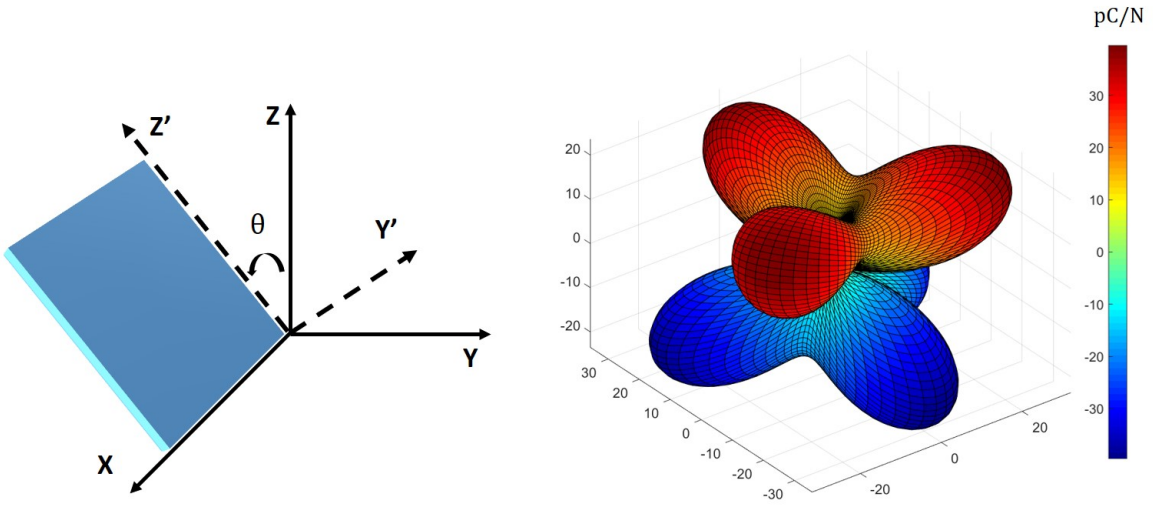

Figure 1.18: (a) Representation of piezoelectric element rotated around X-axis. (b) Tridimensional piezoelectric tensor for $LiNbO_3$.

of the tensor are represented. The anysotropy is representative of 3m group in similarly to $LiTaO_3$. We can rotate the piezoelectric tensor to find the optimal orientation as in [92]. The polarization is normally along Z-axis, and this leads in using d_{31} with parallel plate electrodes, or d_{33} with IDTs. But in the case of $LiNbO_3$, we are considering single crystal cuts that are rotated around X-axis. Generally they are defined using IEEE standard [22] notation as (YXl)/θ°, which means that the piezoelectric plate has length (l) along X-axis and thickness along Z-axis being parallel to Y-axis for a given rotation (θ). For $LiNbO_3$, as found in Nakamura's work [93] the piezoelectric polarization remains along Y'-axis (i.e. rotated direction 2), while the length of the beam can be oriented along both X- or Z'-axis (i.e. direction 1, 3). Performing the rotation for the given angle in this notation gives the commonly known Y-cuts. Anyways in literature, sometime the reported orientation is 32 [94, 95] or 31 [96]. Furthermore, a full theoretical study for Z oriented $LiNbO_3$ is given by Yue and Yi-jiang in [91], where the notation adopted was the regular one with the investigation of k'_{31} and k'_{33}. In particular, $LiNbO_3$ presents dielectric constant much lower than lead-based piezoelectric materials, which is very interesting in terms of electro-mechanical coupling. Moreover, in form of single crystal $LiNbO_3$ has very high quality factor and low dielectric losses (typically under 0.1%) [97].

Energy harvesting demonstrations were investigated so far by using industrially available $LiNbO_3$ wafers with thickness of 300 to 1000 μm. The use of $LiNbO_3$ as transducer has been considered in some papers using inverted domain bulk plates or simple bulk single crystal. For instance, Funasaka et al. [98] fabricated a piezoelectric generator where an impact hammer applied vibrations to $LiNbO_3$ 140°-Y crystal cut beam and electrical energy was yielded from the vibrations, obtaining 10 V in open circuit conditions and high resonance frequency 5.17 kHz. Nakamura et al. [93] identified $LiNbO_3$ 137°-Y crystal

cut, as the most suitable for bending actuation. This orientation presented piezoelectric strain coefficient $d_{23} = 30$ pC/N, very low dielectric constant ($\varepsilon^{T}_{22}/\varepsilon_0 = 58.8$), and thus high transverse electro-mechanical coupling factor, $k_{23} = 0.51$. Unfortunately, this single crystal orientation is not commercially available, and can be purchased only as custom cut. More recently, Vidal et al.[96], designed and tested a low-frequency vibration energy harvester, using the same reversed domain technology and obtaining a thick bimorph $LiNbO_3$ 128° Y-cut patch (1 mm) bonded with epoxy on a metal substrate. However, they achieved low resonance frequency 32 Hz and high power density 9.2 $mW.g^{-2}$ with a very large resistive load 65 MΩ, because of very poor capacitance (38 pF). Moreover, Bedekar et al. [99], comparatively studied mechanical energy harvesting from single crystal materials (YCOB, LGS, and $LiNbO_3$) for high temperature applications, where Y-36° bulk single crystal $LiNbO_3$ was mechanically excited in thickness mode. Also Kawamata and Morita worked with $LiNbO_3$ (Y-36° crystal cut) in thickness mode as stack actuator [100, 101], finding it suitable for a multilayered device.

In the case of micro-energy harvesters where lateral dimensions are limited, thick wafers cannot be used due to issues in impedance–matching with energy harvesting circuits as well as structural compatibility with the substrate. Moreover, bulk $LiNbO_3$ crystals are very brittle and only low displacement can be attained. Therefore, $LiNbO_3$ *film* technology has to be implemented in vibrational energy harvesting to overcome such issues and provide realistic operations. Despite their promising properties, the application of $LiNbO_3$ films in piezoelectric vibrational energy harvesting is still very little studied and considerable efforts have to be done towards their integration in the conventional processing of MEMS and energy harvesting devices. Eventually, we have to identify what is the optimized orientation for our application among the commercially available $LiNbO_3$ single crystal cuts, considering its electro-mechanical properties as well as the possibility of integration in a suitable micro-fabrication process.

1.6 Comparison of Piezoelectric Properties

Now we can compare all material with $LiNbO_3$ using the FOMs and coupling presented in the previous section (1.4.2). In Table (1.8) we present the most used materials for energy harvesting applications in transverse mode. For $LiNbO_3$ we reported the values of transverse coupling k_{23}.

Clearly, lead materials have a net advantage over the others in terms of coupling and FOMs. Excluding the case of $LiNbO_3$ (YXl)/137°, all other Pb-free materials have hardly the same magnitude of electro-mechanical coupling. One exception is represented by $BaTiO_3$, which as $LiNbO_3$ is a ferroelectric, and has coupling in the same order of magnitude of PZT-5A. Generally speaking wurtzites (ZnO and AlN) have lower coupling and FOMs, but they present other advantages: bio-compatibility, implementation with CMOS technology and decent features. While in terms of Q-factor, they perform very well, es-

pecially AlN. Polymers on the contrary have low Q-factor, decent coupling and very low

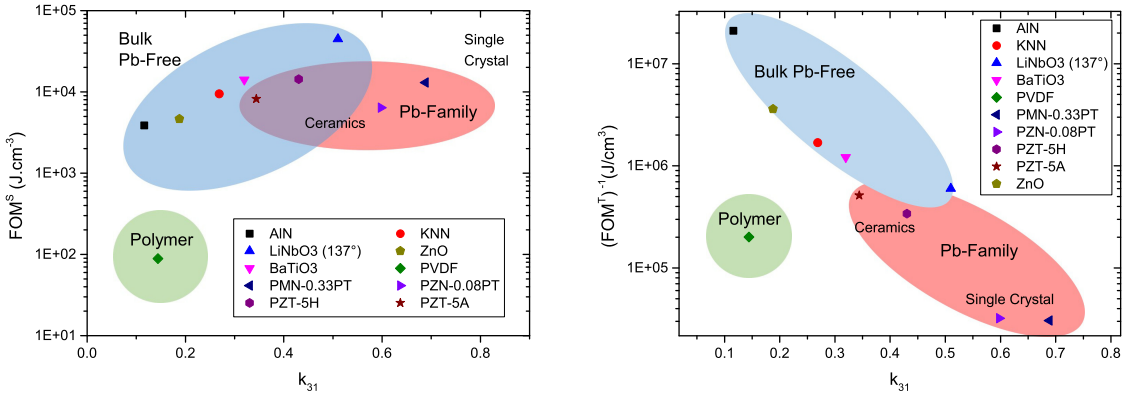

(a) *(b)*

Figure 1.19: Comparison of EH materials: (a) FOM for strain-driven harvesters; (b) FOM^{-1} for stress-driven harvesters.

stiffness. These features are interesting for sensor applications or human body movement energy harvesting, where robustness and flexibility have priority over high coupling.

Relaxor ferroelectrics such as PMN-PT and PZN-PT have the best FOM for stress-driven harvesters and very high coupling factor, but have the drawback of cost and brittleness, which drives them into specific fields of application, and rarely in energy harvesting.

Eventually, $LiNbO_3$ (YXl)/137° has the best overall compromise between coupling, FOMs and Q-factor. It has comparable FOMs with commonly used Pb ceramics (both *soft* and *hard*), and generally higher coupling, even if not as high as relaxors. Other advantages are the cost of manufacturing and the easy CMOS implementation, which would be interesting for industrial up-scaling.

Table 1.8: Comparison of transverse k_{31} and FOMs of piezoelectric materials.

Material	s_{11}^E (pm^2N^{-1})	s_{11}^D (pm^2N^{-1})	$\varepsilon_{33}^T/\varepsilon_0$	d_{31} (pCN^{-1})	k_{31}	$(FOM^T)^{-1}$ ($MJ.cm^{-3}$)	FOM^S ($KJ.cm^{-3}$)	Q_m	Ref.
AlN	3.5	3.5	9.5	2	0.12	21	3.9	10^3	[102]
$BaTiO_3$	8.1	7.24	168	35	0.32	1.21	14.1	400	[103]
KNN	8.2	7.6	496	51	0.27	1.69	9.5	-	[104]
$LiNbO_3$ (137° Y-cut)	6.7	4.9	58.8	30.0	0.51	0.6	52	10^4	[91]
PMN-0.33PT	69	36.3	8200	1540	0.69	0.03	13.1	>100	[105]
PZN-0.08PT	87	55.9	7700	1455	0.6	0.03	6.4	40	[106]
PZT-5A	16.4	14.5	1700	171	0.34	0.52	8.2	80	[33]
PZT-5H	15.9	12.9	3935	320	0.44	0.34	14.3	75	[33]
PVDF	239	234	13	23.9	0.14	0.20	0.09	17.2	[83]
ZnO	7.9	7.6	11	-5.2	0.19	3.6	4.7	-	[107]

1.7 Comparison of Pyroelectric Properties

In Table 1.9 the principal pyroelectric materials are presented, along with their properties and Curie temperature. Differently from the previous case, the coupling is very diverse for the reported materials, and it ranges between two orders of magnitude. Wurtizites have very low pyroelectric coefficient (AlN and ZnO), and even if they have low dielectric constant, their FOM^{py} is typically one order of magnitude lower than the perovskite counterpart. Other Pb-free materials (PVDF, KNN-LT and $BaTiO_3$) have higher FOM^{py} but still not comparable to PZT. Single crystal $LiNbO_3$ when in Z-cut orientation has de-

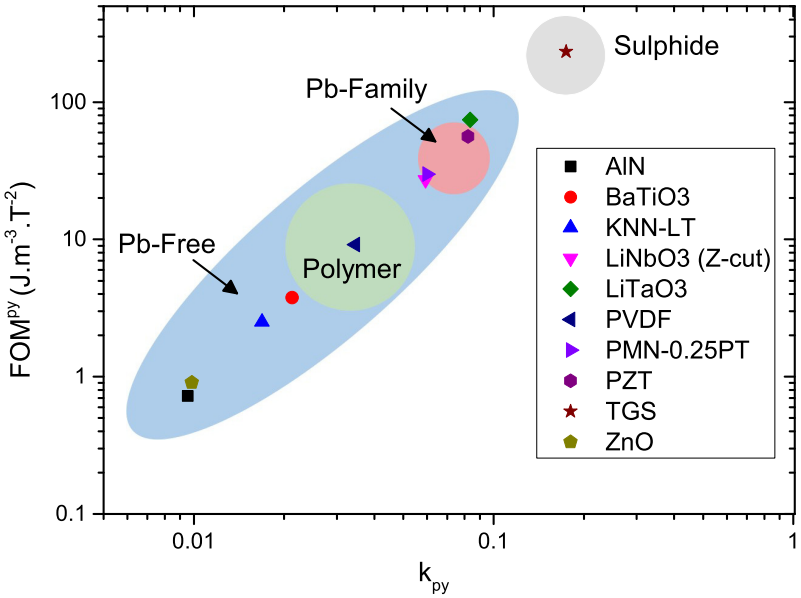

Figure 1.20: Comparison of pyroelectric coupling factor and FOM^{py}.

cent pyroelectric coefficient and the highest Curie Temperature, which could be useful in harsh environmental conditions. As a pyroelectric tranducer it has been studied in form of full wafer in some works [108, 109], achieving maximum power output at the temperature of 75-100°C. $LiTaO_3$ has very interesting figure of merit and decent Θ_c, and is already extensively used in pyorelectric sensor applications [110].

Pb-based materials such as PZT or PMN-PT have very interesting FOM^{py}, and PMN-PT has interesting properties for pyroelectric energy harvesting near the MPB [111]. TGS, which is the short name for $(NH_2CH_2COOH)_3H_2SO_4$, is a single crystal from glycine group. It has the highest FOM^{py} for pyroelectric energy harvesting, but due to his brittleness it is rarely used. Recently the use of thin films was introduced for harvesting by Ghane-Motlagh and Woias [112].

1.8 Conclusion

With this introduction I gave a general overview of what are the motivation and challenges regarding the implementation of energy harvesting for IoT applications. Where

Table 1.9: Comparison of pyroelectric materials k_{th} and FOM^{py}

Material	p ($\mu C.m^{-2}.K^{-1}$)	$\varepsilon^{T}_{ii}/\varepsilon_0$	C_E ($MJ.m^{-3}.K^{-1}$)	k_{py} T = 300 K	FOM^{py} ($J.m^{-3}.K^{-2}$)	T_c (°C)	Ref.
AlN	8	10	2.38	9.1e-5	0.72	N/A	[113]
$BaTiO_3$	200	1200	2.5	4.5e-4	3.76	120	[110]
KNN-LT	165	1230	2.63	2.9e-4	2.5	-	[113]
$LiNbO_3$ (Z-cut)	83	28.7	2.32	3.5e-3	27.1	1210	[110]
$LiTaO_3$	176	47	3.2	7e-3	74.5	665	[110]
PMN-0.25PT	746	2100	2.5	3.6e-3	29.9	-	[114]
PZT	380	290	2.5	6.8e-3	56.3	200	[115]
PVDF	27	9	2.3	1.2e-3	9.2	80	[110]
TGS	280	38	2.3	3e-2	233	49	[115]
ZnO	9.4	11	2.8	9.7e-5	0.91	N/A	[116]

the number of devices connected increases, the need of renewable power sources that can harvest energy in non-standard conditions is becoming much more important. Especially for the automotive sector, particularly interesting is the vibrational harvesting that can be exploited in different ways: electromagnetic, electrostatic and piezoelectric. As we may see in Table 1.3, different types of transducers come with diverse features. Because the range of frequency from vehicle vibration is limited (with peaks between 10 to 300 Hz), piezoelectric harvesting looks like a promising technology to be exploited for our application. Moreover, with ferroelectric materials, we could also exploit temperature variation close to the engine (T = 150 °C), or couple the piezoelectric effect with electromagnetic devices for hybrid harvesting. Moreover, I discussed about energy harvesting materials including ferroelectric and pyroelectric materials, presenting both a brief summary of the main properties in order to compare their performances. Therefore, terms of electro-mechanical coupling and figure of merits were introduced, as well as piezoelectric and pyroelectric harvesting applications. Considering different crystal structure we saw that ferroelectric materials have in general better performances as compared to wurtizite or polymers. In the state of the art especially for vibrational harvesting at mesoscale, Pb-based materials are dominating, excluding some notable exceptions. But most interesting, for MEMs applications, Pb-free materials are representing a good choice as well, and promising materials are coming up (AlScN or BFO). In particular, $LiNbO_3$ compared to Pb or Pb-free piezoelectrics, has demonstrated to be an interesting choice, showing high electro-mechanical coupling, low dielectric losses, high FOMs, and high Q-factor.

Therefore, in this thesis, we will investigate lead-free $LiNbO_3$ piezoelectric material as

transducer for energy harvesting applications, with special focus regarding its optimized material properties and electronic interface. Eventually, the objective of this work within ENHANCE project, it is to provide stabilized output voltage in 1-3 V range form the hybrid harvesters, with piezoelectric figure of merit of 20 GJ/m^3 and considerable mechanical quality factor (> 300). Furthermore, the design of high-performance energy harvesting systems with operational frequencies in the range of 10-500 Hz available in vehicles and sufficient power density (300-500 $\mu W/cm^2/g^2$), has to be developed for systems of compact dimensions (< 1 cm^3).

Bibliography

[1] D. Evans, "The Internet of Things. How the Next Evolution of the Internet Is Changing Everything," *CISCO white paper*, no. April, pp. 1–78, 2011.

[2] S. Boisseau, G. Despesse, and B. Ahmed, "Electrostatic Conversion for Vibration Energy Harvesting," *Small-Scale Energy Harvesting*, pp. 1–39, 2012.

[3] L. Gammaitoni, "There's plenty of energy at the bottom (micro and nano scale nonlinear noise harvesting)," *Contemporary Physics*, vol. 53, no. 2, pp. 119–135, 2012.

[4] STMicroelectronics, "Capacitive digital sensor for relative humidity and temperature," no. April, pp. 1–31, 2015.

[5] F. Y. Tsang, "Lithium battery," vol. 2, pp. 1–8, 2012.

[6] W. Xu, "GIV 2025 Unfolding the Industry Blueprint of an Intelligent World," *Huawei Tech.*, 2018.

[7] T. Nokes, S. Stephenson, A.-L. Kaar, J. Norris, J. Tweed, C. Brannigan, H. Sindano, and T. Scarbrough, "Preparation for collection and monitoring of real-world fuel consumptino data for light and heavy duty vehicle," no. 5, 2019.

[8] I. Neri, F. Travasso, R. Mincigrucci, H. Vocca, F. Orfei, and L. Gammaitoni, "A real vibration database for kinetic energy harvesting application," *Journal of Intelligent Material Systems and Structures*, vol. 23, no. 18, pp. 2095–2101, 2012.

[9] P. Mehne, F. Lickert, E. Bäumker, M. Kroener, and P. Woias, "Energy-autonomous wireless sensor nodes for automotive applications, powered by thermoelectric energy harvesting," *Journal of Physics: Conference Series*, vol. 773, no. 1, 2016.

[10] C. B. Williams and R. B. Yates, "Analysis of a micro-electric generator for microsystems," *Sensors and Actuators, A: Physical*, vol. 52, no. 1-3, pp. 8–11, 1996.

[11] S. Roundy and E. Takahashi, "A planar electromagnetic energy harvesting transducer using a multi-pole magnetic plate," *Sensors and Actuators, A: Physical*, vol. 195, pp. 98–104, 2013.

[12] N. G. Elvin and A. A. Elvin, "An experimentally validated electromagnetic energy harvester," *Journal of Sound and Vibration*, vol. 330, no. 10, pp. 2314–2324, 2011.

[13] Perpetuum, "Perpetuum Data Sheet," pp. 1–6, 2013.

[14] Y. Suzuki, D. Miki, M. Edamoto, and M. Honzumi, "A MEMS electret generator with electrostatic levitation for vibration-driven energy-harvesting applications," *Journal of Micromechanics and Microengineering*, vol. 20, no. 10, 2010.

[15] D. Isarakorn, D. Briand, P. Janphuang, A. Sambri, S. Gariglio, J. M. Triscone, F. Guy, J. W. Reiner, C. H. Ahn, and N. F. De Rooij, "The realization and performance of vibration energy harvesting MEMS devices based on an epitaxial piezoelectric thin film," *Smart Materials and Structures*, vol. 20, no. 2, 2011.

[16] Ö. Zorlu, E. T. Topal, and H. Külah, "A vibration-based electromagnetic energy harvester using mechanical frequency up-conversion method," *IEEE Sensors Journal*, vol. 11, no. 2, pp. 481–488, 2011.

[17] S. P. Beeby, R. N. Torah, M. J. Tudor, P. Glynne-Jones, T. O'Donnell, C. R. Saha, and S. Roy, "A micro electromagnetic generator for vibration energy harvesting," *Journal of Micromechanics and Microengineering*, vol. 17, no. 7, pp. 1257–1265, 2007.

[18] G. Despesse, J. J. Chaillout, T. Jager, J. M. Léger, A. Vassilev, S. Basrour, and B. Charlot, "High damping electrostatic system for vibration energy scavenging," *ACM International Conference Proceeding Series*, vol. 121, no. october, pp. 283–286, 2005.

[19] G. J. Sheu, S. M. Yang, and T. Lee, "Development of a low frequency electrostatic comb-drive energy harvester compatible to SoC design by CMOS process," *Sensors and Actuators, A: Physical*, vol. 167, no. 1, pp. 70–76, 2011.

[20] H. Wu, L. Tang, Y. Yang, and C. K. Soh, "A novel two-degrees-of-freedom piezoelectric energy harvester," *Journal of Intelligent Material Systems and Structures*, vol. 24, no. 3, pp. 357–368, 2013.

[21] L. Dhakar, H. Liu, F. E. Tay, and C. Lee, "A new energy harvester design for high power output at low frequencies," *Sensors and Actuators, A: Physical*, vol. 199, pp. 344–352, 2013.

[22] "IEEE Standard on Piezoelectricity: An American National Standard," in *ANSI/IEEE Std 176-1987*, 1988.

[23] C. D. Richards, M. J. Anderson, D. F. Bahr, and R. F. Richards, "Efficiency of energy conversion for devices containing a piezoelectric component," *Journal of Micromechanics and Microengineering*, vol. 14, no. 5, pp. 717–721, 2004.

[24] P. Muralt, "Piezoelectric thin films for mems," *Integrated Ferroelectrics*, vol. 17, no. 1-4, pp. 297–307, 1997.

[25] C. R. Bowen, H. A. Kim, P. M. Weaver, and S. Dunn, "Piezoelectric and ferroelectric materials and structures for energy harvesting applications," *Energy and Environmental Science*, vol. 7, no. 1, pp. 25–44, 2014.

[26] T. Rödig, A. Schönecker, and G. Gerlach, "A survey on piezoelectric ceramics for generator applications," *Journal of the American Ceramic Society*, vol. 93, no. 4, pp. 901–912, 2010.

[27] J. I. Roscow, H. Pearce, H. Khanbareh, S. Kar-Narayan, and C. R. Bowen, "Modified energy harvesting figures of merit for stress- and strain-driven piezoelectric systems," *European Physical Journal: Special Topics*, vol. 228, no. 7, pp. 1537–1554, 2019.

[28] C. R. Bowen, J. Taylor, E. Leboulbar, D. Zabek, A. Chauhan, and R. Vaish, "Pyroelectric materials and devices for energy harvesting applications," *Energy and Environmental Science*, vol. 7, no. 12, pp. 3836–3856, 2014.

[29] G. Sebald, E. Lefeuvre, and D. Guyomar, "Pyroelectric energy conversion: Optimization principles," *IEEE Transactions on Ultrasonics, Ferroelectrics, and Frequency Control*, vol. 55, no. 3, pp. 538–551, 2008.

[30] G. Sebald, L. Seveyrat, D. Guyomar, L. Lebrun, B. Guiffard, and S. Pruvost, "Electrocaloric and pyroelectric properties of 0.75Pb(Mg 1/3Nb2/3)O3-0.25PbTiO3 single crystals," *Journal of Applied Physics*, vol. 100, no. 12, pp. 0–6, 2006.

[31] N. Izyumskaya, Y. I. Alivov, S. J. Cho, H. Morkoç, H. Lee, and Y. S. Kang, "Processing, structure, properties, and applications of PZT thin films," *Critical Reviews in Solid State and Materials Sciences*, vol. 32, no. 3-4, pp. 111–202, 2007.

[32] K. Uchino, *Ferroelectric Devices*. 2018.

[33] A. Erturk and D. J. Inman, *Piezoelectric energy harvesters*. 2011.

[34] R. W. Schwartz, T. J. Boyle, S. J. Lockwood, M. B. Sinclair, D. Dimos, and C. D. Buchheit, "Sol-gel processing of pzt thin films: A review of the state-of-the-art and process optimization strategies," *Integrated Ferroelectrics*, vol. 7, no. 1-4, pp. 259–277, 1995.

[35] T. Maeder and P. Muralt, "In-situ thin film growth of PbTiO3 by multi target sputtering," *Materials Research Society Symposium - Proceedings*, vol. 341, pp. 361–366, 1994.

[36] P. Muralt, M. Marzencki, B. Belgacem, F. Calame, and S. Basrour, "Vibration Energy Harvesting with PZT Micro Device," *Procedia Chemistry*, vol. 1, no. 1, pp. 1191–1194, 2009.

[37] N. Chidambaram, D. Balma, R. Nigon, A. Mazzalai, R. Matloub, C. S. Sandu, and P. Muralt, "Converse mode piezoelectric coefficient for lead zirconate titanate thin

film with interdigitated electrode," *Journal of Micromechanics and Microengineering*, vol. 25, no. 4, p. 45016, 2015.

[38] S. C. Lin and W. J. Wu, "Piezoelectric micro energy harvesters based on stainless-steel substrates," *Smart Materials and Structures*, vol. 22, no. 4, 2013.

[39] W. J. Wu, C. T. Chen, S. C. Lin, C. L. Kuo, Y. J. Wang, and S. P. Yeh, "Comparison of the piezoelectric energy harvesters with Si- MEMS and metal-MEMS," *Journal of Physics: Conference Series*, vol. 557, no. 1, 2014.

[40] C. L. Kuo, S. C. Lin, and W. J. Wu, "Fabrication and performance evaluation of a metal-based bimorph piezoelectric MEMS generator for vibration energy harvesting," *Smart Materials and Structures*, vol. 25, no. 10, pp. 1–10, 2016.

[41] H. G. Yeo, T. Xue, S. Roundy, X. Ma, C. Rahn, and S. Trolier-McKinstry, "Strongly (001) Oriented Bimorph PZT Film on Metal Foils Grown by rf-Sputtering for Wrist-Worn Piezoelectric Energy Harvesters," *Advanced Functional Materials*, vol. 28, no. 36, pp. 1–9, 2018.

[42] H. G. Yeo and S. Trolier-McKinstry, "Effect of piezoelectric layer thickness and poling conditions on the performance of cantilever piezoelectric energy harvesters on Ni foils," *Sensors and Actuators, A: Physical*, vol. 273, pp. 90–97, 2018.

[43] E. E. Aktakka, H. Kim, and K. Najafi, "WAFER LEVEL FABRICATION OF HIGH PERFORMANCE MEMS USING BONDED AND THINNED BULK PIEZOELECTRIC SUBSTRATES," pp. 849–852, 2009.

[44] E. E. Aktakka, R. L. Peterson, and K. Najafi, "Thinned-PZT On SOI Process and Design Optimization for Piezoelectric Inertial Energy Harvesting," *Transducers'11*, pp. 1649–1652, 2011.

[45] G. Tang, B. Yang, C. Hou, G. Li, J. Liu, X. Chen, and C. Yang, "A piezoelectric micro generator worked at low frequency and high acceleration based on PZT and phosphor bronze bonding," *Scientific Reports*, vol. 6, no. December, pp. 2–11, 2016.

[46] Z. Yi, B. Yang, G. Li, J. Liu, X. Chen, X. Wang, and C. Yang, "High performance bimorph piezoelectric MEMS harvester via bulk PZT thick films on thin beryllium-bronze substrate," *Applied Physics Letters*, vol. 111, no. 1, 2017.

[47] H. A. Sodano, D. J. Inman, and G. Park, "Comparison of Piezoelectric Energy Harvesting Devices for Recharging Batteries," vol. 16, no. October, pp. 799–807, 2005.

[48] L. Tang and Y. Yang, "A nonlinear piezoelectric energy harvester with magnetic oscillator," *Applied Physics Letters*, vol. 101, no. 9, 2012.

[49] A. F. Arrieta, T. Delpero, A. E. Bergamini, and P. Ermanni, "Broadband vibration energy harvesting based on cantilevered piezoelectric bi-stable composites," *Applied Physics Letters*, vol. 102, no. 17, pp. 17–20, 2013.

[50] H. Luo, G. Xu, P. Wang, and Z. Yin, "Growth and characterization of relaxor ferroelectric PMNT single crystals," *Ferroelectrics*, vol. 231, no. 1 -4 pt 3, pp. 37–41, 1999.

[51] M. Dutta, A. S. Bhalla, and R. Guo, "Directional dependence figure of merit analysis of piezoelectric materials," *Integrated Ferroelectrics*, vol. 174, no. 1, pp. 26–33, 2016.

[52] A. Erturk, O. Bilgen, and D. J. Inman, "Power generation and shunt damping performance of a single crystal lead magnesium niobate-lead zirconate titanate unimorph: Analysis and experiment," *Applied Physics Letters*, vol. 93, no. 22, 2008.

[53] C. Sun, L. Qin, F. Li, and Q. M. Wang, "Piezoelectric energy harvesting using single crystal Pb(Mg1/3Nb2/3)O 3-xPbTiO3 (PMN-PT) Device," *Journal of Intelligent Material Systems and Structures*, vol. 20, no. 5, pp. 559–568, 2009.

[54] E. Lefeuvre, A. Badel, A. Benayad, L. Lebrun, C. Richard, and D. Guyomar, "A comparison between several approaches of piezoelectric energy harvesting," *Journal De Physique. IV : JP*, vol. 128, pp. 177–186, 2005.

[55] A. Badel, A. Benayad, E. Lefeuvre, L. Lebrun, C. Richard, and D. Guyomar, "Single crystals and nonlinear process for outstanding vibration-powered electrical generators," *IEEE Transactions on Ultrasonics, Ferroelectrics, and Frequency Control*, vol. 53, no. 4, pp. 673–683, 2006.

[56] D. Gibus, P. Gasnier, A. Morel, F. Formosa, L. Charleux, S. Boisseau, G. Pillonnet, C. A. Berlitz, A. Quelen, and A. Badel, "Strongly coupled piezoelectric cantilevers for broadband vibration energy harvesting," *Applied Energy*, vol. 277, no. July, p. 115518, 2020.

[57] Z. Yang and J. Zu, "Comparison of PZN-PT, PMN-PT single crystals and PZT ceramic for vibration energy harvesting," *Energy Conversion and Management*, vol. 122, pp. 321–329, 2016.

[58] R. Bechmann, "Elastic, Piezoelectric, and Dielectric Constants of Polarized Barium Titanate Ceramics and Some Applications of the Piezoelectric Equations," *Journal of the Acoustical Society of America*, vol. 28, no. 3, pp. 347–350, 1956.

[59] M. M. Vijatović, J. D. Bobić, and B. D. Stojanović, "History and challenges of barium titanate: Part II," *Science of Sintering*, vol. 40, no. 3, pp. 235–244, 2008.

[60] J. I. Roscow, R. W. Lewis, J. Taylor, and C. R. Bowen, "Modelling and fabrication of porous sandwich layer barium titanate with improved piezoelectric energy harvesting figures of merit," *Acta Materialia*, vol. 128, pp. 207–217, 2017.

[61] P. Wang and H. Du, "ZnO thin film piezoelectric MEMS vibration energy harvesters with two piezoelectric elements for higher output performance," *Review of Scientific Instruments*, vol. 86, no. 7, 2015.

[62] M. Marzencki, Y. Ammar, and S. Basrour, "Integrated power harvesting system including a MEMS generator and a power management circuit," *Sensors and Actuators, A: Physical*, vol. 145-146, no. 1-2, pp. 363–370, 2008.

[63] R. Elfrink, T. M. Kamel, M. Goedbloed, S. Matova, D. Hohlfeld, Y. Van Andel, and R. Van Schaijk, "Vibration energy harvesting with aluminum nitride-based piezoelectric devices," *Journal of Micromechanics and Microengineering*, vol. 19, no. 9, pp. 249–252, 2009.

[64] R. Elfrink, M. Renaud, T. M. Kamel, C. De Nooijer, M. Jambunathan, M. Goedbloed, D. Hohlfeld, S. Matova, V. Pop, L. Caballero, and R. Van Schaijk, "Vacuum-packaged piezoelectric vibration energy harvesters: Damping contributions and autonomy for a wireless sensor system," *Journal of Micromechanics and Microengineering*, vol. 20, no. 10, 2010.

[65] Y. Jia and A. A. Seshia, "Power Optimization by Mass Tuning for MEMS Piezoelectric Cantilever Vibration Energy Harvesting," *Journal of Microelectromechanical Systems*, vol. 25, no. 1, pp. 108–117, 2016.

[66] A. B. Alamin Dow, A. Bittner, U. Schmid, and N. P. Kherani, "Design, fabrication and testing of a piezoelectric energy microgenerator," *Microsystem Technologies*, vol. 20, no. 4-5, pp. 1035–1040, 2014.

[67] R. Andosca, T. G. McDonald, V. Genova, S. Rosenberg, J. Keating, C. Benedixen, and J. Wu, "Experimental and theoretical studies on MEMS piezoelectric vibrational energy harvesters with mass loading," *Sensors and Actuators, A: Physical*, vol. 178, pp. 76–87, 2012.

[68] Z. Cao, J. Zhang, and H. Kuwano, "Design and characterization of miniature piezoelectric generators with low resonant frequency," *Sensors and Actuators, A: Physical*, vol. 179, pp. 178–184, 2012.

[69] R. Matloub, M. Hadad, A. Mazzalai, N. Chidambaram, G. Moulard, C. S. Sandu, T. . Metzger, and P. Muralt, "Piezoelectric Al1-xScxN thin films: A semiconductor compatible solution for mechanical energy harvesting and sensors," *Applied Physics Letters*, vol. 102, no. 15, pp. 10–13, 2013.

[70] M. Akiyama, K. Umeda, A. Honda, and T. Nagase, "Influence of scandium concentration on power generation figure of merit of scandium aluminum nitride thin films," *Applied Physics Letters*, vol. 102, no. 2, 2013.

[71] P. M. Mayrhofer, C. Rehlendt, M. Fischeneder, M. Kucera, E. Wistrela, A. Bittner, and U. Schmid, "ScAlN MEMS Cantilevers for Vibrational Energy Harvesting Purposes," *Journal of Microelectromechanical Systems*, vol. 26, no. 1, pp. 102–112, 2017.

[72] S. Barth, H. Bartzsch, D. Gloess, P. Frach, T. Herzog, S. Walter, and H. Heuer, "Sputter deposition of stress-controlled piezoelectric AlN and AlScN films for ultrasonic and energy harvesting applications," *IEEE Transactions on Ultrasonics, Ferroelectrics, and Frequency Control*, vol. 61, no. 8, pp. 1329–1334, 2014.

[73] L. V. Minh, M. Hara, T. Yokoyama, T. Nishihara, M. Ueda, and H. Kuwano, "Highly piezoelectric MgZr co-doped aluminum nitride-based vibrational energy harvesters [Correspondence]," *IEEE Transactions on Ultrasonics, Ferroelectrics, and Frequency Control*, vol. 62, no. 11, pp. 2005–2008, 2015.

[74] L. Van Minh, M. Hara, and H. Kuwano, "High Performance Nonlinear Micro Energy Harvester Integrated with (K,Na)NbO3/Si Composite Quad-Cantilever," *The 27TH International Conference on MEMS*, pp. 397–400, 2014.

[75] I. Kanno, T. Ichida, K. Adachi, H. Kotera, K. Shibata, and T. Mishima, "Power-generation performance of lead-free (K,Na)NbO 3 piezoelectric thin-film energy harvesters," *Sensors and Actuators, A: Physical*, vol. 179, pp. 132–136, 2012.

[76] T. Shiraishi, N. Kaneko, M. Kurosawa, H. Uchida, Y. Suzuki, T. Kobayashi, and H. Funakubo, "Vibration-energy-harvesting properties of hydrothermally synthesized (K,Na)NbO3 films deposited on flexible metal foil substrates," *Japanese Journal of Applied Physics*, vol. 54, no. 10, 2015.

[77] S. S. Won, J. Lee, V. Venugopal, D. J. Kim, J. Lee, I. W. Kim, A. I. Kingon, and S. H. Kim, "Lead-free Mn-doped (K0.5,Na0.5)NbO3 piezoelectric thin films for MEMS-based vibrational energy harvester applications," *Applied Physics Letters*, vol. 108, no. 23, pp. 0–5, 2016.

[78] M. Aramaki, K. Izumi, T. Yoshimura, S. Murakami, K. Satoh, K. Kanda, and N. Fujimura, "Investigation of mechanical nonlinear effect in piezoelectric MEMS vibration energy harvesters," *Japanese Journal of Applied Physics*, vol. 57, no. 11, pp. 1–4, 2018.

[79] M. Aramaki, T. Yoshimura, S. Murakami, K. Satoh, and N. Fujimura, "Demonstration of high-performance piezoelectric MEMS vibration energy harvester using

BiFeO 3 film with improved electromechanical coupling factor," *Sensors and Actuators, A: Physical*, vol. 291, pp. 167–173, 2019.

[80] T. Yoshimura, S. Murakami, K. Wakazono, K. Kariya, and N. Fujimura, "Piezoelectric vibrational energy harvester using lead-free ferroelectric BiFeO3 films," *Applied Physics Express*, vol. 6, no. 5, pp. 2–6, 2013.

[81] S. Murakami, T. Yoshimura, K. Satoh, K. Wakazono, K. Kariya, and N. Fujimura, "Development of piezoelectric MEMS vibration energy harvester using (100) oriented BiFeO3 ferroelectric film," *Journal of Physics: Conference Series*, vol. 476, no. 1, 2013.

[82] S. S. Won, M. Sheldon, N. Mostovych, J. Kwak, B. S. Chang, C. W. Ahn, A. I. Kingon, I. W. Kim, and S. H. Kim, "Piezoelectric poly(vinylidene fluoride trifluoroethylene) thin film-based power generators using paper substrates for wearable device applications," *Applied Physics Letters*, vol. 107, no. 20, 2015.

[83] J. Song, G. Zhao, B. Li, and J. Wang, "Design optimization of PVDF-based piezoelectric energy harvesters," *Heliyon*, vol. 3, no. 9, 2017.

[84] R. Sriramdas, S. Chiplunkar, R. M. Cuduvally, and R. Pratap, "Performance enhancement of piezoelectric energy harvesters using multilayer and multistep beam configurations," *IEEE Sensors Journal*, vol. 15, no. 6, pp. 3338–3348, 2015.

[85] A. Bartasyte, S. Margueron, T. Baron, S. Oliveri, and P. Boulet, "Toward High-Quality Epitaxial LiNbO3 and LiTaO3 Thin Films for Acoustic and Optical Applications," *Advanced Materials Interfaces*, vol. 4, no. 8, pp. 1–36, 2017.

[86] P. F. Bordui, R. G. Norwood, C. D. Bird, and G. D. Calvert, "Compositional uniformity in growth and poling of large-diameter lithium niobate crystals," *Journal of Crystal Growth*, vol. 113, no. 1-2, pp. 61–68, 1991.

[87] J. R. Carruthers, G. E. Peterson, M. Grasso, and P. M. Bridenbaugh, "Nonstoichiometry and crystal growth of lithium niobate," *Journal of Applied Physics*, vol. 42, no. 5, pp. 1846–1851, 1971.

[88] A. W. Warner, M. Onoe, and G. A. Coquin, "Determination of Elastic and Piezoelectric Constants for Crystals," *The Journal of the Acoustical Society of AmericaAcoustical Society of America*, vol. 930, no. October 1966, pp. 1223–1231, 1968.

[89] G. Kovacs, M. Anhorn, H. E. Engan, G. Visintini, and C. C. Ruppel, "Improved material constants for LiNbO3 and LiTaO3," *Ultrasonics Symposium Proceedings*, vol. 1, pp. 435–438, 1990.

[90] V. Gopalan, V. Dierolf, and D. A. Scrymgeour, "Defect–Domain Wall Interactions in Trigonal Ferroelectrics," *Annual Review of Materials Research*, vol. 37, no. 1, pp. 449–489, 2007.

[91] W. Yue and J. Yi-Jian, "Crystal orientation dependence of piezoelectric properties in LiNbO3 and LiTaO3," *Optical Materials*, vol. 23, no. 1-2, pp. 403–408, 2003.

[92] K. Nakamura and H. Shimizu, "Ferroelectrics Hysteresis-free piezoelectric actuators using LiNbO 3 plates with a ferroelectric inversion layer," *Ferroelectrics*, no. Vol. 93, pp. 211–216, 1989.

[93] K. Nakamura, H. Ando, and H. Shimizu, "Bending vibrator consisting of a LINBO3plate with a ferroelectric inversion layer," *Japanese Journal of Applied Physics*, vol. 26, pp. 198–200, 1987.

[94] I. V. Kubasov, A. V. Popov, A. S. Bykova, A. A. Temirov, A. M. Kislyuk, R. N. Zhukov, D. A. Kiselev, M. V. Chichkov, M. D. Malinkovich, and Y. N. Parkhomenko, "Deformation Anisotropy of Y + 128°-Cut Single Crystalline Bidomain Wafers of Lithium Niobate," *Russian Microelectronics*, vol. 46, no. 8, pp. 557–563, 2017.

[95] J. V. Vidal, A. V. Turutin, I. V. Kubasov, M. D. Malinkovich, Y. N. Parkhomenko, S. P. Kobeleva, A. L. Kholkin, and N. A. Sobolev, "Equivalent Magnetic Noise in Magnetoelectric Laminates Comprising Bidomain LiNbO3 Crystals," *IEEE Transactions on Ultrasonics, Ferroelectrics, and Frequency Control*, vol. 64, no. 7, pp. 1102–1119, 2017.

[96] J. V. Vidal, A. V. Turutin, I. V. Kubasov, A. M. Kislyuk, M. D. Malinkovich, Y. N. Parkhomenko, S. P. Kobeleva, O. V. Pakhomov, N. A. Sobolev, and A. L. Kholkin, "Low-Frequency Vibration Energy Harvesting with Bidomain LiNbO3 Single Crystals," *IEEE Transactions on Ultrasonics, Ferroelectrics, and Frequency Control*, vol. 66, no. 9, pp. 1480–1487, 2019.

[97] C. Cochard, T. Spielmann, N. Bahlawane, A. Halpin, and T. Granzow, "Broadband characterization of congruent lithium niobate from mHz to optical frequencies," *Journal of Physics D: Applied Physics*, vol. 50, no. 36, 2017.

[98] T. Funasaka, M. Furuhata, Y. Hashimoto, and K. Nakamura, "Piezoelectric generator using a LiNbO 3 plate with an inverted domain," *Proceedings of the IEEE Ultrasonics Symposium*, vol. 1, pp. 959–962, 1998.

[99] V. Bedekar, J. Oliver, S. Zhang, and S. Priya, "Comparative study of energy harvesting from high temperature piezoelectric single crystals," *Japanese Journal of Applied Physics*, vol. 48, no. 9 Part 1, pp. 0914061–0914065, 2009.

[100] T. Morita, T. Niino, H. Asama, and H. Tashiro, "Fundamental study of a stacked lithium niobate transducer," *Japanese Journal of Applied Physics, Part 1: Regular Papers and Short Notes and Review Papers*, vol. 40, no. 5 B, pp. 3801–3806, 2001.

[101] A. Kawamata, H. Hosaka, and T. Morita, "Non-hysteresis and perfect linear piezoelectric performance of a multilayered lithium niobate actuator," *Sensors and Actuators, A: Physical*, vol. 135, no. 2, pp. 782–786, 2007.

[102] K. Tsubouch and N. Mikoshiba, "Zero-Temperature-Coefficient SAW Devices on AlN Epitaxial Films," *IEEE Transactions on Sonics and Ultrasonics*, vol. 32, no. 5, pp. 634–644, 1985.

[103] B. Jaffe, C. W., and J. H., *Piezoeletric ceramics*, vol. 3. 1971.

[104] R. E. Jaeger and L. Egerton, "Hot Pressing of Po tassiu m-Sodiu m," *Journal of the American Ceramic Society*, vol. 45, no. 1960, p. 209, 1962.

[105] R. Zhang, B. Jiang, and W. Cao, "Elastic, piezoelectric, and dielectric properties of multidomain 0.67Pb(Mg1/3Nb2/3)O3-0.33PbTiO3 single crystals," *Journal of Applied Physics*, vol. 90, no. 7, pp. 3471–3475, 2001.

[106] W. Jiang, R. Zhang, B. Jiang, and W. Cao, "Characterization of piezoelectric materials with large piezoelectric and electromechanical coupling coefficients," *Ultrasonics*, vol. 41, no. 2, pp. 55–63, 2003.

[107] H. Jaffe and D. A. Berlincourt, "Piezoelectric Transducer Materials," *Proceedings of the IEEE*, vol. 53, no. 10, pp. 1372–1386, 1965.

[108] H. Karim, M. R. H. Sarker, S. Shahriar, M. A. I. Shuvo, D. Delfin, D. Hodges, T. L. Tseng, D. Roberson, N. Love, and Y. Lin, "Feasibility study of thermal energy harvesting using lead free pyroelectrics," *Smart Materials and Structures*, vol. 25, no. 5, 2016.

[109] L. A. Chavez, F. O. Zayas Jimenez, B. R. Wilburn, L. C. Delfin, H. Kim, N. Love, and Y. Lin, "Characterization of Thermal Energy Harvesting Using Pyroelectric Ceramics at Elevated Temperatures," *Energy Harvesting and Systems*, vol. 5, no. 1-2, pp. 3–10, 2018.

[110] S. B. Lang, "Pyroelectricity: From ancient curiosity to modern imaging tool," *Physics Today*, vol. 58, no. 8, pp. 31–36, 2005.

[111] R. Kandilian, A. Navid, and L. Pilon, "The pyroelectric energy harvesting capabilities of PMN-PT near the morphotropic phase boundary," *Smart Materials and Structures*, vol. 20, no. 5, pp. 20–22, 2011.

[112] R. Ghane-Motlagh and P. Woias, "A pyroelectric thin film of oriented Triglicine sulfate nanocrystals for thermal energy harvesting," *Smart Materials and Structures*, vol. 28, no. 10, 2019.

[113] S. T. Lau, C. H. Cheng, S. H. Choy, D. M. Lin, K. W. Kwok, and H. L. Chan, "Lead-free ceramics for pyroelectric applications," *Journal of Applied Physics*, vol. 103, no. 10, 2008.

[114] G. Sebald, D. Guyomar, and A. Agbossou, "On thermoelectric and pyroelectric energy harvesting," *Smart Materials and Structures*, vol. 18, no. 12, 2009.

[115] S. B. Lang and D. K. Das-Gupta, *Chapter 1 – Pyroelectricity: Fundamentals and applications*, vol. 4. 2001.

[116] D. Lingam, A. R. Parikh, J. Huang, A. Jain, and M. Minary-Jolandan, "Nano/microscale pyroelectric energy harvesting: Challenges and opportunities," *International Journal of Smart and Nano Materials*, vol. 4, no. 4, pp. 229–245, 2013.

2 Experimental Techniques

In this chapter I will introduce the methods and techniques used for the microfabrication of $LiNbO_3$ harvesters. I will briefly illustrate the possible approaches for the fabrication: bottom-up of $LiNbO_3$ films or top-down methodologies. In particular I will give some details regarding chemical vapor deposition for thin films and micro machining of thick films. Standard processes such as UV-Lithography, Electron-Beam Evaporation, Etching and Au-Au bonding process of $LiNbO_3$ wafers will be presented. After presenting the flowchart for the microfabrication process, the basic characterization techniques used for determining the dielectric, piezoelectric and pyroelectric properties of the chosen $LiNbO_3$ orientations.

2.1 Fabrication of $LiNbO_3$ Films

In FEMTO-ST technological facilities, we can work with different approaches to obtain $LiNbO_3$ films. One of them is the bottom-up approach, where by means of Pulsed Injection Metal-Organic Chemical Vapor Deposition (PI-MOCVD), we can deposit thin films (50-500 nm) on various substrates. The film grows textured on the substrate with a given orientation, and its properties can be tuned by different parameters, such as temperature, pressure and solution composition. Even if the quality of the film is extremely high, at the moment the thickness of the piezoelectric layer is limited, while for energy harvesting applications thick films represent the best option [1]. In order to obtain films with thickness of 1-100 µm, we can exploit a top-down approach. In this case, the single crystal is bonded to a host wafer (silicon or metal), which represents the substrate of the device. Afterwards, the active material has to reach the required thickness for the application, which can be attained with two methods: Smart-Cut^{TM}[2] or mechanical lapping-polishing. Smart-Cut^{TM} (2.1) is a process where the active material wafer once bonded to the susceptor, is then split by mean of ion-slicing. In this way only a thin film of $LiNbO_3$ remains bonded to the host substrate, $0.3 \div 1$ µm thick. However, the film thickness is still limited for energy harvesting applications and the process is quite costly. Another option is mechanical thinning by means of rectification, lapping and micro-polishing.

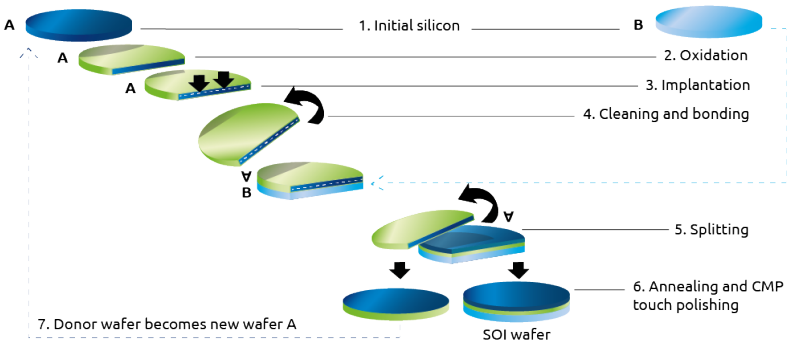

Figure 2.1: Schematical representation of top-down approach with Smart-Cut^{TM} [2]

This method is well developed and effective, can be used with all the available crystal cuts and on different kind of substrates. The precision of the layer thickness depends on the overall volume needed for the application, namely, for thin films (1 µm) the piezoelectric layer could have an inhomogeneous thickness. Further details will be discussed in details in the next sections.

2.1.1 PI-MOCVD of $LiNbO_3$ Thin Films

In vibrational energy harvesting, we can exploit transverse mode of piezoelectric elements, to convert mechanical strain along the length of a cantilever beam, in charge displacement along its thickness. Due to $LiNbO_3$ anisotropy, it is possible to obtain good values of piezoelectric coefficient, choosing the correct orientation. So far, only six orientations (X, Y, Z, Y-33°, Y-128°, X-30°) of $LiNbO_3$ can be grown epitaxially [3]. According to our simulations, $LiNbO_3$ Y-33° (corresponds to (012) crystallographic planes of hexagonal cell) presents the highest efficient piezoelectric coefficient (d_{23}=19 pC/N) than other grown orientations. Therefore, our objective is to grow Y-33° textured $LiNbO_3$ films on Si and metal substrates. However, only Z and Y-33° orientation can be obtained on Si substrates. In order to avoid charge leakage from electrodes to the substrate, dielectric layer, such as SiO_2, has to be inserted between Si and metal electrode. Furthermore, the bottom electrode has to withstand deposition temperature of piezoelectric film (typically > 600°C). In this work we will consider Pt bottom electrodes and a buffer layer to highly orient $LiNbO_3$ films.

2.1.1.1 Growth of $LiNbO_3$ Thin Films

The $LiNbO_3$ thin film synthesis was done by PI-MOCVD method in MIMENTO clean room facility. The commercial precursors used in the synthesis are: 99% $Nb(TMHD)_4$ and 98% Li(TMHD), where TMHD stands for 2,2,6,6-tetramethyl-3,5-heptandione. The two chemicals were provided by ABCR GmbH & Co and Strem Chemicals, Inc. respectively. The lithium and niobium precursors were dissolved in a solvent (1,2-dimethoxyethane 99.5%, by Sigma-Aldrich), and the mixture was injected into the evaporator inside the reactor (Fig. 2.2). The frequency and the opening time of the piezoelectric shutter was modu-

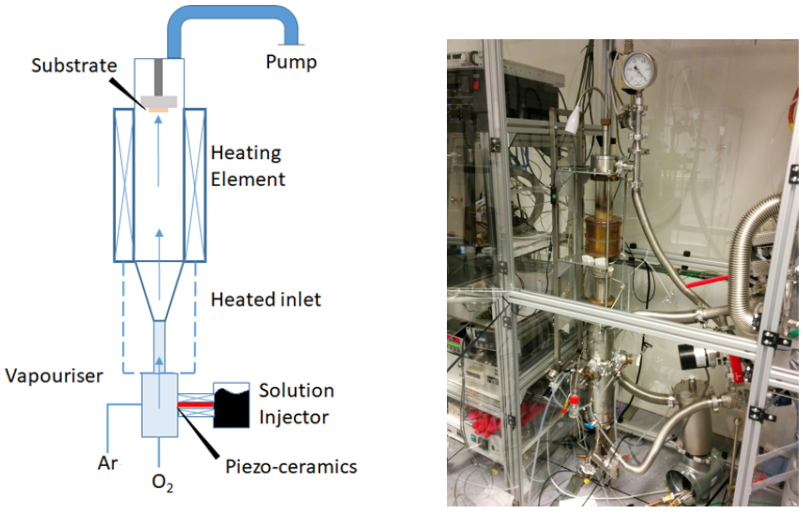

(a) *(b)*

Figure 2.2: $LiNbO_3$ thin films PIMOCVD: (a) schematic representation of PIMOCVD reactor; (b) home-made PIMOCVD reactor in MIMENTO.

lated by the computer, with the purpose of controlling the liquid injection delivery system of the reactor. Injector and evaporator were heated in order to avoid condensation of the precursors, while a pump controlled the pressure inside the reactor. Once the droplet was vaporized, Ar and O_2 transported the mixture on the heated susceptor, where substrates were fixed. Typically, up to 4 different substrates of 100 mm^2 could be positioned on the sample holder for one deposition or a 2 inch wafer. For the synthesis of lithium niobate thin films, a typical set of parameters is showed in Table (2.1). A deposition of 20 ml of precursors correspond to roughly 1.5 h deposition, for a total 270-300 nm of thin film thickness. The molar ratio of precursors was usually $Li(TMHD) : Nb(TMHD)_4 = 2 : 1$. Several different substrates were used during the process in order to investigate the epitaxial growth of the $LiNbO_3$ films: Si/SiO_2, Sapphire (A, R, M, C). The characterization was done by X-ray diffraction, optical microscopy and Raman spectroscopy.

Table 2.1: Typical PIMOCVD parameters for $LiNbO_3$ thin film deposition.

Frequency (Hz)	Open time (ms)	N° injection (#)	T dep (°C)	T evap (°C)	T inj (°C)	P (Torr)	Ar/O_2 (sccm)
1	2	5000	775	220	125	7	200/100

2.1.2 Wafer on Wafer (WoW) Technology

Using a top-down approach meant to work with $LiNbO_3$ single crystal in two possible scenarios: Smart-Cut^{TM} or mechanical lapping-polishing of single crystal $LiNbO_3$. The first way, is an expensive alternative to get piezoelectric layer of maximum 1 µm thickness.

Eventually we opted for micro-machining of $LiNbO_3$ crystal Au-Au bonded to Si substrate. This route is less expensive than Smart-Cut^{TM}, moreover we can choose arbitrarily the thickness of $LiNbO_3$, even if we have to take into account that the process of lapping and polishing could be difficult to control in terms of homogeneity, especially for very thin thicknesses.

2.1.2.1 Au-Au Bonding on Si

Since the early 2000s there has been great interest of bonding technology between piezoelectric wafers with different substrates. The most common substrates used were of glass, sapphire or silicon. One of the advantages is the possibility to exploit bulk electroactive materials on standard dimension wafers, instead of using deposition techniques to deposit thin films and optimize their growth. In this way we can fabricate highly coupled devices for acoustic or optic applications, using standard CMOS techniques. In particular, there was much effort to bond silicon with piezoelectric materials such as quartz, $LiNbO_3$ or $LiTaO_3$, in order to produce high frequency devices for filters applications [4]. One limit is to use substrate whose coefficient of thermal expansion is not very different from the one of the piezoelectric layer. This much is true for processes where the annealing of the substrate is needed, even though this process could damage the active or passive surface by cracking either of them. Another aspect is the difference in thickness between the two wafers, residual stresses due to previous processing, can bend the bonded counterpart and increase the bow of the entire structure. For this reason we tend to work with full wafers and reduce the thickness afterwards, according to the target application. Moreover, as discussed in the previous chapter, $LiNbO_3$ is pyroelectric, thus is better to work at room temperature, because annealing could lead to high surface potential, compromising the bonding process and generating cracks. Some examples of room temperature bonding are in [4], where $LiNbO_3$ is bonded to Si by surface-activated bonding. With this method, wafer surfaces are sputter etched by Ar beam and then bonded in vacuum. While this technique is useful and doesn't require thermal annealing of the specimens, the doped silicon as bottom substrate has to be used. In MIMENTO, due to long years expertise in the fabrication process of bonded acoustic wave devices on $LiNbO_3$ or $LiTaO_3$ [5–7], is commonly performed Au-Au bonding by thermo-compression at room temperature.

In this case, the two wafers have to be carefully cleaned (piranha solution for Si wafer and chromic acid for $LiNbO_3$ to avoid pyroelectricity). Afterwards we deposit by sputtering the Au layer to perform bonding. In order to have good adhesion, a thin layer of Cr is deposited (40-50 nm) before the Au thin film (150 nm). Once the wafers are prepared, we bond by thermo-compression in vacuum using EVG wafer bonding machine. To avoid mismatch of thermal expansion coefficient, the whole process is carried out at room temperature. Eventually, the time and pressure of compression are the only two parameters

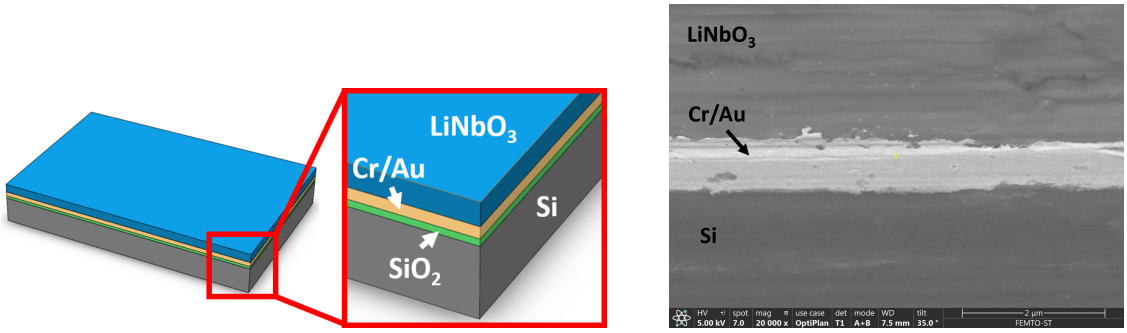

(a) (b)

Figure 2.3: $LiNbO_3$ /Si layer interface: (a) schematics of hetero-structure after bonding; (b) SEM image of interface between silicon and $LiNbO_3$ after dicing.

that have to be optimized for the whole process [8]. In Fig. (2.3) a schematic representaiton of the heterostructure after bonding, and a typical range of the diced sample cross-section are presented. Generally, important aspects to have high quality bonding are:

- Optical quality of polished surfaces for both wafers;
- Extremely clean surfaces, other than the use of acid for the first step, also ion-etching before sputtering is recommended;
- Total Thickness Variation (TTV) of the wafers below 2 µm;
- Small or complementary bow (or deviation from the median surface) of the wafers.

2.1.2.2 Ultrasonic Characterization

After the bonding process, we can characterize the bonding quality by ultrasonic non-destructive testing [9]. For these tests we clamped the wafer on a holder completely immersed in water. An ultrasonic emitter and a receiver are facing each other, while the bonded wafer is placed in between them. In this way it is possible to investigate the quality of the bonding by transmission. The two transducers (Sonaxis, 15 MHz central frequency) can scan the whole surface of the wafer moving simultaneously. If the received wave encounters a defect on the surface of the bonded wafer, the amplitude will not be the same as in perfect bonded areas, leading to a reflection of the incident wave. In Fig. (2.4) the bonding quality of $LiNbO_3$ /Si wafer is illustrated. The good quality of bonding corresponds to red color, while whenever the signal is saturating the color is white, blue and green are related to bonding defects due to impurities or dust particle in the two wafers interface. As showed in the picture, we can achieve high quality Au-Au bonding of $LiNbO_3$ wafers on Si substrate.

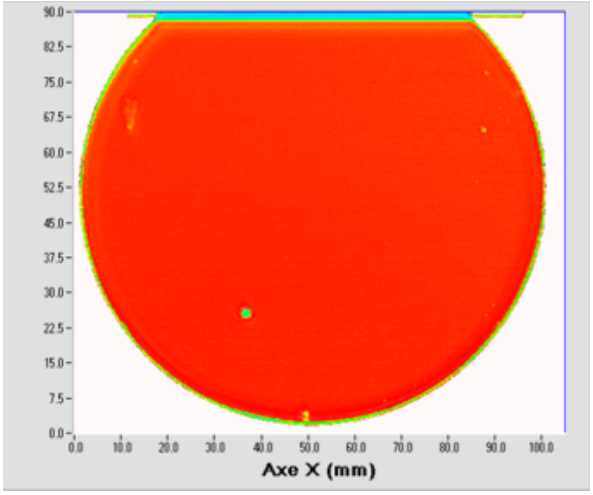

Figure 2.4: Image of ultrasonic characterization for $LiNbO_3$ /Si wafer.

2.1.2.3 Crystal Thinning

In this thesis, the work on $LiNbO_3$ thinning has been done in collaboration with F. Bassignot (FEMTO-Engineering) and M. Ouhabaz (FEMTO-ST). Once the wafers are bonded we can thin the piezoelectric layer in order to achieve the required thickness. In fact, $LiNbO_3$ is a very chemically inert material, and it is very challenging to etch by chemicals or by deep reactive etching a bulk wafer. Therefore, we adjust the thickness of the piezoelectric layer by mechanically polishing the wafers. Differently, Si is usually processed with deep reactive-ion etching (DRIE). The thickness of the active material is very important for several reasons. First of all, the frequency response of the device depends strongly on the geometry of the cantilever, hence the thickness is an instrumental aspect in order to tune the response of the prototypes. Moreover, the voltage response is thickness dependant, being proportional to the volume of the piezoelectric material under stress. However, in the case of $LiNbO_3$, using full wafer thickness is not optimal. Essentially because the relative permittivity, ε_r, is small compared to PZT (by two order of magnitude smaller), thus the thicker the material the lower the capacitance of the piezoelectric layer. This fact could lead to impedance matching issues, because for a bulk $LiNbO_3$ layer, clamped capacitance would be in *pF* range which leads to high resistive loads for the electronic interfacing, and issues during AC-DC rectification. In our work, in a general optimization approach, we opted to use $LiNbO_3$ thick films (4-120 µm), to have optimized transduction and electronic interfacing for different kinds of device geometries. The thinning steps were carried out in two phases: mechanical rectification, which has a high speed of processing up to 10 µm/min, in order to remove most of the material, then a fine step lapping at lower speed (3 µm/min), to adjust the thickness, and finally, depending on the surface quality demanded, an additional micro-polishing step (1 µm/min) to achieve optical grade surface. After the polishing, the piezoelectric layer is ready for electrode patterning. In Fig. (2.5) a single crystal thick film of (YXl)/163° with 10 µm average

thickness after processing is presented. The homogeneity in terms of thickness depends on the presence of defects during bonding or bow of the wafer, where the goal is usually to stay under 2 µm TTV.

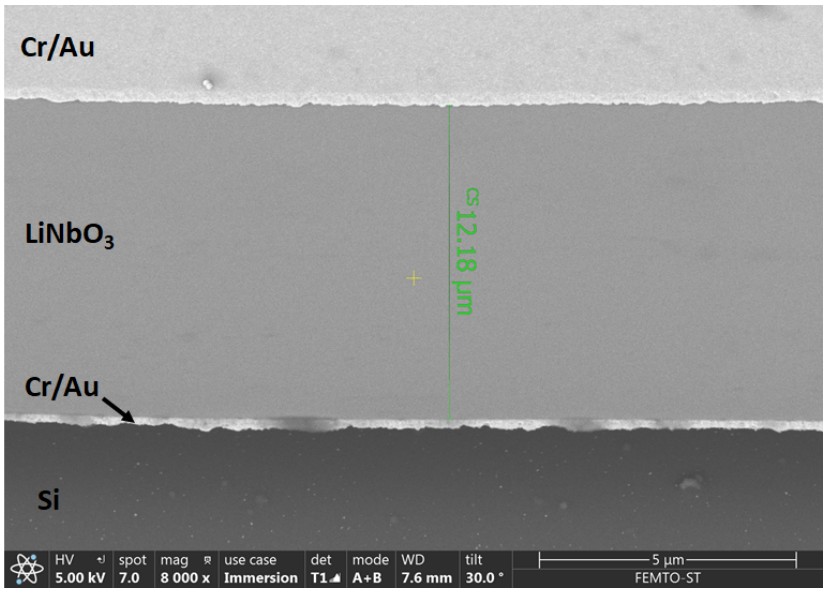

Figure 2.5: SEM image of $LiNbO_3$ layer after thinning. The bonded piezoelectric wafer on Si, was lapped and polished until 10 µm (2 µm TTV).

2.1.2.4 Electrode Patterning

To pattern the electrodes on $LiNbO_3$ surface we used UV-Lithography and lift-off process. The first step necessary to pattern the electrode is the design of a mask that reflects the features that we want to achieve with our devices. In this work, we opted almost exclusively for parallel plate electrodes exploiting transverse mode, but some tests were done also in IDT configuration for thickness mode. The more important aspect to address in our case, in order to bond the wafers, is that a metal layer is required. Therefore, while that would be the case of parallel plate electrodes, could be an issue for IDTs, where usually the two comb-like electrodes are placed on the surface of the active layer. In the IDTs case, SiO_2 insulation layer should be used. Furthermore, for the latter electrode configuration, poling of the ferroelectric element is required, in order to align the polarization between the the branches of the IDTs. Due to time constraints, IDT based devices were not fabricated. For this reason we patterned top full electrodes (parallel plate case) with metallic layers (Al or Cr/Au), choosing the electrode length as half or 2/3 of the free length of the cantilever, to optimize the effect of the piezoelectric material under strain, having a $LiNbO_3$ thickness of 4-40 µm. For thicker films (40-120 µm) we decided to cover the whole length to compensate the loss in terms of clamped capacitance. A simplified schematics of the process is presented in Fig. (2.6a). Typically, the surface morphology or cross-section of the samples was investigated with scanning electron microscope (SEM-Apreo S) or optical microscope (Leica DM8000), while the thickness of the films and photoresist

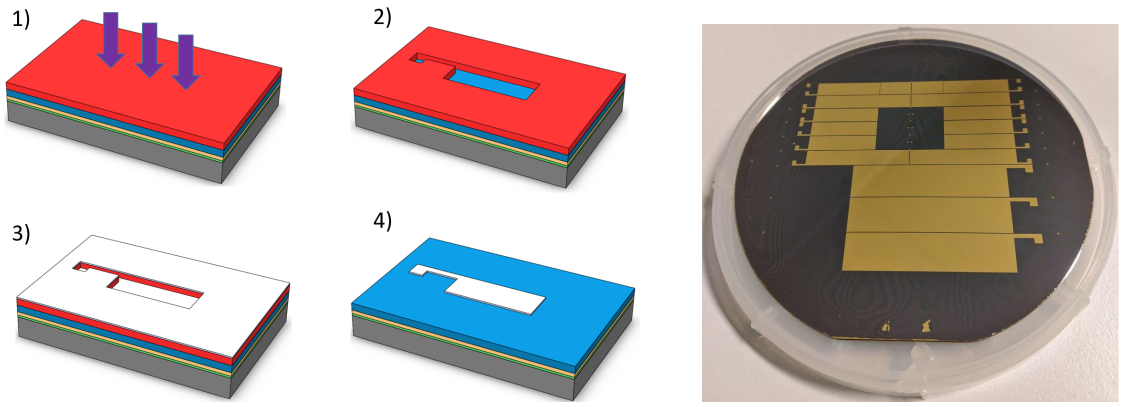

(a) *(b)*

Figure 2.6: (a) Schematic representation of flowchart used for electrode patterning: 1. the photoresist is spincoated on the surface of $LiNbO_3$, then the polymer is exposed to UV through the mask; 2. the photoresist is developed; 3. the electrode are deposited by electrode-beam evaporation; 4. lift-off is performed to pattern the metal layer; (b) Optical image of wafer after electrode patterning.

was measured with a stylus profilometer (DEKTAK XT).

After the fabrication of the mask, we have patterned the photoresist on the wafer by UV-lithography. Firstly, we used photoresist Ti Prime to grant higher adhesion, after baking at 120°C for one minute, a negative photoresist (Ti09 XR) was spin-coated on the wafer. The expected thickness of the resin was 0.8-1.2 µm. We developed the light sensitive material through exposition to UV-light (80 mJ/cm^2 for 10 s), transferring the pattern on the mask to the $LiNbO_3$ surface. Image reversal bake made this part of resist insoluble in developing phase. Later, flood exposure (without mask) with a dose of 300 mJ/cm^2 for 30 s, made unexposed resist soluble. Eventually, we did post exposure baking for 4 minutes at 130 °C, so that bonded areas of exposed resist would become insoluble. Samples were then developed with MF26A solvent for 60s, after post exposure baking, and carefully rinsed with de-ionized water. After developing with solvents and hard baking of the photoresist, we could deposit a metallic thin film on the whole surface of the wafer. The method used to deposit the electrodes was electron-beam physical vapor deposition (Evap MEB600). The evaporation takes place in high vacuum condition (10^{-6} mbar), where the metallic pellets are heated until they reach vapor form, by a focused electron beam coming from a tungsten filament. A thin metal film (Al or Cr/Au) is deposited on all the surface of the chamber (1 nm/s deposition velocity ratio), including the substrate. The key film properties that we can achieve with this method are low roughness and directional deposition, which is very important to have a good lift-off process resolution. In the last step of the process we have to remove the photoresist and to leave the desired electrode patterns. Typically, we did lift-off with acetone heated at 60-70 °C for 1 hour, and using small doses of ultrasound to facilitate the process. Eventually the samples were rinsed, cleaned and then spin-coated with a resin in order to protect the surface during

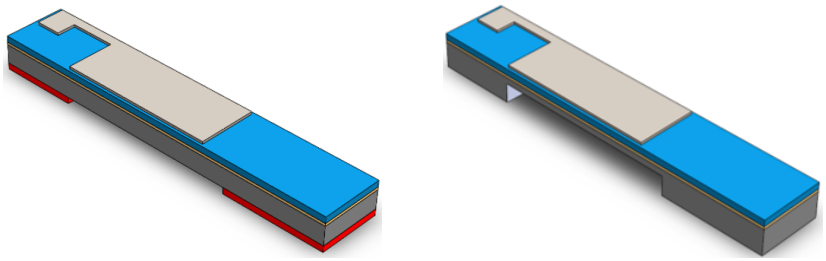

(a) *(b)*

Figure 2.7: Silicon patterning: (a) Spin-coating of resist on backside of $LiNbO_3$ /Si cantilever (in red), (b) sample after DRIE etching.

dicing. The final result of Cr/Au top electrodes patterning is presented in Fig. (2.6b).

2.1.2.5 Substrate Patterning

Once the wafers are ready, the samples are diced by using of a high precision dicing saw (L. Gautier-Manuel, FEMTO-ST). With this tool it is possible to simultaneously cut through different kind of materials, and precisely release the specimens in their cantilever form. During the fabrication we successfully managed to cut through both silicon and metal wafers bonded to $LiNbO_3$. The last step of the microfabrication is deep silicon etching (Bosch technique [10]). During this process the silicon backside of the cantilever is exposed to highly energetic ion bombardment, where alternatively deposition of polymeric material on the side walls and etching from ion impact are happening. The parts of the cantilever that have to be protected, like the clamping part or the tip mass, are covered with a thick film of photoresist (Fig. (2.7a)). After the etching, the cantilever can be wire-bonded to a PCB in order to start the testing (Fig. (2.7b)).

Regarding the fabrication process for thick film cantilevers, SiO_2/Si substrate was Au-Au bonded to $LiNbO_3$ (YXl)/θ° crystal using EVG bonding machine. The piezoelectric layer was subsequently lapped down and polished until the required thickness was reached. Aluminum top electrodes were sputtered by using a stencil mask. Finally, the cantilevers were 15 mm long and 1.5 mm wide, with a resonance frequency ranging from 4.7 to 5.6 kHz, depending on the piezoelectric and substrate thicknesses. The electrodes covered just 2/3 of the beams width. More details can be found in Table (2.2).

Table 2.2: $LiNbO_3$ /Si cantilever geometrical parameters.

Cantilever		Electrode		Thickness	
Length (mm)	Width (mm)	Length (mm)	Width (mm)	Si (µm)	$LiNbO_3$ (µm)
15	1.5	8.5	1	350-500	4-32

2.1.3 Characterization of Film Physical Properties

The fabrication process for $LiNbO_3$ prototypes took place both in FEMTO-ST and EPFL. We fabricated two main types of devices:

- $LiNbO_3$ energy harvesters, fabricated in MIMENTO facility (Besançon);
- $LiNbO_3$ cantilevers for basic characterization properties, fabricated in collaboration with CiM (Lausanne).

The processing of the two batch is similar, in both cases we started from the same structure of $LiNbO_3$ /Si wafers, made by Au-Au bonding in Mimento, whereas the sizes of the devices are quite different, spanning from MEMS to meso-scale. The flowchart for the fabrication was similar, involving the following steps:

- Lithography (UV or with stencil mask);
- Electrode deposition (Evaporation or Sputtering);
- Dicing;
- DRIE etching (only for harvesters).

For the basic characterization of $LiNbO_3$ samples we used the design proposed by Mazzalai et al [11]. In order to calculate the effective piezoelectric coefficient, the cantilevers were oriented so that the polarization was along Y' (2 in tensor notation), the stress along Z' (3), so that we could consider $e_{23,f}$, and the effective pyroelectric coefficient $p_{2,f}$.

The $LiNbO_3$ films thickness ranged between 4-32 µm depending on the cut, and Si substrate thickness varied between 350-530 µm depending on the sample batch. We also characterized dielectric and pyroelectric properties of an optimized batch of deposited $LiNbO_3$ thin films on silicon, but it was not possible to check the converse piezoelectric effect due to the ratio of active/inactive layer of the specimens ($h_p/h_i < 10^{-3}$), with h_p typically ≈100 nm.

2.1.3.1 Dielectric Constant Measurements

As discussed in the previous chapter, the second order tensors of $LiNbO_3$ are isotropic perpendicular to Z-axis, and planes that are perpendicular to it have same value for ε_{11} and ε_{22}. If we approximate the piezoelectric layer as a parallel plate capacitor, then we are interested in measuring ε_{33} value. The dielectric permittivity at constant stress, is defined as the ratio between the relative permittivity of the material and the permittivity of free space, ε_0. This is generally measured far from the mechanical resonance frequency. We derived the value of ε_f from the capacitance measurements at 1 kHz using an HP4194A network analyzer at room temperature. From the capacitance values measured, ε_f could be estimated as:

$$\varepsilon_f = \frac{C_0 h_p}{A\varepsilon_0} \tag{2.1}$$

where C_0 is the measured clamped capacitance, h_p the thickness of the piezoelectric layer, A the surface of the top electrode and ε_0 the permittivity of free space (8.854 pF .m^{-1}). The dielectric losses, $\tan\delta$, are defined as the ratio between the imaginary part (ε''_f) of the relative complex permittivity and its real part (ε'_f) [12, 13], ($\varepsilon^*_f = \varepsilon'_f + i\varepsilon''_f$), which is given by the relation:

$$\tan\delta = \frac{\varepsilon''_f}{\varepsilon'_f} \tag{2.2}$$

From another point of view, $\tan\delta$ is representing the losses of the piezoelectric layer as if we have a capacitance, C_p, and a resistor in parallel, R_p, so that:

$$\tan\delta = \frac{1}{\omega R_p C_p} \tag{2.3}$$

which at a given angular velocity, ω, is how the spectrum analyzer is able to estimate the losses for the dielectric material. The approach of RC circuit, is an approximation where dissipation has an inverse dependency on frequency, but this dispersion is not so prominent in the kHz range [12].

2.1.3.2 Impedance Measurements

The impedance properties of a piezoelectric bender operating close to resonance, can be represented by a lumped-parameter equivalent circuit. To evaluate the equivalent circuit of the resonator, the measurements were done with an impedance analyzer (Keysight E5061B). Here the piezoelectric transducer is modeled as an RLC circuit, using the Butterworth-Van Dyke (BVD) equivalent circuit [14]. In Fig. 2.8 the BVD circuit is represented. The circuit has a motional branch composed by: R, a resistor representing the mechanical dissipation, C, a capacitance representing the compliance, and L, an inductance representing the mass. The motional branch is in series with the static capacitance of the parallel plate capacitor, C_0. The total impedance, Z, of the equivalent circuit is given as:

$$Z = \frac{\frac{1}{j\omega C_0}\left(R + j\omega L + \frac{1}{j\omega C}\right)}{R + j\omega L + \left(\frac{1}{j\omega C_0} + \frac{1}{j\omega C}\right)} \tag{2.4}$$

From the analysis of Z, we can find the series and parallel resonant frequencies, ω_s and ω_p respectively, which are given as:

$$\omega_s = \frac{1}{\sqrt{LC}} \tag{2.5}$$

$$\omega_s = \frac{1}{\sqrt{LC_{eq}}} \tag{2.6}$$

where $C_{eq} = \frac{C_0 C}{C_0 + C}$. Once measured resonance and anti-resonance frequencies, we can

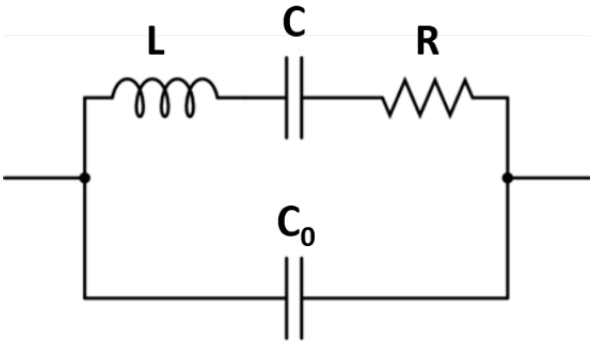

Figure 2.8: Schematic representation of piezoelectric transducer electrical equivalent circuit.

extrapolate the equivalent circuit parameters. For instance, the mechanical quality factor, Q, and the coupling, k^2_{eff}, are defined as:

$$Q = \frac{1}{R}\sqrt{\frac{L}{C}} \tag{2.7}$$

$$k^2_{\text{eff}} = \frac{\omega_p^2 - \omega_s^2}{\omega_p^2} \tag{2.8}$$

2.1.3.3 Piezoelectric Coefficient Measurements

Using $LiNbO_3$ films with (YXl)/θ° orientation, it was possible to investigate piezoelectric (Eq. 1.24) and pyroelectric (Eq. 1.33) figures of merit. Two separate methods were carried on to measure the effective values of the two coefficients on the same structures. In particular, the effective piezoelectric converse coefficient is evaluated from the in-plane stress due to an electric excitation on the clamped cantilever. For this purpose we are considering the relation:

$$e_{23,f} = \frac{\partial T_3}{\partial E_2} \tag{2.9}$$

Where T_3 is the stress along the length of the cantilever, and it is assumed to be constant across the film thickness, while E_2 is the electric field applied on the piezoelectric layer and is perpendicular to the stress direction. The piezoelectric coefficient characterization of $LiNbO_3$ films from bending can be done with several methods and with commercial available tools, for instance with a proximity sensor [15] or with a laser interferometer [11]. Other techniques are provided with four point load for precise estimate of $e_{31,f}$ coefficient [16], or direct piezoelectric effect with mechanical tip actuation of the cantilever [17]. Especially in the case of actuators, it is very important to correctly measure the magnitude of e_{31} stress coefficient of piezoelectric films when an electric field is applied. In EFPL we used a single-laser beam interferometer coupled with an aixACCT^R TF2000 setup, in order to estimate the effective piezoelectric coefficient $e_{23,f}$. The measurement were done

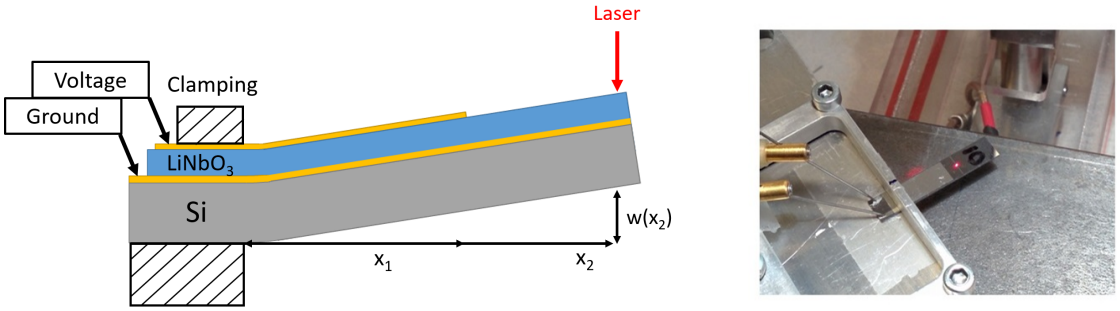

(a) (b)

Figure 2.9: (a) Schematics of converse piezoelectric tests to measure stress coefficient. (b) The cantilever is clamped and activated by an external voltage, while a laser interferometer is measuring the tip displacement.

in collaboration with R. Nigon (EPFL). The methodology adopted for the estimation of the piezoelectric coefficient was the same used by Mazzalai et al. [11]. The clamped beam was excited by a large signal input, while the tip displacement was measured by the interferometer at 160 Hz. The maximum tip displacement was measured for different electric field intensities. The cantilevers were positioned on a clamping stage, while probes were connected to bottom and top electrodes (Fig. 3.8a). One of the probes was configured as virtual ground, the other was representing the voltage input in order to bend the sample by converse piezoelectric effect. On the opposite side of the cantilever, a laser interferometer focused on a reflector was tracking the position of the tip. Once the voltage was applied, we could see contemporary polarization of the film and relative displacement.

In converse mode the in-plane stresses, T_3, is varying in terms of electric field, E_2. The displacement of the tip is quite small due to the ratio between the thickness of the piezoelectric layer (h_p) and the substrate (h_i), typically $h_p/h_i \simeq 10^{-1}$. Hence, the curvature of the cantilever for such structure is:

$$r = \frac{2w(x_2)}{x_1(2x_2 - x_1)} \tag{2.10}$$

where the curvature, r, is taken as constant between 0 and the end of the electrode (x_1), and then it is null until the end of the cantilever, x_2 represents the distance from the end of the electrode to the tip of the beam and $w(x_2)$ is the vertical displacement. The width of the electrode and the beam, are respectively b_e and b. Therefore, the equilibrium condition for the bending of the beam states that the sum of all the momenta has to be zero, $M_p + M_i = 0$:

$$\mathrm{M}_p = -\mathrm{T}_3 b_e h_p \frac{h_i}{2} \tag{2.11}$$

$$\mathrm{M}_i = \left[\frac{b}{s_{11,i}(1-\nu_i)} + \frac{(b-b_e)}{s_{11,i}} \right] \frac{h_i^3}{12} \tag{2.12}$$

Finally it is possible to calculate the stress T_3 as:

$$\mathrm{T}_3 = \frac{1}{3}\frac{[c+(1-c)(1-\nu_i)]}{s_{11,i}(1-\nu_i)c}\frac{2w(x_2)}{x_1(2x_2-x_1)}\frac{h_i^2}{h_p} \tag{2.13}$$

where $c = b_e/b$, and the Eq. (2.13) establishes a linear relation between displacement and in plane stress components. Eventually, we can use Eq.(2.9) to calculate the effective piezoelectric stress coefficient for $LiNbO_3$ for a given orientation. It has to be noted that to get Eq. (2.12-2.11) we used the Stoney formula [18] for bi-axial stress, which is just an approximation of the real case for $LiNbO_3$. With this approximation is licit to consider the uniaxial stress for the surface of piezoelectric material under the electrode, and that the Young modulus can be rewritten as $1/(s_{11,i}(1-\nu_i))$. For the silicon substrate in (100) orientation we assumed the following parameters $s_{11,i} = \frac{1}{169}$ GPa and $\nu_i = 0.064$ [19]. Finally the piezoelectric coefficient is given by:

$$e_{23,f} = -\frac{1}{3}\frac{[c+(1-c)(1-\nu_i)]}{s_{11,i}(1-\nu_i)c}\frac{2w(x_2)}{x_1(2x_2-x_1)}\frac{h_i^2}{\mathrm{V}} \tag{2.14}$$

In Eq. (2.14) is a function of both the displacement $w(x_2)$ and the voltage V that is imposed from the system, most interesting $e_{23,f}$ does not depend on the thickness of the piezoelectric material, hence we can use this approximation for specimen that have different h_p.

2.1.3.4 Pyroelectric Constant Measurements

Concerning pyroelectricity, this effect arises when the material is experiencing a variation of temperature over time, consequently an alteration of spontaneous polarization in the crystal allows the charges on the surface to rearrange, generating pyroelectric current. Generally, in Z-cut $LiNbO_3$ this can be described by the equation:

$$d\mathrm{P}_3 = p_3 d\Theta \tag{2.15}$$

Where P_3 represents the polarization along the Z-axis, which is parallel to the relative movement of lithium towards niobium ions, p_3 is the pyroelectric coefficient, and Θ the temperature. In literature the value reported for Z-cut $LiNbO_3$ pyroelectric coefficient is -83 $\mu C.m^{-2}.K^{-1}$ [20]. The magnitude of this effect depends strongly on the heating threshold used in the experiments, and the pyroelectric coefficient typically increases with the temperature [21]. In our case, due to the tilted orientation of the crystal cut, the pyroelectric coefficient considered is $p_{2,f}$, and it is a projection of p_3 on Y ($\theta°$) axis. In order to test pyroelectricity on the $LiNbO_3$ fabricated samples, we had the opportunity to use two different test-benches. Both of them involve dynamic measurement of the pyroelectric coefficient, p, while heated [22, 23], therefore they use temperature functions

with specific waveform shapes in order to change the spontaneous polarization, P_s, of the sample. The pyroelectric contribution is measured through to current or voltage sensing, while the temperature ramp is measured with a thermocouple. Because of the insulating silicon substrate, we could not use the surface of the heating element as an electrode, therefore two metallic probes were positioned on the top and bottom electrode of samples (Fig. 2.10). The samples that were investigated were mostly tilted $LiNbO_3$ cuts, so the use perpendicular electrodes gave a projection p_f of p, which eventually was including both *primary* and *secondary* pyroelectric effect. The distinction of the two effects is achievable only in total clamping condition, which was not an available configuration for our setup. The dynamic tests took place in two different facilities:

- EPFL, estimate of pyroelectric current from a triangular waveform at room temperature (in collaboration with D. Park);
- FEMTO-ST, measurement of pyroelectric voltage from a square waveform for temperature up to 200°C.

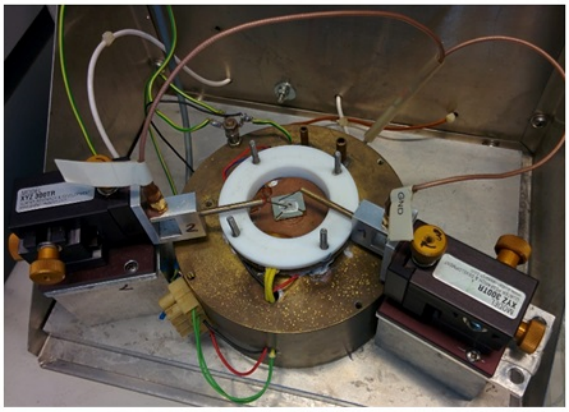

Figure 2.10: Setup for pyroelectric characterization in EPFL.

In both cases setup, we positioned the samples over a heating module (Peltier element) that was varying the temperature on the bottom side of the sample. The charges were collected from the top and bottom electrode with two different probes. With a Labview interface we could also change the time period, threshold temperature and number of heating cycles [15, 24].

For the measurements in EPFL, we estimated the pyroelectric coefficient from the electric current generated by the sample, following the relation:

$$p_f = \frac{i_{py}}{\mathrm{A}\frac{d\Theta}{dt}} \tag{2.16}$$

where i_{py} is the pyroelectric current, A the electrode active surface and $\frac{d\Theta}{dt}$ the rate of temperature over time. This dynamic method investigates p_f using a constant rate $\frac{d\Theta}{dt}$,

which was widely adopted by the research community since Byer and Roundy and later by Daglish [25, 23]. Another approach is to investigate the piezoelectric voltage response from the specimen at constant temperature rate. Therefore we use the relation:

$$V_{py} = \frac{p_f h_p \Delta\Theta}{\varepsilon_f \varepsilon_0} \tag{2.17}$$

where the V_{py} is proportional to the product of piezoelectric layer thickness h_p and temperature change $\Delta\Theta$. In this configuration the sample has to be investigated in in open circuit condition, so that the pyroelectric charges are contributing to the total voltage response [26].

2.2 Transducers Fabrication

2.2.1 High Frequency $LiNbO_3$ Harvesters on Si

A commercial 500 µm thick $LiNbO_3$ (YXl)/36° wafer (from Roditi) was used to fabricate thick film on Si substrate (Fig. 2.11). 200 nm thick Au layers with Cr adhesive layers, were deposited on one side of the $LiNbO_3$ wafer and on one side of a 500 µm thick Si wafer. The Si wafer presented thermal oxide with thickness of 0.5 µm. Then, the $LiNbO_3$ and Si wafers were bonded by means of mechanical compression of Au layers The $LiNbO_3$ wafer was subsequently thinned by lapping steps to an overall thickness of 32 µm, which was followed by a micro-polishing step. Then, the Si wafer was polished down to 360 µm thickness. Aluminum electrodes with thickness of 300 nm were structured on the $LiNbO_3$ surface by lift-off process using UV lithography and evaporation deposition technique. The cantilevers were diced mechanically from (32 µm)$LiNbO_3$ /(400 nm)Au-Cr/(1 µm)SiO_2/(360 µm)Si wafer by means of a dicing saw. The final dimensions of the cantilevers, without considering the clamping, were 20 mm in length and 5 mm in width. The electrode was partially covering the structure, resulting in an active surface of 46 mm^2. The Cr/Au layer used for wafer bonding was also acting as bottom electrode of the device. Fig. (2.11e) shows the cross-section of the cantilever. The photograph was taken with optical microscope from a lateral side, we could clearly see the Cr/Au bottom electrode, while the upper layer was $LiNbO_3$, and the bottom one the Si/SiO_2 substrate. Finally, Fig. (2.11f) presents the cantilever after dicing.

2.2.2 Low Frequency $LiNbO_3$ Harvester on Si

The flowchart for the second batch of samples on silicon, was similar to the first set of samples, and it is depicted in Fig (2.12). The substrates used were a [100] single crystal silicon wafer 500 µm thick, and a 350 µm single crystal $LiNbO_3$ wafer with orientation (YXl)/128°. After cleaning and rinsing, a layer of 30 nm Cr was sputtered on the polished surface of both wafers as an adhesion layer, then followed by 170 nm of Au (Fig. 2.12a).

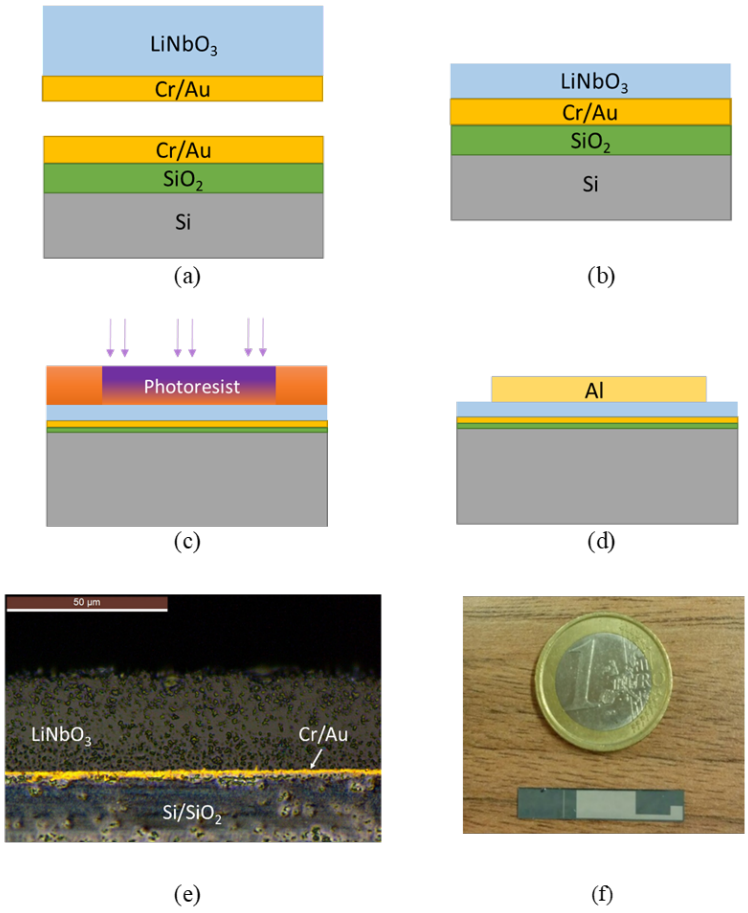

Figure 2.11: Microfabrication process flowchart for (YXl)/36° $LiNbO_3$ /Cr/Au/Cr/SiO_2/Si heterostructure: (a) 200 nm of Cr/Au were sputtered on the surface of both Si and $LiNbO_3$. (b) The two wafers were bonded together by mechanical compression and then thinned down by lapping. (c) The photoresist was spin-coated on the surface of $LiNbO_3$, and then exposed to UV light though a mask. (d) After evaporation of 300 nm of Al, the top electrode was patterned by lift-off. (e) Optical microscope cross-section photograph for the layer structure after dicing. (f) Eventually, the structures were mechanically diced in cantilever shape with an active surface of 46 mm^2.

Once the surfaces were prepared, Au-Au bonding by means of EVG thermo-compression was performed at room temperature (Fig. 2.12b). The quality of the bonding was controlled by ultrasonic testing showing good adhesion and very few imperfections due to surface pollution. In order to reach the required clamped capacitance levels, the thickness of $LiNbO_3$ is thinned down to approximately 30 µm (2 µm TTV), by lapping and micro-polishing to adjust surface morphology (Fig. 2.12c). We have used UV lithography to pattern the top electrodes (Fig. 2.12d). Once the photoresist was developed, a 200 nm thick Cr/Au layer was deposited using electron-beam evaporation (Fig. 2.12e). The resist was lifted-off with a solvent leaving just the Cr/Au electrodes on the surface. Once the devices were diced mechanically by a dicing saw (Fig. 2.12f), we have performed deep reactive ion etching (DRIE) on silicon substrate (Fig. 2.12g). The Si backside was patterned in order to leave a 10 mm by 10 mm tip mass, while the central part was etched until 300

µm thickness.

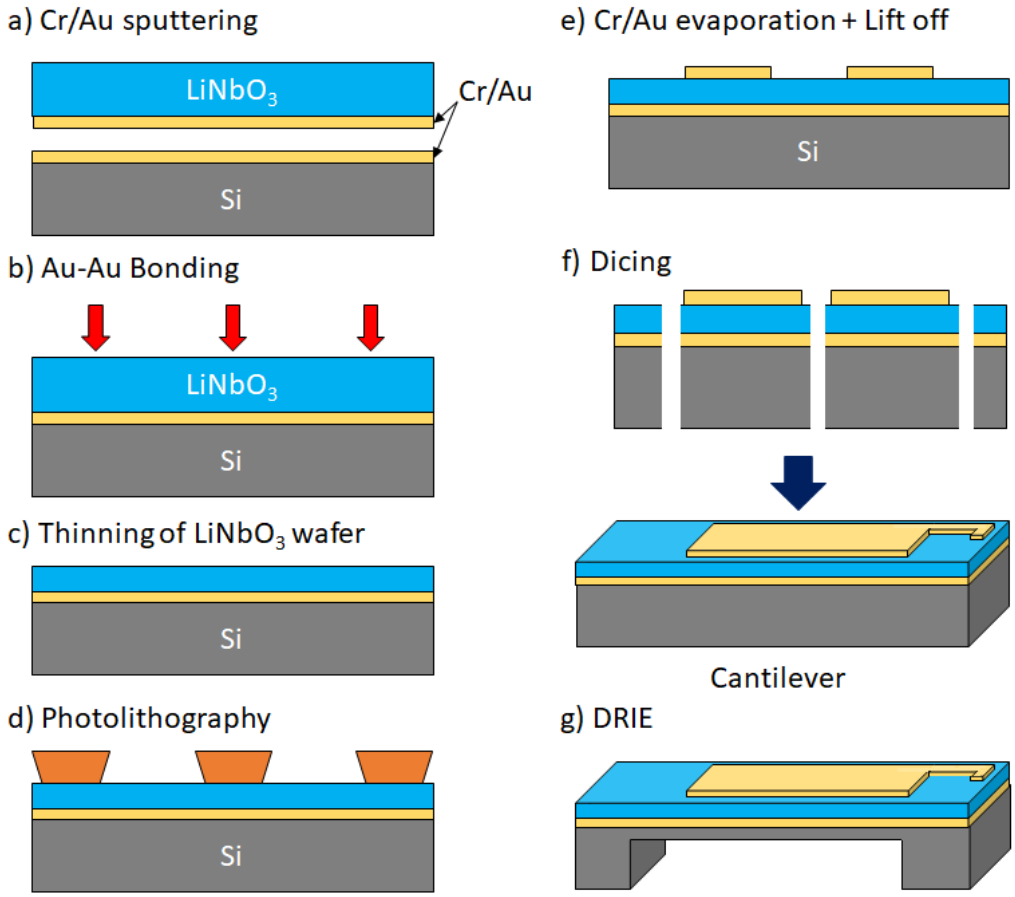

Figure 2.12: Flowchart of micro-fabrication process of (YXl)/128°/Si: (a) sputtering of Cr/Au layers on silicon and $LiNbO_3$ wafers; b) bonding by thermo-compression at room temperature; c) lapping and micro-polishing of $LiNbO_3$ surface; d) UV photo-lithography step; e) evaporation of top Cr/Au electrodes; f) mechanical dicing; g) deep reactive ion etching of silicon substrate.

The main difference respect to the previous process is the use of Au top layer to have a better conduction and same band gap for top and bottom electrodes. Moreover, we added an etching step to pattern the silicon substrate, in order to increase the coupling and reduce the resonance frequency. Eventually, the top electrodes were wire-bonded to a PCB and clamped on an Al clamping system (Fig. 5.8a). The final prototype presented here had a length of 65 mm and 10 mm width, with a top electrode covering 2/3 of the total length. In Fig. (5.8b) we can see the cross-section of the sample after dicing, where $LiNbO_3$ is the top layer, and silicon is the substrate of the structure. The thin white line is the bonding interface between the two wafers. The quality of the bonding was excellent, even if we didn't use a SiO_2 insulation layer.

2.2.3 $LiNbO_3$ Harvesters on Metal

Several metal substrate are available on the market, but often foils with thickness below 100 µm have residual stress present after lamination of the materials. We have purchased a large foil of brass (nominal value 75 µm) and then laser cut it in form of 4 inch wafers, in order to implement the material as a substrate in our fabrication process (Fig. 2.13). Also the stainless steel was considered as a host wafer for the fabrication of the devices, because it has typically higher quality factor with respect to the brass. Eventually, the first results of stainless steel laser cutting did not show the expected quality, while for brass we have attained low bow and no visible edge imperfections of wafers. Therefore we have implemented brass as the first host candidate.

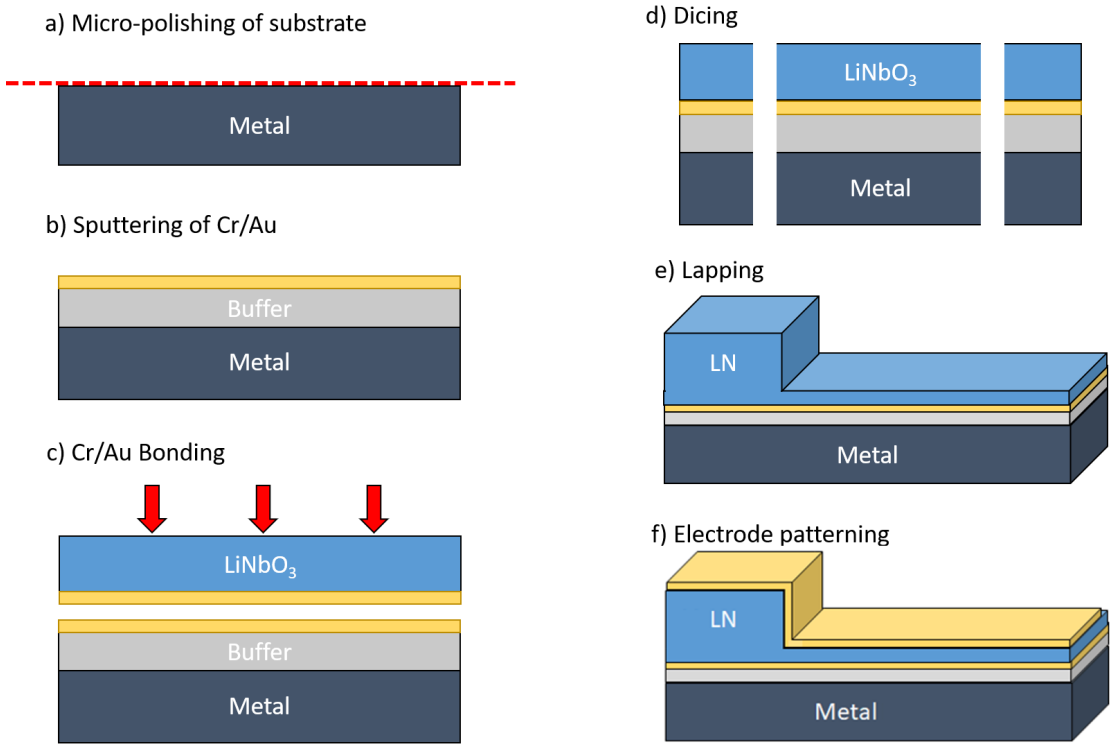

Figure 2.13: Microfabrication of $LiNbO_3$ /Brass transducer: a) surface preparation with micro-polishing step of susceptor surface; b) deposition of buffer and Cr/Au layer by sputtering; c) Au-Au bonding of $LiNbO_3$ and metal substrate; d) dicing of cantilever devices; e) lapping by rectification of $LiNbO_3$ layer and patterning for clamp/tip mass; f) top electrode sputtering (Cr/Au).

In order to have better adhesion, the wafer host was micro-polished before the Au-Au bonding step (Fig. 2.13a), so that he surface had very low roughness (< 90 nm). Once the substrate was ready, we cleaned with solvents and rinsed the host before the deposition step. Afterwards, a buffer layer was deposited on the top surface of brass to improve the conditions for bonding (Fig. 2.13b).

Eventually Cr-Au layers were sputtered on both brass and $LiNbO_3$ wafers. Later on, we performed Au-Au bonding by means of EVG bonder at room temperature (Fig. 2.13c).

The structure was diced in order to have singular cantilevers 40 mm by 10 mm in sizes (Fig. 2.13d), including the clamping. In order to attain specific properties, the $LiNbO_3$ layer of the cantilevers was lapped down to reach the required thickness (Fig. 2.13e). The investigated samples had $LiNbO_3$ thickness ranging from 10 to 120 µm. The adhesion between the two materials was excellent, and no critical issues were observed during the lapping or dicing. As a final step, we have sputtered with a stencil mask Cr/Au top electrodes on the full size of the cantilevers (Fig. 2.13f). With this approach we have simplified the micro-fabrication route having less critical steps and avoiding complications.

2.3 Conclusions

In this chapter I summarized all the possible routes of fabrication for $LiNbO_3$ films. With top-down or bottom-up approaches we can achieve high quality $LiNbO_3$ films. We presented both PIMOCVD films which can be grown textured on silicon substrates, or thick films from single crystal $LiNbO_3$ Au-Au bonded to silicon or metal. Nevertheless, for energy harvesting applications is better to consider thick films, because the power output depends strongly on the volume of active material under strain. I presented also the methodology for dielectric, piezoelectric and pyroelectric properties characterization with standardized electrode and cantilever dimensions. In the next chapters, I will show that also $LiNbO_3$ can be considered a rightfull option in terms of piezoelectric and pyroelectric energy harvesting.

Bibliography

[1] S. Roundy, P. K. Wright, and J. M. Rabaey, *Energy Scavenging for Wireless Sensor Networks*. Springer, 2004.

[2] "Smart Cut™ technology, Smart Choice - Soitec https://www.soitec.com/en/products/smart-cut," pp. 1–7.

[3] A. Bartasyte, S. Margueron, T. Baron, S. Oliveri, and P. Boulet, "Toward High-Quality Epitaxial LiNbO3 and LiTaO3 Thin Films for Acoustic and Optical Applications," *Advanced Materials Interfaces*, vol. 4, no. 8, pp. 1–36, 2017.

[4] H. Takagi, R. Maeda, N. Hosoda, and T. Suga, "Room-temperature bonding of lithium niobate and silicon wafers by argon-beam surface activation," *Applied Physics Letters*, vol. 74, no. 16, pp. 2387–2389, 1999.

[5] T. Baron, E. Lebrasseur, J. P. Romand, S. Alzuaga, S. Queste, G. Martin, D. Gachon, T. Laroche, S. Ballandras, J. Masson, and S. Ballandras, "Temperature compensated radio-frequency harmonic bulk acoustic resonators pressure sensors," *Proceedings - IEEE Ultrasonics Symposium*, pp. 2040–2043, 2010.

[6] S. Ballandras, T. Baron, E. Lebrasseur, G. Martin, A. Reinhardt, P.-p. Lassagne, J.-m. Friedt, L. Chommeloux, D. Rabus, S. Ballandras, T. Baron, E. Lebrasseur, G. Martin, and D. Gachon, "High overtone Bulk Acoustic Resonators : application to resonators , filters and sensors To cite this version : HAL Id : hal-00811239 High overtone Bulk Acoustic Resonators : application to resonators , filters and sensors," 2012.

[7] E. Lebrasseur, T. Baron, J.-j. Boy, L. Couteleau, S. Ballandras, E. Lebrasseur, T. Baron, J.-j. Boy, and L. Couteleau, "Design and fabrication of an acoustic bragg mirror for miniaturized quartz resonators To cite this version : Design and fabrication of an acoustic bragg mirror for miniaturized quartz resonators," 2012.

[8] F. Bassignot, "Nouveau type d'oscillateur exploitant des transducteurs à domaines ferroélectriques alternés et des matériaux de guidage pour l'excitation d'ondes ultrasonores d'interface," 2011.

[9] T. Baron, D. Hermelin, J.-p. Romand, S. Alzuaga, S. Queste, J.-y. Rauch, J.-f. Leguen, B. Belgasem, and S. Ballandras, "10ème C ongrès F rançais d ' A coustique SAW pressure sensor on quartz membrane lapping," pp. 2–5, 2010.

[10] F. Laerme, A. Schilp, K. Funk, and M. Offenberg, "Bosch Deep Silicon Etching: Improving Uniformity and Etch Rate for Advanced MEMS Applications," *Technical Digest. IEEE International MEMS 99 Conference.*, pp. 211–216, 1999.

[11] A. Mazzalai, D. Balma, N. Chidambaram, R. Matloub, and P. Muralt, "Characterization and Fatigue of the Converse Piezoelectric Effect in PZT Films for MEMS Applications," *Journal of Microelectromechanical Systems*, vol. 24, no. 4, pp. 831–838, 2015.

[12] S. Sherrit and B. K. Mukherjee, "Characterization of Piezoelectric Materials for Transducers," no. Nye, 2007.

[13] A. Morel, G. Pillonnet, Y. Wanderoild, and A. Badel, "Dielectric losses considerations for piezoelectric energy harvesting," *Journal of Low Power Electronics*, vol. 14, no. 2, pp. 244–254, 2018.

[14] "IEEE Standard on Piezoelectricity: An American National Standard," in *ANSI/IEEE Std 176-1987*, 1988.

[15] A. Biancoli, "Breaking of the macroscopic centric symmetry in Ba 1-x Sr x TiO 3 ceramics and single crystals PAR," vol. 6366, 2014.

[16] K. Prume, P. Muralt, F. Calame, T. Schmitz-Kempen, and S. Tiedke, "Piezoelectric Thin Films: Evaluation of Electrical and Electromechanical Characteristics for MEMS Devices," *IEEE Transactions on Ultrasonics, Ferroelectrics, and Frequency Control*, vol. 54, no. 1, pp. 8–14, 2007.

[17] M. A. Dubois and P. Muralt, "Measurement of the effective transverse piezoelectric coefficient e31,f of AlN and Pb(Zrx,Ti1-x)O3 thin films," *Sensors and Actuators, A: Physical*, vol. 77, no. 2, pp. 106–112, 1999.

[18] L. B. Freund and S. Suresh, *Thin Film Materials Stress, Defect Formation and Surface Evolution*. Cambridge University Press, 2004.

[19] M. Hopcroft, W. Nix, and W. Kenny, "What is the Young ' s Modulus of Silicon ? What is the Crystal Orientation in a Silicon Wafer ?," *JOURNAL OF MICROELECTROMECHANICAL SYSTEMS*, vol. 19, no. 2, pp. 229–238, 2010.

[20] S. Lang, "Pyroelectricity : From ancient curiosity to modern imaging tool Pyroelectricity," *Physics Today*, vol. 58, no. August, p. 31, 2005.

[21] L. A. Chavez, F. O. Zayas Jimenez, B. R. Wilburn, L. C. Delfin, H. Kim, N. Love, and Y. Lin, "Characterization of Thermal Energy Harvesting Using Pyroelectric Ceramics at Elevated Temperatures," *Energy Harvesting and Systems*, vol. 5, no. 1-2, pp. 3–10, 2018.

[22] S. Jachalke, E. Mehner, H. Stöcker, J. Hanzig, M. Sonntag, T. Weigel, T. Leisegang, and D. C. Meyer, "How to measure the pyroelectric coefficient?," *Applied Physics Reviews*, vol. 4, no. 2, 2017.

[23] M. Daglish, "A dynamic method for determining the pyroelectric response of thin films," *Integrated Ferroelectrics*, vol. 22, no. 1-4, pp. 473–488, 1998.

[24] G. Clementi, S. Margueron, M. A. Suarez, T. Baron, B. Dulmet, and A. Bartasyte, "Piezoelectric and Pyroelectric Energy Harvesting from Lithium Niobate Films," *Journal of Physics: Conference Series*, vol. 1407, no. 1, 2019.

[25] R. L. Byer and C. B. Roundy, "Pyroelectric coefficient direct measurement technique and application to a nsec response time detector," *Ferroelectrics*, vol. 3, no. 1, pp. 333–338, 1972.

[26] J. Fraden, *Handbook of Modern Sensors*. 2016.

3 Piezoelctric and Pyroelectric Properties of Lithium Niobate Films

In the first part of the chapter, the simulations concerning the piezoelectric and pyroelectric properties of $LiNbO_3$ are presented and both coupling and figure of merits are discussed. A subsection is devoted to the analysis of the orientation study of $LiNbO_3$ for energy harvesting purposes, comparing three particular orientations investigated in this work: (YXl)/36°, /128° and /163°. A the end of the chapter, a section will be devoted to the characterization of $LiNbO_3$ thick and thin films, where their dielectric, piezoelectric and pyroelectric properties, measured experimentally will be presented. In the conclusion I will point out what are the future challenges and recommendations to implement $LiNbO_3$ as transducer for energy harvesting.

3.1 Orientations of $LiNbO_3$

The optimized direction for piezoelectric measurement was firstly investigated by Nakamura et al. [1], where was considered the bending of a $LiNbO_3$ plate with a ferroelectric inversion layer for actuation. Nakamura ponted out that there are preferential orientations in order to implement $LiNbO_3$ as a bender. Later, by Shur et al [2], was shown that the piezoelectric constant increases from 0 up to 27.3 pC/N using 128° Y-cut, so this crystal cut was identified as a suitable choice for bending actuators.

In this thesis we will use the notation first proposed by Nakamura [3], and the cut will be defined as $LiNbO_3$ (YXl)/θ°. The transformation of the crystallographic axis involves the rotation not only of the piezoelectric tensor but also of the dielectric and elastic properties of $LiNbO_3$. To perform the study, we have to take into account the transformation in a tridimensional system of reference. In this case, given the reference of crystallographic axis as (a,b,c) and considering the polarization along c-axis, we define a new orthogonal triad of axis (X,Y,Z) where Z is parallel to c-axis, a is parallel to X, and Y completes the system with 90° from both the other axis. Now we can define the rotation using the Euler angles (ϕ,θ,ψ), they can be seen as consecutive rotations, and they are introduced in matrix notation as follows [4].

To make a rotation counterclockwise of ϕ around Z:

$$a_{\mathrm{I}} = \begin{pmatrix} \cos\phi & \sin\phi & 0 \\ -\sin\phi & \cos\phi & 0 \\ 0 & 0 & 1 \end{pmatrix} \tag{3.1}$$

To make a rotation counterclockwise of θ around X':

$$a_{\mathrm{II}} = \begin{pmatrix} 1 & 0 & 0 \\ 0 & \cos\theta & \sin\theta \\ 0 & -\sin\theta & \cos\theta \end{pmatrix} \tag{3.2}$$

To make a rotation counterclockwise of ψ around Z'':

$$a_{\mathrm{III}} = \begin{pmatrix} \cos\psi & \sin\psi & 0 \\ -\sin\psi & \cos\psi & 0 \\ 0 & 0 & 1 \end{pmatrix} \tag{3.3}$$

The general rotation is then the product of all the transformations done so far:

$$a = a_{\mathrm{I}} a_{\mathrm{II}} a_{\mathrm{III}} \tag{3.4}$$

Now, we can apply this formalism to make a rotation of the dielectric, elastic and piezoelectric tensors. We can use the compressed notation from [5, 6] and the bond strain notation matrix, **R**, which gives the following set of equations for a representation of $LiNbO_3$ Y-cut crystal cut:

$$\varepsilon' = a_{\mathrm{II}} a_{\mathrm{I}} \cdot \varepsilon \cdot a_{\mathrm{I}}^t a_{\mathrm{II}}^t \tag{3.5}$$

$$d' = a_{\mathrm{II}} a_{\mathrm{I}} \cdot d \cdot \mathrm{R}_{\mathrm{I}}^t \mathrm{R}_{\mathrm{II}}^t \tag{3.6}$$

$$s' = \mathrm{R}_{\mathrm{II}} \mathrm{R}_{\mathrm{I}} \cdot s \cdot \mathrm{R}_{\mathrm{I}}^t \mathrm{R}_{\mathrm{II}}^t \tag{3.7}$$

where **R** is defined as the matrix:

$$\mathbf{R} = \begin{pmatrix} a_{11}^2 & a_{12}^2 & a_{13}^2 & a_{12}a_{13} & a_{13}a_{11} & a_{11}a_{12} \\ a_{21}^2 & a_{22}^2 & a_{23}^2 & a_{22}a_{23} & a_{23}a_{21} & a_{21}a_{22} \\ a_{31}^2 & a_{32}^2 & a_{33}^2 & a_{32}a_{33} & a_{33}a_{31} & a_{31}a_{32} \\ 2a_{21}a_{31} & 2a_{22}a_{32} & 2a_{23}a_{33} & a_{22}a_{33}+a_{32}a_{23} & a_{23}a_{31}+a_{33}a_{21} & a_{21}a_{32}+a_{31}a_{22} \\ 2a_{31}a_{11} & 2a_{32}a_{12} & 2a_{33}a_{13} & a_{32}a_{13}+a_{12}a_{33} & a_{33}a_{11}+a_{13}a_{31} & a_{31}a_{12}+a_{11}a_{32} \\ 2a_{11}a_{21} & 2a_{12}a_{22} & 2a_{13}a_{23} & a_{12}a_{23}+a_{22}a_{13} & a_{13}a_{21}+a_{23}a_{11} & a_{11}a_{22}+a_{21}a_{12} \end{pmatrix} \tag{3.8}$$

So that the piezoelectric tensor will be transformed as:

$$\delta_{lmn} = a_{li} a_{mj} a_{nk} d_{ijk} \tag{3.9}$$

As pointed out in [7], when the angle θ is considered, and the rotation takes place from Y'-axis, the thickness and transverse coefficients will be d_{2j} and not d_{31} as in ceramics. For this reason, in this work we will consider the following coefficients: d_{21}, d_{23} for transverse mode, and d_{22} for thickness mode. The resulting equations for the transformations are:

$$\begin{aligned} d'_{21} &= d_{31}\sin\theta - d_{22}\cos\theta \\ d'_{23} &= \sin\theta\left(d_{31}\sin^2\theta + d_{33}\cos^2\theta\right) + \cos\theta\left(d_{22}\sin^2\theta - d_{15}\cos\theta\sin\theta\right) \end{aligned} \tag{3.10}$$

In Eq. (3.10) d' represents the rotated coefficient. The main difference between them is the dependence on other piezoelectric coefficients. The advantage of d'_{23} over d'_{21} is the dependency over the shear coefficient d_{15} which has the highest value among the others (68 pC/N). In thickness mode instead we will have for d'_{22}:

$$d'_{22} = d_{33}\sin^3\theta + (d_{31} + d_{15})\cos^2\theta\sin\theta + d_{22}\cos^3\theta \tag{3.11}$$

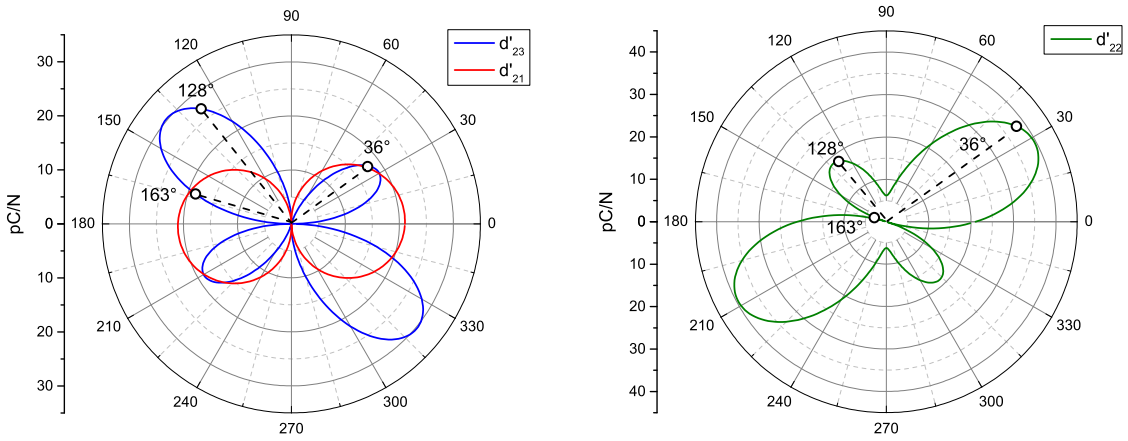

Figure 3.1: Polar plot for $LiNbO_3$ piezoelectric tensor: (a) d'$_{21}$ and d'$_{23}$; (b) d'$_{22}$ rotated by θ.

Otherwise, in order to investigate the rotation around *Y'*, we can use the following matrix:

$$a_{\mathrm{II}} = \begin{pmatrix} \cos\phi & 0 & \sin\phi \\ 0 & \cos\phi & 0 \\ -\sin\phi & 0 & \cos\phi \end{pmatrix} \tag{3.12}$$

Hence, we can select an orientation of Y-cut (rotation around *X* axis) and then counter-check the tensor values while the rotation is in the plane (rotation around *Y'* axis). For

instance, the piezoelectric coefficient of interest, d_{2j}, is defined as:

$$d'_{2j} = \sin^2\phi(d_{31}\sin\theta - d_{22}\cos\theta) + \cos^2\phi(d_{22}\sin^2\theta\cos\theta + d_{31}\sin^3\theta - d_{15}\sin\theta\cos^2\theta + d_{33}\sin\theta\cos^2\theta) \tag{3.13}$$

where the rotated piezoelectric coefficient is depending on both rotation angles (θ,ϕ). Finally, in Fig. (3.1a) are plotted the moduli of the two piezoelectric tensors, d'_{21}, d'_{23} and separately d'_{22}, while rotating around X-axis with an angle $\theta = [0,360°]$. Generally, d'_{21} has lower magnitude, thus we will focus our analysis on d'_{23}. We can see that the difference between the orientations becomes very important above 90°, which represents a regular Z-cut, and approaching 140°, where we obtain a maximum for the piezoelectric coefficient, namely 30.2 pC/N. Otherwise, we have similar performance for 36° and 163°, which can attain similar piezoelectric strain coefficient, 18 pC/N. Eventually, in the case of commercial cuts, the best value attainable is 27 pC/N cut for 128°-Y cut. For the thickness mode instead, we plotted d'_{22} in Fig. (3.1b). Differently than from the transverse case, the best orientation appears to be 36° having 38.2 pC/N, while for 163° the mode is totally inefficient.

In Fig. (3.2) is represented the piezoelectric tensor d_{2j}, where the polarization is along *Y'* and j is representing the direction of the stress in the plane. We represented the three orientation of choice (θ=36°, 128° and 163°), while $\phi = [0,360°]$. The study is confirming that the highest magnitude of the coefficient is obtained for (YXl)/128°, namely when $j = 3$, hence $\phi = 0$, with 27 pC/N, and the other orientation have typically lower values. However, for d_{21} ($\phi = 90°$) coefficient the best orientation is (YXl)/163° with 19.8 pC/N.

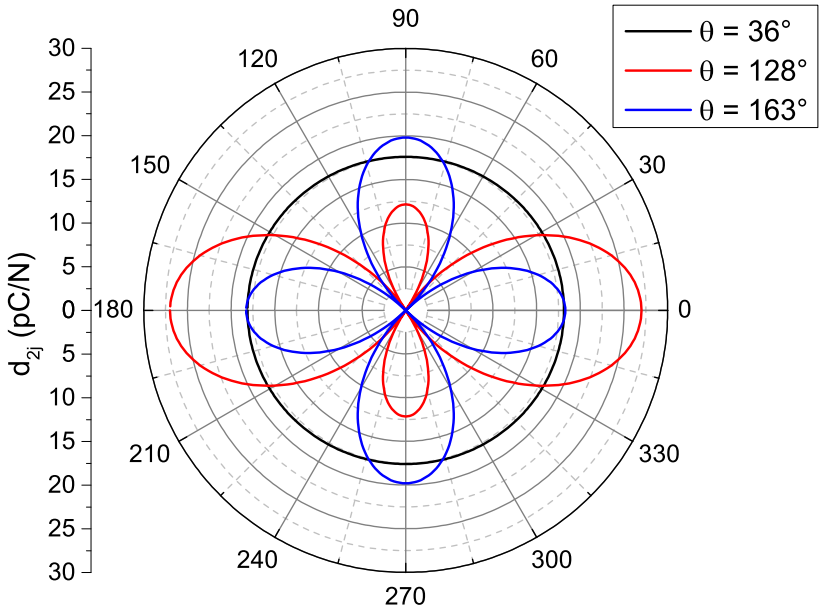

Figure 3.2: Rotation in the plane by ϕ *of the piezoelectric coefficient* d_{2j}.

In order to investigate the electro-mechanical coupling factor in transverse mode, all the coefficients of Eq. (1.20) have to be taken into account. The rotation around X-axis is implemented also for compliance s'_{ii} and dielectric constant ε'_{jj}, where the superscript of constant stress (T) is neglected in the Eq. (3.14,3.16).

$$s'_{33} = s_{11}\sin^4\theta + 2s_{14}\sin^3\theta\cos\theta + (s_{44}+2s_{13})\sin^2\theta\cos^2\theta + s_{33}\cos^4\theta \tag{3.14}$$

$$\varepsilon'_{22} = \varepsilon_{33}\sin^2\theta + \varepsilon_{11}\cos^2\theta \tag{3.15}$$

While for thickness mode we use the same permittivity ε'_{22}, but different compliance coefficient, s'$_{22}$:

$$s'_{22} = s_{33}\sin^4\theta + (s_{44}+2s_{13})\cos^2\theta\sin^2\theta - 2s_{14}\cos^3\theta\sin\theta + s_{11}\cos^4\theta \tag{3.16}$$

Clearly in Fig. (3.3a), we see that s'_{11} is not affected by the rotation, hence the value is constant ($5.78{\cdot}10^{-12}\mathrm{P}a^{-1}$). More interesting for s'_{33}, we noticed a dependence on both diagonal (s_{11},s_{33} and s_{44}) and non-diagonal terms (s_{13} and s_{14}). The rotation around X-axis then has two relative peaks: one is observed around 41°, and a second one below 128°. Analyzing the coefficient values we may state that with tilted cuts the stiffness increases with respect to a standard Z-cut, which can be interesting when designing strain-driven harvesters. Meanwhile in Fig. (3.3b), s'_{22} is represented. For thickness mode, we see that s'_{22} has a similar behavior to s'_{33} but 90° tilted, due to an exchanged sine and cosine product between the terms in Eq. 3.16. In terms of permittivity, ε'_{22} depends on both ε_{33} and ε_{11}. We see in Fig. (3.3c), that ε'_{22} has a minimum for Z-Cut whereas it reaches 30, while the highest value for the cuts examined is for 163° reaching 79.4, finally for 128° goes as low as 50.5.

The coupling in transverse mode for the selected piezoelectric coefficients is calculated by the following relations:

$$k'_{21} = \frac{d'_{21}}{\sqrt{s'_{11}\varepsilon'_{22}}} \tag{3.17}$$

$$k'_{23} = \frac{d'_{23}}{\sqrt{s'_{33}\varepsilon'_{22}}} \tag{3.18}$$

Whereas the thickness mode, k'_{22} will be defined as:

$$k'_{22} = \frac{d'_{22}}{\sqrt{s'_{22}\varepsilon'_{22}}} \tag{3.19}$$

Finally, in Fig. (3.4) both electro-mechanical couplings are plotted against the angle $\theta = [0, 180°]$. For transverse mode k'_{23}, the maximum achievable is at 137° (0.51), while is 0.49 for 128°. The other coupling k'_{21} is generally lower respect to k'_{23}, but almost compa-

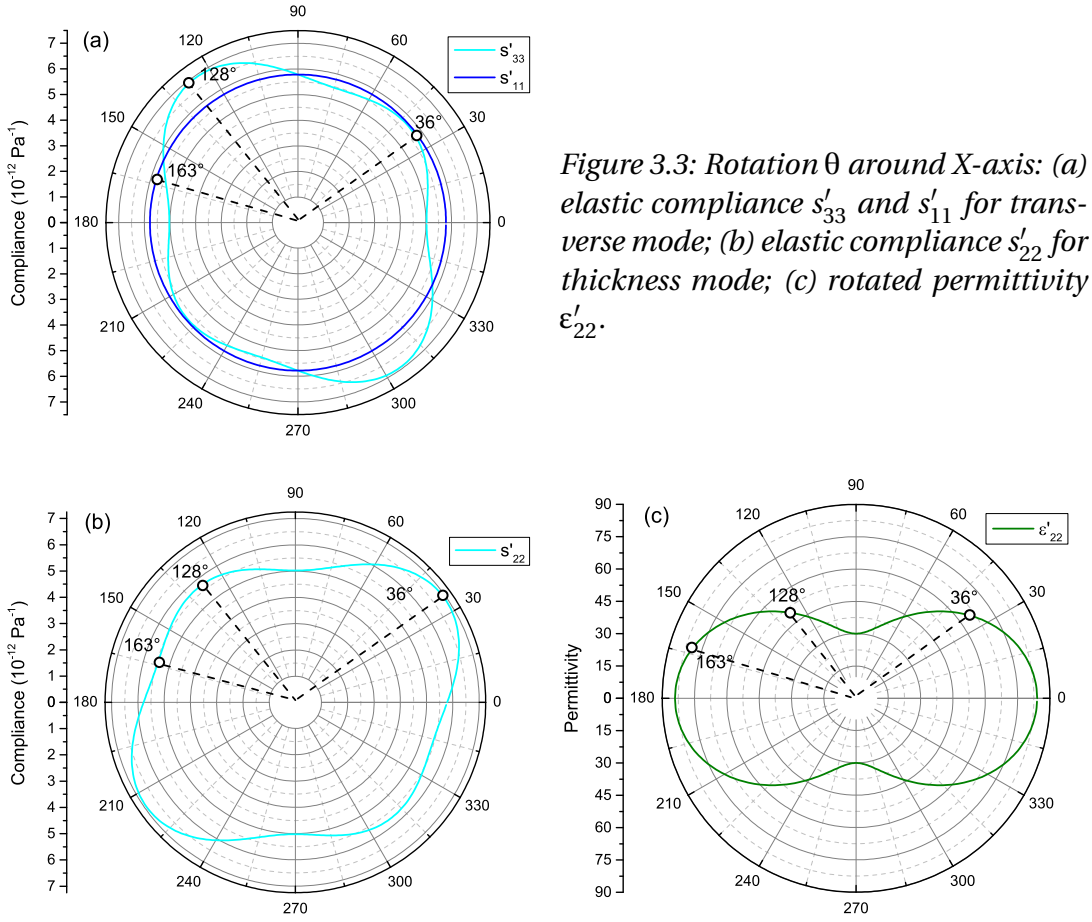

Figure 3.3: Rotation θ around X-axis: (a) elastic compliance s'_{33} and s'_{11} for transverse mode; (b) elastic compliance s'_{22} for thickness mode; (c) rotated permittivity ε'_{22}.

rable for 36° and 163° cuts. Instead in thickness mode, as expected the best orientation is 36°, with a value of 0.61, against 128° presenting $k'_{22} = 0.36$. Therefore $LiNbO_3$ (YXl)/36° is the most suitable with the use of IDTs.

As seen in Eq. (3.17) and (3.18), we should consider also s'_{3j} and ε'_{2j} in order to calculate k_{2j}. With a similar approach, we can investigate the magnitude of compliance and dielectric constant in terms of the angle ϕ. The result of the study is given in Fig. (3.5), and it is showing that the highest coupling is attained for k_{23} for (YXl)/128°, while k_{21} the value for (YXl)/36° and (YXl)/163° is approximately 0.3. In Fig. (3.6) the coupling k_{2j} as a function of both angles θ = [0,180°] and ϕ = [0,90°] is presented. As a result, (YXl)/36° orientation can be implemented in almost all orientations in the plane with respect to ϕ, because it presents small variations of transverse coupling k_{2j}. On the contrary, (YXl)/128° and (YXl)/163° orientations, are strongly dependent on the value of ϕ, therefore extreme attention has to be paid whenever choosing the direction of propagation for cantilevers during design phase.

In Tables (3.2) and (3.1) the values of transverse and longitudinal electro-mechanical coupling are reported for the orientation study. For k'_{23}, $LiNbO_3$ has preferentially one orientation, that is (YX*l*)/137°. Also looking at the FOMs we can come to the same conclusion. For strain-driven harvester also 36° and 163° represent a good choice, especially considering the fact that they have higher dielectric constant. We recommend those cuts

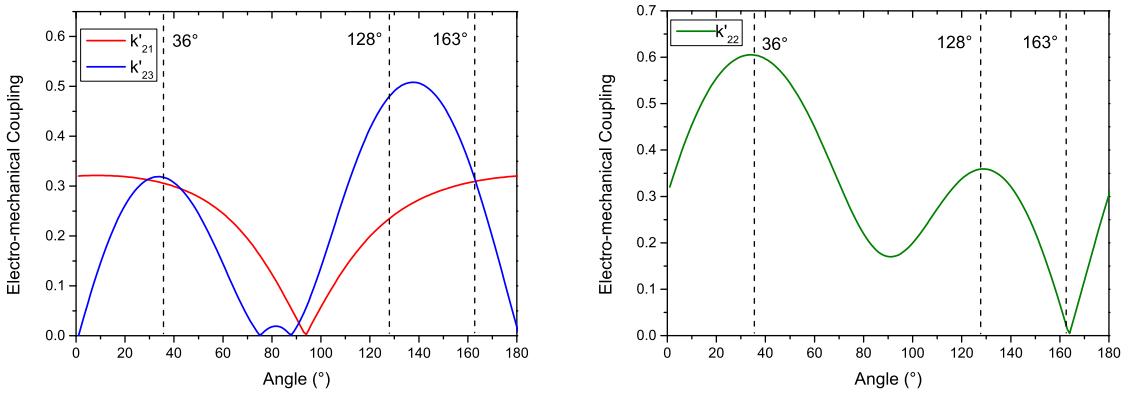

Figure 3.4: Electromechanical coupling factor: (a) transverse mode k'_{23} and k'_{21}; (b) thickness mode k'_{22}

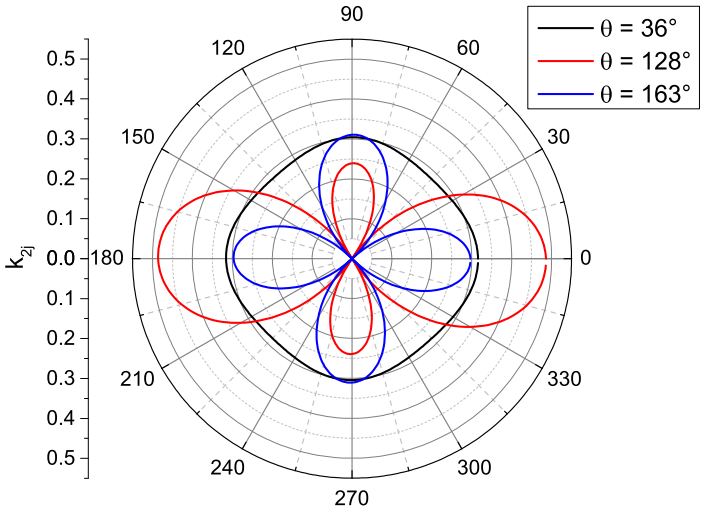

Figure 3.5: Rotation in the plane by ϕ of electromechanical coupling coefficient k_{2j}.

for MEMS application where lateral dimension are limited and small clamped capacitance could be an issue. Overall, 128° remains the best compromise between the available cuts, in terms of both FOMs and electro-mechanical coupling. For k'_{22} instead, as expected the best solution is 36° orientation, attaining higher values of FOMs compared to its transverse counterpart 128°. In this work, we investigated the three principal orientations in transverse mode (parallel plate electrodes): 36°, 128° and 163°. For all of the mentioned cuts, electro-mechanical coupling is above 0.3, so typically comparable with poled ceramics such as PZT-5A or -5H.

Table 3.1: Comparison of transverse k'$_{23}$ and FOM for $LiNbO_3$, reference values from [5].

(YXl)/θ	s_{33}^{E} (pm^2N^{-1})	s_{33}^{D} (pm^2N^{-1})	$\varepsilon_{22}^{T}/\varepsilon_0$	d_{23} (pCN^{-1})	k_{23}	$(FOM^{T})^{-1}$ ($MJ.cm^{-3}$)	FOM^{S} ($KJ.cm^{-3}$)
0°	5.02	5.02	84.0	0	0	-	0
36°	5.70	5.10	65.3	18.1	0.32	1.76	19.5
41°	5.72	5.21	60.8	16.6	0.30	1.96	17.1
90°	5.78	5.78	30.0	1.0	0.03	266	0.1
128°	6.91	5.28	50.5	27.0	0.49	0.61	44.7
137°	6.68	4.94	58.8	30.0	0.51	0.60	52.0
163°	5.40	4.92	79.4	18.3	0.30	2.1	17.9

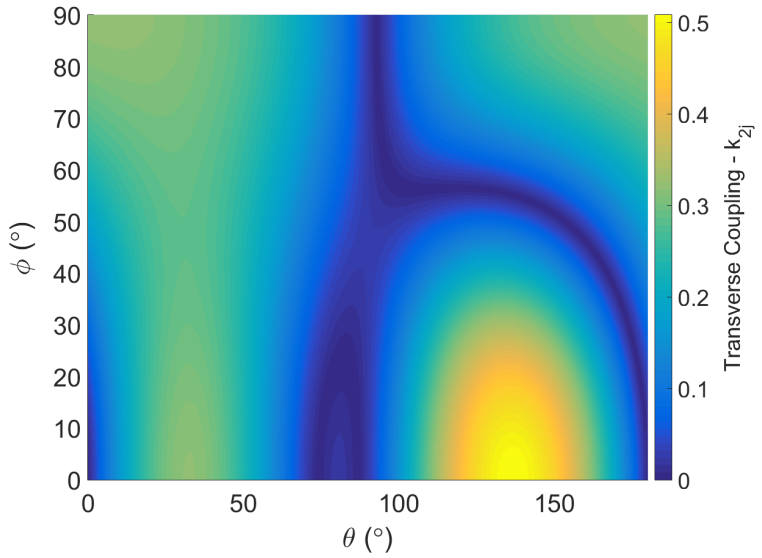

Figure 3.6: Rotation in the plane by ϕ *and* θ *of electromechanical coupling coefficient* k_{2j}.

3.2 Characterization of Piezoelectric and Pyroelectric Properties of Lithium Niobate films

In the following section I will present the results of basic dielectric, piezoelectric and pyroelctric characterization of $LiNbO_3$ films. Both thick ($h_p > 5$ µm) and thin ($h_p \approx 100$ nm) $LiNbO_3$ films on silicon substrate were investigated. In case of single crystal films bonded on Si, the orientations involved were 36° Y, 128° Y and 163° Y-cut, while for textured films on Si only one orientation was investigated, 33° Y. For the latter, also some results on optimization (Raman, X-Ray diffraction and AFM characterization) of the textured film growth will be presented.

Table 3.2: Comparison of longitudinal k'$_{22}$ and FOM for $LiNbO_3$, reference values from [5].

(YXl)/θ	s_{22}^E (pm^{2}N^{-1})	s_{22}^D (pm^{2}N^{-1})	$\varepsilon_{22}^T/\varepsilon_0$	d_{22} (pCN^{-1})	k_{22}	(FOM^T)$^{-1}$ (MJ.cm^{-3})	FOM^S (KJ.cm^{-3})
0°	5.78	5.19	84.0	21	0.32	1.69	19.8
36°	6.92	4.40	65.3	38.2	0.61	0.39	82.6
41°	6.86	4.47	60.8	35.8	0.59	0.42	77.8
90°	5.02	4.88	30.0	6.2	0.17	6.91	5.9
128°	5.71	4.97	50.5	18.1	0.36	1.36	25.9
137°	5.70	5.07	58.8	18.2	0.33	1.57	22.0
163°	5.44	5.44	79.4	0.3	0	-	-

3.2.1 Thick $LiNbO_3$ Films on Si

Typically, the permittivity and tan δ for a piezoelectric harvester are measured at 1 kHz, but we choose to measure also for other frequencies in order to investigate frequency dispersion. In Fig. (3.7) we represent the relative permittivity and losses for the three cuts (36° Y-, 128° Y- and 163° Y-cut) as a function of the frequency. The values of ε_f are given with an error of ±2 taking into account the thickness variation of the piezoelectric layer, only (YXl)36° is slightly below (60.9) the expected value (65.3), while for the other orientations the simulated values match the measured ones considering the relative error. As expected in the kHz range we do not have important variations of the permittivity, while losses slightly change, having a minimum above 10 kHz. The very low value of tan δ, is proving the very good quality of the piezoelectric crystal [8], having losses ranging from 1.3÷3.3 mU at 1 kHz, which is much lower than other ceramics (for PZT 10 mU [9]). Finally, higher dielectric losses are observed at 1 MHz, due to electronic interface noise or relaxation effect [10]. In Table (3.3) we summarized the theoretical dielectric permittivity values (ε_{22}^T) and experimental ones (ε_f) with relative losses (tan δ), measured a 1 kHz.

Table 3.3: Dielectric permittivity and losses at 1 kHz for $LiNbO_3$ (YXl)/θ°.

(YXl)/θ°	$\varepsilon_{22}^T/\varepsilon_0$	$\varepsilon_f/\varepsilon_0$	tan δ(U)
36°	65.3	60.9	0.001
128°	50.5	49.9	0.003
163°	79.4	79.6	0.003

In Fig. (3.8b-d) the magnitude of the polarization and displacement are plotted for the three orientations (36° Y-, 128° Y- and 163° Y-cut). The measurement was done switching the polarization and averaging the response for 30 cycles. Here we represent just the results for the cantilever with longer electrode (8.5 mm) but also other lengths were system-

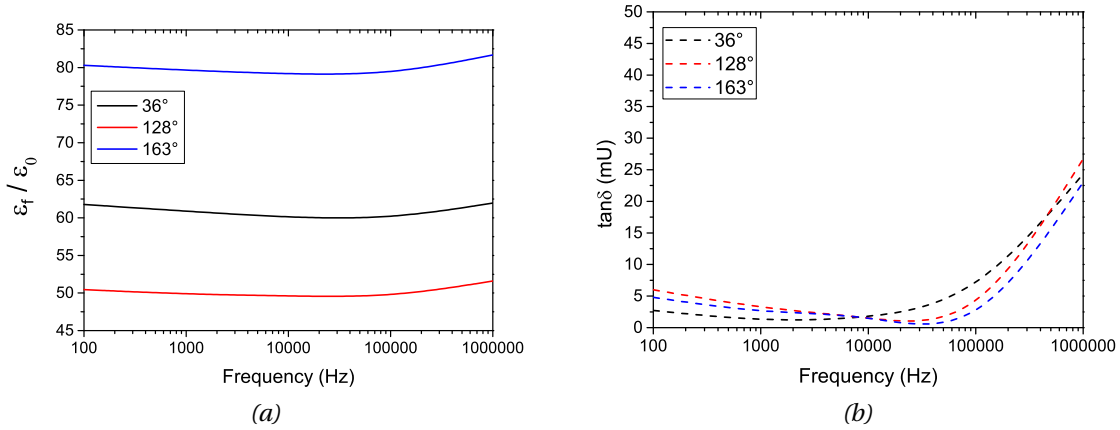

Figure 3.7: 36° Y-, 128° Y- and 163° Y-cut $LiNbO_3$ dielectric properties as a function of frequency: (a) dielectric constant; (b) dielectric losses.

atically tested. In the case of $LiNbO_3$ (YXl)/36° the applied electric field is smaller because of the thicker sample under investigation (namely 32 ± 2 µm) and therefore the induced polarization. Moreover, $LiNbO_3$ has a very high coercive field (for congruent composition 207 kV/cm), and given the thick film under investigation, the applied voltage was not sufficient to reverse the spontaneous polarization ($V_{max} = 24$ V). Hence the shape of the polarization and displacement have not the typical behavior showed in Chapter 1 (Fig. 1.9), and the crystals behave like a capacitor, without reaching the saturation point. Anyways, the response is linear as expected for a single crystal sample [3], and there is no sign of hysteresis, even though the displacement is influenced by the presence of low frequency noise coming from the electronic setup. The magnitude of displacement changes considerably with the thickness of the substrate. Normally the Si thickness for both $LiNbO_3$ (YXl)/36° and 163° was 350 µm, while for (YXl)/128° was 530 µm. Even if the samples were thinner compared to the other orientations, 128° was able to reach 283 nm tip displacement.

In Fig. (3.9a) are represented the calculated in-plane stress and the resulting piezoelectric stress coefficient. The stress component T_3 is plotted for different magnitude of applied field, and when same electrode length was considered. The maximum stress is given by 128° Y-cut as expected, and the value ranging from 2÷18 MPa, is reasonably under the threshold of film cracking which is 500 MPa. Moreover we see that the response is linear for all the orientations, so we can assume there are no bifurcations during the bending of the cantilevers. Eventually we can estimate $e_{23,f}$ from the stress measurements. The values are represented in Fig. (3.9b), as expected the best configuration is experimentally achieved with $LiNbO_3$ (YXl)/128° which showed constant value for different electrode lengths achieving 3.54 $C.m^{-2}$ with an error of less than 5%. Only in the case of 36° Y-cut we had higher relative error, 7%, due to slightly higher bending response for smaller electrode lengths.

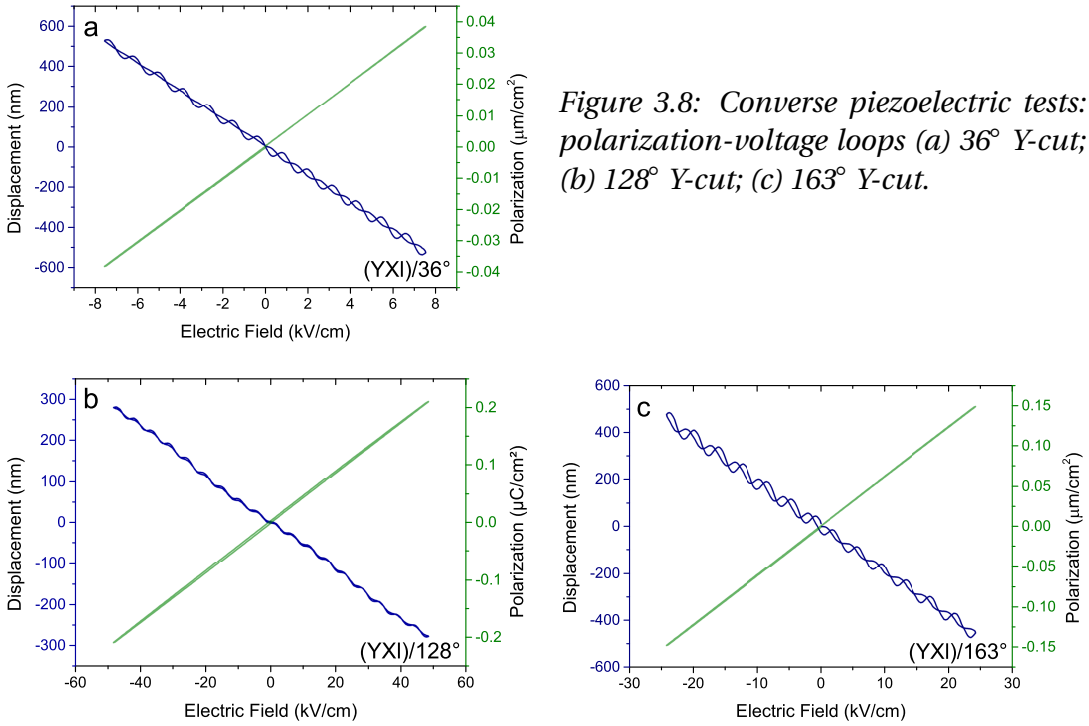

Figure 3.8: Converse piezoelectric tests: polarization-voltage loops (a) 36° Y-cut; (b) 128° Y-cut; (c) 163° Y-cut.

If we make a comparison with the rotated values from the orientation study, we see the measured values are generally higher. As stated in [11], the value of the effective coefficient is always higher ($|\, e_{31,f}\,| > |\, e_{31}\,|$), because we have to consider both in plane stress components, T_1 and T_3. The difference between the values can be high, for instance in the case of PZT ceramics the ratio between the two piezoelectric coefficients, $e_{31,f}/e_{31}$, can be even $3 \div 4$ times larger [12]. In Table 3.4 are reported some values for ceramics and the one from the orientation study of $LiNbO_3$. As expected the values are higher than the simulated counterpart, when rotating $LiNbO_3$ we have to consider not only the transverse coefficients but also the shear ones, so also e_{24} contributes to the final coefficient magnitude of $e_{23,f}$.

Table 3.4: Comparison of theoretical e_{ij} and effective $e_{ij,f}$ coefficients of $LiNbO_3$ and PZT ceramics.

Material	e_{ij} ($C.m^{-2}$)	$e_{ij,f}$ ($C.m^{-2}$)
$LiNbO_3$ (YXl)/36°	-1.42	-2.94
$LiNbO_3$ (YXl)/128°	-2.43	-3.54
$LiNbO_3$ (YXl)/163°	-1.68	-2.47
PZT-4	-5.2	-15
PZT-5H	-6.55	-23.3

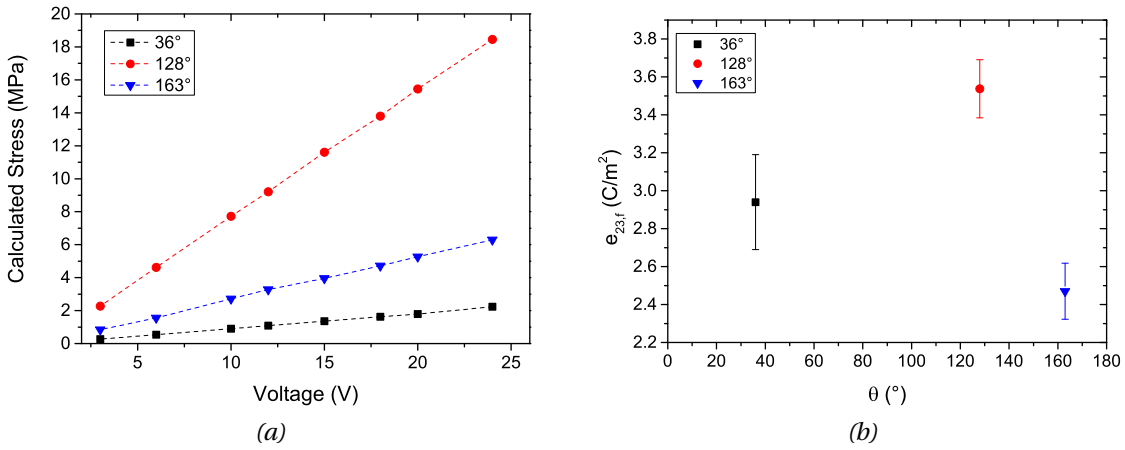

Figure 3.9: Piezoelectric properties of 36° Y-, 128° Y- and 163° Y-cut $LiNbO_3$ samples: (a) in-plane stress as a function of voltage; (b) piezoelectric stress coefficient as a function of $LiNbO_3$ cut.

Finally, we will end our analysis with the experimental results of pyroelectric current and relative orientation investigation. In the system used by A. Biancoli [13], a triangular wave was changing periodically with a given temperature rate of roughly ± 2 °C and a period of 100 s. The generated current is measured by a Labview controlled system, which converts the signal into voltage and it amplifies its magnitude so that the output signal is measured by a multi-meter. In Fig. (3.10a) we can see the specimen positioned over the Peltier element without the insulating cover, and the two probes measuring the pyroelectric response of the material from top and bottom electrodes. In Fig. (3.10b-d) the pyroelectric current responses for different crystal cut orientations are plotted. The red curve represents the triangular temperature waveform imposed on the sample, while the blue is the squared response of the material to the heating cycle. Typically, the specimens are heated around R_T, and whenever the temperature reaches the maximum value imposed, the heating ramp changes slope causing the sample to cool down. In this way the charges that were migrating in one direction are forced to switch polarization, reversing the current phase. When all the charges available have migrated towards the surface of the electrodes, the pyroelectric current reaches a threshold value that represent the maximum of i_{py}. In the calculation of Eq. (2.16) we use $i_{py}/2$ averaging on the value of the peaks to extrapolate the pyroelectric coefficient, while $d\Theta/dt$ is derived directly from the slope of the triangular wave. The pyroelectric response is not symmetrical for all the samples, this could be due to a difference between the metal used for top and bottom electrode.

The calculated pyroelectric coefficients are listed in Table (3.5). As expected the values are lower than the regular Z-cut, because we are measuring just a projection of the pyrolectric coefficient, p_3. If we compare with the expected value in Table 3.6, we have a discrepancy between two orientations, 36° and 163° most likely because of non-uniform

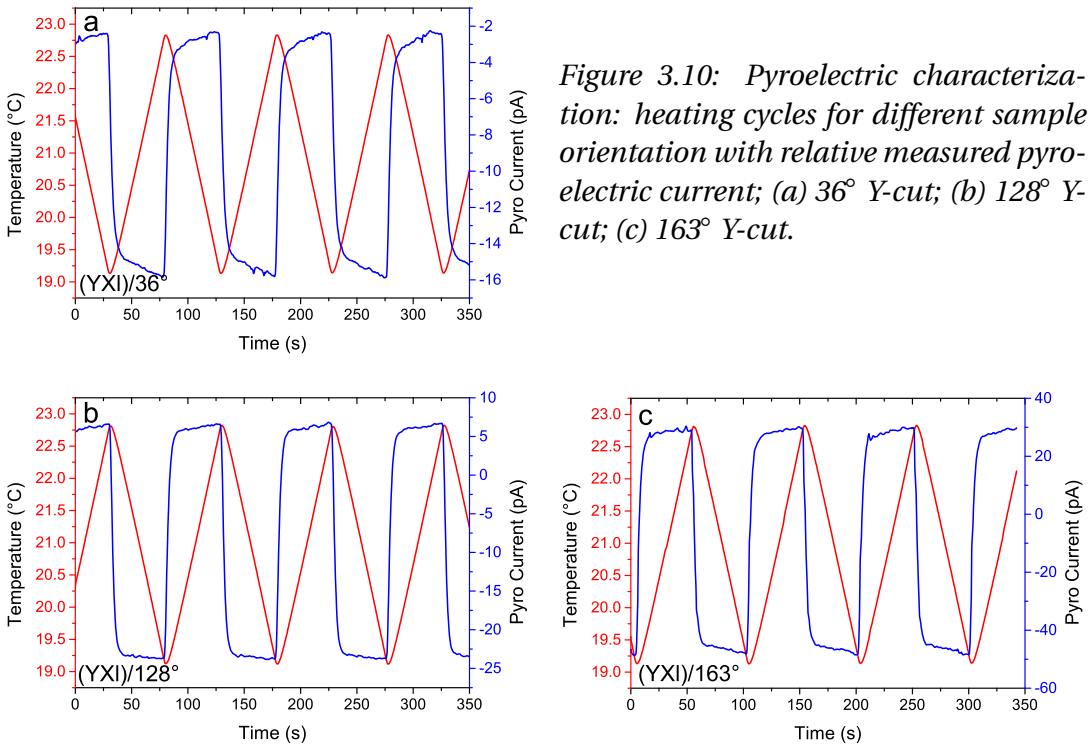

Figure 3.10: Pyroelectric characterization: heating cycles for different sample orientation with relative measured pyroelectric current; (a) 36° Y-cut; (b) 128° Y-cut; (c) 163° Y-cut.

heating of the samples or leakage currents during the measurement, but we exclude presence of *tertiary* pyroelectric effect (or false effect) [14]. Nevertheless, the results for 128° orientation are matching the simulated values.

Table 3.5: Pyroelectric coefficient magnitude for $LiNbO_3$ (YXl)/θ° in ($\mu C.m^{-2}.K^{-1}$)

(YXl)/θ°	36°	128°	163°
$p_{2,f}$	25	-51	-56
$p\cos\theta$	67	-51	-79

The last test on pyroelectric response was the measurement of the pyroelectric voltage. Two geometries of pyroelectric specimens were characterized, measuring the voltage response for different threshold temperatures with a squared waveform at 1 MΩ resistive load, using 36° Y-cut $LiNbO_3$ (100 µm thick). The electrodes had circular (ThEH-1) or square (ThEH-2) shape, but same conductive area (5 mm^2). The typical pyroelectric voltage behavior during one cycle is shown in Fig. (3.11a). After increasing the temperature of the furnace to 100°C, it was possible to observe that the voltage was slowly ascending, reaching 1 mV when at the maximum cycle temperature. While the temperature was steady, the voltage was quickly reaching zero, mainly because there was no change in polarization of $LiNbO_3$. This proved a fast response of the device to external heating sources. Finally, it was possible to make a comparison between the two geometries (Fig. (3.11b). The collected voltages using different electrode shape were identical within the

error range. Both of them increased with the temperature reaching the maximum value V_{max}=2.6 mV at 200°C. The pyroelectric voltage increased non-linearly with the increase average cycling temperature and this relationship can be described by the second order polynomial function. The slope of the curve is related to the increase of the pyroelectric coefficient along with the threshold temperature. Eventually our measurement confirms the pyroelectric response of the material increases until it reaches Θ_C where no spontaneous polarization is present, therefore p drops to zero [15]. It has to be noted that during the measurement we could not use higher resistive loads, so the voltage measured does not corresponds to the open circuit value. However, the trend shows good agreement with the expected properties of pyroelectric materials.

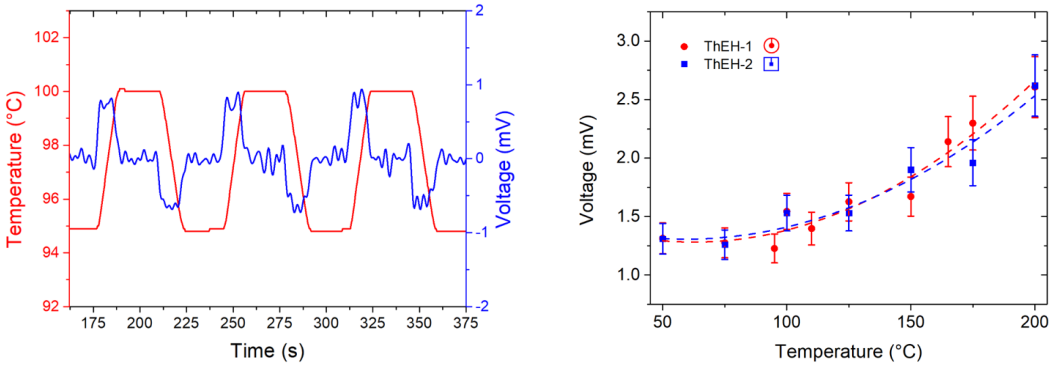

Figure 3.11: Pyroelectric voltage of 36° Y-cut $LiNbO_3$: (a) Generated pyroelectric voltage by ThEH-1 as a function of temperature cycle in the temperature range from 95 °C to 100 °C; (b) Comparison of temperature dependence of pyroelectric voltages generated by using circular and square electrodes.

3.2.2 Thin $LiNbO_3$ Films on Si

A great part of the experimental analysis consisted in the control of the composition of the volatile element Li_2O, in order to avoid Li-poor ($LiNb_3O_8$) and Li-rich (Li_3NbO_4) phases. In this way, we would check the single-phase composition of interest of the thin films, $LiNbO_3$. To understand and optimize the growth conditions of $LiNbO_3$ orientations, different cut of sapphire substrates were used. We can grow epitaxially X-, Z-, Y- and 33°Y-$LiNbO_3$ oriented thin films on A-, C-, M- and R-Sapphire. The XRD analysis was done in order to investigate the crystalline phase. The analysis revealed that parasitical Li-rich phase was present in films grown from solution with Li(THD) concentration > 0.02 M. Once the concentration was optimized, we could see sharp reflections of single $LiNbO_3$ phase in XRD patterns. A more precise stoichiometry analysis of the samples was done by means of Raman spectroscopy. In fact, from the width (FWHM) of the measured Raman modes, we could estimate how Li_2O non-stoichiometry effect. Therefore, we estimated Li_2O concentration from the width of E(1TO) Raman mode, that was clearly visible at 154

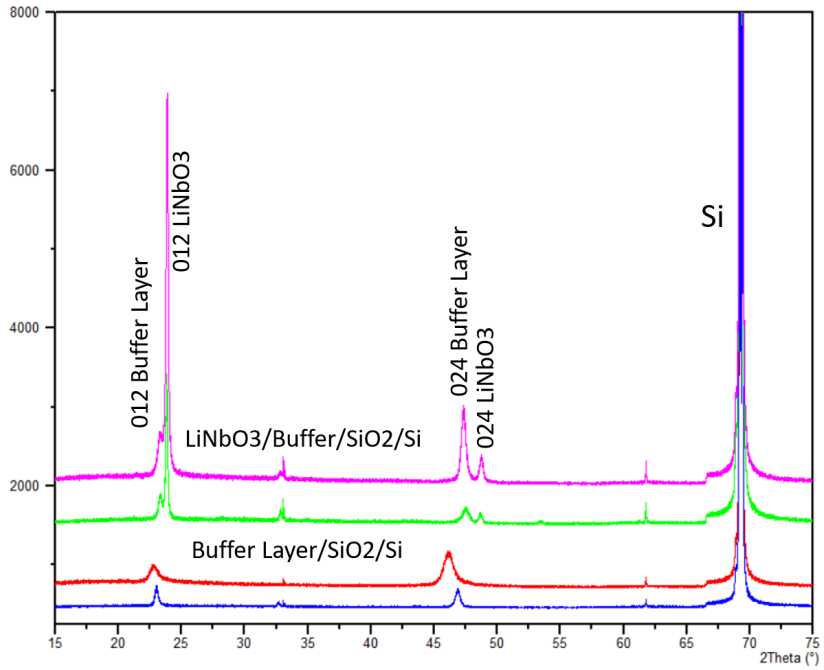

Figure 3.12: $LiNbO_3$ thin films growth by MOCVD: θ/2θ X-ray diffraction pattern of $LiNbO_3$ /Buffer/SiO_2/Si.

cm^{-1}, while taking as a reference E(1TO) mode measured on congruent (48.3 mol%) and stoichiometric (50 mol%) $LiNbO_3$ single crystals. Finally, after the optimization of the molar concentration of the Li precursor, we achieved E(1TO) mode, with width below 10 cm^{-1}, indicating a stoichiometry of films close to that of congruent crystals.

The following step was the optimization of the (012) $LiNbO_3$ films growth on electrode and SiO_2/Si substrates. For this purpose, we have optimized (012) textured growth of our buffer layer films by magnetron sputtering (the works were done by S. Kuprenaite PhD 2019). The films presenting single (012) texture were obtained as it can be seen from XRD patterns (Fig. 3.12). The buffer layer presented extremely smooth surface with roughness of 0.85 nm (Fig. 3.13a). Then $LiNbO_3$ films were successfully grown with single (012) texture on these templates. It is important to note, that the highly coupled (012) $LiNbO_3$ orientation was never reported in litterature on SiO_2/Si substrates. The roughness of $LiNbO_3$ films was of 6.5 nm (Fig. 3.13b). However, the $LiNbO_3$ films presented cracks due to high thermal stresses. These cracks can be eliminated by adapting the cooling rate after deposition and by adjusting different thicknesses of buffer layers in order to minimize the thermal stresses. Even though we optimized the fabrication of textured $LiNbO_3$ thin films on Si substrate, the thickness that we could achieve (50 - 500 nm) is limiting the application in energy harvesting, where the volume of the piezoelectric material under strain has a central role. For this reason, we preferred to use $LiNbO_3$ single crystal thick films.

Highly oriented $LiNbO_3$ thin films were deposited on a Si/SiO_2 substrate by means of Direct Liquid Injection-MOCVD by V. Astié. The thickness of the films was 100 nm, and the growth was on the top of a buffer layer to induce textured growth with on Pt bottom

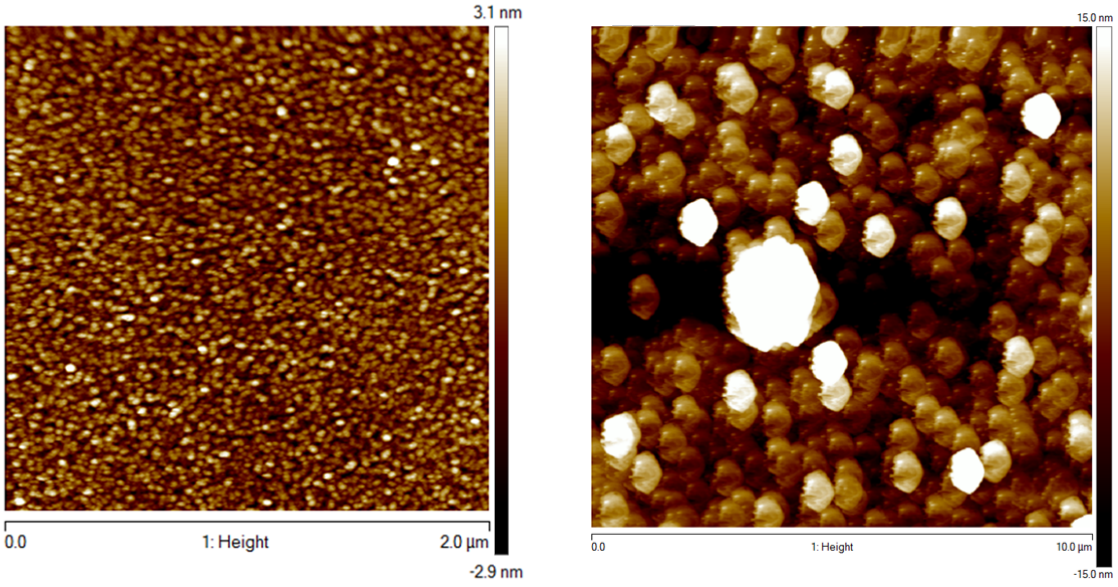

(a) *(b)*

Figure 3.13: AFM images: (a) (012) oriented buffer layer grown on SiO_2/Si substrates by magnetron sputtering; (b) (012) textured $LiNbO_3$ films grown on (012) buffer layer/SiO_2/Si templates by PI MOCVD.

electrode. The final stack of materials was 33° Y $LiNbO_3$ /Buffer/Pt/TiO_2/SiO_2/Si. Afterwards, Al top electrodes were sputtered with a stencil mask and eventually the cantilevers were diced. In order to investigate the dielectric permittivity we used a lock-in system used by Makarov and Damjanovic [16], so that is possible to reach frequencies ranging from 0.01 Hz to 10 kHz. This is particularly interesting to see how the losses are affecting the dielectric properties of the piezoelectric layer at low frequency. In Fig. (3.14a) we also made a comparison with a single crystal $LiNbO_3$ Z-cut in order to see a difference between thin films and bulk counterpart. We see that the dielectric permittivity for $LiNbO_3$ 33° is lower than the the bulk single crystal until we go below 10 Hz. Here the losses for the thin films start to increase along with the dielectric permittivity. This behavior is due to domain walls rearrangements. From the interpretation of Fedorenko et al. [17], depends on the poling state of the dielectric medium or creep-like motion at very low frequency [10]. Anyways the permittivity close to 1 kHz has a stable and lower value compared to the single crystal (Z-cut), which are respectively 36 and 44. In Fig. (3.14b) we can see the results of the pyroelectric study on thin films. With a dynamic measurement setup we managed to measure the pyroelectric current as in the single crystal case. Even for thin films we have a positive pyroelectric coefficient, which in this case is 11 $\mu C.m^{-2}.K^{-1}$. The value it is smaller than $LiNbO_3$ (YXl)/36° (67 $\mu C.m^{-2}.K^{-1}$), but it can be improved by poling the films.

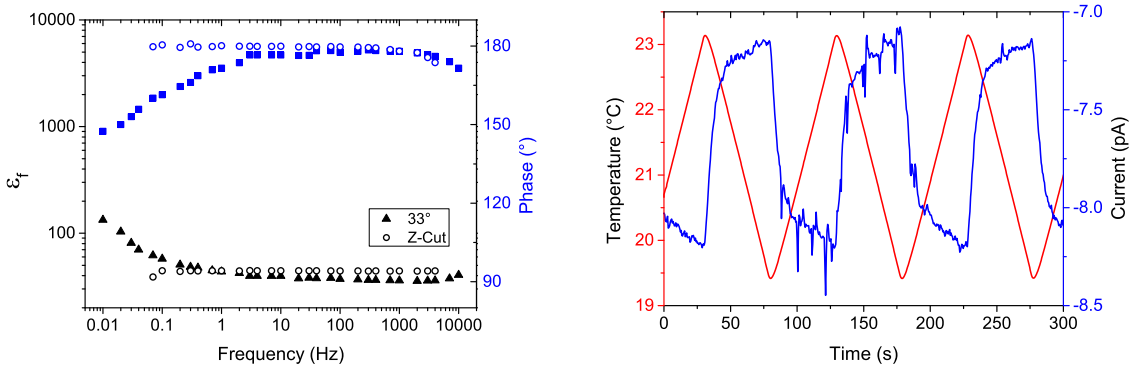

Figure 3.14: (a) $LiNbO_3$ Y-33° textured film dielectric permittivity frequency dispersion. (b) Pyroelectric current measured during triangular wave heating cycle.

3.3 Piezoelectric and Pyroelctric FOMs

Finally we can calculate the figure of merit for the $LiNbO_3$ films, considering $e_{23,f}$ and $p_{2,f}$ measured. The equations for the FOMs are given in Chapter 1, in Eq. (1.24) and (1.33), which are respectively:

$$\text{FOM}^f = \frac{e_{ij}^2}{\varepsilon_{jj,f}^{\text{T}}}$$

$$\text{FOM}^{py} = \frac{p^2}{\varepsilon_{33}^{\text{T}}}$$

We will use the dielectric constant ε_f measured previously for the different cuts and thin films. As explained by Chidambaram et al [18], the value of $e_{23,f}$ depends not only on the piezoelectric response but also on the properties of the Si substrate. For this reason, we will calculate FOM^f considering Poisson's ratio of silicon: $(1-\nu_s)e_{23,f}$. The highest result in terms of piezoelectric FOM^f was obtained for $LiNbO_3$ (YXl)/128°, while for thin films we could not measure the piezoelectric coefficient. In terms of pyroelectric FOM^{py}, we observed that for the fabricated batch of samples, the best solution was 128° as well. Eventually, even if the thin films have the lowest dielectric constant measured so far, we need to pole them to achieve a better FOM^{py}.

3.4 Conclusions

As expected from our simulations regarding the orientation study of $LiNbO_3$, we demonstrated that $LiNbO_3$ (YXl)/128° is the best orientation among the fabricated samples. Promising outcomes are given by the results of deposition of $LiNbO_3$ thin films which have high quality orientation, but the *nm* scale thickness, at the moment is limiting the application to acoustics. In order to obtain cantilevers with optimized FOMs, we could consider a design that exploit inter-digitated electrodes, on $LiNbO_3$ ZX plate or Z-cut. The main ad-

Table 3.6: Final comparison between all orientation studied in terms of piezoelectric and pyroelectric FOMs.

(YXl)/ θ°	FOM^f (GJ.m^{-3})	FOM^{py} (J.m^{-3}.K^{-1})	Thickness (µm)
33°	-	0.4	0.1
36°	15	1.2	32
128°	26.6	6	5
163°	8.1	4.5	10

vantage would be using piezoelectric thickness coefficient e_{33}=-2.42 C.m^{-2}, that is generally higher than the transverse coefficient e_{23} [19], and also optimize the pyroelectric response having p_3=-83 µC.m^{-2}.K^{-1}. Simulations are showing that for the considered plate we could exploit a very low dielectric permittivity 2.54e-10 F/m and the two optimized figure of merit would be respectively FOM^f = 23 GJ.m^{-3} and FOM^{py} = 27 J.m^{-3}.K^{-1}, but experimental tests on IDTs are still in preliminary phase.

Bibliography

[1] K. Nakamura and H. Shimizu, "Ferroelectrics Hysteresis-free piezoelectric actuators using LiNbO 3 plates with a ferroelectric inversion layer," *Ferroelectrics*, no. Vol. 93, pp. 211–216, 1989.

[2] V. Y. Shur, I. S. Baturin, E. A. Mingaliev, D. V. Zorikhin, A. R. Udalov, and E. D. Greshnyakov, "Hysteresis-free high-temperature precise bimorph actuators produced by direct bonding of lithium niobate wafers," *Applied Physics Letters*, vol. 106, no. 5, 2015.

[3] K. Nakamura, H. Ando, and H. Shimizu, "Bending vibrator consisting of a LINBO3plate with a ferroelectric inversion layer," *Japanese Journal of Applied Physics*, vol. 26, pp. 198–200, 1987.

[4] R. E. Newnham, *Properties of materials*. 2005.

[5] W. Yue and J. Yi-Jian, "Crystal orientation dependence of piezoelectric properties in LiNbO3 and LiTaO3," *Optical Materials*, vol. 23, no. 1-2, pp. 403–408, 2003.

[6] A. W. Warner, M. Onoe, and G. A. Coquin, "Determination of Elastic and Piezoelectric Constants for Crystals," *The Journal of the Acoustical Society of AmericaAcoustical Society of America*, vol. 930, no. October 1966, pp. 1223–1231, 1968.

[7] A. Kawamata, H. Hosaka, and T. Morita, "Non-hysteresis and perfect linear piezoelectric performance of a multilayered lithium niobate actuator," *Sensors and Actuators, A: Physical*, vol. 135, no. 2, pp. 782–786, 2007.

[8] C. Cochard, T. Spielmann, N. Bahlawane, A. Halpin, and T. Granzow, "Broadband characterization of congruent lithium niobate from mHz to optical frequencies," *Journal of Physics D: Applied Physics*, vol. 50, no. 36, 2017.

[9] P. Muralt, "Micromachined Infrared Detectors Based on Pyroelectric Thin Films," pp. 81–113, 2005.

[10] W. Kleemann, J. Dec, and R. Pankrath, "Dielectric non-debye domain wall response and aging of SBN :Ce," *Ferroelectrics*, vol. 291, no. March 2015, pp. 75–82, 2003.

[11] P. Muralt, "Piezoelectric thin films for mems," *Integrated Ferroelectrics*, vol. 17, no. 1-4, pp. 297–307, 1997.

[12] N. Chidambaram, D. Balma, R. Nigon, A. Mazzalai, R. Matloub, C. S. Sandu, and P. Muralt, "Converse mode piezoelectric coefficient for lead zirconate titanate thin film with interdigitated electrode," *Journal of Micromechanics and Microengineering*, vol. 25, no. 4, p. 45016, 2015.

[13] A. Biancoli, “Breaking of the macroscopic centric symmetry in Ba 1-x Sr x TiO 3 ceramics and single crystals PAR,” vol. 6366, 2014.

[14] M. Daglish, “A dynamic method for determining the pyroelectric response of thin films,” *Integrated Ferroelectrics*, vol. 22, no. 1-4, pp. 473–488, 1998.

[15] C. R. Bowen, J. Taylor, E. Leboulbar, D. Zabek, A. Chauhan, and R. Vaish, “Pyroelectric materials and devices for energy harvesting applications,” *Energy and Environmental Science*, vol. 7, no. 12, pp. 3836–3856, 2014.

[16] M. Morozov, “Softening and Hardening Transitions in Ferroelectric Pb(Zr,Ti)O 3 Ceramics,” vol. 3368, 2005.

[17] A. A. Fedorenko, V. Mueller, and S. Stepanow, “Dielectric response due to stochastic motion of pinned domain walls,” *Physical Review B - Condensed Matter and Materials Physics*, vol. 70, no. 22, 2004.

[18] N. Chidambaram, A. Mazzalai, and P. Muralt, “Measurement of effective piezoelectric coefficients of PZT thin films for energy harvesting application with interdigitated electrodes,” *IEEE Transactions on Ultrasonics, Ferroelectrics, and Frequency Control*, vol. 59, no. 8, pp. 1624–1631, 2012.

[19] G. Kovacs, M. Anhorn, H. E. Engan, G. Visintini, and C. C. Ruppel, “Improved material constants for LiNbO3 and LiTaO3,” *Ultrasonics Symposium Proceedings*, vol. 1, pp. 435–438, 1990.

4 Theoretical Considerations on Piezoelectric Energy Harvesters

In this Chapter I will discuss the different methods involved to predict and optimize the performance of our prototypes: finite element analysis (FEA) and single degree of freedom model. Especially for FEA, our approach consists in a restricted set of inputs and outputs suitable for energy harvesting systems, which can be a starting point to optimize the harvester properties and finally use commercial software such as Comsol Multiphysics to refine the design. On the other hand, we found useful the lumped model for inertial energy harvesters, as a phenomenological approach, which starting from a set of electro-mechanical equations helps to investigate and unveil the mechanical properties of devices and their optimal electronic configuration.

4.1 Finite Element Analysis

Refined FEA discretizations involving thousands of degrees of freedom (DOF) lead to realistic simulations, but their complexity is also leading to a huge amount of time for model improvement and parameter optimization. Therefore, starting from a minimal FEA simulation, it is a good opportunity both to investigate and to understand the key aspects of the system in a pedagogical approach. We start our analysis modeling a unimorph piezoelectric bender consisting of *one element* in order to fin out the physics behind the electromechanical behavior of the actual devices and then compare the results with higher accuracy simulations performed with Comsol. The unique finite element must be submitted to clamped boundary conditions at one end at to free boundary conditions at the other end, representing the free tip of the bar.

4.1.1 Neutral Axis

We define our unimorph bender as a piezoelectric layer bonded to a substrate. The thickness of the piezoelectric element is h_p, and the thickness of the metal foil h_i. In our system of reference the thickness dimension lies in the Z-axis of the element, and we chose the $Z = 0$ in the interface between the active layer and the substrate. The schematic representation of the element in pure bending is depicted in Fig. (4.1), where the upper part

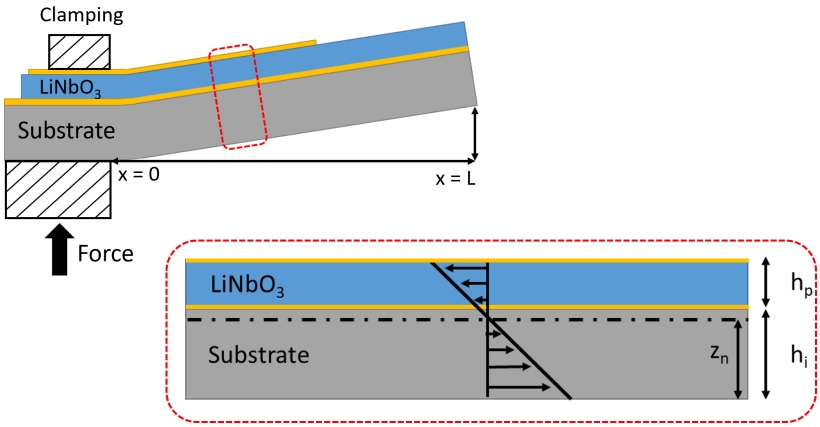

Figure 4.1: Schematics representation of clamped cantilever under excitation. The model shows the cross section with highlighted neutral axis.

of the unimorph beam is in compression, and the lower part in extension. We define the coordinate for the neutral fiber of the bender, z_n, which is the place where there is no longitudinal stress or longitudinal fibers don't change in length. At the equilibrium the balance of forces yields:

$$\int_0^{h_p} \frac{(z-z_n)}{s_{11}^p} dz + \int_{-h_i}^{0} \frac{(z-z_n)}{s_{11}^i} dz = 0 \tag{4.1}$$

Integrating over h_p and h_i leads to the expression for z_n:

$$z_n = \frac{h_p^2 s_{11}^i - h_i^2 s_{11}^p}{2(h_p s_{11}^i + h_i s_{11}^p)} \tag{4.2}$$

Therefore the neutral fiber position depends on the thickness of the two layers, and their elastic properties represented by s_{11}^i for the substrate layer, and s_{11}^p for the piezoelectric one, respectively . If the considered materials are following Hooke's law and no axial forces are deforming the cross-section, then z_n belongs to the centroid of the cross-sectional area. Eq. (4.2) will be extensively used in the following sections in order to calculate the properties of the $LiNbO_3$ based devices.

4.1.2 Variational Principle

We can start our analysis of the electro-mechanical problem with the Hamilton's Principle for a beam clamped-free in bending conditions:

$$\delta \int_V (\mathcal{T} - \mathcal{U})\, dV + \delta \int_S \mathcal{W}\, dS = 0 \tag{4.3}$$

where $\mathcal{T}$ is the kinetic energy term, $\mathcal{U}$ the potential energy for the considered volume V, and $\mathcal{W}$ is the work done by external forces on the boundaries of the structure, thereby explaining the integration over the surface, S. Hamilton's principle has two fundamental characteristics: it is equivalent to the local form of balance equations and boundary

conditions, and it equitably distributes the error of approximate solutions between the volume and the surface of the body, in contrast with finite difference methods. For energy harvesting considerations, Hamilton's principle has been adopted in other works, but with different hypothesis [1, 2].

Adding pure extension to Bernoulli's model of pure cylindrical flexure, we have:

$$\begin{cases} u_1 = -x_3 w_{3,1} + w_1 \\ u_3 = w_3 \end{cases}$$

with x_3 is the vertical coordinate with origin at the level of the neutral plane, (u_1, u_3) are local displacements and (w_1, w_3) represent global displacements. The w_1 is the axial displacement of the cross-section measured at the neutral plane. In other words, it is the axial displacement that we get if we stretch the beam without bending it. Conversely, w_3 is the vertical displacement of the neutral plane when we bend the plate.

In Bernoulli's bending $w_1 = 0$, but $u_1 = f(x_1, x_3)$ and $w_3 = f(x_1)$, where $u_3 \equiv w_3$, because, due to the cumulative rotations of the beam cross-sections, the global transverse displacement of the beam is much larger than its local vertical displacements induced by axial stress through Poisson's effect. The generalized Hooke's law predicts that the local value of T_1 implies that $u_{3,3}/u_{1,1} = s_{12}/s_{11}$, which is finite. However, the results in smaller vertical displacement than axial ones because vertical displacement is obtained by integrating $w_{3,3}$ along a small thickness. Whereas the axial displacement is integrated from $w_{1,1}$ along a large length. This is why the thin plate/beam assumption implies $w_3 \sim c^t/x_3$ or at least $w_{3,3} \ll w_{3,1}$.Finally, when we add a global axial stretch to the flexure, assuming $w_1 = f(x_1)$ instead of $w_1 = 0$, while $u_1 = f(x_1, x_3)$ and $u_3 \simeq w_3 = f(x_1)$ still holds. In the layers where we add the piezoelectric effect in transverse direction d_{31}, the hypotheses are:

$$\begin{cases} u_1 = -x_3 w_{3,1} + w_1 \\ u_3 = w_3 \\ \varphi = f(x_3) \end{cases} \tag{4.4}$$

where φ is a function of x_3, and represents the piezoelectric potential arising from the bending of the structure, in which the piezoelectric effect is exploited in transverse mode using d_{31} coefficient. It has to be noted that in this chapter we will use the standard notation for transverse mode benders, so for the piezoelectric properties we use the general notation d_{31} and s_{11}, regardless of the orientation of $LiNbO_3$ element.

4.1.3 Piezoelectricity and Thermodynamic Potentials

From the predominance of T_1 and the initial assumptions of Eq. (4.4), the best form of the various sets of electro-mechanical equations for piezoelectricity is:

$$\begin{aligned} \mathrm{S_I} &= s^{\mathrm{E}}_{\mathrm{IJ}}\mathrm{T_J} + d_{k\mathrm{I}}\mathrm{E}_k \\ \mathrm{D}_i &= d_{i\mathrm{J}}\mathrm{T_J} + \varepsilon^{\mathrm{T}}_{ij}\mathrm{E}_j \end{aligned} \tag{4.5}$$

Here, T^{E} and E are the independent variables in the differential forms of the potential energy variations. Besides, it is known that a correct thermodynamic potential for the variational formulation leading to a full model of piezoelectric devices is:

$$\rho\chi = \frac{1}{2}c_{\mathrm{IJ}}\mathrm{S_I}\mathrm{S_J} - \frac{1}{2}\varepsilon^{\mathrm{S}}_{ij}\mathrm{E}_i\mathrm{E}_j - e_{ikl}\mathrm{E}_i\mathrm{S}_{kl} \tag{4.6}$$

which gives the partial derivatives identifications:

$$\mathrm{T_I} = \frac{\partial\rho\chi}{\partial\mathrm{S_J}} \quad \mathrm{D}_i = -\frac{\partial\rho\chi}{\partial\mathrm{E}_i} \tag{4.7}$$

and the following form of constitutive equations of piezoelectricity:

$$\begin{aligned} \mathrm{T_I} &= c^{\mathrm{E}}_{\mathrm{IJ}}\mathrm{S_J} - e_{k\mathrm{I}}\mathrm{E}_k \\ \mathrm{D}_i &= \varepsilon^{\mathrm{S}}_{ij}\mathrm{E}_j + e_{i\mathrm{J}}\mathrm{S_J} \end{aligned} \tag{4.8}$$

$\rho\chi$ corresponds to the enthalpy $\mathrm{H(S,E)} = \mathrm{U} - \mathrm{ED}$, where $\mathrm{U} = \mathrm{U(S,D)}$ is the internal energy. Differentiating U leads to:

$$d\mathrm{U} = \mathrm{E}d\mathrm{D} + \mathrm{T}d\mathrm{S} \tag{4.9}$$

Then:

$$d\mathrm{H} = \mathrm{T}d\mathrm{S} - \mathrm{D}d\mathrm{E} \tag{4.10}$$

The constitutive equations (4.5) are associated to the use of Gibbs' function as thermodynamic potential:

$$\mathrm{G(T,E)} = \mathrm{U} - \mathrm{TS} - \mathrm{ED}$$

$$d\mathrm{G} = -\mathrm{S}d\mathrm{T} - \mathrm{D}d\mathrm{E}$$

Then if we substitute this equation in the potential equation, we obtain:

$$\rho\mathrm{G} = -\frac{1}{2}s_{\mathrm{IJ}}\mathrm{T_I}\mathrm{T_J} - \frac{1}{2}\varepsilon^{\mathrm{T}}_{ij}\mathrm{E}_i\mathrm{E}_j - d_{i\mathrm{J}}\mathrm{E}_i\mathrm{T_J} \tag{4.11}$$

where the derivatives are:

$$\begin{aligned} \mathrm{S_I} &= -\frac{\partial\mathrm{G}}{\partial\mathrm{T_I}}\Big|_{\mathrm{E}} \\ \mathrm{D_I} &= -\frac{\partial\mathrm{G}}{\partial\mathrm{E}}\Big|_{\mathrm{T}} \end{aligned} \tag{4.12}$$

In variational studies, it is known that the integral over the volume for the kinetic energy can be expressed as:

$$\int_{\mathrm{V}} \delta\mathcal{T}\, d\mathrm{V} = -\int_{\mathrm{V}} \rho \ddot{u}_i \delta u_i d\mathrm{V} = \int_{\mathrm{V}} \rho\omega^2 \vec{u}\cdot\delta\vec{u} d\mathrm{V} \tag{4.13}$$

Then, the variational principle should be written in terms of the energy potential:

$$\int_{\mathrm{V}} \left(\delta\mathcal{T} - \delta\chi\right) d\mathrm{V} + \int_{\mathrm{S}} \delta\mathcal{W}\, d\mathrm{S} = 0 \tag{4.14}$$

that explicitly brings us to:

$$\int_{\mathrm{V}} \rho\omega^2 \vec{u}\cdot\delta\vec{u} d\mathrm{V} + \int_{\mathrm{V}} \left(\frac{\partial\chi}{\partial\mathrm{S}}\delta\mathrm{S} + \frac{\partial\chi}{\partial\mathrm{E}}\delta\mathrm{E}\right) d\mathrm{V} + \int_{\mathrm{S}} \left(\vec{f}\delta\vec{u} - \sigma\delta\varphi\right) d\mathrm{S} = 0 \tag{4.15}$$

Assuming that T_1 and E_3 are the only significant physical quantities, differentiating the energy potential, $\rho\chi$, of the continuous 3D FEA are reduced to:

$$\int_{\mathrm{V}} \rho\delta\chi d\mathrm{V} = \int_{\mathrm{V}} \left(\mathrm{T}_1\delta\mathrm{S}_1 - \mathrm{D}_3\delta\mathrm{E}_3\right) d\mathrm{V} \tag{4.16}$$

where T and D are usually expressed in terms of S_1, D_3 variables and c_{11}^{E}, $\varepsilon_{33}^{\mathrm{S}}$ and e_{31} constants in 3D continuous FEA models: Now, if we consider Gibb's function, we get:

$$\mathrm{G} = -\frac{1}{2}s_{11}\mathrm{T}_1^2 - \frac{1}{2}\varepsilon_{33}^{\mathrm{T}}\mathrm{E}_3^2 - d_{31}\mathrm{E}_3\mathrm{T}_1 \tag{4.17}$$

where both dominant independent variables are T_1 and E_3. After factoring T_1 we obtain:

$$\mathrm{G} = -\mathrm{T}_1\left(\frac{1}{2}s_{11}\mathrm{T}_1 + d_{31}\mathrm{E}_3\right) - \frac{1}{2}\varepsilon_{33}^{\mathrm{T}}\mathrm{E}_3^2$$

But for the piezoelectric material we have that:

$$\mathrm{T}_1 = \frac{1}{s_{11}}(\mathrm{S}_1 - d_{31}\mathrm{E}_3) \tag{4.18}$$

If we substitute T_1 in (4.17) then we obtain:

$$\mathrm{G} = -\frac{1}{2s_{11}}(\mathrm{S}_1^2 - d_{31}^2\mathrm{E}_3^2) - \frac{1}{2}\varepsilon_{33}^{\mathrm{T}}\mathrm{E}_3^2$$

The variational term can be written as:

$$\delta\mathrm{G} = -\mathrm{S}_1\delta\mathrm{T}_1 - \mathrm{D}_3\delta\mathrm{E}_3 = -\frac{1}{s_{11}}\mathrm{S}_1\delta\mathrm{S}_1 + \left(\frac{1}{s_{11}}d_{31}^2 - \varepsilon_{33}^{\mathrm{T}}\right)\mathrm{E}_3\delta\mathrm{E}_3. \tag{4.19}$$

This variational form of energy potential is not appropriate for our needs, because it does not couple the mechanical and electrical variables. We found that transforming δT into δS is forbidden in the variational principle [1]. Using a consistent set of material parameters,

[1] Actually, any substitution of variables is allowed in the factors of the variations, but exchanging the variation variables themselves is forbidden.

we found that the proper form of variation of enthalpy function is written as follows:

$$\int_V \rho\delta\chi\, dV = \int_V \left[\frac{1}{s_{11}} (S_1 - d_{31}E_3)\,\delta S_1 - \left(\frac{d_{31}}{s_{11}} S_1 + \left(\varepsilon_{33}^T - \frac{d_{31}^2}{s_{11}} \right) E_3 \right) \delta E_3 \right] dV. \tag{4.20}$$

Finally, the variations of χ can be expressed in terms of the variations of well–defined derivatives of the unknown continuous field–variables w_1, w_3 and φ retained in the initial assumptions (Eq.4.4) of our FEA model. Thus, the local expression of $\delta\chi$ is:

$$\begin{aligned} \rho\delta\chi \;=\; & \frac{1}{s_{11}}(x_3^2 w_{3,11} - x_3 w_{1,1} - x_3 d_{31}\varphi_{,3})\delta(w_{3,11}) \\ & + \frac{1}{s_{11}}(-x_3 w_{3,11} + w_{1,1} + d_{31}\varphi_{,3})\delta(w_{1,1}) \\ & + \left[\frac{d_{31}}{s_{11}}\left(-x_3 w_{3,11} + w_{1,1}\right) - \left(\varepsilon_{33}^T - \frac{d_{31}^2}{s_{11}} \right) \varphi_{,3} \right] \delta\varphi_{,3} \end{aligned}$$

Upon performing the volume integration, we remark that all material properties must be kept within the integrals because they vary along z, according to the layered nature of the studied beam. The generalized unknown are curvature, $w_{3,11}$, extension, $w_{1,1}$, and $\varphi_{,3}$ gradient (*i.e.* $-\vec{E}$). The integral over z must be performed layer by layer, but $w_{3,11}$ and $w_{1,1}$ do not depend on x_3 because w_3 and w_1 depend on x_1 only. However, $\varphi_{,3}$ must be integrated separately in the piezoelectric layer. Moving w_3 and w_1 outside the vertical integration, we can finally write $\rho\delta\chi$ in the following form:

$$\begin{aligned} \int_V \rho\delta\chi dV \;=\; & \int_0^L \delta(w_{3,11}) \left[w_{3,11} \int_z \frac{x_3^2}{s_{11}} dz - w_{1,1} \int_z \frac{x_3}{s_{11}} dz - \int_z \varphi_{,3} \frac{x_3 d_{31}}{s_{11}} dz \right] dx \\ & + \int_0^L \delta(w_{1,1}) \left[-w_{3,11} \int_z \frac{x_3}{s_{11}} dz + w_{1,1} \int_z \frac{1}{s_{11}} dz + \int_z \varphi_{,3} \frac{d_{31}}{s_{11}} dz \right] dx \\ & + \int_0^L \left[-w_{3,11} \int_z \frac{x_3 d_{31}}{s_{11}} \delta\left(\varphi_{,3}\right) dz + w_{1,1} \int_z \frac{d_{31}}{s_{11}} \delta\left(\varphi_{,3}\right) dz \right. \\ & \left. - \int_z \varphi_{,3} \left(\varepsilon_{33}^T - \frac{1}{s_{11}} d_{31}^2 \right) \delta\left(\varphi_{,3}\right) dz \right] dx. \end{aligned} \tag{4.21}$$

Because φ and $\delta\varphi$ are a function of z, we have left them in the integrals over z, and all the variables are considered per unit width. At this moment, we shall stick to linear interpolations of the potential, so that its derivative in a given piezoelectric layer is constant. The same situation occurs for material constants. They may differ from a material to another, but they are constant along the integration over the thickness of a given material layer. Also, one must remember that the origin of the integration over z is the neutral plane of the unimorph, z_n.

4.1.4 Kinetic Energy

As previously mentioned, in harmonic regime, the volume integral of kinetic energy contributing to Hamilton's principle is:

$$\int_{\mathrm{V}} \delta\mathscr{T}\, d\mathrm{V} = \int_{\mathrm{V}} \rho\omega^2 \vec{u}\cdot\delta\vec{u}\, d\mathrm{V}. \tag{4.22}$$

From the kinematic assumptions (4.4), we obtain:

$$\int_{\mathrm{V}} \delta\mathscr{T}\, d\mathrm{V} = \omega^2 \int_{\mathrm{V}} \rho\left[\left(-x_3 w_{3,1} + w_1\right)\left(-x_3\delta w_{3,1} + \delta w_1\right) + w_3\delta w_3\right] d\mathrm{V}$$

After separating z and x integrations, it results in:

$$\boxed{\begin{aligned}\int_{\mathrm{V}} \delta\mathscr{T}\, d\mathrm{V} = \omega^2 \int_0^{\mathrm{L}} \Bigg[& w_{3,1}\delta w_{3,1}\int_z \rho x_3^2 dz - w_1\delta w_{3,1}\int_z \rho x_3 dz - w_{3,1}\delta w_1\int_z \rho x_3 dz \\ & + w_1\delta w_1\int_z \rho dz + w_3\delta w_3\int_z \rho dz\Bigg] dx.\end{aligned}} \tag{4.23}$$

The mass density ρ must be kept within the z integrals because it is liable to take different values in the material layers constituting the unimorph.

4.1.5 Interpolations

Now we are ready to evaluate the interpolations that we will use to expand the curvature, the stretch and the gradient of potential and their respective variations in terms of the so–called degrees of freedom and their variations. To represent the bending by the vertical displacement of the neutral plane and the associated rotation of the cross-section, we need to build consistent interpolations relating the current displacement and rotation inside the element to their values at the two ends of the element. Because there are 4 such values with the status of degrees of freedom in FEA terminology, the law ruling the bending of the beam element must be cubic:

$$\begin{bmatrix} w_3(x) \\ w_{3,1}(x)\end{bmatrix} = \begin{bmatrix} 1 & x & x^2 & x^3 \\ 0 & 1 & 2x & 3x^2\end{bmatrix}\begin{bmatrix} a \\ b \\ c \\ d\end{bmatrix} \tag{4.24}$$

Using a classical procedure, we obtain:

$$\left[\mathbf{P}\right] = \begin{bmatrix} 1 & 0 & 0 & 0 \\ 0 & 1 & 0 & 0 \\ 1 & \mathrm{L} & \mathrm{L}^2 & \mathrm{L}^3 \\ 0 & 1 & 2\mathrm{L} & 3\mathrm{L}^2\end{bmatrix} \text{ and } \begin{bmatrix} a \\ b \\ c \\ d\end{bmatrix} = \left[\mathbf{P}\right]^{-1}\begin{bmatrix} w_3^0 \\ w_{3,1}^0 \\ w_3^{\mathrm{L}} \\ w_{3,1}^{\mathrm{L}}\end{bmatrix} \tag{4.25}$$

The inverse of the constant matrix $\mathbf{P}$ is easily found as:

$$\left[\mathbf{P}\right]^{-1} = \begin{bmatrix} 1 & 0 & 0 & 0 \\ 0 & 1 & 0 & 0 \\ -\dfrac{3}{\mathrm{L}^2} & -\dfrac{2}{\mathrm{L}} & \dfrac{3}{\mathrm{L}^2} & -\dfrac{1}{\mathrm{L}} \\ \dfrac{2}{\mathrm{L}^3} & \dfrac{1}{\mathrm{L}^2} & -\dfrac{2}{\mathrm{L}^3} & \dfrac{1}{\mathrm{L}^2} \end{bmatrix} \tag{4.26}$$

Substituting this result into the initial guess (Eq. 4.24) gives the required interpolation of the displacement, $w_3(x)$, and the rotation, $w_{3,1}(x)$, but interpolating the curvature, $w_{3,11}(x)$, is also required because it appears as the dependent mechanical quantity for bending in Eq. 4.22, qualified as *generalized unknown*. Hence:

$$\begin{bmatrix} w_3(x) \\ w_{3,1}(x) \\ w_{3,11}(x) \end{bmatrix} = \begin{bmatrix} 1 & x & x^2 & x^3 \\ 0 & 1 & 2x & 3x^2 \\ 0 & 0 & 2 & 6x \end{bmatrix} \left[\mathbf{P}\right]^{-1} \begin{bmatrix} w_3^0 \\ w_{3,1}^0 \\ w_3^{\mathrm{L}} \\ w_{3,1}^{\mathrm{L}} \end{bmatrix} = \left[\mathbf{N}\right] \begin{bmatrix} w_3^0 \\ w_{3,1}^0 \\ w_3^{\mathrm{L}} \\ w_{3,1}^{\mathrm{L}} \end{bmatrix} \tag{4.27}$$

where $\mathbf{N}(x)$ is the matrix of so–called shape functions:

$$\left[\mathbf{N}(x)\right] = \begin{bmatrix} 1-3\frac{x^2}{\mathrm{L}^2}+2\frac{x^3}{\mathrm{L}^3} & x-2\frac{x^2}{\mathrm{L}}+\frac{x^3}{\mathrm{L}^2} & 3\frac{x^2}{\mathrm{L}^2}-2\frac{x^3}{\mathrm{L}^3} & -\frac{x^2}{\mathrm{L}}+\frac{x^3}{\mathrm{L}^2} \\ -6\frac{x}{\mathrm{L}^2}+6\frac{x^2}{\mathrm{L}^3} & 1-4\frac{x}{\mathrm{L}}+3\frac{x^2}{\mathrm{L}^2} & 6\frac{x}{\mathrm{L}^2}-6\frac{x^2}{\mathrm{L}^3} & -2\frac{x}{\mathrm{L}}+3\frac{x^2}{\mathrm{L}^2} \\ -6\frac{1}{\mathrm{L}^2}+12\frac{x}{\mathrm{L}^3} & -\frac{4}{\mathrm{L}}+6\frac{x}{\mathrm{L}^2} & \frac{6}{\mathrm{L}^2}-12\frac{x}{\mathrm{L}^3} & -2\frac{1}{\mathrm{L}}+6\frac{x}{\mathrm{L}^2} \end{bmatrix} \tag{4.28}$$

We shall also need the corresponding interpolation of the *variation* of curvature, because it is a generalized unknown:

$$\begin{aligned} \delta w_{3,11}(x) \quad = \quad & \left(-6\frac{1}{\mathrm{L}^2}+12\frac{x}{\mathrm{L}^3}\right)\delta w_3^0+\left(-\frac{4}{\mathrm{L}}+6\frac{x}{\mathrm{L}^2}\right)\delta w_{3,1}^0 \\ & +\left(\frac{6}{\mathrm{L}^2}-12\frac{x}{\mathrm{L}^3}\right)\delta w_3^{\mathrm{L}}+\left(-2\frac{1}{\mathrm{L}}+6\frac{x}{\mathrm{L}^2}\right)\delta w_{3,1}^{\mathrm{L}}. \end{aligned} \tag{4.29}$$

For the stretch, the interpolations of w_1 and $w_{1,1}$ are:

$$w_1(x) = \left(1-\frac{x}{\mathrm{L}}\right)w_1^0+\frac{x}{\mathrm{L}}w_1^{\mathrm{L}} \;\; ; \;\; w_{1,1}(x) = -\frac{1}{\mathrm{L}}w_1^0+\frac{1}{\mathrm{L}}w_1^{\mathrm{L}} \tag{4.30}$$

together with

$$\delta w_{1,1}(x) = -\frac{1}{\mathrm{L}}\delta w_1^0+\frac{1}{\mathrm{L}}\delta w_1^{\mathrm{L}}. \tag{4.31}$$

For the gradient of the field the corresponding interpolations φ and $\varphi_{,3}$ are:

$$\varphi(z) = \left(1 - \frac{z}{h_p}\right)\varphi^0 + \frac{z}{h_p}\varphi^{h_p} \;\; ; \;\; \varphi_{,3}(z) = -\frac{1}{h_p}\varphi^0 + \frac{1}{h_p}\varphi^{h_p} \;\; \text{and} \;\; \delta\varphi_{,3}(z) = -\frac{\delta\varphi^0}{h_p} + \frac{\delta\varphi^{h_p}}{h_p}. \tag{4.32}$$

4.1.6 Final System and Elementary Matrices

As a general rule, after substituting the interpolations in the integral variation of kinetic energy, potential energy and work done by external forces, the variational equation is put in the following form:

$$\int_{t_0}^{t_1} \sum_e \left\{ \int_{V_e} \left[\langle \delta \mathbf{U}^n \rangle [\mathbf{B}(x)]^T [\mathbf{D}] [\mathbf{B}(x)] \{\mathbf{U}^n\} - \omega^2 \langle \delta \mathbf{U}^n \rangle [\mathbf{N}(x)]^T \left[\boldsymbol{\rho}\right] [\mathbf{N}(\mathbf{x})] \{\mathbf{U}^n\} \right] dV \right. \\ \left. - \int_{S_e} \left[\langle \delta \mathbf{U}^n \rangle [\mathbf{N}(x)]^T \{\mathbf{f}\} \right] dS \right\} dt = 0. \tag{4.33}$$

In this equation, $\mathbf{U}^n$ contains the DOFs and $\mathbf{B}^n$ contains the derivatives of interpolating functions required to compute the generalized unknown (our dependent variables) consisting in the curvature, $w_{3,11}$, the stretch, $w_{1,1}$, and the distinct values of the gradient of potential, $\varphi_{,3}$, occuring in the piezoelectric layer. The expansion of all these quantities must be consistent with their occurence in Eq. (4.21). $\mathbf{D}$ contains the material characteristics integrated or separated over z as they appear in Eq. (4.21). $\mathbf{N}$ contains all shape functions and $\boldsymbol{\rho}$ contains the integrated mass density. Zeroes may occur in any matrix in places where involved quantities are not cross–connected.

The whole obtained formula is stationary with respect to the variations of the degrees of freedom. It means that the coefficients of each DOF is null.

$$\sum_e \left\{ \left[\underbrace{\int_{V_e} [\mathbf{B}(x)]^T [\mathbf{D}] [\mathbf{B}(x)] \, dV_e}_{[\mathbf{K}]^e} - \omega^2 \underbrace{\int_{V_e} [\mathbf{N}(x)]^T [\boldsymbol{\rho}] [\mathbf{N}(x)] \, dV_e}_{[\mathbf{M}]^e} \right] \{\mathbf{U}^n\} = \underbrace{\int_{S_e} [\mathbf{N}(x)]^T \{\boldsymbol{f}\} \, dS_e}_{\{\mathbf{F}^n\}} \right\} \tag{4.34}$$

Here, the e subscript denotes the index used for numbering the elements. The piezoelectric layer has a ground electrode that can be accessed, while we shall denote by L and b the total length and width of the beam, respectively.

In FEA, the build of matrixes is not unique: The ordering of DOFs can be arbitrary. Here, we shall retain the 8 degrees of freedom enumerated below, placing them inside $\mathbf{U}^n$ in the order described below:

$$\left[\mathbf{U}^n\right] = \left[w_3^0 \quad w_{3,1}^0 \quad w_1^0 \quad \varphi_0 \quad \varphi_h \quad w_3^L \quad w_{3,1}^L \quad w_1^L \right]^T \tag{4.35}$$

1) w_3^0 is the transverse displacement of the left end of beam ($x = 0$);

2) $w_{3,1}^0$ is the rotation of the left end of beam ($x = 0$);

3) w_1^0 is the axial displacement of the left end of beam ($x = 0$);

4) φ_0 is the potential at the bottom surface of the piezoelectric layer ($z = 0$);

5) φ_h is the potential of the top surface of the piezoelectric layer ($z = h_p$);

6) w_3^{L} is the transverse displacement of the right end of beam ($x = \mathrm{L}$);

7) $w_{3,1}^{\mathrm{L}}$ is the rotation of the right end of beam ($x = \mathrm{L}$);

8) w_1^{L} is the axial displacement of the right end of beam ($x = \mathrm{L}$).

By principle, there must be as many variations as degrees of freedom, and we shall consider them in the same order as the degrees of freedom: δw_3^0, $\delta w_{3,1}^0$, δw_1^0, $\delta\varphi_0$, $\delta\varphi_h$, δw_3^{L}, $\delta w_{3,1}^{\mathrm{L}}$ and δw_1^{L}. The interpolation of $\varphi(z)$ is just in the piezoelectric layer. In these conditions, we must substitute in Eq. (4.21) the following expansions:

$$\begin{aligned} w_{3,11}(x) = &\left(-6\frac{1}{\mathrm{L}^2}+12\frac{x}{\mathrm{L}^3}\right)\mathrm{U}(1)+\left(-\frac{4}{\mathrm{L}}+6\frac{x}{\mathrm{L}^2}\right)\mathrm{U}(2),\\ &+\left(\frac{6}{\mathrm{L}^2}-12\frac{x}{\mathrm{L}^3}\right)\mathrm{U}(6)+\left(-2\frac{1}{\mathrm{L}}+6\frac{x}{\mathrm{L}^2}\right)\mathrm{U}(7),\\ w_{1,1}(x) = &-\frac{1}{\mathrm{L}}\mathrm{U}(3)+\frac{1}{\mathrm{L}}\mathrm{U}(8)\\ \varphi_{,3}(z) = &-\frac{1}{h}\mathrm{U}(4)+\frac{1}{h}\mathrm{U}(5), \quad \forall z\in[0,h_p] \end{aligned} \tag{4.36}$$

and the same interpolations for their variations.

4.1.7 Derivation of the Stiffness Matrix

According to the previous developments, the stiffness matrix, **K**, must clearly be of dimensions $[8\times 8]$, and the interpolation matrix, **B**, must be of dimensions $[3\times 8]$. Then we must check that we can setup the material characteristics matrix, **D**, as a $[3\times 3]$ one. To make things easier to compare with the system (Eq.4.34), we shall rewrite Eq. (4.21) exchanging the places of the generalized unknown and the variations:

$$\begin{aligned} \int_{\mathrm{V}}\rho\delta\chi d\mathrm{V} = &\int_0^{\mathrm{L}}\delta(w_{3,11})\left[\int_z\frac{x_3^2}{s_{11}}dz\,w_{3,11}-\int_z\frac{x_3}{s_{11}}dz\,w_{1,1}-\int_z\frac{x_3d_{31}}{s_{11}}dz\varphi_{,3}\right]dx\\ &+\int_0^{\mathrm{L}}\delta(w_{1,1})\left[-\int_z\frac{x_3}{s_{11}}dz\,w_{3,11}+\int_z\frac{1}{s_{11}}dz\,w_{1,1}+\int_z\frac{d_{31}}{s_{11}}dz\varphi_{,3}\right]dx\\ &+\int_0^{\mathrm{L}}\delta\left(\varphi_{,3}\right)\left[-\int_z\frac{x_3d_{31}}{s_{11}}dz\,w_{3,11}+\int_z\frac{d_{31}}{s_{11}}dz\,w_{1,1}-\int_z\left(\varepsilon_{33}^{\mathrm{T}}-\frac{d_{31}^2}{s_{11}}\right)\varphi_{,3}dz\right]dx \end{aligned} \tag{4.37}$$

Taking into account the symmetries, we get:

$$\left[\mathbf{D}\right] = \begin{bmatrix} \mathrm{EI}^{equiv} & 0 & -\dfrac{d_{31}\left(h_p^2 - 2h_p z_n\right)}{2s_{11}^p} \\ 0 & \mathrm{Y}h^{equiv} & \dfrac{d_{31}h_p}{s_{11}^p} \\ -\dfrac{d_{31}\left(h_p^2 - 2h_p z_n\right)}{2s_{11}^p} & \dfrac{d_{31}h_p}{s_{11}^p} & -\varepsilon_{equiv}^{\mathrm{S}} \end{bmatrix} \tag{4.38}$$

where

$$\begin{aligned} &\mathrm{EI}^{equiv} = \int_z \frac{(z-z_n)^2}{s_{11}} dz = \int_0^{h_p} \frac{(z-z_n)^2}{s_{11}^p} dz + \int_{-h_i}^0 \frac{(z-z_n)^2}{s_{11}^i} dz = \\ &\frac{\left(h_p - z_n\right)^3 + z_n^3}{3s_{11}^p} + \frac{\left(h_i + z_n\right)^3 - z_n^3}{3s_{11}^i} \\ &-\frac{d_{31}\left(h_p^2 - 2h_p z_n\right)}{2s_{11}^p} \text{ occurs for } -\int_0^{h_p} \frac{(z-z_n)d_{31}}{s_{11}^p} dz \\ &\mathrm{Y}h^{equiv} = \int_z \frac{1}{s_{11}} dz = \frac{h_p}{s_{11}^p} + \frac{h_i}{s_{11}^i} \\ &\varepsilon_{equiv}^{\mathrm{S}} = h_p\left(\varepsilon_{33}^{\mathrm{T}} - \frac{d_{31}^2}{s_{11}^p}\right) \\ &\frac{d_{31}h_p}{s_{11}^p} = \int_z \frac{d_{31}}{s_{11}} dz \end{aligned} \tag{4.39}$$

In the **D** matrix:

- EI^{equiv} is the flexural rigidity of the unimorph beam;
- $\mathrm{Y}h^{equiv}$ is the axial rigidity of the unimorph beam;
- $\varepsilon_{equiv}^{\mathrm{S}}$ the structural dielectric constant of the unimorph, giving the ratio at zero strain between the net electric charge and the electrical field in a given piezoelectric layer. The minus signs come from the writing in terms of potential gradient instead of field;
- $\frac{d_{31}\left(h_p^2 - 2h_p z_n\right)}{2s_{11}^p}$ is the structural piezoelectric coupling between the curvature and the gradient of potential;
- $\frac{d_{31}h_p}{s_{11}^p}$ is the structural piezoelectric coupling between the stretch and the gradient of potential.

There is no coupling between bending and stretch, and the capacitance will arise from the permittivity coefficient of the piezoelectric layer. It is possible to fit φ by a linear inter-

polation, because it permits to easily account for the z integrations, so that the remaining integrations in the computation of the stiffness matrix, $\mathbf{K}$, will be over the product of derivatives of the shape functions of the mechanical data. In accordance with Eq. (4.36) and Eq. (4.38) the $[3 \times 8]$ $\mathbf{B}$ matrix is:

$$\left[\mathbf{B}\right] = \begin{bmatrix} -6\frac{1}{\mathrm{L}^2}+12\frac{x}{\mathrm{L}^3} & -\frac{4}{\mathrm{L}}+6\frac{x}{\mathrm{L}^2} & 0 & 0 & 0 & \frac{6}{\mathrm{L}^2}-12\frac{x}{\mathrm{L}^3} & -2\frac{1}{\mathrm{L}}+6\frac{x}{\mathrm{L}^2} & 0 \\ 0 & 0 & -\frac{1}{\mathrm{L}} & 0 & 0 & 0 & 0 & \frac{1}{\mathrm{L}} \\ 0 & 0 & 0 & -\frac{1}{h_p} & \frac{1}{h_p} & 0 & 0 & 0 \end{bmatrix} \tag{4.40}$$

Computing the stiffness matrix by the formula $\mathbf{K} = \int_0^{\mathrm{L}} \left(\mathbf{B}^{\mathrm{T}}.\mathbf{D}.\mathbf{B}\right) dx$ provides with the following result:

$$[\mathbf{K}] = \begin{bmatrix} \frac{12EI}{\mathrm{L}^3} & \frac{6EI}{\mathrm{L}^2} & 0 & 0 & 0 & -\frac{12EI}{\mathrm{L}^3} & \frac{6EI}{\mathrm{L}^2} & 0 \\ \frac{6EI}{\mathrm{L}^2} & \frac{4EI}{\mathrm{L}} & 0 & \frac{d_{31}(2z_n-h_p)}{2{s_{11}}^p} & -\frac{d_{31}(2z_n-h_p)}{2{s_{11}}^p} & -\frac{6EI}{\mathrm{L}^2} & \frac{2EI}{\mathrm{L}} & 0 \\ 0 & 0 & \frac{Yh}{\mathrm{L}} & \frac{d_{31}}{{s_{11}}^p} & -\frac{d_{31}}{{s_{11}}^p} & 0 & 0 & -\frac{Yh}{\mathrm{L}} \\ 0 & \frac{d_{31}(2z_n-h_p)}{2{s_{11}}^p} & \frac{d_{31}}{{s_{11}}^p} & -\frac{\mathrm{L}\varepsilon}{{h_p}^2} & \frac{\mathrm{L}\varepsilon}{{h_p}^2} & 0 & -\frac{d_{31}(2z_n-h_p)}{2{s_{11}}^p} & -\frac{d_{31}}{{s_{11}}^p} \\ 0 & -\frac{d_{31}(2z_n-h_p)}{2{s_{11}}^p} & -\frac{d_{31}}{{s_{11}}^p} & \frac{\mathrm{L}\varepsilon}{{h_p}^2} & -\frac{\mathrm{L}\varepsilon}{{h_p}^2} & 0 & \frac{d_{31}(2z_n-h_p)}{2{s_{11}}^p} & \frac{d_{31}}{{s_{11}}^p} \\ -\frac{12EI}{\mathrm{L}^3} & -\frac{6EI}{\mathrm{L}^2} & 0 & 0 & 0 & \frac{12EI}{\mathrm{L}^3} & -\frac{6EI}{\mathrm{L}^2} & 0 \\ \frac{6EI}{\mathrm{L}^2} & \frac{2EI}{\mathrm{L}} & 0 & -\frac{d_{31}(2z_n-h_p)}{2{s_{11}}^p} & \frac{d_{31}(2z_n-h_p)}{2{s_{11}}^p} & -\frac{6EI}{\mathrm{L}^2} & \frac{4EI}{\mathrm{L}} & 0 \\ 0 & 0 & -\frac{Yh}{\mathrm{L}} & -\frac{d_{31}}{{s_{11}}^p} & \frac{d_{31}}{{s_{11}}^p} & 0 & 0 & \frac{Yh}{\mathrm{L}} \end{bmatrix} \tag{4.41}$$

4.1.8 Derivation of the Mass Matrix

Rearranging the products in Eq. (4.23), we obtain:

$$\int_{\mathrm{V}} \delta\mathscr{T}\, d\mathrm{V} = \omega^2 \int_0^{\mathrm{L}} \left[\delta w_3\, w_3 \int_z \rho dz + \delta w_{3,1}\, w_{3,1} \int_z \rho x_3^2 dz - \delta w_{3,1}\, w_1 \int_z \rho x_3 dz - \delta w_1\, w_{3,1} \int_z \rho x_3 dz + \delta w_1\, w_1 \int_z \rho dz \right] dx. \tag{4.42}$$

In the general form of FEA system (Eq. 4.34), the shape functions, ($\mathbf{N}$), and the interpolations matrix, ($\mathbf{B}$), relate different quantities to the generalized displacement vector, ($\mathbf{U}^n$), defined in Eq. (4.35) and holding all DOFs. Here, (4.42) involves only $w_{3,1}$, w_3 and w_1 to the variations of the same quantities. At the same time, we need to keep the notations consistent with the ordering of the DOFs in ($\mathbf{U}^n$). In these conditions, ($\mathbf{N}$) is properly defined as a $[3 \times 8]$ matrix. The ordering of its 3 lines is arbitrary as long as the $\boldsymbol{\rho}$ matrix is

consistent with it. In these conditions, retaining the ordering of lines:

$$1)\ w_3\ 2)\ w_{3,1}\ 3)\ w_1$$

implies the following **N** matrix for use in the FEA system Eq. (4.34) specific to our problem:

$$\left[\mathbf{N}\right] = \begin{bmatrix} 1-3\frac{x^2}{L^2}+2\frac{x^3}{L^3} & x-2\frac{x^2}{L}+\frac{x^3}{L^2} & 0 & 0 & 0 & 3\frac{x^2}{L^2}-2\frac{x^3}{L^3} & -\frac{x^2}{L}+\frac{x^3}{L^2} & 0 \\ -6\frac{x}{L^2}+6\frac{x^2}{L^3} & 1-4\frac{x}{L}+3\frac{x^2}{L^2} & 0 & 0 & 0 & 6\frac{x}{L^2}-6\frac{x^2}{L^3} & -2\frac{x}{L}+3\frac{x^2}{L^2} & 0 \\ 0 & 0 & 1-\frac{x}{L} & 0 & 0 & 0 & 0 & \frac{x}{L} \end{bmatrix} \tag{4.43}$$

whereas the $[3\times 3]$ $\boldsymbol{\rho}$ matrix consistent with Eq. (4.42) contains the following inertial characteristics of the cross–section of the piezoelectric beam:

$$\left[\boldsymbol{\rho}\right] = \begin{bmatrix} \rho_{ext} & 0 & 0 \\ 0 & \rho_{flex} & -\rho_{inter} \\ 0 & -\rho_{inter} & \rho_{ext} \end{bmatrix} \tag{4.44}$$

where

$$\begin{aligned} \rho_{ext} &= \int_z \rho(z)\,dz = \rho_i h_i + \rho_p h_p, \\ \rho_f &= \int_0^{h_p} \rho_p\,(z-z_n)^2\,dz + \int_{-h_i}^{0} \rho_i\,(z-z_n)^2\,dz = \frac{\rho_p}{3}\left[(h_p-z_n)^3+z_n^3\right] + \frac{\rho_i}{3}\left[(h_i+z_n)^3-z_n^3\right], \\ \rho_{inter} &= \int_0^{h_p} \rho_p\,(z-z_n)dz + \int_{-h_i}^{0} \rho_i\,(z-z_n)\,dz = \frac{\rho_p}{2}\left[h_p^2-2h_p z_n\right] - \frac{\rho_i}{2}\left[h_i^2+2h_i z_n\right]. \end{aligned} \tag{4.45}$$

The ordering of lines is arbitrary, but we must keep the contents of ρ consistent with it. Also, the **N** matrix aimed to comply with here–considered form of system (Eq. 4.34) differs from the shape functions of pure bending presented in page 114 because we want now to add the required terms to account for the kinetic energy variation of the length–extensional mode of vibration. Computing the mass matrix of the system as

$$[\mathbf{M}] = \int_0^{L} \mathbf{N}^{T}(x)\cdot\boldsymbol{\rho}\cdot\mathbf{N}(x)\,dx,$$

we obtain:

$$[\mathbf{M}] = \begin{bmatrix}
\frac{42\rho_f+13L^2\rho_e}{35L} & \frac{21\rho_f+11L^2\rho_e}{210} & \frac{\rho_i}{2} & 0 & 0 & -\frac{84\rho_f-9L^2\rho_e}{70L} & \frac{42\rho_f-13L^2\rho_e}{420} & \frac{\rho_i}{2} \\
\frac{21\rho_f+11L^2\rho_e}{210} & \frac{14L\rho_f+L^3\rho_e}{105} & -\frac{L\rho_i}{12} & 0 & 0 & -\frac{42\rho_f-13L^2\rho_e}{420} & -\frac{14L\rho_f+3L^3\rho_e}{420} & \frac{L\rho_i}{12} \\
\frac{\rho_i}{2} & -\frac{L\rho_i}{12} & \frac{L\rho e}{3} & 0 & 0 & -\frac{\rho_i}{2} & \frac{L\rho_i}{12} & \frac{L\rho e}{6} \\
0 & 0 & 0 & 0 & 0 & 0 & 0 & 0 \\
0 & 0 & 0 & 0 & 0 & 0 & 0 & 0 \\
-\frac{84\rho_f-9L^2\rho_e}{70L} & -\frac{42\rho_f-13L^2\rho_e}{420} & -\frac{\rho_i}{2} & 0 & 0 & \frac{42\rho_f+13L^2\rho_e}{35L} & -\frac{21\rho_f+11L^2\rho_e}{210} & -\frac{\rho_i}{2} \\
\frac{42\rho_f-13L^2\rho_e}{420} & -\frac{14L\rho_f+3L^3\rho_e}{420} & \frac{L\rho_i}{12} & 0 & 0 & -\frac{21\rho_f+11L^2\rho_e}{210} & \frac{14L\rho_f+L^3\rho_e}{105} & -\frac{L\rho_i}{12} \\
\frac{\rho_i}{2} & \frac{L\rho_i}{12} & \frac{L\rho e}{6} & 0 & 0 & -\frac{\rho_i}{2} & -\frac{L\rho_i}{12} & \frac{L\rho e}{3}
\end{bmatrix} \tag{4.46}$$

4.1.9 Derivation of the Second Member

Here, we don't take the stress stiffening into account so that the flexure is similar to the model of Maisonnet and Dulmet [3]. In structural analysis, the stress stiffening (geometric stiffening) is a change of rigidity resulting from the static load and the deformed shape. For instance, the static extension of a beam increases its resonant frequency, like in the well-known stretched string problem (explaining the tuning of a violin or a guitar, for instance). We can ignore it here since the beam is a cantilever. Because the description of the unimorph beam is concentrated on its neutral fiber, the surface integration in the variation of work done by external actions takes a simple form:

$$\begin{aligned}
\delta\int_S W dS &= \int_S \left(\vec{f}\delta\vec{u} - \sigma\delta\varphi\right) dS = F_z^0\delta w_3^0 + C_y^0\delta w_{3,1} + F_x^0\delta w_1^0 \\
&\quad -Q^0\delta\varphi^0 - Q^h\delta\varphi^h + F_z^L\delta w_3^L + C_y^L\delta w_{3,1}^L + F_x^L\delta w_1^L
\end{aligned} \tag{4.47}$$

zeroing the coefficient of the variation of each DOF. In Hamilton's principle, we find that the factors of the DOFs variations occurring in the right hand member are the components of the the second member vector of the FEA system equivalent to Eq. (4.34) for our specific problem[2]

$$\delta\left[\int_V (\mathscr{U} - \mathscr{T})\, dV\right] = \delta\int_s \mathscr{W} dS \quad \Leftrightarrow \quad \sum_e \left(\left[\mathbf{K}_e\right] - \omega^2\left[\mathbf{M}_e\right]\right)\{\mathbf{U}^n\} = \{\mathbf{F}^n\}$$

Of course, the vectors $\mathbf{U}^n$ and $\mathbf{F}^n$ have the same dimensions. The generalized–force vector $\mathbf{F}^n$ holds the external forces and torques as well as *the opposite* of the electric charge respectively associated to the corresponding DOFs, namely transverse displacement, ro-

[2] According to the kinematic assumptions (4.4) ruling the continuous variables in the unimorph, we do not need the shape functions **N** here.

tation, axial displacement, potential. Indeed, we shall consider them in the same order. Keeping the ordering consistent with Eq. (4.35) p. 115, the successive components of this vector are:

1) F_z^0 is the transverse force at the left end of beam ($x = 0$);

2) C_y^0 is the momentum exerted at the left end of beam ($x = 0$);

3) F_1^0 is the axial force at the left end of beam ($x = 0$);

4) Q_0 is the charge at the bottom electrode of the piezoelectric layer ($z = 0$);

5) Q_h is the potential of the top surface of the piezoelectric layer ($z = h_p$);

6) $\mathrm{F}_z^{\mathrm{L}}$ is the transverse displacement of the right end of beam ($x = \mathrm{L}$);

7) $\mathrm{C}_y^{\mathrm{L}}$ is the momentum exerted at the right end of beam ($x = \mathrm{L}$);

8) $\mathrm{F}_1^{\mathrm{L}}$ is the axial force at the right end of beam ($x = \mathrm{L}$).

Then, the general FEA system can be detailed as follows:

$$\left(\begin{bmatrix} \mathrm{K}_{11} & \mathrm{K}_{12} & \mathrm{K}_{13} & \mathrm{K}_{14} & \mathrm{K}_{15} & \mathrm{K}_{16} & \mathrm{K}_{17} & \mathrm{K}_{18} \\ \mathrm{K}_{21} & \mathrm{K}_{22} & \mathrm{K}_{23} & \mathrm{K}_{24} & \mathrm{K}_{25} & \mathrm{K}_{26} & \mathrm{K}_{27} & \mathrm{K}_{28} \\ \mathrm{K}_{31} & \mathrm{K}_{32} & \mathrm{K}_{33} & \mathrm{K}_{34} & \mathrm{K}_{35} & \mathrm{K}_{36} & \mathrm{K}_{37} & \mathrm{K}_{38} \\ \mathrm{K}_{41} & \mathrm{K}_{42} & \mathrm{K}_{43} & \mathrm{K}_{44} & \mathrm{K}_{45} & \mathrm{K}_{46} & \mathrm{K}_{47} & \mathrm{K}_{48} \\ \mathrm{K}_{51} & \mathrm{K}_{52} & \mathrm{K}_{53} & \mathrm{K}_{54} & \mathrm{K}_{55} & \mathrm{K}_{56} & \mathrm{K}_{57} & \mathrm{K}_{58} \\ \mathrm{K}_{61} & \mathrm{K}_{62} & \mathrm{K}_{63} & \mathrm{K}_{64} & \mathrm{K}_{65} & \mathrm{K}_{66} & \mathrm{K}_{67} & \mathrm{K}_{68} \\ \mathrm{K}_{71} & \mathrm{K}_{72} & \mathrm{K}_{73} & \mathrm{K}_{74} & \mathrm{K}_{75} & \mathrm{K}_{76} & \mathrm{K}_{77} & \mathrm{K}_{78} \\ \mathrm{K}_{81} & \mathrm{K}_{82} & \mathrm{K}_{83} & \mathrm{K}_{84} & \mathrm{K}_{85} & \mathrm{K}_{86} & \mathrm{K}_{87} & \mathrm{K}_{88} \end{bmatrix} - \omega^2 \begin{bmatrix} \mathrm{M}_{11} & \mathrm{M}_{12} & \mathrm{M}_{13} & \mathrm{M}_{14} & \mathrm{M}_{15} & \mathrm{M}_{16} & \mathrm{M}_{17} & \mathrm{M}_{18} \\ \mathrm{M}_{21} & \mathrm{M}_{22} & \mathrm{M}_{23} & \mathrm{M}_{24} & \mathrm{M}_{25} & \mathrm{M}_{26} & \mathrm{M}_{27} & \mathrm{M}_{28} \\ \mathrm{M}_{31} & \mathrm{M}_{32} & \mathrm{M}_{33} & \mathrm{M}_{34} & \mathrm{M}_{35} & \mathrm{M}_{36} & \mathrm{M}_{37} & \mathrm{M}_{38} \\ \mathrm{M}_{41} & \mathrm{M}_{42} & \mathrm{M}_{43} & \mathrm{M}_{44} & \mathrm{M}_{45} & \mathrm{M}_{46} & \mathrm{M}_{47} & \mathrm{M}_{48} \\ \mathrm{M}_{51} & \mathrm{M}_{52} & \mathrm{M}_{53} & \mathrm{M}_{54} & \mathrm{M}_{55} & \mathrm{M}_{56} & \mathrm{M}_{57} & \mathrm{M}_{58} \\ \mathrm{M}_{61} & \mathrm{M}_{62} & \mathrm{M}_{63} & \mathrm{M}_{64} & \mathrm{M}_{65} & \mathrm{M}_{66} & \mathrm{M}_{67} & \mathrm{M}_{68} \\ \mathrm{M}_{71} & \mathrm{M}_{72} & \mathrm{M}_{73} & \mathrm{M}_{74} & \mathrm{M}_{75} & \mathrm{M}_{76} & \mathrm{M}_{77} & \mathrm{M}_{78} \\ \mathrm{M}_{81} & \mathrm{M}_{82} & \mathrm{M}_{83} & \mathrm{M}_{84} & \mathrm{M}_{85} & \mathrm{M}_{86} & \mathrm{M}_{87} & \mathrm{M}_{88} \end{bmatrix}\right) \begin{bmatrix} w_3^0 \\ w_{3,1}^0 \\ w_1^0 \\ \varphi_0 \\ \varphi_h \\ w_3^{\mathrm{L}} \\ w_{3,1}^{\mathrm{L}} \\ w_1^{\mathrm{L}} \end{bmatrix} = \begin{bmatrix} \mathrm{F}_z^0 \\ \mathrm{C}_y^0 \\ \mathrm{F}_x^0 \\ -\mathrm{Q}_0 \\ -\mathrm{Q}_h \\ \mathrm{F}_z^{\mathrm{L}} \\ \mathrm{C}_y^{\mathrm{L}} \\ \mathrm{F}_x^{\mathrm{L}} \end{bmatrix} \tag{4.48}$$

This system contains every possible consequence and applications of our model.

4.2 Introducing Internal Damping

Introducing internal damping in our model calls for very–well known notions and formulas. Nevertheless, some confusion could arise from the fact that the presentation and the notations used to describe damped oscillatory systems in forced regime vary according to the field of application: basic mathematics, mechanics, electronics or system control. Hence, we find helpful to start from the very beginning and in a detailed way. We will use concepts commonly used in vibration analysis of which Lord Rayleigh is largely recognized as the most illustrious pioneer and founder. As a matter of fact, the approach is relatively simple since it consists in taking advantage of the known results for a single-degree–of–freedom system within the treatment of multiple–degrees–of–freedom systems.

4.2.1 The Simple Case of Single Degree–of–Freedom System

The best starting point for system–level analysis of damped vibrations consists in studying the differential equation of a single-degree-of-freedom mechanical system, namely the simple system spring/mass/damper:

$$m\ddot{u} + c\dot{u} + ku = \mathrm{F}(t). \tag{4.49}$$

It is customary to define specific values of angular frequency and damping coefficient as follows

$$\begin{aligned} \omega_0^2 &= \frac{k}{m}, && \text{natural (angular) frequency,} \\ c_0 &= 2\sqrt{km} = 2m\omega_0, && \text{critical damping.} \end{aligned} \tag{4.50}$$

Then, considering that $c = \lambda c_0$, where λ is by definition the dimensionless damping ratio, we may rewrite the initial equation as:

$$\ddot{u} + 2\lambda\omega_0\dot{u} + \omega_0^2 u = \frac{\mathrm{F}(t)}{m}. \tag{4.51}$$

From the well–known theory of differential equations, the solution of this differential equation of second order with constant coefficients is the sum of a particular solution with the second member and the general solution without the second member. The easy part may be the particular solution with the second member. Let us denote it by $\widetilde{u}$ and introduce the following complex notations:

$$\widetilde{u}(t) = \hat{u}e^{j\omega t}, \quad \mathrm{F}(t) = \widetilde{\mathrm{F}}\,e^{j\omega t}, \tag{4.52}$$

where $\hat{u}$ and $\widetilde{\mathrm{F}}$ are complex constants with the meaning of amplitude coefficients. Then an obvious particular solution is:

$$\hat{u}(\omega) = \frac{\hat{\mathrm{F}}}{m\left[\omega_0^2 - \omega^2 + 2j\lambda\omega\omega_0\right]}. \tag{4.53}$$

This is named the "solution in permanent harmonic regime". In the academic terminology commonly used in the field of vibration, the solution $\hat{u}$ is said to belonging to the spectral domain, because it is time–constant and at the same time a function of ω.

4.2.2 Rayleigh Damping Model

This is a model that defines the damping from values of mass and stiffness:

$$c = \alpha m + \beta k \tag{4.54}$$

where α and β are fixed coefficients. Because, according to Eq. (4.50) $c = \lambda c_0 = \lambda 2\omega_0 m$, therefore we obtain:

$$\frac{1}{2\mathrm{Q}} = \lambda = \frac{1}{2}\left(\frac{\alpha}{\omega_0} + \beta\omega_0\right) \Rightarrow \mathrm{Q} = \frac{1}{\frac{\alpha}{\omega_0} + \beta\omega_0}. \tag{4.55}$$

In good–quality quartz BAW resonators, the losses come almost exclusively from viscoelastic damping. This corresponds to the case $\alpha = 0$ and

$$\mathrm{Q} = \frac{1}{\beta\omega_0}. \tag{4.56}$$

One remarks that the product $\mathrm{Q} \times f$ is constant. Conversely, if we put $\beta = 0$, we obtain:

$$\mathrm{Q} = \frac{\omega}{\alpha}. \tag{4.57}$$

This assumption permits to take into account some structural effects, for instance, where fundamental mode has a much lower Q than the overtones and there are more energy losses through the anchors. Also, in flexure mode, the phenomenon of thermoelasic damping due to a coupling between equation of conduction–diffusion of heat and the equation of dynamics indicates an optimal frequency band for the Q factor [4–8]. α and β are not extensively measured for any combination of materials and given structures, but Rayleigh formula permits to keep some balance between the two inverse frequency behaviors of damping. Hence, we suggest to assume that $\alpha = 0$ and to use the corresponding formula to easily tune up the damping ratio used in the equations to attain a certain Q. If we want more elaborate analysis, we can assign the value of targeted damping at 2

different frequencies f_1 and f_2 and obtain α and β by solving the linear system:

$$\begin{bmatrix} \frac{1}{2\pi f_1} & 2\pi f_1 \\ \frac{1}{2\pi f_2} & 2\pi f_2 \end{bmatrix} \begin{bmatrix} \alpha \\ \beta \end{bmatrix} = \begin{bmatrix} \frac{1}{Q_1} \\ \frac{1}{Q_2} \end{bmatrix} \tag{4.58}$$

as suggested by Comsol documentation, though with slightly different notations. Now we are all set to start looking at damped systems with multiple degrees of freedom, such as our FEA harvester system.

4.3 Reduction of FEA System from Boundary Conditions

In this section I will finally summarize the results of the minimalist FEA applied in the case of energy harvesting, even though we could define similar boundary conditions for actuation. At the end of the section I will present the possibility of connecting the harvester to the external load and the derivation of the electro-mechanical coupling.

4.3.1 Operation as Harvester

Force, torque and charge become "reaction" quantities when the DOF is forced to a fixed value. Then, if a DOF is fixed to zero, the corresponding line and column of the system (Eq. 4.48) can be put aside to determine one of the reactions after the unknown DOFs are computed. Accordingly, if we fix to zero w_3^0, $w_{3,1}^0$, $w_{1,1}^0$ and φ_0 *i.e* the DOFs numbered 1, 2, 3, and 4, we are left with a $[4\times4]$ system consisting of the subsystem of Eq. (4.34) obtained by removing lines and columns 1, 2, 3 and 4:

$$\left(\begin{bmatrix} K_{55} & K_{56} & K_{57} & K_{58} \\ K_{65} & K_{66} & K_{67} & K_{68} \\ K_{75} & K_{76} & K_{77} & K_{78} \\ K_{85} & K_{86} & K_{87} & K_{88} \end{bmatrix} - \omega^2 \begin{bmatrix} M_{55} & M_{56} & M_{57} & M_{58} \\ M_{65} & M_{66} & M_{67} & M_{68} \\ M_{75} & M_{76} & M_{77} & M_{78} \\ M_{85} & M_{86} & M_{87} & M_{88} \end{bmatrix} \right) \begin{bmatrix} \varphi_h \\ w_3^L \\ w_{3,1}^L \\ w_1^L \end{bmatrix} = \begin{bmatrix} -Q_h \\ F_z^L \\ C_y^L \\ F_x^L \end{bmatrix} \tag{4.59}$$

Solving this system, the unknown values of w_3^L, $w_{3,1}^L$, $w_{1,1}^L$, and φ_h are obtained from the imposed values of F_z^L, C_y^L, F_x^L and Q_h. These imposed values can be null or not, it depends on the boundary conditions. For instance, we have the right to impose the following right member in Eq. (4.59)

$$\left[\boldsymbol{f}^n \right] = \begin{bmatrix} 0 & (-M_s \Gamma_z) & 0 & 0 \end{bmatrix}^T \tag{4.60}$$

in the case of a Γ_z acceleration–driven harvester with a punctual seismic mass M_s. Once the unknowns are obtained, the previously–removed lines and columns of Eq. (4.48) are

recalled to get the values of the reactions

$$\begin{bmatrix} \mathrm{F}_z^0 \\ \mathrm{C}_y^0 \\ \mathrm{F}_x^0 \\ -\mathrm{Q}_0 \end{bmatrix} = \left(\begin{bmatrix} \mathrm{K}_{15} & \mathrm{K}_{16} & \mathrm{K}_{17} & \mathrm{K}_{18} \\ \mathrm{K}_{25} & \mathrm{K}_{26} & \mathrm{K}_{27} & \mathrm{K}_{28} \\ \mathrm{K}_{35} & \mathrm{K}_{36} & \mathrm{K}_{37} & \mathrm{K}_{38} \\ \mathrm{K}_{45} & \mathrm{K}_{46} & \mathrm{K}_{47} & \mathrm{K}_{48} \end{bmatrix} - \omega^2 \begin{bmatrix} \mathrm{M}_{15} & \mathrm{M}_{16} & \mathrm{M}_{17} & \mathrm{M}_{18} \\ \mathrm{M}_{25} & \mathrm{M}_{26} & \mathrm{M}_{27} & \mathrm{M}_{28} \\ \mathrm{M}_{35} & \mathrm{M}_{36} & \mathrm{M}_{37} & \mathrm{M}_{38} \\ \mathrm{M}_{45} & \mathrm{M}_{46} & \mathrm{M}_{47} & \mathrm{M}_{48} \end{bmatrix} \right) \begin{bmatrix} \varphi_h \\ w_3^{\mathrm{L}} \\ w_{3,1}^{\mathrm{L}} \\ w_1^{\mathrm{L}} \end{bmatrix} \tag{4.61}$$

If we recopy Eq. (4.59) here while taking into account the zeroes occurring in the specific stiffness and mass matrices, we find:

$$\left(\begin{bmatrix} \mathrm{K}_{55} & 0 & \mathrm{K}_{57} & \mathrm{K}_{58} \\ 0 & \mathrm{K}_{66} & \mathrm{K}_{67} & 0 \\ \mathrm{K}_{75} & \mathrm{K}_{76} & \mathrm{K}_{77} & 0 \\ \mathrm{K}_{85} & 0 & 0 & \mathrm{K}_{88} \end{bmatrix} - \omega^2 \begin{bmatrix} 0 & 0 & 0 & 0 \\ 0 & \mathrm{M}_{66} & \mathrm{M}_{67} & \mathrm{M}_{68} \\ 0 & \mathrm{M}_{76} & \mathrm{M}_{77} & \mathrm{M}_{78} \\ 0 & \mathrm{M}_{86} & \mathrm{M}_{87} & \mathrm{M}_{88} \end{bmatrix} \right) \begin{bmatrix} \varphi_h \\ w_3^{\mathrm{L}} \\ w_{3,1}^{\mathrm{L}} \\ w_1^{\mathrm{L}} \end{bmatrix} = \begin{bmatrix} -\mathrm{Q}_h \\ \mathrm{F}_z^{\mathrm{L}} \\ \mathrm{C}_y^{\mathrm{L}} \\ \mathrm{F}_x^{\mathrm{L}} \end{bmatrix} \tag{4.62}$$

which gives the following system of equations:

$$\begin{array}{llll} \mathrm{K}_{55}\varphi_h & & +\mathrm{K}_{57}\, w_{3,1}^{\mathrm{L}} & +\mathrm{K}_{58}\, w_1^{\mathrm{L}} = -\mathrm{Q}_h \\ & \left(\mathrm{K}_{66} - \omega^2 \mathrm{M}_{66}\right) w_3^{\mathrm{L}} & + \left(\mathrm{K}_{67} - \omega^2 \mathrm{M}_{67}\right) w_{3,1}^{\mathrm{L}} & -\omega^2 \mathrm{M}_{68}\, w_1^{\mathrm{L}} = \mathrm{F}_z^{\mathrm{L}} \\ \mathrm{K}_{57}\varphi_h & + \left(\mathrm{K}_{67} - \omega^2 \mathrm{M}_{67}\right) w_3^{\mathrm{L}} & + \left(\mathrm{K}_{77} - \omega^2 \mathrm{M}_{77}\right) w_{3,1}^{\mathrm{L}} & -\omega^2 \mathrm{M}_{78}\, w_1^{\mathrm{L}} = \mathrm{C}_y^{\mathrm{L}} \\ \mathrm{K}_{58}\varphi_h & -\omega^2 \mathrm{M}_{68}\, w_3^{\mathrm{L}} & -\omega^2 \mathrm{M}_{78}\, w_{3,1}^{\mathrm{L}} & + \left(\mathrm{K}_{88} - \omega^2 \mathrm{M}_{88}\right) w_1^{\mathrm{L}} = \mathrm{F}_x^{\mathrm{L}} \end{array} \tag{4.63}$$

where we used the identifications given previously:

$$\begin{aligned} \mathrm{K}_{55} &= -\frac{\varepsilon \mathrm{L}}{h_p^2}, & \mathrm{K}_{57} &= \frac{d_{31}\left(h_p - 2z_n\right)}{2 s_{11}^p}, & \mathrm{K}_{58} &= \frac{d_{31}}{s_{11}^p}. \\ \mathrm{K}_{66} &= \frac{12 \mathrm{EI}^e}{\mathrm{L}^3}, & \mathrm{K}_{67} &= -\frac{6 \mathrm{EI}^e}{\mathrm{L}^2}. \\ \mathrm{K}_{77} &= \frac{4 \mathrm{EI}^e}{\mathrm{L}}, & \mathrm{K}_{88} &= \frac{\mathrm{Y} h^e}{\mathrm{L}}. \end{aligned} \tag{4.64}$$

The expressions of the elements of the mass matrix of the composite beam were given in Eq. (4.46) page 120.

4.3.2 Modal Mass and Stiffness

Adding damping to our FEA system (Eq. 4.59) consists in determining a pertinent damping matrix, $\boldsymbol{\eta}$, playing in the system the role of c in the one DOF mass–spring–damper

system:

$$\mathbf{K}\mathbf{U}^n + j\omega\boldsymbol{\eta}\mathbf{U}^n - \omega^2\mathbf{M}\mathbf{U}^n = \mathbf{F}^n. \tag{4.65}$$

The entire discussion of this section is for a permanent harmonic regime, dealing with the homogeneous problem or the forced problem. We expect $\mathbf{K}$ to be invertible because the system, $\mathbf{F} = \mathbf{K}\mathbf{U}$, has a solution in static regime, but obviously $\mathbf{M}$ is not invertible because of its many zeroes arising from the fundamental lack of of mutual relation between inertia and electrical variables. Then the number of eigenvalue / eigenvector pairs, obtained by vanishing $\mathbf{F}$, is lower than the size of the diagonal of $\mathbf{M}$. It is known that adding piezoelectricity to a system doesn't change the number of eigenmodes. In other words, piezoelectricity does not add any vibration mode w.r.t. mechanics, but it modifies the mechanical modes of resonance [9]. Accordingly, because Eq. (4.62) bears 3 mechanical DOFs, we expect that it will yield 3 pairs of eigenvalues /eigenvectors instead of 4, which is the actual dimension of the square matrices. Let ω_i and $\mathbf{U}_i$ be one of the pairs of eigenvalue / eigenvector of the homogeneous equation without damping. If we multiply the equation satisfied by this pair by one of the other eigenvectors, say $\mathbf{U}_j$, we obtain:

$$\mathbf{U}_j^{\mathrm{T}}\mathbf{K}\mathbf{U}_i - \omega_i^2\mathbf{U}_j^{\mathrm{T}}\mathbf{M}\mathbf{U}_i = 0. \tag{4.66}$$

If we do it by subtracting the two equations obtained in this way, and using the symmetry of the mass and stiffness matrices, it is classically demonstrated that:

$$\left(\omega_j^2 - \omega_i^2\right)\mathbf{U}_j^{\mathrm{T}}\mathbf{M}\mathbf{U}_i = 0. \tag{4.67}$$

Please note that $\mathbf{U}_j^{\mathrm{T}}\mathbf{M}\mathbf{U}_i$ is a scalar, because of the product chain $[1\times 4].[4\times 4].[4\times 1] = [1\times 1]$. As far as the eigenfrequencies are distinct, we see that

$$\mathbf{U}_j^{\mathrm{T}}\mathbf{M}\mathbf{U}_i = 0 \text{ for } i \neq j \text{ and } \omega_i \neq \omega_j. \tag{4.68}$$

similarly:

$$\mathbf{U}_j^{\mathrm{T}}\mathbf{K}\mathbf{U}_i = 0 \text{ for } i \neq j \text{ and } \omega_i \neq \omega_j. \tag{4.69}$$

This is the way how orthogonality of eigenmodes appears in FEA systems. This being said, if we consider all 9 possibilities to mix i and j, we can build the $[3\times 3]$ matrix, $\mathscr{M}$, whose elements are $\mathbf{U}_j^{\mathrm{T}}\mathbf{M}\mathbf{U}_i$:

$$\mathscr{M} = \begin{bmatrix} \mathbf{U}_1^{\mathrm{T}}\mathbf{M}\mathbf{U}_1 & \mathbf{U}_1^{\mathrm{T}}\mathbf{M}\mathbf{U}_2 & \mathbf{U}_1^{\mathrm{T}}\mathbf{M}\mathbf{U}_3 \\ \mathbf{U}_2^{\mathrm{T}}\mathbf{M}\mathbf{U}_1 & \mathbf{U}_2^{\mathrm{T}}\mathbf{M}\mathbf{U}_2 & \mathbf{U}_2^{\mathrm{T}}\mathbf{M}\mathbf{U}_3 \\ \mathbf{U}_3^{\mathrm{T}}\mathbf{M}\mathbf{U}_1 & \mathbf{U}_3^{\mathrm{T}}\mathbf{M}\mathbf{U}_2 & \mathbf{U}_3^{\mathrm{T}}\mathbf{M}\mathbf{U}_3 \end{bmatrix} \tag{4.70}$$

But, due to Eq. (4.68), this matrix is diagonal. Indeed, due to Eq. (4.69), the $\mathscr{K}$ matrix formed as:

$$\mathscr{K} = \begin{bmatrix} \mathbf{U}_1^{\mathrm{T}}\mathbf{K}\mathbf{U}_1 & \mathbf{U}_1^{\mathrm{T}}\mathbf{K}\mathbf{U}_2 & \mathbf{U}_1^{\mathrm{T}}\mathbf{K}\mathbf{U}_3 \\ \mathbf{U}_2^{\mathrm{T}}\mathbf{K}\mathbf{U}_1 & \mathbf{U}_2^{\mathrm{T}}\mathbf{K}\mathbf{U}_2 & \mathbf{U}_2^{\mathrm{T}}\mathbf{K}\mathbf{U}_3 \\ \mathbf{U}_3^{\mathrm{T}}\mathbf{K}\mathbf{U}_1 & \mathbf{U}_3^{\mathrm{T}}\mathbf{K}\mathbf{U}_2 & \mathbf{U}_3^{\mathrm{T}}\mathbf{M}\mathbf{U}_3 \end{bmatrix} \tag{4.71}$$

it is also diagonal. Then we obtain:

$$\mathscr{M} = \begin{bmatrix} m_1 & 0 & 0 \\ 0 & m_2 & 0 \\ 0 & 0 & m_3 \end{bmatrix} \text{ and } \mathscr{K} = \begin{bmatrix} k_1 & 0 & 0 \\ 0 & k_2 & 0 \\ 0 & 0 & k_3 \end{bmatrix} \tag{4.72}$$

where the m_i-s and k_i-s are the *modal masses* and *modal stiffnesses*, respectively. In fact, this is a method of diagonalization since

$$k_i = \omega_i^2 m_i \text{ (here no implicit sum over } i.) \tag{4.73}$$

Then, if we define the damping matrix $\boldsymbol{\eta}$ of (4.65) in the same manner as the Rayleigh damping calculation of the damping factor c of the 1-DOF mass–spring–damper system:

$$\boldsymbol{\eta} = \alpha\mathbf{M} + \beta\mathbf{K}, \tag{4.74}$$

the matrix $\mathscr{H}$ whose elements are

$$\mathscr{H}(i,j) = \mathbf{U}_i^{\mathrm{T}}\boldsymbol{\eta}\mathbf{U}_j = \alpha\mathbf{U}_i^{\mathrm{T}}\mathbf{M}\mathbf{U}_j + \beta\mathbf{U}_i^{\mathrm{T}}\mathbf{K}\mathbf{U}_j \tag{4.75}$$

is diagonal since it is a linear combination of diagonal matrices. Then the damping will affect each eigenmode in the same way as it would affect a 1-DOF having the same resonant frequency as the considered resonance. It has the drawback that various resonant modes in a close frequency vicinity will have the same Q factor and this does not mach the reality, when visco–elastic damping is dominant. But in our FEA model, if we stick to a single element, the expected 3 modes consist of: fundamental of flexure, first harmonic of flexure, and fundamental of length–extensional. If Rayleigh damping coefficients are set to predict a sensible Q value of the fundamental flexure, the model is accurate enough to give results in agreements with the experiments. Another possibility is to assign an arbitrary Q value to each mode. It is equivalent to setting the damping of each 1-DOF model corresponding to a given pair of modal mass and modal stiffness.

4.3.3 Connecting External Elements

Taking into account the zeroes and the symmetries of $\mathbf{K}$ and $\mathbf{M}$, the FEA system (4.62), we want to consider the possibility of connecting a resistance R (in the model R represents the

resistance per unit width) between the two poles at 0 and h_p. We shall consider positive the current flowing from the pole φ_h to the pole φ_0. Then, the constraints imposed to (4.62) must be:

$$\boxed{\mathrm{Q}_0 = -\mathrm{Q}_h}, \quad \mathrm{I} = \frac{d\mathrm{Q}_h}{dt} = j\omega \mathrm{Q}_h = \frac{\varphi_0 - \varphi_h}{\mathrm{R}}, \quad \boxed{\mathrm{Q}_h = -\frac{\varphi_h}{j\omega \mathrm{R}}} \tag{4.76}$$

where last part of (4.76) was obtained under the assumption that φ_0 is grounded. Hence, substituting this relation in the system (4.62), we obtain:

$$\boxed{\varphi_h = -\frac{\mathrm{K}_{58} w_1^{\mathrm{L}} + \mathrm{K}_{57} w_{3,1}^{\mathrm{L}}}{\mathrm{K}_{55} - \frac{1}{j\omega \mathrm{R}}}} \tag{4.77}$$

Then the other relations are:

$$\boxed{\begin{array}{lll}
\left(\mathrm{K}_{66} - \omega^2 \mathrm{M}_{66}\right) w_3^{\mathrm{L}} & + \left(\mathrm{K}_{67} - \omega^2 \mathrm{M}_{67}\right) w_{3,1}^{\mathrm{L}} & - \omega^2 \mathrm{M}_{68} w_1^{\mathrm{L}} = \mathrm{F}_z^{\mathrm{L}} \\
\left(\mathrm{K}_{67} - \omega^2 \mathrm{M}_{67}\right) w_3^{\mathrm{L}} & + \left(\mathrm{K}_{77} - \frac{\mathrm{K}_{57}^2}{\mathrm{K}_{55} - \frac{1}{j\omega \mathrm{R}}} - \omega^2 \mathrm{M}_{77}\right) w_{3,1}^{\mathrm{L}} & - \left(\frac{\mathrm{K}_{57}\mathrm{K}_{58}}{\mathrm{K}_{55} - \frac{1}{j\omega \mathrm{R}}} + \omega^2 \mathrm{M}_{78}\right) w_1^{\mathrm{L}} = \mathrm{C}_y^{\mathrm{L}} \\
- \omega^2 \mathrm{M}_{68} w_3^{\mathrm{L}} & - \left(\frac{\mathrm{K}_{57}\mathrm{K}_{58}}{\mathrm{K}_{55} - \frac{1}{j\omega \mathrm{R}}} + \omega^2 \mathrm{M}_{78}\right) w_{3,1}^{\mathrm{L}} & + \left(\mathrm{K}_{88} - \frac{\mathrm{K}_{58}^2}{\mathrm{K}_{55} - \frac{1}{j\omega \mathrm{R}}} - \omega^2 \mathrm{M}_{88}\right) w_1^{\mathrm{L}} = \mathrm{F}_x^{\mathrm{L}}
\end{array}} \tag{4.78}$$

Therefore φ_h is the potential of the top electrode and depends on both axial displacement w_1^{L} and the rotation $w_{3,1}^{\mathrm{L}}$ terms, remembering that both $\mathbf{K}$ and $\mathbf{M}$ are integrated over the width of the beam.

4.3.4 Electromechanical Coupling

For a given set of mechanical solicitations $(\mathrm{F}_x^{\mathrm{L}}, \mathrm{C}_y^{\mathrm{L}})$, the amplitudes of transverse displacement and rotation when properly connecting an external load resistance for flexural actuation are fixed by the final system (Eq. 4.78). We can estimate the electromechanical coupling for our given device as:

$$k_{eff}^2 = \frac{\omega_{oc}^2 - \omega_{sc}^2}{\omega_{oc}^2} \tag{4.79}$$

knowing the values at short- and open-circuit ω_{sc} and ω_{oc}, which can be derived by zeroing the determinant of Eq. (4.62). Therefore the system would be:

$$(\mathbf{K} - \omega^2 \mathbf{M})\mathbf{U}^n = \mathbf{F}^n. \tag{4.80}$$

$$\det[\mathbf{K} - \omega^2 \mathbf{M}] = 0 \tag{4.81}$$

Three resonance peaks are expected because our model, with our cubic interpolations and a single finite element, ends up with three DOFs. If we neglect the small frequency shift between damped and undamped models, the location of resonance peaks will respectively correspond to the three frequencies zeroing the determinant of the system.

If the diagonal terms are dominant for $\mathbf{M}$ in the initial linear system, we can calculate the determinant of the following simplified matrix:

$$\det\left(\begin{bmatrix} K_{66}-M_{66}\omega^2 & K_{67} & 0 \\ K_{67} & K_{77}-\frac{K_{57}^2}{K_{55}-\frac{1}{j\omega R}}-M_{77}\omega^2 & -\left(\frac{K_{57}K_{58}}{K_{55}-\frac{1}{j\omega R}}\right) \\ 0 & -\left(\frac{K_{57}K_{58}}{K_{55}-\frac{1}{j\omega R}}\right) & K_{88}-\frac{K_{58}^2}{K_{55}-\frac{1}{j\omega R}}-M_{88}\omega^2 \end{bmatrix}\right)=0 \tag{4.82}$$

The value of R is either 0 or ∞, which corresponds to either short-circuit or open circuit conditions. Therefore, for the short circuit case, we can simplify the matrix as:

$$\det\left(\begin{bmatrix} K_{66}-M_{66}\omega^2 & K_{67} & 0 \\ K_{67} & K_{77}-M_{77}\omega^2 & 0 \\ 0 & 0 & K_{88}-M_{88}\omega^2 \end{bmatrix}\right)=0 \tag{4.83}$$

Its determinant is a biquadratic equation multiplied by a term which corresponds to a higher mode (M_{88} and K_{88}).

$$\left(M_{88}\omega^2-K_{88}\right)\left(M_{66}M_{77}\omega^4-(K_{66}M_{77}+K_{77}M_{66})\omega^2+(K_{66}K_{77}-{K_{67}}^2)\right) \tag{4.84}$$

We are interested in considering the quadratic term which is in the following form:

$$A\omega^4-B\omega^2+C=0. \tag{4.85}$$

where A and C are real and positive, and we find that Δ can be approximated to a simpler form upon reducing it to the diagonal matrix elements. Let us study the discriminant of the equation:

$$\Delta_{sc}=(K_{66}M_{77}+M_{66}K_{77})^2+4M_{66}M_{77}K_{67}^2 \tag{4.86}$$

Hence, because the dominant terms of Δ are the sum of two perfect squares, we can assume that $B^2-4AC>0$.

The roots are given by:

$$\omega_{sc}^2=\frac{B\pm\sqrt{\Delta_{sc}}}{2A} \tag{4.87}$$

That is explicitly written as:

$$\omega_{sc}^2=\frac{K_{66}M_{77}+K_{77}M_{66}+\sqrt{(K_{66}M_{77}+M_{66}K_{77})^2+4M_{66}M_{77}K_{67}^2}}{2M_{66}M_{77}} \tag{4.88}$$

The positive roots of this approximation are representing the first two modes of the system in short circuit condition.

For open circuit, things are a bit more complicated:

$$\det\left(\begin{bmatrix} K_{66}-M_{66}\omega^2 & K_{67} & 0 \\ K_{67} & -M_{77}\omega^2+K_{77}-\frac{{K_{57}}^2}{K_{55}} & -\frac{K_{57}K_{58}}{K_{55}} \\ 0 & -\frac{K_{57}K_{58}}{K_{55}} & -M_{88}\omega^2+K_{88}-\frac{{K_{58}}^2}{K_{55}} \end{bmatrix}\right)=0 \tag{4.89}$$

The roots in this case can be solved numerically and the results are complex numbers. Considering the real part of the solutions, we eventually find that $\omega_{oc} > \omega_{sc}$. In other words, we fall back on the classical configuration yielding higher frequency in open–circuit than in short–circuit. This permits to estimate the electro-mechanical coupling from the frequency difference. Because of the approximations carried over in above calculations, it is better to numerically compute the coupling from the exact expressions of Eq. (4.78) computed in both cases of electrical boundary conditions. It is not given with a satisfactory accuracy because the cubic interpolation along a single finite element is a poor approximation of the known second mode shape in the series of flexural modes. To get it more accurately, we can increase the numbers of finite elements along the length of the beam. This is one limitation of our FEA approach in comparison with the traditional full analytic solving which is "neutral" about the overtone rank because the analytical solving yields trigonometric and hyperbolic exact solutions instead of polynomial approximated solutions.

Is it worth increasing the number of elements ? Actually, in any case, despite its pedagogic benefits, the model will carry over the limitations of Bernoulli's assumptions. Improving the model with shear effects, like in Timoshenko's theory, will add complexity that could be judged unnecessary due to the large availability of both extensive FEA software and capable computers. Hence it is worth examining the use of full 3D FEA for precise optimization of the cantilever piezoelectric harvester.

4.4 Comsol Simulations

Comsol Multiphysics is a commercial software which is able to simulate different problems in various physics fields. In our case we used this simulation tool to have predictive results on frequency, voltage and power levels of our devices before starting the fabrication process. It is also useful to countercheck the expected experimental results in order to refine the simulations and improve the whole approach for more reliable predictions. Both 2D and 3D studies were implemented in order to achieve the highest possible accuracy.

4.4.1 Simulation Framework

The first step to build successful simulation routines with this software dealing with $LiNbO_3$, is to take into account the anisotropy of the crystal. It is very important to countercheck this aspect of the simulation in order to be sure to implement the right orientation during the study. In order to do that we have two possible lines of action: to define a custom orientation for the piezoelectric layer using the Euler's angle feature, or directly define the material properties for the given single crystal cut. The latter is especially attractive because we can use the values measured during characterization as a reference and simulate then the devices with realistic values.

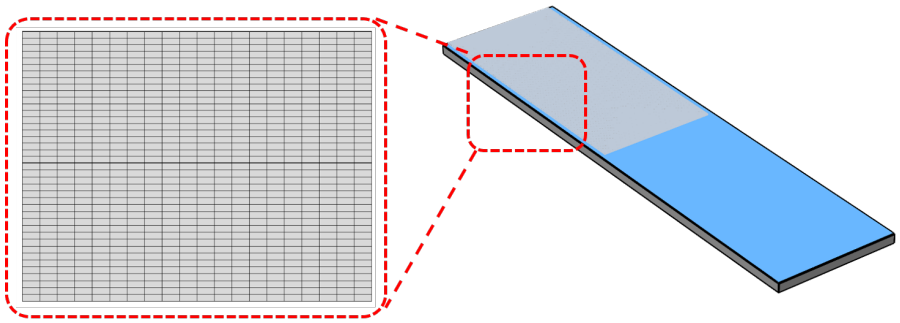

Figure 4.2: Example of mesh for a cantilevered beam in Comsol. The represented mesh corresponds to 11603 degrees of freedom.

Afterwards it is necessary to correctly define the geometry of the harvester considering the device features like thickness of each layer: substrate, piezoelectric element and electrodes. Also the tip mass has been taken into account and modeled especially for Si beam, where the fabrication route can lead to devices with good performance in terms of coupling and frequency tuning. To mesh the device, we mapped the layers with different element size in order to consider more carefully the most interesting parts of the device while keeping the computation as smart as possible. In fact the risk, especially in 3D, is to increase the numbers of elements with no effective gain in terms of accuracy.

The simulated device configurations were mostly beam structures with boundary conditions on the the clamped part of the device and electric connections for top and bottom electrodes. The load on the beam was applied uniformly taking into account the density of the materials.

Parametric sweep of thickness, length and width of the prototypes are particularly useful to optimize the frequency and voltage response of the device. Typically the studies, implemented concerning the harvester performances were regarding the eigenfrequencies of the beams and the voltage response while driven by an imposed acceleration. While for the effective coupling we have investigated the impedance response of the devices in converse mode. Similarly to the FEA model, the k^2_{eff} was calculated from the short and

open circuit frequencies. The two frequencies can be also investigated by plotting the displacement of the device in short or open circuit conditions.

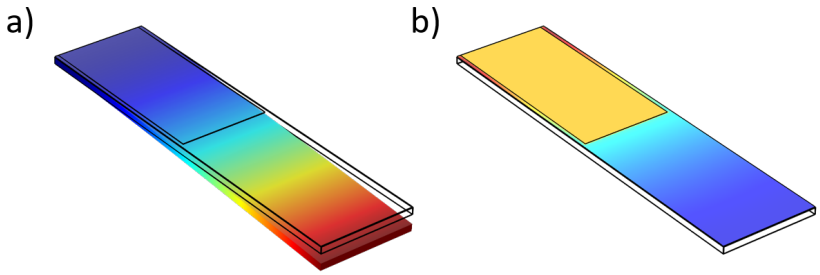

Figure 4.3: Rendering of clamped beam from Comsol: a) study of cantilever displacement; b) voltage collected from top electrode.

A very important aspect of the simulation is the quality factor (Q) or damping (ζ) imposed on the beam. Generally the relation that bonds the two quantities is given as:

$$Q = \frac{1}{2\zeta\sqrt{1-\zeta^2}} \approx \frac{1}{2\zeta} \tag{4.90}$$

In general the most used is the isotropic loss factor (η), which is proportional to the displacement and gives a quick result in terms of structural damping. Taking into account the losses of the material considering the Young modulus we will have the following relation between stress and strain:

$$T = (E' + iE'')S \tag{4.91}$$

where E' is the real part which stores the elastic energy of the material, while E'' is the imaginary part which is representing the mechanical losses. Then the isotropic loss factor will be defined as a phase shift between the applied T and S:

$$\tan\delta = \frac{E''}{E'} = \eta \tag{4.92}$$

When the considered frequency is approaching the resonance frequency, $\eta \approx 2\zeta$ which is valid for a SDOF system. Whereas for multiple resonances the difference between the two indexes is more pronounced.

Most interesting is Rayleigh damping which is defined like in our FEA model, so eventually it is possible to impose a certain quality factor for a precise frequency with the help of the parameters α and β. Anyways, due to the difficulty of finding data on damping ratio for $LiNbO_3$ structures, the best way is to impose a reasonable factor considering the damping of the substrate and then countercheck with the experiments.

4.5 Comparison of Minimalist FEA and Comsol

The design optimization started with the orientation and property study of $LiNbO_3$ films to implement in the harvesters. Particular attention was dedicated to the study of tensors and electro-mechanical coupling factor. A comparison was made using a script on Matlab dedicated to orientation study of piezoelectric tensors, and then a simulation on Comsol provided a crosscheck for the tensor values. In transverse excitation mode, the rotation of the piezoelectric tensor shows that not only d_{31} contributes to the piezoelectric response, but other coefficients as well. In order to have optimal values for the piezoelectric coefficients, we have investigated the effect of rotation of the crystal. The rotation of piezoelectric tensor around X-axis by an angle θ angle showed strong variation of piezoelectric coefficients. Therefore, the configuration that was investigated in the simulations was $LiNbO_3$ (YXl)/128° wafer cut, where we found higher d_{23} = 27 pC/N, and higher coupling factor k_{23} = 0.49. To understand the possibility of integration of $LiNbO_3$ films in the prototypes, we started our analysis of material substrate in order to achieve the highest coupling. Moreover an other interesting aspect was to match the resonance of the devices to the frequency spectrum available in cars, especially where the acceleration has maximum magnitude. Being $LiNbO_3$ the piezoelectric element for electro-mechanical conversion, particular attention must be given to the range of clamped capacitance. In our case, the goal is to stay in $10^{-1} \div 10^{1}$ nF range, therefore we implemented in the simulation films with thickness 1÷150µm, while considering the capacitance from the equation:

$$C_0 = \frac{\varepsilon_{33}^S \varepsilon_0 A}{h_p} \tag{4.93}$$

As a first step study we considered the whole surface of the piezoelectric element as the top electrode, A, afterwards we have performed a parametric study the thickness of the piezoelectric element, h_p. From the study outcomes, a reasonable range of C_0 can be obtained with a surface of 50÷500 mm^2 for a given piezoelectric element thickness. Special care has to be placed in the simulation of the electrode length, which can have an impact on the voltage and power output. This effect was simulated only in Comsol where we are not limited in the number of nodes for the structure, whether for minimal FEA full electrode length was considered.

4.5.1 Eigenfrequency Analysis

The simulation of the transducer was done with Comsol. In order to test the validity of our energy harvester, we designed a 2D unimorph cantilevered beam for eigenfrequency analysis. In the investigation we used three different materials as substrates: brass, stainless steel and silicon. All of them have different properties as density and Young's modulus (Tab. 4.1).

Table 4.1: Reference properties of substrates, used in FEA and Comsol Simulations.

Material	s_{11} ($pm^2.N^{-1}$)	ρ ($Kg.m^{-3}$)
Brass	8	8730
Silicon	5.92	2330
Stainless Steel	5	7700

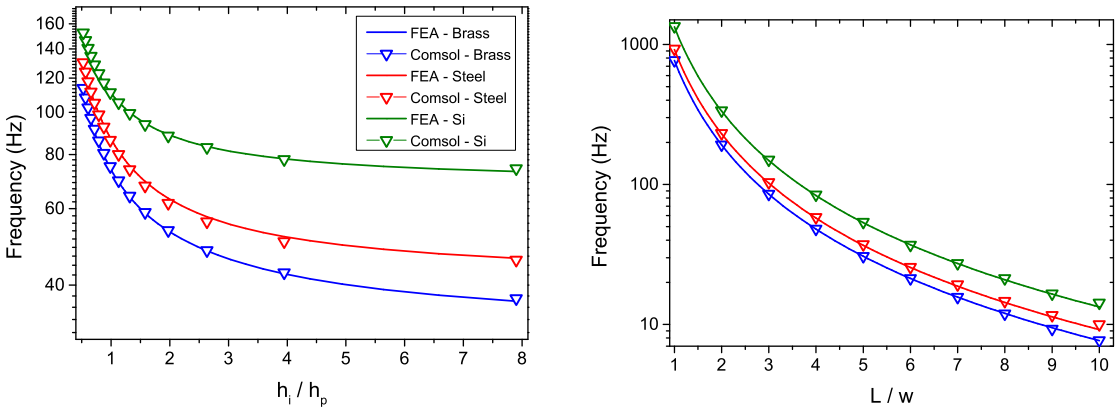

Figure 4.4: Tuning of resonance frequency as a function of the ratio: (a) $\frac{h_i}{h_p}$; (b) $\frac{L}{w}$.

The investigations were done in order to identify the resonance frequencies useful in car environment. A parametric sweep was performed to implement 2D simulations in Comsol for eigenfrequency analysis, where the resonance frequencies of the system were investigated. The parameters used in the study, were thickness of substrate and piezoelectric layer along with the length and width of the devices. The first mode (or bending mode) is especially interesting, whereas the cantilever offers maximum power output due to maximum amplitude of displacement. The study of this system by Comsol simulations and FEA model were in good agreement. Typically, the discrepancy was within 2% (Fig. 4.4). This effect of frequency shift was increasing with the value of h_p, so the modeling of the piezoelectric element require further refinements. Anyways, the good agreement is the most important aspect of a simple parametric model able to locate good ranges of design parameters in a "quick and dirty" first step.

In Fig. (4.4a), the study was done considering the ratio between the two thicknesses in open circuit conditions, obtaining low resonance frequencies whenever using a $LiNbO_3$ thick film. Metal hosting structures represent an alternative to silicon due to their flexibility and robustness. Furthermore, they can be introduced as substrates for deposition of thin films. In this case both brass and steel are achieving lower resonance frequencies compared to silicon, but the implementation of these materials in the fabrication process

are still challenging. Moreover, h_p has to be optimized in terms of coupling, and not only as a parameter to tune the resonance. However, in Fig. (4.4b) we can see that the length has a very important effect on the frequency tuning, considering mesoscale structures, already with a ratio of 3÷4, the response attains useful values (below 500 Hz). Considering the Rayleigh damping as discussed in the previous section, we have investigated the system under the same conditions. We modeled a thick $LiNbO_3$ film (60 μm) on a steel substrate to perform the investigation in the frequency domain, imposing a quality factor of 100 at the resonance frequency (ω_0=100 Hz), leading to β=1.6E-5 s and considering α=0. Afterwards, we simulated both FEA and Comsol in open circuit conditions, as showed by the results in Fig. (4.5). The resonance frequency is shifted in the case of Comsol by 1%, while the voltage (φ_h) is decreased by 2.3%. The reason could be that the coefficients are slightly different for the considered orientation of $LiNbO_3$, and this leads to a small discrepancy in terms of voltage magnitude.

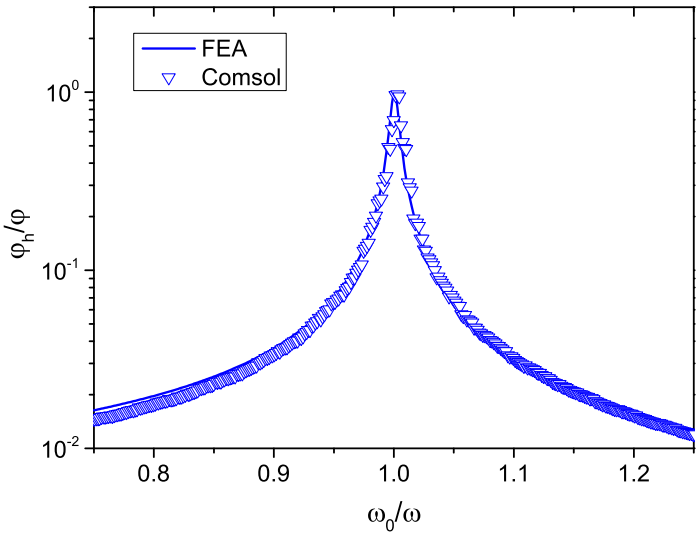

Figure 4.5: Normalized voltage response as a function of normalized frequency with Rayleigh damping approximation (β = 1.6E-5 s).

4.5.2 Electro-Mechanical Coupling Analysis

It is also interesting to investigate the electro-mechanical coupling of the harvesters by performing a parametric study of the geometry. The setup for the simulation was the same as in the previous section, but this time we have considered both the short and open circuit resonance of the beam. The width and length aspect ratio was chosen according to the previous section, namely fixed to 10 mm and 40 mm, respectively. The impact of the piezoelectric element thickness on the coupling of the structure depends on the substrate. The first approach, in Comsol simulations, is to tune the loss factor of the system considering different substrates. In Fig. (4.6a) the transducer impedance response of a $LiNbO_3$ on steel structure with $\frac{h_i}{h_p} \approx 1$ has been investigated. We can see that if η increases, quality factor of the system increases as well.

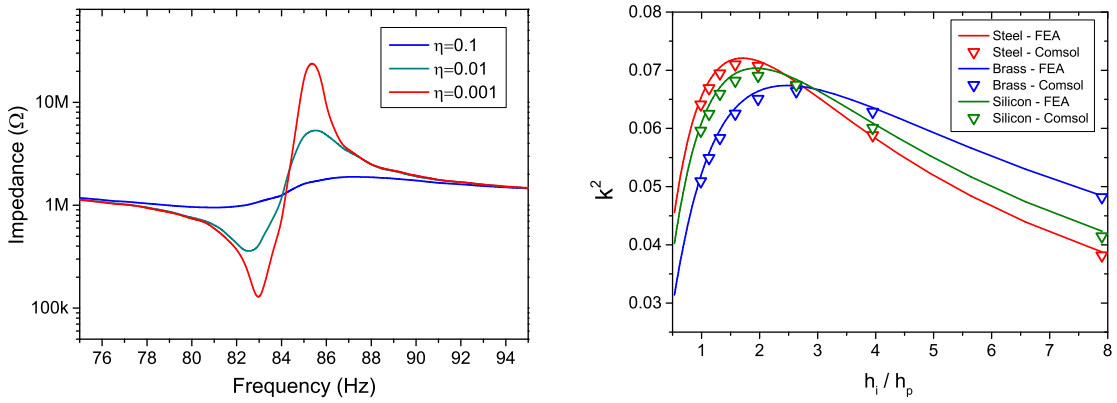

Figure 4.6: Simulation of electro-mechanical coupling: (a) impedance as a function the loss factor η*; (b) calculated* k^2 *as a function of ratio* $\frac{h_i}{h_p}$ *for different substrate.*

Eventually, we have considered the value $\eta = 0.01$ that is a reasonable compromise for $LiNbO_3$ structures, and represents a straightforward approach when dealing with several different eigenfrequency modes. Moreover, around this value the short and open circuit frequencies do not undergo a substantial shift. Once the parameters are set, we can study the k^2 changing substrate materials. For instance, in Fig. (4.6b),a comparison between the FEA model and Comsol is given. As in the case of the eigen-frequency analysis the discrepancy between the models is within 2% under the same thickness ratio. The conclusion is that with substrates which are less stiff (like brass), $LiNbO_3$ has to be thicker as compared to stiffer substrates (steel or silicon). From the study, we conclude that the achievable k^2 with a $LiNbO_3$ simple beam is comparable to PZT material coupling, typically around 5÷7% [10]. Another way to increase the coupling is the use of a tip mass, which was studied mostly by simulations in Comsol, even though the rotation of the mass can be implemented in our FEA model. Anyways, the implementation of large tip mass was already studied for silicon substrates, and is easily achievable experimentally using DRIE etching [11]. Unfortunately, the structure are very fragile, therefore it is used mostly for MEMS scale devices rather than mesoscale ones, where metal substrates are used with heavy magnetic or tungsten tip masses [12].

4.6 Lumped Model

The single degree of freedom (SDOF) model or lumped model, was mostly considered during characterization and electronic interfacing of the prototypes. In a phenomenological approach we have used the identifications from the equivalent circuit to extrapolate results concerning the coupling and quality factor, and then interpreting the outcomes to configure the optimized electronic interface. Moreover, the identifications of the force factor and the lumped model parameters have allowed to predict effectively the power

level of the harvesters.

4.6.1 Equivalent Circuit for Inertial Harvester

When considering a high-level analysis of the system, the piezoelectric device can be modeled as a SDOF oscillator resonating near one of its resonance frequencies [13]. Consequently, the structure can be modeled as a spring-mass-damper system dynamically excited by an external force (or equivalently an acceleration), and generating a voltage, V from the deformation displacement, x. In Fig. (4.7), we depict the two completely equivalent interpretations of the energy harvester. A mechanical interpretation of the system is given in Fig. (4.7a), while in Fig. (4.7b) we have an equivalent circuit composed of the mechanical branch, the electrical branch, and finally the transformer connecting the two of them.

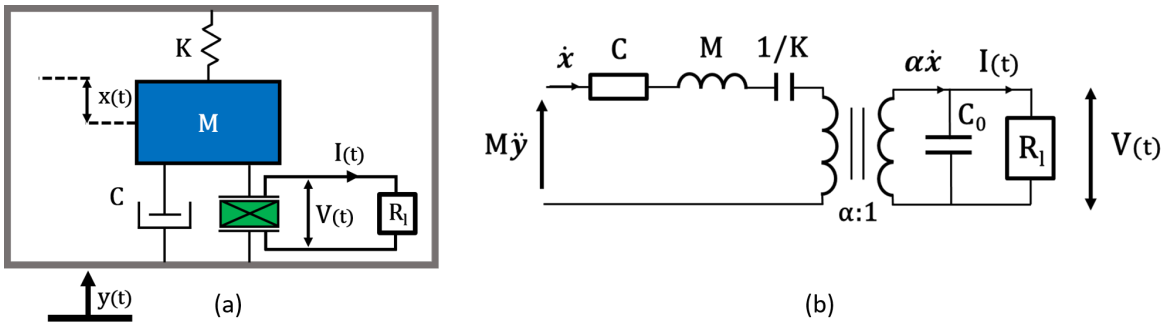

Figure 4.7: Schematics representations of inertial energy harvester connected to a resistive load: a) inertial harvester; b) equivalent circuit.

The system can then be described by the following set of dynamic equations:

$$\begin{cases} \mathrm{M}\ddot{y} = \mathrm{M}\ddot{x} + \mathrm{C}\dot{x} + \mathrm{K}x + \alpha \mathrm{V} \\ \mathrm{I} = \alpha\dot{x} - \mathrm{C}_0\dot{\mathrm{V}} \end{cases} \tag{4.94}$$

where F is the external force, K the open-circuit stiffness of the system, M the dynamic mass, α is the electromechanical force factor, I the current, C the viscous damping and C_0 the clamped capacitance. The electromechanical equivalent circuit for the piezoelectric transducer is presented in Fig. (4.7b), in which the coupling term is represented by a transformer. The external force applied on the mechanical branch of the circuit generates a base velocity, $\dot{x}$, that is equivalent to a current in the electrical model, then the transformer with α ratio is converting the mechanical velocity into current in the electrical branch of the circuit. In particular, when the piezoelectric element is in open circuit condition, we can find that the force factor is:

$$\alpha = \frac{\mathrm{C}_0 \mathrm{V}_{oc}}{x_{\mathrm{M}}} \tag{4.95}$$

where x_{M} represents the peak magnitude of the displacement, and V_{oc} the open circuit voltage. Now we can rewrite Eq. (4.94) in function of the current in the following way:

$$\frac{\mathrm{M}\ddot{y}}{\alpha} = \frac{\mathrm{M}}{\alpha^2}\frac{d}{dt}(-\alpha\dot{x}) + \frac{\mathrm{C}}{\alpha^2}(-\alpha\dot{x}) + \frac{\mathrm{K}}{\alpha^2}\int(-\alpha\dot{x})\,dt + \mathrm{V}$$

Then we can define $\mathrm{V}_{eq} = \frac{\mathrm{M}\ddot{y}}{\alpha}$ and $\mathrm{I}_{eq} = -\alpha\dot{x}$, getting to the equivalent system of equations:

$$\begin{cases} \mathrm{V}_{eq} = \mathrm{L}_m\dot{\mathrm{I}} + \mathrm{R}_m\mathrm{I} + \dfrac{\mathrm{Q}}{\mathrm{C}_m} + \mathrm{V} \\ \mathrm{I}_{eq} = \mathrm{I} + \mathrm{C}_0\dot{\mathrm{V}} \end{cases} \tag{4.96}$$

From this system, the following identifications are given between the mechanical branch elements (L_m,R_m and C_m) of the equivalent circuit:

$$\begin{aligned} \mathrm{L}_m &= \frac{\mathrm{M}}{\alpha^2} \\ \mathrm{R}_m &= \frac{\mathrm{C}}{\alpha^2} \\ \mathrm{C}_m &= \frac{\alpha^2}{\mathrm{K}} \end{aligned} \quad . \tag{4.97}$$

The two formulations are totally equivalent, but the identifications are useful to link the measurements from impedance analyzer to the energy harvesting ones.

Finally, we can calculate the electro-mechanical coupling factor for the structure, k^2, defined as:

$$k^2 = \frac{\alpha^2}{\mathrm{C}_0\mathrm{K} + \alpha^2} \tag{4.98}$$

which represents the effective coupling of the structure during the energy conversion process. Furthermore, the quality factor of the structure can be found as:

$$\mathrm{Q} = \frac{\sqrt{\mathrm{MK}}}{\mathrm{C}} \tag{4.99}$$

and as already seen in Eq. (4.90), the damping ratio from mechanical losses ζ as:

$$\zeta = \frac{1}{2\mathrm{Q}}$$

Some issues regarding the lumped parameter model can lead to inaccurate predictions close to resonance frequency. This is especially noticeable if the proof mass has same value as the beam mass, in this case we need to introduce a correction factor [14]. Especially for cantilevers with no tip mass, a large error occurs at resonance. Anyways, the power varies according to the mass and usually in harvester architectures large masses are

used, and lumped model provides fairly accurate results in this case. To solve this issues Erturk and Inman proposed an alternative model which is using Euler-Bernoulli beam theory for giving more accurate results [2].

4.7 Impedance Matching

Now that we have described the SDOF system, we know that the voltage output of the piezoelectric element is an AC sinusoidal signal, hence we need a rectification circuit in order to convert it to continuous DC signal, useful to power up sensors or store it in a battery or super-capacitor. In the energy balance approach [13], the equations (4.94), are multiplied by the velocity and the voltage, respectively, and they are integrated over a half-period of time (from t_0 to t_1). The result is given as:

$$\int_{t_0}^{t_1} \mathrm{M}\ddot{y}\dot{x}dt = \int_{t_0}^{t_1} \mathrm{M}\ddot{x}\dot{x}dt + \int_{t_0}^{t_1} \mathrm{C}\dot{x}\dot{x}dt + \int_{t_0}^{t_1} \mathrm{K_E}x\dot{x}dt + \int_{t_0}^{t_1} \alpha \mathrm{V}\dot{x}dt \tag{4.100}$$

Eq. (4.100) gives us a full description of the energies in the system: kinetic energy, mechanical losses, potential elastic energy, and transferred energy.

4.7.1 Instantaneous Power

Now we can consider the power output of the harvester and its most simple electronic configuration. For a low coupled transducer ($\alpha << 0$), we approximate the harvester to a current generator and capacitor $\mathrm{C_0}$, which are representing the electrical branch of the equivalent circuit, connected to a resistive load where the power is dissipated. The schematic representation is depicted as in Fig. (4.8).

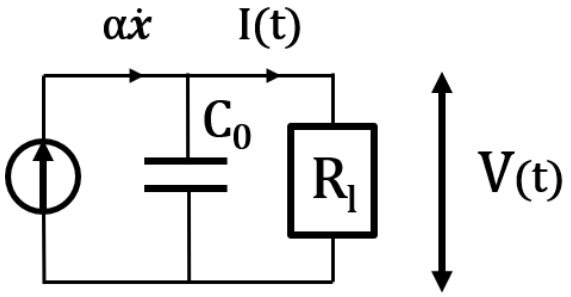

Figure 4.8: Low coupled harvester approximation with resistive load.

In a permanent harmonic regime, the current is described by:

$$\mathrm{I} = j\omega\alpha x - j\omega \mathrm{C_0 V} \tag{4.101}$$

knowing that $\mathrm{I} = \frac{\mathrm{V}}{\mathrm{R}_l}$, and considering the impedance for V, we obtain:

$$\mathrm{V} = \frac{j\omega \mathrm{R}_l \alpha}{1 + j\omega \mathrm{R}_l \mathrm{C_0}} x \tag{4.102}$$

Considering that $P = \frac{VV^*}{2R_l}$, finally the power output of the harvester is:

$$P = \frac{1}{2}\frac{R_l\omega^2\alpha^2}{1+(\omega R_l C_0)^2}x_M^2 \tag{4.103}$$

where we can find the maximum power point, which is:

$$P_{max} = \frac{1}{4}\frac{\alpha^2}{C_0}\omega x_M^2 \tag{4.104}$$

for the optimal impedance matching found at $R_{opt} = \frac{1}{C_0\omega}$.

We can also rewrite the power as a function of the force in the frequency domain. Under the hypothesis that the force F and the velocity $\dot{x}$ are in phase, one can find that:

$$F = \left[C + \frac{\alpha^2 R_l}{1+(j\omega R_l C_0)^2}\right] j\omega x \tag{4.105}$$

and finally the instantaneous power for low coupled harvesters is:

$$P = \frac{F_M^2}{2C^2}\frac{R_l\alpha^2}{1+(\omega R_l C_0)^2} \tag{4.106}$$

which has the following maximum value:

$$P_{max} = \frac{F_M^2}{C^2}\frac{\alpha^2}{4\omega C_0} \tag{4.107}$$

This is the power dissipated in the resistive load by the harvester, but it doesn't give us a full description of the capabilities to charge a battery or a capacitor in order to use the energy whenever is needed. Moreover, here the capacitance has a fundamental role, because the optimal load is inversely proportional to C_0 and the frequency of excitation, making the impedance matching very important during the design of the harvester. If the

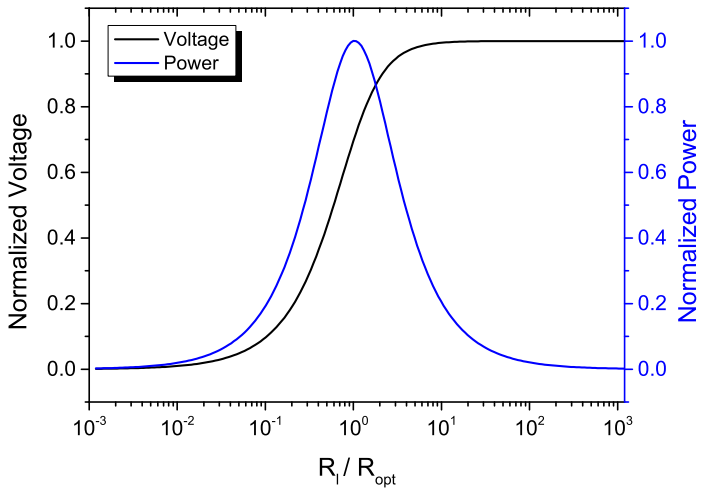

Figure 4.9: Normalized power and voltage for optimal impedance matching conditions of low coupled harvester with resistive load.

optimal load is too high, the impedance matching with the electronic interface presents serious issues, so we recommend to keep the value of R_{opt} in a reasonable range, from kΩ to few MΩ.

Very often, harvesters are designed without considering the capabilities of the device to charge a capacitor and successfully convert the AC voltage in DC. For this reason a compromise has to be reached during the implementation of the transducer in terms of capacitance.

4.7.2 Full-Bridge Rectifier

As discussed, the power of the system in Eq. (4.107) represents the instantaneous power of the system in AC conditions. In order to rectify the voltage of the harvester, we could use a standard electronic interface, for instance a full-bridge rectifier (Fig. 4.10. In this case we have 4 rectifying diodes and a smoothing capacitor C_r which is connected in parallel to the resistive load. Let us go back to system (Eq.4.100), considering transferred energy, we can write it explicitly as the sum of the electrostatic energy stored in the transducer and energy used by the load:

$$\int_{t_0}^{t_1} VI dt = \int_{t_0}^{t_1} V\alpha\dot{x} dt - \int_{t_0}^{t_1} VC_0\dot{V} \tag{4.108}$$

From Eq (4.108) we can integrate over two values of time (t_0 and t_1), as in Fig. 4.11, to obtain the value of the V_{DC}:

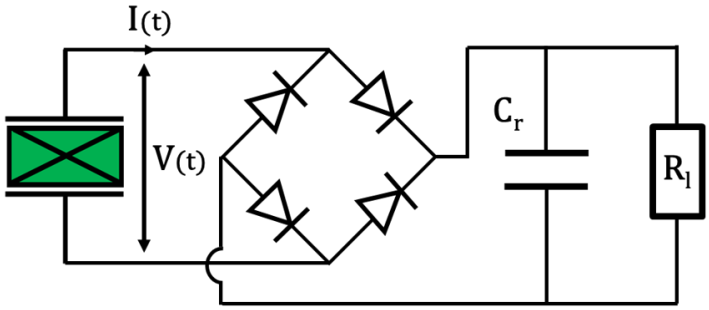

Figure 4.10: Schematic representation of standard rectification circuit: full bridge rectifier with smoothing capacitor C_r and resistive load R_l.

$$\int_{t_0}^{t_1} I dt = \frac{T}{2}\frac{V_{DC}}{R} \tag{4.109}$$

which is giving:

$$-2\alpha x_M + 2C_0 V_{DC} = \frac{T}{2}\frac{V_{DC}}{R} \tag{4.110}$$

and finally the voltage expression is:

$$V = \frac{\omega R_l \alpha}{\frac{\pi}{2} + \omega R_l C_0} x_M \tag{4.111}$$

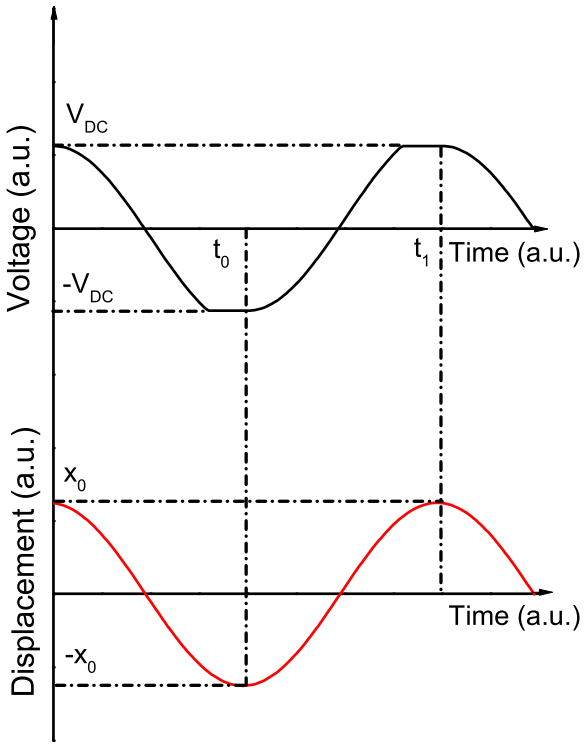

Figure 4.11: Voltage and displacement as a function of time for full bridge rectifier.

Eventually the power on dissipated on the load is $P = \frac{V_{DC}^2}{R_l}$:

$$P = \frac{\omega^2 \alpha^2 R_l}{\left(\frac{\pi}{2} + \omega C_0 R_l\right)^2} x_M \tag{4.112}$$

This expression gives the power in terms of the displacement magnitude, x_M, but it can be defined also in terms of the excitation force, F_M, for a weakly coupled harvester:

$$P = \frac{\alpha^2 R_l}{\left(\frac{\pi}{2} + \omega C_0 R_l\right)^2} \frac{F_M^2}{C^2} \tag{4.113}$$

In this case, it has a different optimal load and power:

$$R_{opt} = \frac{\pi}{2 C_0 \omega} \tag{4.114}$$

$$P_{max} = \frac{\alpha^2}{2\pi C_0 \omega} \frac{F_M^2}{C^2} \tag{4.115}$$

4.7.3 Highly Coupled Harvester

A different situation arises if the force factor, α, is not negligible, for the so called highly coupled harvesters. Full description of this systems is given by Shu [15]. If the system is highly coupled we have to take into account the damping imposed from the electrical interface. Starting our analysis from the energy balance, we can also consider that the force and the velocity are not in phase, hence:

$$x(t) = x_{\mathrm{M}} \sin(\omega t - \theta) \tag{4.116}$$

After taking into account the energy balance equations, and integrating them, we obtain the following expression of the force:

$$\frac{\pi}{2} \mathrm{F_M} x_{\mathrm{M}} \sin\theta = \frac{\pi}{2} \mathrm{C}\omega x_{\mathrm{M}}^2 + \frac{\pi}{\omega} \frac{\mathrm{VDC}^2}{\mathrm{R}_l} \tag{4.117}$$

$$\mathrm{F_M} \cos\theta = \left[\mathrm{K} - \mathrm{M}\omega^2 + \frac{\alpha^2}{\mathrm{C}_0} \right] x_{\mathrm{M}} - \frac{\pi\alpha}{2\mathrm{C}_0\omega\mathrm{R}_l} \mathrm{V_{DC}} \tag{4.118}$$

Combining both Eq. (4.117) and Eq. (4.118) and rewriting the displacement in terms of the force, we obtain:

$$x_{\mathrm{M}} = \frac{\mathrm{F_M}}{\left[\left(\mathrm{C}\omega + \frac{2\omega\alpha^2\mathrm{R}_l}{(\mathrm{C}_0\omega\mathrm{R}_l + \frac{\pi}{2})^2} \right)^2 + \left(\mathrm{K} - \omega^2\mathrm{M} + \frac{\omega\alpha^2\mathrm{R}_l}{\mathrm{C}_0\omega\mathrm{R}_l + \frac{\pi}{2}} \right)^2 \right]^{\frac{1}{2}}} \tag{4.119}$$

For the damped result we can substitute Eq. 4.119 in Eq. 4.111 and obtain the following power equation:

$$\mathrm{P} = \frac{\omega^2\alpha^2\mathrm{R}_l}{\left(\frac{\pi}{2} + \omega\mathrm{C}_0\mathrm{R}_l\right)^2} \frac{\mathrm{F_M}}{\left[\left(\mathrm{C}\omega + \frac{2\omega\alpha^2\mathrm{R}_l}{(\mathrm{C}_0\omega\mathrm{R}_l + \frac{\pi}{2})^2} \right)^2 + \left(\mathrm{K} - \omega^2\mathrm{M} + \frac{\omega\alpha^2\mathrm{R}_l}{\mathrm{C}_0\omega\mathrm{R}_l + \frac{\pi}{2}} \right)^2 \right]^{\frac{1}{2}}} \tag{4.120}$$

In order to distinguish low and highly coupled harvesters, we can use the product of $k^2\mathrm{Q}$, and its value can give an idea of the device behavior. For this analysis we will use some notation to keep the results more readable: $\Omega = \frac{\omega_0}{\omega}$ and $r = \mathrm{C}_0\omega\mathrm{R}_l$. Then the resistive loads in short and open conditions are:

$$\Omega_{sc} = 1 \tag{4.121}$$

$$\Omega_{oc} = \sqrt{1 + k^2} \tag{4.122}$$

Respectively the two load optimal conditions are found as:

$$r_{sc}^{opt} \approx \left(\frac{\pi^2}{\sqrt{16 + \pi^2}} \right) \frac{1}{k^2 2\mathrm{Q}} \tag{4.123}$$

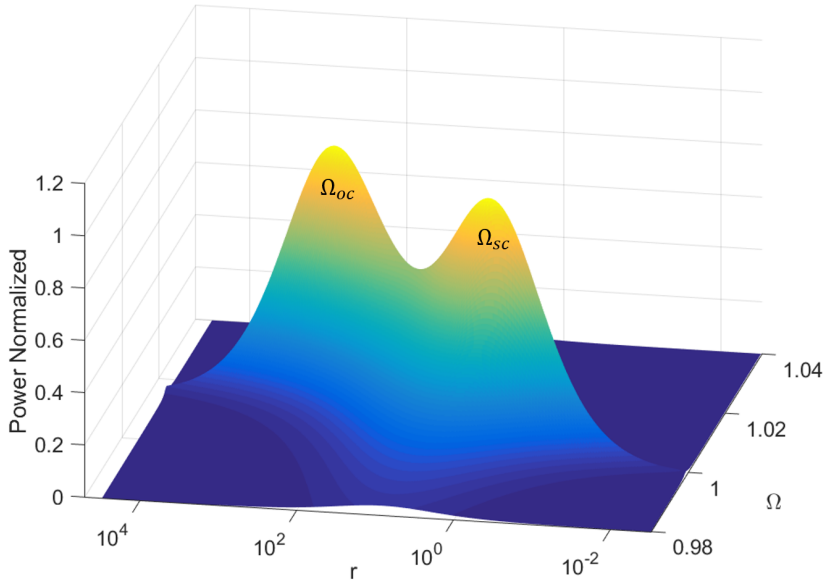

Figure 4.12: Double identical power peaks for highly coupled harvester.

$$r_{oc}^{opt} \approx \frac{\sqrt{16+\pi^2}}{4} \frac{k^2 2Q}{1+k^2} \tag{4.124}$$

The optimal power for both circuit conditions is identical:

$$P_{sc-oc} \approx \frac{F_0^2 2Q}{\omega_0 M} \frac{1}{8+2\sqrt{16+\pi^2}} \tag{4.125}$$

Highly coupled devices have two identical power peaks at different resistive loads and frequencies (Fig. 4.12), which can be used to enhance the frequency bandwidth of the harvester. Moreover, we observe that in this case, the power output is limited mostly by the damping or the quality factor of the structure, while for low coupled systems the device is limited mostly by the coupling.

4.8 Conclusion

With the orientation study it was possible to investigate and optimize the tensor values and the electro-mechanical coupling of $LiNbO_3$, identifying (YXl)/128° as the best choice. Starting form these results, our FEA model can be a starting point to investigate electro-mechanical systems like harvesters or actuators. With a single element it is possible to describe the behavior of a simple cantilever beam, introducing structural and electrical damping and obtaining useful system parameters. Later, with a commercial software like Comsol Multiphysics, we can implement refined simulations for the cantilevers. In this chapter we compared the frequency response and electro-mechanical response of such structures, showing that is possible to tune the system using either a silicon or metallic substrates, achieving the requested performances. Finally, we presented the lumped model, which can be used as an additional analysis method, especially during

electronic configuration. Moreover, with this formalism we can take into account both low and highly coupled harvesters, in order to optimize the impedance matching. Using the modal mass and stiffness, along with k^2 provided by minimal FEA, the computed parameters can easily be passed to the parametric analysis. Moreover, Comsol provides the necessary tools to compute modal mass and stiffness together with k^2. Then, the complete path from continuous multiphysics equations to lumped parameters parametric system analysis and electrical exploitation is smoothly ran over.

Bibliography

[1] N. E. DuToit, B. L. Wardle, and S. Kim, "Integrated Ferroelectrics : An MEMS-scale Piezoelectric Mechanical Vibration Energy Havesters," *Taylor & Francis*, no. November 2012, pp. 121–160, 2006.

[2] A. Erturk, *Electromechanical Modeling of Piezoelectric Energy Harvesters*. PhD thesis, 2009.

[3] J. Maisonnet and B. Dulmet, "Integrated finite element analysis of an electrostatically-driven vibrating beam used as a gyrosensor," *Proceedings - IEEE Ultrasonics Symposium*, vol. 0, no. 1, pp. 1–4, 2009.

[4] C. Zener, "Internal friction in solids I Theory of internal friction in reeds," *Physical Review*, vol. 52, pp. 230–235, 1937.

[5] C. Zener, "Internal friction in solids II General theory of thermoelastic internal friction," *Physical Review*, vol. 53, pp. 90–99, 1938.

[6] L. D. Landau and E. Lifshitz, *Theory of elasticity*. Oxford: Pergamon Press, 1959.

[7] R. Lifshitz and L. R. Roukes, "Thermoelastic dampling in micro- and nanomechanical systems," *Physical Review B*, vol. 61, no. 8, pp. 5600–5609, 2000.

[8] A. E. Duwel, R. N. Candler, T. W. Kenny, and M. Varghese, "Engineering MEMS Resonators with Low Thermoelastic Damping," *IEEE JMEMS*, vol. 15, no. 6, pp. 1437 – 1445, 2006.

[9] J. A. Lewis, "The effect of driving electrode shape on the electrical properties of piezoelectric crystals," *Bell System Technical Journal*, vol. 40, no. 5, pp. 1259–1280, 1961.

[10] Q. M. Wang, X. H. Du, B. Xu, and L. Eric Cross, "Electromechanical coupling and output efficiency of piezoelectric bending actuators," *IEEE Transactions on Ultrasonics, Ferroelectrics, and Frequency Control*, vol. 46, no. 3, pp. 638–646, 1999.

[11] M. Marzencki, *Conception de microgénérateurs intégrés pour systèmes sur puce autonomes*. PhD thesis, 2007.

[12] S. Roundy, *Energy scavenging for wireless sensor nodes with a focus on rotation to electricity conversion*. PhD thesis, 2007.

[13] D. Guyomar, A. Badel, E. Lefeuvre, and C. Richard, "Toward energy harvesting using active materials and conversion improvement by nonlinear processing," *IEEE Transactions on Ultrasonics, Ferroelectrics, and Frequency Control*, vol. 52, no. 4, pp. 584–594, 2005.

[14] A. Erturk and D. J. Inman, “Issues in mathematical modeling of piezoelectric energy harvesters,” *Smart Materials and Structures*, vol. 17, no. 6, 2008.

[15] Y. C. Shu and I. C. Lien, “Analysis of power output for piezoelectric energy harvesting systems,” *Smart Materials and Structures*, vol. 15, no. 6, pp. 1499–1512, 2006.

5 Lithium Niobate Energy Harvesters

In this chapter I will introduce the results concerning the harvesting performances of our prototypes. Three sections of the chapter are presenting the results concerning modeling and characterization of $LiNbO_3$ energy harvesters. Two of these sections are dealing with $LiNbO_3$ on silicon transducers, while the last one concerns devices with metal substrates. Even if they present different features, the results are in the state of the art, both in terms of performances and quality of the final prototypes. Their implementation is accompanied by an electronic optimized configuration.

5.1 Introduction

In this Chapter, we experimentally demonstrate that, with a suitable micro-fabrication process, we have successfully implemented vibrational energy harvesters based on thick (10 µm to 120 µm) single-crystal $LiNbO_3$ films bonded on Si and metal substrates. The capacitance, electro-mechanical coupling and power density were studied analytically and designed with respect to the target application, while resonant frequencies, voltage and displacement response of studied structures were simulated by Finite Element Method. Hence, the potentials of $LiNbO_3$ piezoelectric films for EH are confirmed, showing comparable and even higher power densities than conventional Pb-based and Pb-free energy harvesters.

The lack of a standard geometry or design to compare performances of piezoelectric vibrational energy harvesters, leads researchers to compare the results of their investigations in terms of areal or volumetric power densities. In order to compare our devices with the state of the art, we extensively used areal normalized power density ($\mu W/cm^2/g^2/Hz$), which is usually employed whenever we make a comparison of materials performances. Anyways, the volumetric power density ($\mu W/cm^3/g^2/Hz$) is presented to compare different generation of $LiNbO_3$ harvesters. The detailed fabrication flowcharts are discussed in Chapter 2.

5.2 High Frequency Harvesters on Silicon

Lead-free $LiNbO_3$ piezoelectric transducer is considered as a substitute to lead-based solutions for vibrational energy scavenging applications. Taking into account the much lower dielectric constant of $LiNbO_3$ crystal compared to conventional piezoceramics (for instance PZT), we implement, in a global optimization approach, a thick single crystal film on silicon substrate with optimized clamped capacitance for better impedance matching conditions. We have designed a piezoelectric cantilever based on (YXl)/36° $LiNbO_3$ cut, enhancing the output voltage to achieve piezoelectric transducer performance compatible with harvesting device standards.

5.2.1 Simulations

In this section, I will discuss how to tailor the material electro-mechanical coupling factor in order to have realistic impedance–matching between the piezoelectric transducer and the electronic interface, while for the structural coupling we will present the value measured for our given device. To achieve some predictive results concerning the voltage output and the displacement response of our system, finite element modeling (FEM) was carried out with Comsol Multiphysics software in different dynamic conditions. We modeled the structure in 3D as a unimorph bender with silicon substrate and $LiNbO_3$ as piezoelectric element. Euler angles were used to implement the oriented cut. Resonant frequency, vibrational modes and material properties were simulated thereafter by FEM. In particular, the material properties of (YXl)/36° $LiNbO_3$ cut, were simulated with both FEM software and analytical model. In the case of a rotation of 36° around X-axis, the relative unconstrained permittivity, $\varepsilon'_r/\varepsilon_0$, is 65.3, and the effective piezoelectric coefficient d'_{23}, is -18.1 pC/N [1].

For dynamic modeling, we have used the same 3D model and proceeded to simulate the voltage response and displacement of the structure, based on the proposed design. The investigations were done at different acceleration levels in order to have a reference and to counter-check the cantilever response and the expected results. In Fig. (5.1) the results of the simulations are shown, with the acceleration levels ranging from 0.1 g to 3.6 g. The study was performed in the frequency domain, considering the bending resonance frequency of 1.163 kHz, and studying the displacement and voltage response in open circuit conditions. The peak displacement, taking as a reference the free–end edge of the cantilever, is plotted for each considered acceleration. The low entity of the tip displacement is the result of the silicon substrate stiffness, which was modeled considering Si (100) orientation. The displacement was measured approximately around the free end of the cantilever, so that the simulated value reached a maximum of 26.4 µm. On the right-hand side of Fig. (5.1), the voltage response is presented. In this case, considering the piezoelectric coupling given by $LiNbO_3$ (YXl)/36° orientation, the simulated peak voltage is reaching a maximum value of 23.9 V. Also, at lower acceleration levels (1 g), the

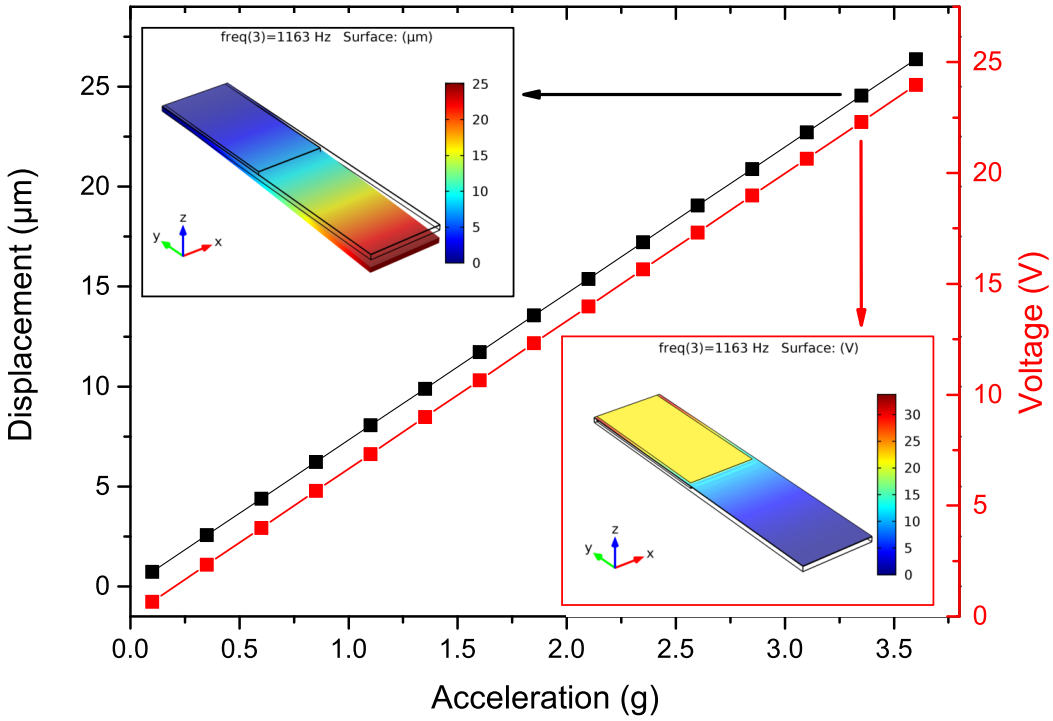

Figure 5.1: Displacement and peak voltage results from FEM simulation at different acceleration levels. (insets) Deformation and voltage response of cantilever at resonance for 3.4 g.

voltage response is in a useful range of values, with the peak voltage around 6.4 V. The results are given using the isotropic loss–factor approximation for the structure. As expected for a simple cantilever, both displacement and voltage are evolving linearly when increasing the acceleration levels. The 3D insets in Fig. (5.1) are representing the response at the simulated resonance frequency for the structure at 3.4 g, in order to compare with the experimental results.

Typically, the output voltage from a piezoelectric generator is sinusoidal, whereas in order to power a sensor node, a DC voltage supply is needed. Hence, the rectification circuit designed for our prototype is a half-bridge rectifier (Fig. 5.2). In this configuration we have used two diodes and two smoothing capacitors C_r connected to an equivalent resistive load R_l. This interface can rectify and double the voltage amplitude degraded by the threshold voltage of the diodes. Eventually, V_{DC} generated at resonance frequency f_0, can be expressed as a function of the displacement magnitude x_M as:

$$V_{DC} = \frac{2\alpha f_0 R_l}{f_0 R_l C_0 + 1} x_M \tag{5.1}$$

The harvested power from the rectified V_{DC} voltage, is simply $P = \frac{V_{DC}^2}{R_l}$, giving the following equation:

$$P = \frac{4\alpha^2 f_0^2 R_l}{\left(f_0 R_l C_0 + 1\right)^2} x_M^2 \tag{5.2}$$

In the experimental section, more details will be given regarding the electronic interface, along with a comparison between the theoretical and experimental harvested power.

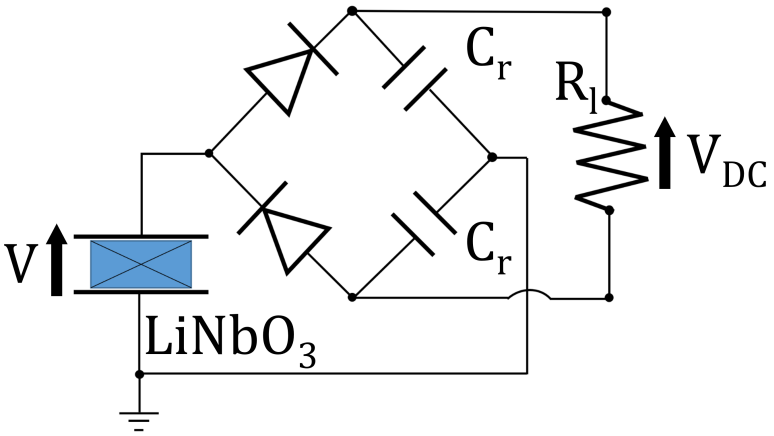

Figure 5.2: $LiNbO_3$ generator connected to voltage doubler circuit and resistive load R_l.

5.2.2 Experimental Result and Discussion

The dimensions of the cantilevers, without considering the clamping, were 20 mm in length and 5 mm in width. The electrode was partially covering the structure, resulting in an active surface of 46 mm^2. The Cr/Au layer used for wafer bonding was also acting as bottom electrode of the device. We show the cross-section of the cantilever in Fig. (5.3a). The cross-section image was taken with optical microscope, we could clearly see the Cr/Au bottom electrode, while the upper layer was $LiNbO_3$ and the bottom one the Si/SiO_2 substrate. Finally, Fig. (5.3b) presents the cantilever after dicing with Al top electrode.

During tests, the piezoelectric beam was clamped on a 3D-printed sample holder, while the top and bottom electrodes were put on a PCB board for the connection to the energy extraction circuit as well as monitoring the voltage output. The samples were characterized with a HP4194A network analyzer in order to investigate the capacitance and electro-mechanical coupling of the fabricated cantilevers. The structural electro-mechanical coupling factor, k^2, and the quality factor, Q, were estimated from measured resonance and anti-resonance frequencies [2]. The dynamic characterization of voltage response and displacement was carried out separately. The associated experimental setup was composed of a shaker providing a base excitation, controlled by a waveform generator and a power amplifier. An oscilloscope was used for monitoring the voltage output of the piezoelectric sample through a high impedance probe (Fig. 5.4a). As previously mentioned, the thickness of the piezoelectric transducer has to be adjusted in or-

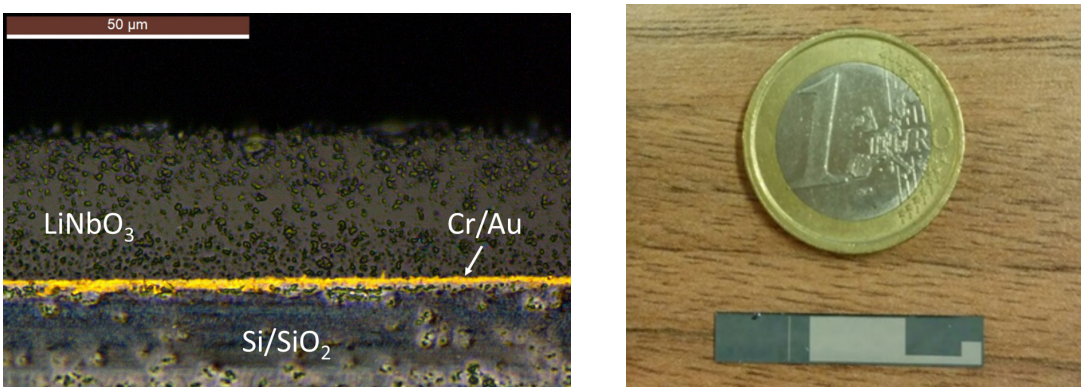

(a) *(b)*

Figure 5.3: (YXl)/36° $LiNbO_3$ /Cr/Au/Cr/SiO_2/Si harvester: (e) optical microscope cross-section image of the layered structure after dicing; (f) mechanically diced cantilever with an active surface of 46 mm^2.

der to attain minimum necessary capacitance (*nF* order of magnitude) to ensure realistic impedance matching conditions. The dependence of clamped capacitance on the thickness of the lithium niobate layer with active surface area of 46 mm^2 is presented in Fig. (5.4b). The $LiNbO_3$ thickness of about 32 µm was selected for the experimentally studied structure as a trade-off between voltage magnitude, capacitance value, impedance matching conditions and structural (global) electro-mechanical coupling coefficient (i.e., taking into account the Si layer). The clamped capacitance, C_0, of (YXl)/36° $LiNbO_3$ layer measured through an impedance analyzer was 0.79 nF (at 2 kHz), which was very close to the expected simulated value (0.83 nF). The frequency dependence of impedance modulus of the 32 µm thick piezoelectric (YXl)/36° $LiNbO_3$ crystal orientation in free conditions is presented in the inset of Fig. (5.4b). According to the equivalent lumped circuit, the structural coupling k^2 of the structure was equal to 0.013. The *Q*–factor of the complete device, including the clamping system, estimated from the experimental data, was 23. This parameter can be improved changing the clamping system by means of thicker and heavier materials, which can lower the energy dissipation during the vibration cycles at the cost of size and weight.

Table 5.1: Comparison of measured and simulated parameters for $LiNbO_3$ cantilever beam at 3.4 g.

Parameters	f_0 (Hz)	x_p (µm)	C_0 (nF)	V_{rms} (V)
Measured	1140	21.2	0.79	14.9
FEM	1163	24.5	0.83	15.8

The displacement and resonance frequency of the cantilevered (YXl)/36° $LiNbO_3$ /Si

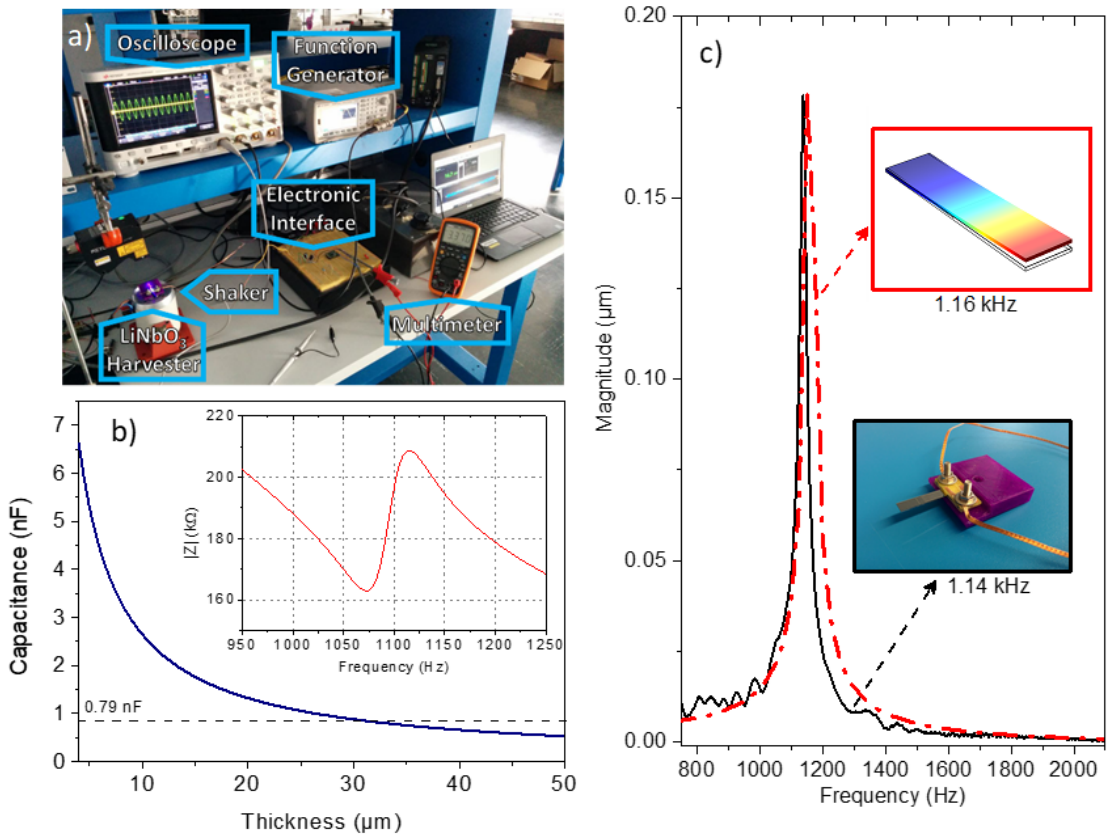

Figure 5.4: (a) Photograph of setup for dynamic measurements testing in INSA - Lyon. (b) Thickness dependence of parallel plate capacitor based on (YXl)/36° $LiNbO_3$ with active area of 46 mm^2 (b, inset) and frequency response of impedance modulus. (c) Displacement predicted by FEM simulation and measured experimentally by using optical vibrometer, of the studied (32 µm) (YXl)/36° $LiNbO_3$ /Au/SiO_2/(360 µm)Si heterostructure. (c, inset) The simulated cantilever deformation (increases from blue to red) and the photograph of the experimentally fabricated transducer are given in the inset.

beam tip were measured by means of an optical vibrometer (Polytec MSA-500). For this purpose, the beam was driven with a periodic, slowly varying chirp focused around the first resonance bending mode. The mechanical response of the cantilever as a function of frequency is given in Fig. (5.4c). The measured resonance frequency value f_0 was 1.14 kHz. Finite element simulations for this multilayer structure were also carried out, resulting in a first bending resonance mode at 1.16 kHz (Fig. 5.4c inset), in good agreement with the frequency found experimentally. The slight discrepancy was acceptable (5 % difference), and can be attributed to the perfect clamping conditions in simulation, fluctuations on the thickness value (± 2 µm) in the experimental apparatus and tolerance on the material elastic constants of both $LiNbO_3$ and Si.

After the characterization of the structure, we proceeded to test the device under constant excitation with the shaker, in order to investigate the piezoelectric harvesting possibility. In Fig. (5.5a) are shown sinusoidal voltage and displacement signals measured under 3.4 g base acceleration at resonance frequency. The peak voltage amplitude ob-

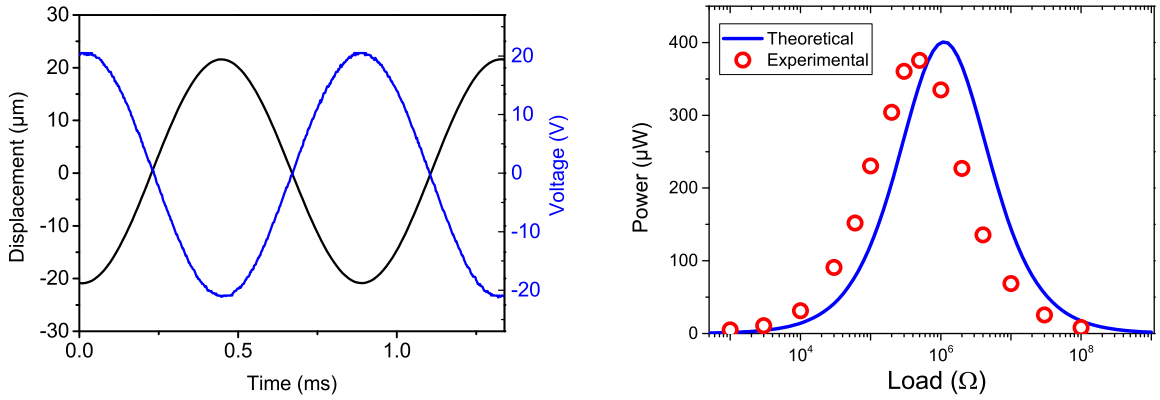

(a) *(b)*

Figure 5.5: (a) Displacement and generated voltage obtained through dynamic excitation with acceleration of 3.4 g. (b) Experimental and theoretical harvested power as a function of load by using (YXl)/36° $LiNbO_3$ /Si harvester.

tained was Vp = 21.1 V, which corresponded to a tip displacement value of up = 21.2 µm, measured with the vibrometer. The root mean squared value of voltage at the resonance frequency was 14.9 V. After comparison with experimental data, FEM simulations results showed a slight overestimation of the voltage and displacement response. In fact, compared to the measured value, FEM overestimated the tip displacement by 3.3 µm. The simulated V_{rms} was approximately 15.8 V, giving a difference from the experimental value of 0.9 V. The reason behind the experimental and FEM values discrepancy (Table 5.1), is mostly due to a slight difference in terms of coupling and quality factors of the cantilever, as a result of using isotropic loss factor that was just an approximation of the real damping for the structure. This aspect can influence the displacement magnitude and thus the voltage response. Eventually, from the measured values we could estimate the force factorα, defined as $\alpha = \frac{V_{pp}}{x_{pp}} C_0$, giving 0.882 mN^{-1}, and displacement magnitude x_M = 18.9 µm. Finally, in order to validate the power that can be extracted from the (YXl)/36° $LiNbO_3$ /Si beam driven by a monochromatic excitation at the vibration frequency f_0, a half-bridge circuit followed by a load, R_l , was connected to the piezoelectric material. The circuit is essentially composed by two 1N4148 diodes (Fast Switching Diode) and two smoothing capacitors, C_r, (each of 220 µF, resulting in an equivalent capacitor of 110 µF). These investigations were done in INSA - Lyon with the collaboration of G. Lombardi. Fig. (5.5b) depicts the extracted experimental and theoretical (Eq. (5.2)) powers as function of load. The maximum power of 380 µW was attained experimentally for a 500 kΩ load impedance. Experimental results showed a good agreement with the theoretical predictions (400 µW maximum power); although a slight difference can be noted probably due to some losses in the diodes (not taken into account in the theoretical model). According to the results, an experimental power density of 8.26 $\mu W.mm^2$ has been measured. This value is consistent with the best results for high-power piezoelectric generators (Ta-

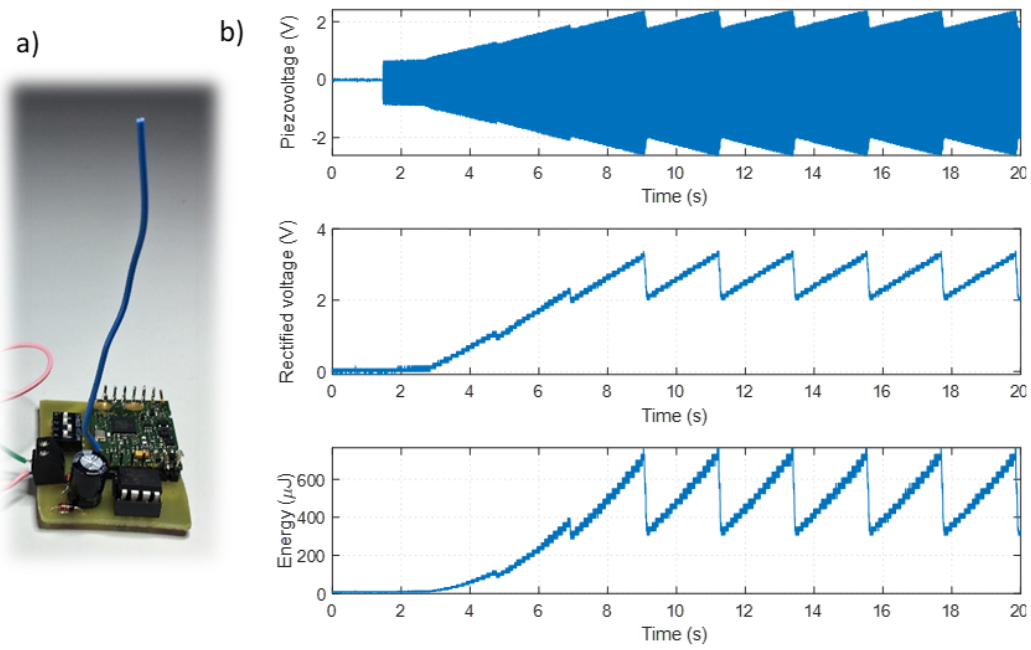

Figure 5.6: (a) Photograph of sensor node featuring PIC 16F15313 micro-controller driving EnOcean PTM 330 RF Transmitter Module. (b) Experimental waveforms of piezoelectric transducer voltage, rectified voltage and available energy by using (YXl)/36° $LiNbO_3$ /Si harvester system (downswing in the waveforms correspond to transmission events).

ble 5.2). It is important to note that the $LiNbO_3$ /Si structures studied in this work were stiff and thus required high acceleration values in order to attain sufficient strain for high power densities. For the purpose of a fair comparison between our work and the state of the art, high frequency Si benders were taken into account. The table shows that even with normalized power density with respect to acceleration levels and frequency, the value of power of our device is comparable and even higher than other typical unimorph PZT and lead-free benders. In general, the power density is strongly correlated to the presence of a tip mass. For this reason, we adapted our finite element simulation to a smaller scale device in such configuration. The results for a micro mechanical transducer with silicon substrate are compared to the state of the art. The simulated device dimensions are 5 mm x 2 mm x 0.03 µm, with a tip mass of 250 µm, where the thickness of the piezoelectric film is reduced to 10 µm. The results show an instantaneous power output of 5.5 µW, that gives a very high normalized power density compared to other harvesters on silicon. Furthermore, with this simulation we can see how the presence of a proof mass lowers the resonance frequency while increasing the power density. Finally, as an application example, the piezoelectric material and its electrical harvesting interface have been connected to a custom sensor node (low-power Microchip PIC 16F15313 microcontroller driving an EnOcean PTM 330 node [3], V_{min} = 2.5 V – Fig. 5.6a). Fig (5.6b) shows the voltage waveforms as well as the available energy on a 110 µF equivalent capacitor in such a configuration. As it can be deduced from Fig (5.6b), the harvesting capabilities of the device

allowed starting the sensor node (from zero energy initial conditions) after 9 seconds and then maintaining the possibility of sending data every 2 seconds (each transmission event consuming approximately 420 µJ) under continuous excitation.

Table 5.2: Comparison of piezoelectric high power density (PD) generators. The works selected represent the state of the art for high frequency silicon based devices. The power is normalized with respect to the active area, acceleration level and frequency.

Material	Tip Mass	Power (µW)	Area mm^2	$\vec{a}$ (g)	Frequency (Hz)	Areal PD ($\mu W.cm^{-2}.g^{-2}$)	Areal NPD ($10^{-2}\mu W.cm^{-2}.g^{-2}.Hz^{-1}$)	Ref.
PZT	Yes	1.4	0.32	2	870	109	12.6	[4]
PZT	Yes	22	120	4	1300	1	0.09	[5]
PZT	No	3.4e-4	2.5	1	9275	0.014	1.5e-4	[6]
	Yes	13	2.5	1	2300	520	22.6	
KNN	No	1.1	56.1	1	1036	2	0.19	[7]
KNN	Yes	0.731	0.21	1.02	1509	335	22.2	[8]
ZnO	Yes	0.98	0.48	1.02	1300	196	15.1	[9]
AlN	Yes	0.8	0.32	2	1495	63	4.18	[10]
AlN	Yes	3.78	2.25	3	1041.4	19	1.79	[11]
AlN	Yes	34.78	27.3	2	572	32	5.57	[12]
AlN	No	0.003	3.21	0.4	4150	0.52	0.0126	[13]
	Yes	0.006	3.21	0.06	1140	52	4.56	
This Work	No*	380	46	3.4	1140	71	6.27	–
LN (YXl)/36°	Yes*	5.5	2	1	684	275	40.2	–

5.2.3 Summary

Here, we reported the implementation of $LiNbO_3$ layers as Pb–free piezoelectric transducers for a complete vibrational energy harvesting application. It was shown that commercially available (YXl)/36° $LiNbO_3$ oriented wafers can be successfully implemented in the form of thick single-crystal films on Si substrate and effectively used by adjusting the thickness of the piezoelectric layer and consequently the capacitance, and by using a proper electronic configuration for energy harvesting. Results showed that the reported system yielded performances close to those of PZT materials. We would like to stress out that such performance of micro-transducers cannot be attained by using bulk $LiNbO_3$ wafers, due to impedance–matching issues. In fact, for bulk single crystals, the low value of the capacitance yields delicate interfacing with typical electrical circuit, while in this paper we are providing a more global approach towards energy harvesting applications. In terms of power density, experimental tests yielded 71 $\mu W.cm^{-2}.g^{-2}$ by using the proposed composite structure vibrating at resonance frequency of 1.14 kHz, that is among

best values even compared to lead-based (and other lead-free) materials commercially available. Moreover, FEM simulations showed promising performances for MEMS scale devices based on $LiNbO_3$. Therefore, this result opens promising outcomes for lead-free energy harvesting solutions and their fast implementation. The fabrication of flexible structures based on thick $LiNbO_3$ layers will be considered in future to attain this efficiency at low frequency and acceleration values [14]. Although one finds some examples of high frequency resonating beams (Table 5.2)[1], we will consider lowering the resonance frequency in order to match frequency spectra available abundantly in the environment, and design and fabricate bimorph structures to further increase the generated power. Concerning the coupling factors, we tailored the properties of the material in order to optimize the electro-mechanical coupling of the material, but future steps will also consider the optimization of the structural coupling in order to have maximum energy efficiency for our device.

5.3 Low Frequency Harvesters on Silicon

After the fabrication and characterization of the first batch of samples, we have decided to improve the power density and reduce the resonance frequency of the harvester. In order to do so, we have worked on etching of the silicon substrate, and we considered a new geometry for the harvester. Moreover, we implemented the optimized $LiNbO_3$ (YXl)/128° crystal cut in order to maximize the electro-mechanical coupling. For this particular orientation we can exploit in transverse mode the coefficient d_{23} = 27 pC/N and dielectric constant $\varepsilon_{33}^{T}/\varepsilon_0$ = 50.5. Therefore, it is possible to increase the electro-mechanical coupling compared to the orientation $LiNbO_3$ (YXl)/36° by more than 15%, finally resulting in k_{23} = 0.49. As discussed before, this value is among the highest compared to commercially available ceramics such as PZT-5A and PZT-5H or other well known lead free materials like KNN, AlN etc. Concerning the design of the structure, also the robustness of the prototype was taken into account, considering silicon beams with thickness above 100 µm, while the piezoelectric layer was kept at 30 µm in order to have capacitance of few *nF* and reasonable voltage levels. Moreover, the silicon substrate thickness was carefully considered in order to perform DRIE etching without using silicon on insulator (SOI) wafers. Especially for MEMS application, using SOI is a standard, where it is possible to use few μm thin silicon layer as effective beam for the harvester [10, 4]. However, this technology is developed along with thin film deposition (up to few μm thickness). If on one side this could mean good impedance matching (typically above 10 nF clamped capacitance), the drawback could be limited voltage output. After a careful consideration of all this aspects, and taking into account also the robustness of the structure, we decided to fabricate a mesoscale device, in order to reach a compromise in terms of coupling,

[1] (*) Experimental values for device without tip mass; (**) Simulated MEMS scale device with tip mass.

impedance matching and power levels.

The objective for the new set of devices was to fabricate harvesters with higher coupling and quality factor. Therefore, we wanted to attain higher performance levels, where in the equivalent circuit of the inertial harvester we have to take into account also the mechanical branch of the structure. The damping will limit the power that the harvester can convert successfully into electrical energy. Typically, the maximum power for such devices, it is proportional to the quality factor. On the other hand, it is known that the highest the quality factor, the smaller will be the frequency bandwidth in which the harvester can work in optimized conditions. Anyways, when coupling and quality factor are properly tuned, it is possible to increase the bandwidth of electro-mechanical conversion. The damped system results are discussed in details in [15]. We will use a simple full-bridge DC converter as electronic interface, but the discussion can be extended also for other types of configurations, such as non-linear interfaces [16].

For this system we can define an important factor that is describing the performances of the harvester: the modified coupling coefficient $k_m^2 = \frac{\alpha^2}{KC_0}$, which is giving the ratio between electrostatic energy stored in the system and the elastic energy. This coefficient does not have a maximum as k^2 and can be higher than 1. Normally for low coupled devices the two coefficients are the same.

Finally we can make a distinction of performances considering the figure of merit $k_m^2 Q$. If the harvester has $k_m^2 Q < 1$, the system is low coupled and the harvested power is fundamentally limited by coupling and mechanical damping, moreover only one peak is observed for the optimal load condition. If the system has $k_m^2\ Q > \pi$ the normalized power is limited by Q. When the figure of merit of the system is higher than this value, it is possible to increase the optimized frequency bandwidth of the harvester, by adjusting the load to maximize the power output.

5.3.1 Simulations

We started the optimization of the parameters of devices targeting resonant frequencies below 200 Hz. Having this in mind, we have investigated the thickness ratio between substrate and piezoelectric layer (h_i/h_p) in order to attain the required frequency levels. The length of the electrode was chosen to be 2/3 of the overall length, in order to optimize the strain effect of the cantilevered beam. Then, considering the piezoelectric thickness and the permittivity of the crystal cut, we have targeted 6 nF clamped capacitance.

Later on, we have simulated the device with a tip mass in order to further decrease the frequency response and also increase the power output. For this simulation we modeled the short- and open-circuit frequencies with FEM software Comsol Multiphysics. The results pointed out that for the chosen geometry we could reach a maximum of effective coupling of 5%, where the two frequencies were respectively 106 Hz and 108.6 Hz.

In the case of a lightly coupled regime, the displacement of the beam is damped. For

Table 5.3: Parameters used for (YXl)/128° $LiNbO_3$ harvester simulation.

f_0(Hz)	C_0(nF)	Q	k^2
100	6	200	0.1÷5 %

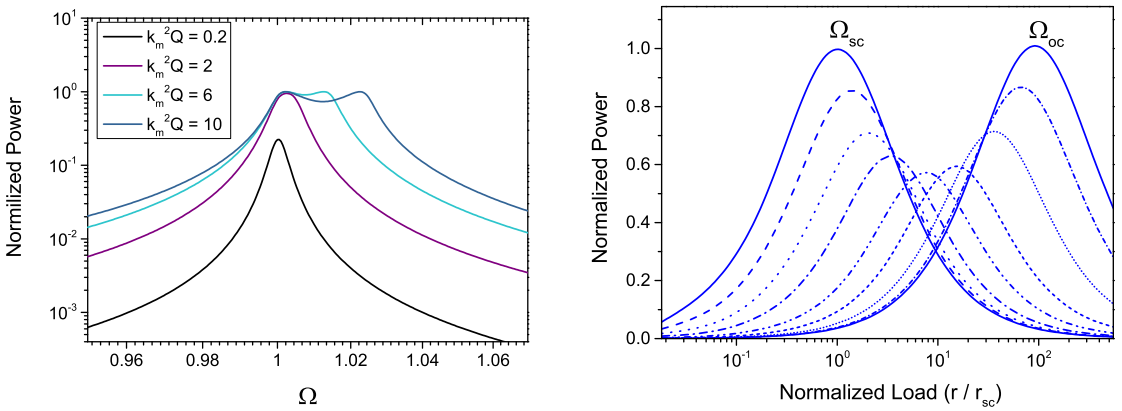

(a) *(b)*

Figure 5.7: Investigation of coupling and quality factor effect on power output: (a) lumped model simulation considering damping of the structure in frequency domain. (b) Study of power output with FEM software for different electric loads.

this reason, we have considered the lumped model with relative rectification interface (standard full-bridge rectifier) and we have used the proposed formalism to investigate the power response of the device. The power output in terms of the product $k_m^2 Q$ is presented in Fig. (5.7a). The parameters used for the simulation are given in the Table (5.3). These parameters were chosen in agreement with 3D FEM simulations, considering the properties of our designed $LiNbO_3$ /Si harvester. Eventually, we have tuned the excitation levels to car environment acceleration, hence below 0.5 g (RMS).

The simulation results presented in Fig. (5.7a), depict different values of the coupling considering a quality factor of 200. As we can see, when the product k_m^2 Q is small, the system is in a sub-optimal region and cannot convert fully the energy provided to the harvester. Once in the optimal region, k_m^2 $Q = 2$, we start to see two different power peaks which have the identical magnitude. For higher values the peaks start to be very far from each other and the bandwidth is increased. In Fig. (5.7b), we present a FEM study of the designed harvester (k^2 = 0.04). In this case, the two power peaks are identical and have the maximum value of 45 µW. As expected, the first peak is around 50 kΩ, while the second is close to 5 MΩ. Once the performances and coupling of the proposed design were investigated, we moved to the fabrication of the specimen on silicon substrate.

5.3.2 Discussion and Results

The prototype had a length of 65 mm and width of 10 mm, with a top electrode covering 2/3 of the total length. The main difference with respect to the previous fabrication process is the use of Cr/Au top layer to have a better conduction and the same band gap for top and bottom electrodes. Moreover, we added an etching step to pattern the silicon substrate, in order to increase the coupling and reduce the resonance frequency. The Si backside was patterned in order to leave a 10 mm by 10 mm tip mass, while the central part was etched until 300 µm thickness. The top electrodes were wire-bonded to a PCB and clamped on an Al clamping system (Fig. 5.8a). In Fig. (5.8b) we can see the cross-section of the sample after dicing, where $LiNbO_3$ is the top layer, and silicon is the substrate of the structure. The thin white line is the bonding interface between the two wafers. The quality of the bonding was excellent, even if we didn't use a SiO_2 insulation layer.

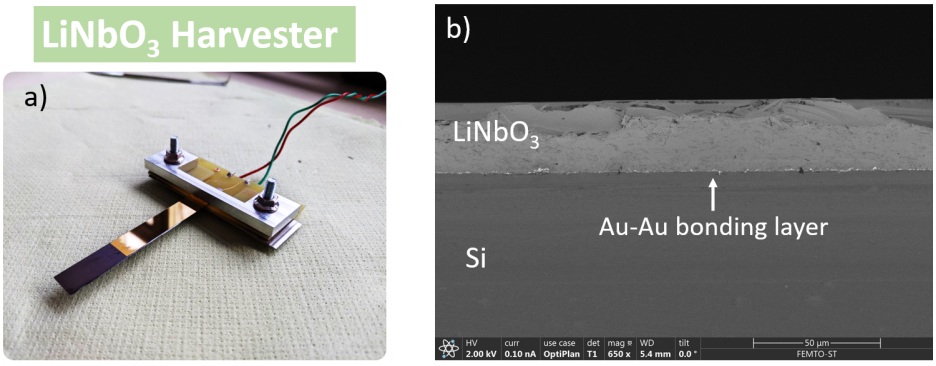

Figure 5.8: (a) Clamped (YXl)/128° $LiNbO_3$ /Si harvester wire bonded to PCB board. (b) SEM cross-section image of sample after dicing.

The characterization of the harvester was done in T&F department at FEMTO-ST. The setup for the measurements is shown in Fig. (5.9), and it consisted in a shaker providing the sinusoidal excitation for the test, coupled with an accelerometer mounted at the base of the clamping system to monitor the magnitude of the input force. Afterwards, the displacement of the tip was tracked by a laser interferometer with 50 µm resolution, giving a relative error of 2.5% for the measurements at resonance. Normally, the acceleration magnitude range used was 0.1±0.02 g. The voltage levels were measured both with an oscilloscope using a 10 MΩ attenuation probe, and a National Instruments Acquisition Card with a dedicated Labview routine.

Meanwhile, the parameters of the equivalent circuit at resonance were investigated with a network analyzer (Keysight E5061B). Clamped capacitance, impedance and phase were measured for a specific set of frequencies (from 10 Hz to 100 kHz) at room temperature, after the calibration of the spectrum analyzer at 50 Ω. The samples showed very small dielectric losses (0.24%), confirming the good quality of the single crystal, and a capacitance of 5.8 nF at 2 kHz. In Fig. (5.10) the impedance spectrum is fitted by us-

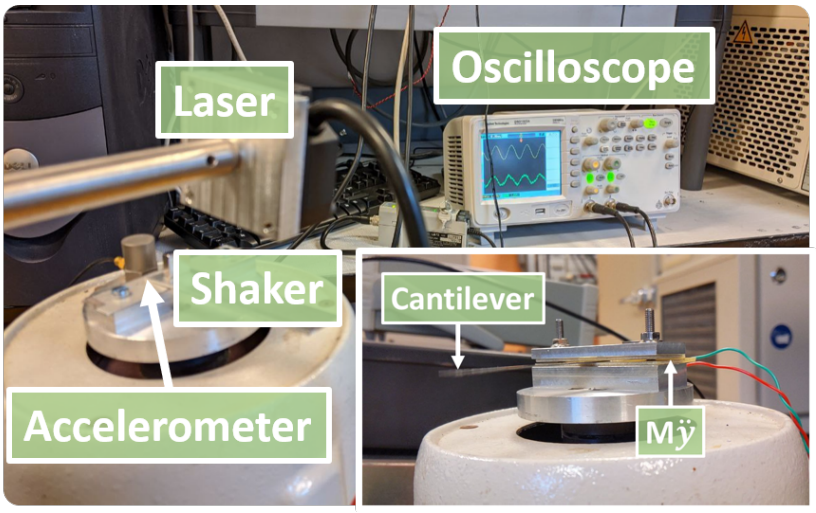

Figure 5.9: Experimental setup in T&F department, FEMTO-ST.

ing RLC circuit model at resonance. The figure shows a resonance and anti-resonance frequency, which are corresponding to the short- (104.5 Hz) and open-circuit (105.9 Hz) frequencies. The simulation given from the equivalent circuit is in good agreement with the measurement, and we can use the experimental identifications to calculate the corresponding parameters for the harvester. In particular, it was estimated the quality factor ($Q = 396$) and the modified structural coupling ($k_m^2 = 0.028$), these values were obtained from the equivalent circuit.

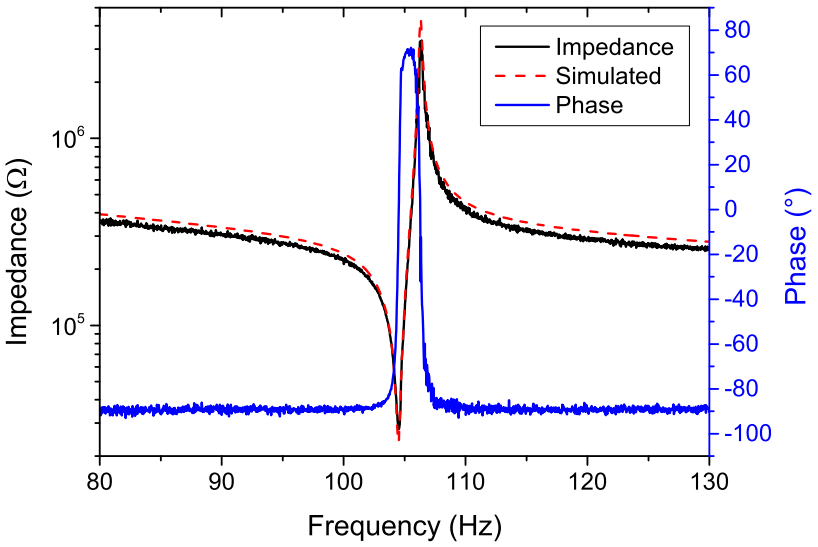

Figure 5.10: Impedance and phase measurement for $LiNbO_3$ harvester at resonance.

After the characterization of the structure with the spectrum analyzer, we have proceeded to test the device under constant sinusoidal excitation using the shaker, in order to investigate the harvesting capabilities of the device. Fig. (5.11a) depicts the results from the measurement in open circuit condition of voltage and displacement. The voltage and displacement signals were measured under 0.1 g base acceleration at the frequency of

105.9 Hz, showing 42.8 V and 1970 µm peak to peak respectively. Eventually the force factor α was estimated to be 0.13 mN.V^{-1}.

Table 5.4: Experimental identifications for (YXl)/128° $LiNbO_3$ /Si harvester.

C_0(nF)	M(g)	C (mN.s.m^{-1})	K (N.m^{-1})	α (mN.V^{-1})
5.8	0.23	0.38	98.08	0.13

Measuring the voltage response in the frequency domain, we found that even at low acceleration level, the magnitude of the displacement was high enough to experience air damping, which lowered the quality factor of the beam. In Fig. (5.11b) we present the voltage response in open circuit measured with an attenuated probe 10 MΩ, where the harvester showed a voltage peak of 15.1 V (RMS). Eventually, from this measurement, we have estimated the quality factor considering the width of the voltage response at 3 dB, which provided the final value of $Q = 194$. Moreover, we can see also that the structure shows light non-linearities which are bending the voltage peak towards lower frequencies. This effect was modeled in some recent works [17], and is an effect that is related to *softening* of the silicon substrate. The second curve in the figure is simulated with FEM and shows the linear behavior of the harvester reaching a voltage peak of 16 V (RMS). The modeled peak presents a shift towards higher frequencies, which has the value of 106.2 Hz. The values were in good agreement with the simulations, even though the voltage levels seems to be slightly overestimated, the reason could lie in the fact that non-linearities were not taken into account in the FEM model. Anyways, the bending mode of the beam was attained in the expected frequency range and at low acceleration levels, which are compatible with car environment.

As stated in the previous chapter, an important feature is the product between coupling, k_m, and quality factor Q. For our device we have estimated a factor $k_m^2 Q = 5.3$, which is related to lightly coupled harvesters. If we make a comparison with other single crystals, the values are in the same order of magnitude of other materials [18]. One of the advantages of using $LiNbO_3$ is the low dielectric losses, which are one order of magnitude lower than in commercially available ceramics.

Finally, to estimate the harvester performances, we have measured the power using a full bridge rectification circuit (Fig. 5.12). The circuit was essentially composed by four 1N4148 diodes (Fast Switching Diode) and one smoothing capacitor, C_r, (12 µF), followed by a resistive load R_l. The rectified voltage V_{DC} is used to estimate the power output as in $P = \frac{V_{DC}^2}{R_l}$. In the case of lightly coupled regime, we can expect to have two power peaks for the two frequencies observed at short- and open-circuit conditions.

A comparison between simulated (Eq. 4.120) and experimental power is given in Fig. (5.13a). The transparent surface represents the simulated power using the proposed

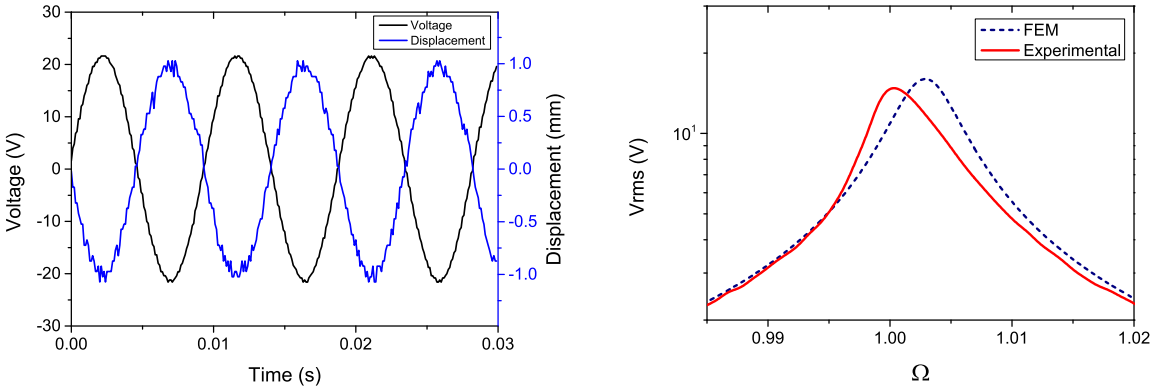

(a) *(b)*

Figure 5.11: Characterization of (YXl)/128° $LiNbO_3$ /Si dynamic response: (a) displacement and generated voltage obtained through dynamic excitation with acceleration of 0.1 g. (b) Experimental and FEM voltage as a function of normalized frequency.

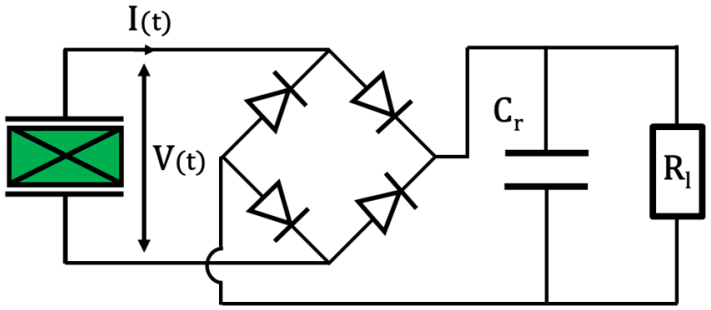

Figure 5.12: Standard full-bridge rectification circuit.

model, while the opaque surface depicts the experimental data. The measured power varied with the resistive load and the frequency as expected. We found two power peaks one relative to the short-circuit resonance (around 50 kΩ) and one at open circuit (2.6 MΩ). These values are slightly different from the one observed in the model, the reason could be the difference in the quality factor due to non-linearities at resonance, or diode loss. Moreover, the used diodes had high voltage threshold (typically 0.6 V), this resulted in having losses for the short-circuit resistive load, where the voltage level was below 1 V. For this reason, we could not attain identical power peaks as showed in the simulation, since diode losses were not taken into account in the model. However, as we can see in Fig. (5.13b) the optimal rectified power output was estimated to be 29 µW and 41.5 µW, for the two peaks, in continuous excitation, respectively. Even though the SC peak is not as high as expected, the result for OC is in good agreement with the expected behavior of lightly coupled energy harvester. Furthermore, we could use lower threshold diodes two use in the rectification circuit or implement a voltage doubler to avoid important diode losses.

Finally, considering the low acceleration level, the obtained power density is considerably high (965 $\mu W/cm^2/g^2$) for a lead-free material. In fact other devices that are working

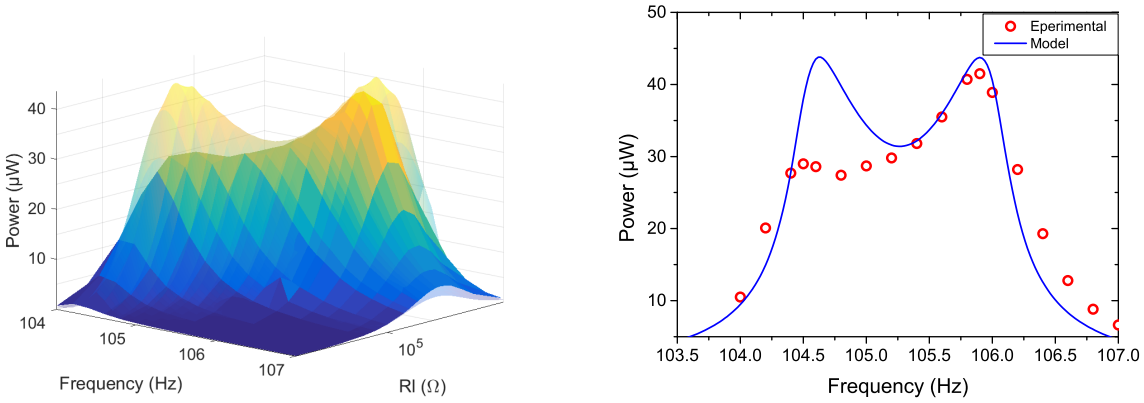

Figure 5.13: Power output of (YXl)/128° $LiNbO_3$ /Si harvester: (a) theoretical (transparent) and measured (opaque) power surface. (b) Comparison of simulated and experimentally measured maximum power peaks in frequency domain.

in such conditions can attain similar power levels but are using typically two piezoelectric layers in bimorph configuration. Even if in the literature $LiNbO_3$ bimorph are fabricated with inversion layers [19], the use of bulk crystals, is limiting their implementation with low power electronics, having very low capacitance. Meanwhile our thick film implementation resulted in having a considerable rectified power response in the lightly coupled regime with an optimized capacitance in *nF* scale. With this approach, it is possible to obtain $LiNbO_3$ on silicon harvester with state of the art performances.

5.3.3 Summary

After the optimization of the hetero-structure properties through the study of orientation of $LiNbO_3$ wafer cuts, it was possible to fabricate a new batch of piezoelectric harvesters. The device showed resonance frequency at 105.9 Hz, and 42.8 V peak-to-peak voltage response, with 5.8 nF clamped capacitance. From these results we could estimate a power density of 965 $\mu W/cm^2/g^2$, that is among the highest results compared to both lead and lead-free current devices. In Tab. (5.5), the normalized power densities of low frequency energy harvesters are presented. The presented state of the art, is a selection of works for both micro-scale devices [20, 21], exploiting materials that are deposited by means of micro-fabrication techniques, and meso-scale [22, 23] exploiting commercially available ceramics or single crystals. Although they have different dimensions, their power is normalized by the active surface and frequency for a fair comparison. Few notable exceptions are showing higher normalized power density compared to our prototype. Generally, in the state of the art the trend is to report instantaneous power, while we present rectified power, confirming that is possible to implement successfully $LiNbO_3$ with a standard electronic interface. Moreover, they have the advantage of using bimorphs on metal substrates [21, 22] or expensive singles crystal materials [24]. Anyways, our device resulted as

the best alternative compared to Pb-free materials.

Compared to our previous results, the product k_m^2Q was increased by one order of magnitude (k_m^2Q=5.3), using a silicon tip mass and considering thinner substrate. Furthermore, the frequency response was reduced to match the environmental frequencies present in cars, and can be also tuned with the use of appropriate tip mass thickness. The next challenge is integrating more flexible substrates, such as metal foils that can provide more robust and reliable devices with improved design. Concerning the electronic interface, we recommend using lower threshold voltage diodes in order to reduce losses in the case of small resistive loads. Eventually also non-linear electronic interface can be implemented in order to further improve the harvester performances.

Table 5.5: Comparison of piezoelectric high power density (PD) generators. The works selected represent the state of the art for low frequency based devices. The power is normalized with respect to the active area, acceleration level and frequency.

Material	Power (μW)	Area (mm^2)	$\vec{a}$ (g)	Frequency (Hz)	Areal PD ($\mu W.cm^{-2}.g^{-2}$)	Areal NPD ($\mu W.cm^{-2}.g^{-2}.Hz^{-1}$)	Ref.
PZT	423	54	1.5	143.5	348	2.43	[25]
PZT	321	55	3	100.8	65	0.64	[26]
PZT	9	38.5	0.15	72	1039	14.43	[21]
PZT-5H	40	204.16	0.2	36	490	13.61	[22]
PMN-PT	1850	50	3.2	102	361	3.54	[27]
PZN-PT	430	72	0.3	37.5	6336	176.95	[24]
KNN	3.62	5	1	132	72.4	0.55	[20]
AlN	32	65.32	0.5	58	196	3.38	[28]
PVDF	8.59	180	0.5	30.8	19	0.62	[23]
LN (YXl)/128°	41.5	430	0.1	105.9	965	9.11	–

5.4 $LiNbO_3$ Harvesters on Metal

After the experience gained in the micro-fabrication of $LiNbO_3$ devices on silicon, few challenges have surfaced. First of all the current vibrational energy harvesting technology on the market is based on metal or acrylic substrates. In fact, for PZT it was shown that using high quality factor substrates like nickel or stainless steel, we can increase the performances of the harvesters [21]. Moreover, the robustness of the devices is improved in comparison with silicon [29]. Nevertheless, silicon remains an affordable and reliable alternative for up-scaling the micro-fabrication process, especially for MEMS scale devices, but in general, companies see the alternative of metal or acrylic more attractive and

cost efficient. For this reason we have implemented a new fabrication process that can successfully bond high quality $LiNbO_3$ crystals on metal substrates, using Au-Au bonding. The advantages in using Au as a bonding material are several. First of all it is a very effective electrode, and the fabrication of thin films by sputtering or evaporation is cost efficient when used on large wafer surfaces. With this approach, several devices can be fabricated from the same substrate, which up to now can be done on a wafer as large as 6 inches. Finally, compared to other kinds of glue or conductive paste, the layer is very thin, and it doesn't affect the mechanical properties of the device. The quality of the bonding that we can attain is reliable, and in principle can be implemented at room temperature on different kind of hosts.

In the simulation, we have used the material properties of brass to simulate a simple beam and to investigate its electro-mechanical coupling. The first aspect of the considered simulation was the thickness of the piezoelectric element to attain during the fabrication process. We have used both FEA and Comsol to derive a model to study the unimorph coupling in order to optimize its performances, and also to tune it to lower frequencies compared to the silicon counterpart. Once found the correct geometry, we have simulated its voltage response, while the power output was simulated with the lumped model approximation for a full bridge rectification circuit. In this section we will present the devices that were implemented on metal substrates, and we will analyze their performances.

5.4.1 Modeling

To model the samples on metal we have used extensively the Finite Element Analysis proposed in Chapter 4. One of the goal was to optimize the coupling of the system and tune the structure to the frequency bandwidth desired. As in the case of silicon, we have counter-checked the results for the model using also FEM software Comsol Multiphysics.

In order to ease the interpretation of comparative results, we find useful to emphasize the most important highlights of our approach below. We can start the analysis of the electro-mechanical problem with Hamilton's Principle for a beam clamped-free in bending conditions:

$$\delta \int_{\mathrm{V}} (\mathscr{T} - \mathscr{U})\, d\mathrm{V} + \delta \int_{\mathrm{S}} \mathscr{W}\, d\mathrm{S} = 0 \tag{5.3}$$

where $\mathscr{T}$ is the kinetic energy term, $\mathscr{U}$ the potential energy for the considered volume V, and $\mathscr{W}$ is the work done by external forces on the boundaries of the structure.

We add to the hypotheses of cylindrical bending and pure extension, the piezoelectric

effect in transverse direction d_{31}, therefore we get the following conditions:

$$\begin{cases} u_1 = -x_3 w_{3,1} + w_1 \\ u_3 = w_3 \\ \varphi = f(x_3) \end{cases} \tag{5.4}$$

where x_3 is the vertical coordinate with origin at the level of the neutral plane, (u_1, u_3) are local displacements and (w_1, w_3) represent global displacements. w_1 is the axial displacement of the cross-section measured at the neutral plane, and w_3 is the vertical displacement of the neutral plane when we bend the plate. Finally, φ is a function of x_3, and represents the piezoelectric potential arising from the bending of the structure, where the piezoelectric effect is exploited in transverse mode using d_{31} coefficient.

We compute the coordinate, z_n, for the neutral fiber of the bender as:

$$z_n = \frac{h_p^2 s_{11}^i - h_i^2 s_{11}^p}{2(h_p s_{11}^i + h_i s_{11}^p)} \tag{5.5}$$

where h_i and h_p are the thickness of the substrate and piezoelectric element, while s_{11}^i and s_{11}^p the compliance element in same configuration.

Now we can use the following sets of electro-mechanical equations to investigate the potential energy derived from piezoelectricity:

$$\begin{aligned} \mathrm{S_I} &= s_{\mathrm{IJ}}^{\mathrm{E}} \mathrm{T_J} + d_{k\mathrm{I}} \mathrm{E}_k \\ \mathrm{D}_i &= d_{i\mathrm{J}} \mathrm{T_J} + \varepsilon_{ij}^{\mathrm{T}} \mathrm{E}_j \end{aligned} \tag{5.6}$$

Here, T^{E} and E are the independent variables in the differential forms of the potential energy variations. Now we can rewrite the variational principle in terms of the energy potential given by the piezoelectricity:

$$\int_{\mathrm{V}} \left(\delta\mathscr{T} - \delta\chi\right) d\mathrm{V} + \int_{\mathrm{S}} \delta\mathscr{W}\, d\mathrm{S} = 0$$

where we found that the proper form of variation of enthalpy ($\rho\chi$) is written as follows:

$$\int_{\mathrm{V}} \rho\delta\chi\, d\mathrm{V} = \int_{\mathrm{V}} \left[\frac{1}{s_{11}} \left(\mathrm{S}_1 - d_{31}\mathrm{E}_3\right) \delta\mathrm{S}_1 - \left(\frac{d_{31}}{s_{11}} \mathrm{S}_1 + \left(\varepsilon_{33}^{\mathrm{T}} - \frac{d_{31}^2}{s_{11}} \right) \mathrm{E}_3 \right) \delta\mathrm{E}_3 \right] d\mathrm{V}. \tag{5.7}$$

Finally, the variations of χ can be expressed in terms of the variations of well–defined derivatives of the unknown continuous field–variables, w_1, w_3 and φ, deriving from our hypotheses. On the other hand, the volume integral of kinetic energy in harmonic regime contributing to Hamilton's principle is:

$$\int_{\mathrm{V}} \delta\mathscr{T}\, d\mathrm{V} = \int_{\mathrm{V}} \rho\omega^2 \vec{u} \cdot \delta\vec{u} d\mathrm{V}. \tag{5.8}$$

From the kinematic hypotheses (5.4), we obtain:

$$\int_{\mathrm{V}} \delta\mathscr{T}\, d\mathrm{V} = \omega^2 \int_{\mathrm{V}} \rho \left[\left(-x_3 w_{3,1} + w_1\right) \left(-x_3 \delta w_{3,1} + \delta w_1\right) + w_3 \delta w_3 \right] d\mathrm{V}$$

After substituting the interpolations in the integral variation of kinetic energy, potential energy and work done by external forces, the variational equation is put in the following form:

$$\sum_e \left\{ \left[\underbrace{\int_{\mathrm{V}_e} [\mathbf{B}(x)]^{\mathrm{T}} [\mathbf{D}] [\mathbf{B}(x)]\, d\mathrm{V}_e}_{[\mathbf{K}]^e} - \omega^2 \underbrace{\int_{\mathrm{V}_e} [\mathbf{N}(x)]^{\mathrm{T}} [\boldsymbol{\rho}] [\mathbf{N}(x)]\, d\mathrm{V}_e}_{[\mathbf{M}]^e} \right] \{\mathbf{U}^n\} = \underbrace{\int_{\mathrm{S}_e} [\mathbf{N}(x)]^{\mathrm{T}} \{\boldsymbol{f}\}\, d\mathrm{S}_e}_{\{\mathbf{F}^n\}} \right\} \tag{5.9}$$

In this equation, $\mathbf{U}^n$ contains the DOFs, $\mathbf{B}^n$ the derivatives of interpolating functions required to compute the generalized unknown (our dependent variables) consisting in the curvature, $w_{3,11}$, the stretch, $w_{1,1}$, and the distinct values of the gradient of potential, $\varphi_{,3}$, occurring in the piezoelectric layer. $\mathbf{D}$ the material characteristics integrated or separated over z, $\mathbf{N}$ all shape functions, $\boldsymbol{\rho}$ the integrated mass density. Here, the e subscript denotes the index used for numbering the elements. Eventually, L and b are the total length and width of the beam.

The compact form for our system will be:

$$\sum_e \left(\left[\mathbf{K}_e\right] - \omega^2 \left[\mathbf{M}_e\right] \right) \{\mathbf{U}^n\} = \{\mathbf{F}^n\} \tag{5.10}$$

Thanks to this formulation we can investigate the coupling by zeroing the determinant of the stiffness and mass matrix:

$$\det[\mathbf{K}_e - \omega^2 \mathbf{M}_e] = 0 \tag{5.11}$$

Hence, we can find the OC and SC angular velocities and then calculate the coupling using the following relation:

$$k^2 = \frac{\omega_{oc}^2 - \omega_{sc}^2}{\omega_{oc}^2} \tag{5.12}$$

While considering the potential we can rewrite it in terms of the material properties of the beam as:

$$\varphi_h = \frac{e_{31}}{\mathrm{C}_0} \frac{1}{(1 - k_{ij}^2)} \left(w_1^{\mathrm{L}} + \frac{1}{2} \left(h_p - 2z_n\right) w_{3,1}^{\mathrm{L}} \right) b \tag{5.13}$$

where we see that the potential in open circuit condition is proportional to the axial displacement, w_1^{L}, and the rotation, $w_{3,1}^{\mathrm{L}}$, of the right end of the beam. Moreover we have

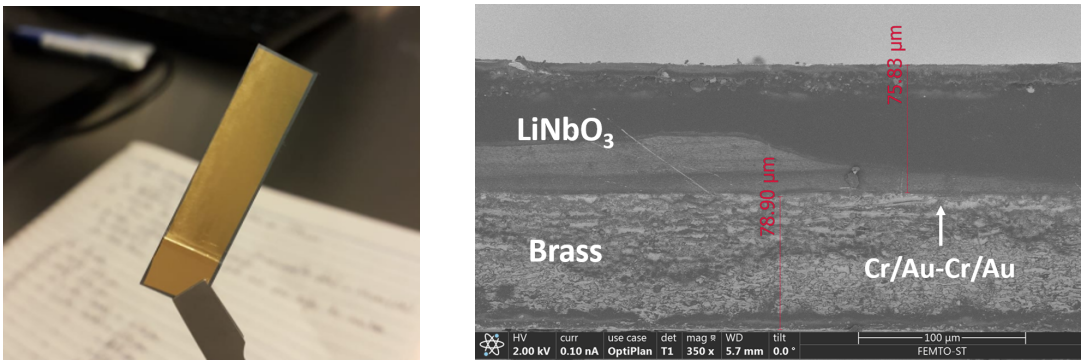

(a) *(b)*

Figure 5.14: Detailed description of harvester micro-fabrication (YXl)/128° $LiNbO_3$ /Brass: (a) optical image of diced cantilever; (b) SEM image of hetero-structure cross-section (75 µm $LiNbO_3$, 79 µm brass).

specified the dependency on the electro-mechanical coupling factor, k_{ij}, as well as the piezoelectric coefficient, e_{31} and, capacitance C_0.

5.4.2 Discussion and Results

In Fig. (5.14a) we present the (YXl)/128° $LiNbO_3$ /Brass cantilever after micro-fabrication process and ready for testing. The piezoelectric layer was lapped selectively to leave a thicker region which can be used as clamping or tip mass (50 mm^2 x 0.35 mm) during the dynamic investigations. For a simple beam, the active area was eventually 26 mm by 10 mm. Finally in Fig. (5.14b) we can see the cross section after dicing of one of the fabricated specimen. The brass layer was 79±2 µm thick while the $LiNbO_3$ was 75±2 µm. Finally the samples were installed on the aluminum clamping structure which was used also as top electrode connection, while a PCB board was serving a ground electrode (Fig. 5.15).

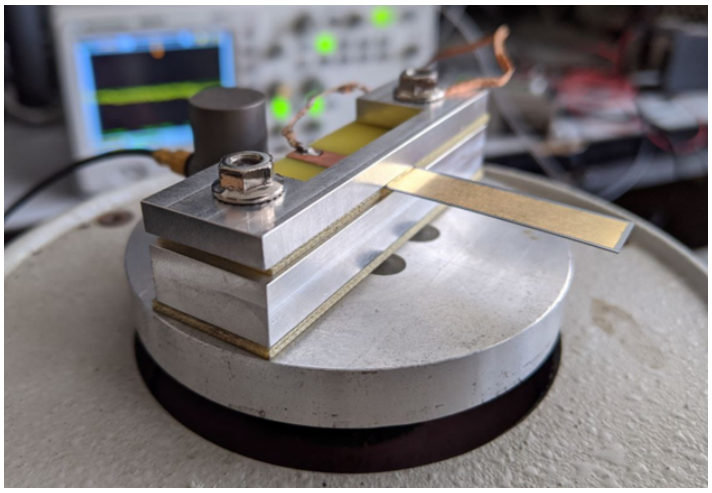

Figure 5.15: (YXl)/128° $LiNbO_3$ /Brass harvester mounted on shaker with accelerometer to monitor base acceleration.

Similarly to the characterization of silicon samples, the first step was the investigation of the coupling. In order to confirm the predictions of FEA model, we have fabricated a batch of samples with different thicknesses to find the optimal conditions of transduction. The impedance spectrum of one sample is shown in Fig. (5.16a). The simulated values of the equivalent parameters was slightly overestimating the position of short- and open-circuit frequencies, leading to higher coupling predictions. For the whole batch of samples, the frequency response was ranging from 50 Hz to 140 Hz. Also in this case, the dielectric losses of the piezoelectric element were low, typically in the order of 0.1%. From the measurements, we have calculated the coupling coefficient and quality factor of the structures, finding the k^2 and Q. In Fig. (5.16b) we can observe the study of the coupling in terms of piezoelectric layer thickness with both FEA and Comsol. For simple beams without tip mass we observed a k^2 maximum of 0.042 for a thickness ratio of $\frac{h_i}{h_p} \approx 2$ and a Q of 115. Instead for samples having a tip mass, the highest coupling observed was $k^2 = 0.03$ and a Q=244, nevertheless, the thickness ratio for this specimen was not optimized. In order to refine the simulations we measured with a three point bending system, the Young modulus of the brass substrate, used for the fabrication, of 110 GPa. The samples fabricated on brass showed coupling in good agreement with the predicted results of the FEA and Comsol modeling, even though the the simulations overestimated the values of k^2. One possible explanation could be the difference in electrode size between model and real case, where we have patterned the top Cr/Au layer with a stencil mask which does not cover the whole surface. Another point is the fact that we clamp directly on the piezoelectric material, and this can reduce the overall effectiveness. Moreover, being the simulation 2D, we considered plane strain configuration, where the piezoelectric strain coefficient is given as $d_{\text{eff}} = d_{23} - d_{21}\frac{s^{\text{E}}_{13}}{s^{\text{E}}_{11}}$, which leads to a smaller value compared to plain stress assumption (-23.5 pC/N). For this reason, we propose to implement 3D simulations in order to have better approximation for upcoming investigations. Anyways, the predicted optimal thickness ratio was close to the observed one in the case of simple beams. In terms of coupling, the cantilevers with tip mass showed better performance compared to their simple beam counterpart, as expected. Further simulations can be implemented in order to investigate specifically samples with tip mass.

After the investigation of the coupling and the parameters of the equivalent circuit, we have analyzed the voltage and frequency response of the samples. The specimen were positioned on the aluminum clamping system and connected to the electronic interface. While the shaker was providing a harmonic sinusoidal excitation with 0.1±0.02 g RMS magnitude, we monitored the input acceleration and measured the tip mass displacement. The samples showed voltage responses between $4 \div 13$ V, depending on the thickness ratio $\frac{h_i}{h_p}$. During the tests, we have observed non-linear behavior close to resonance frequency. Specifically, samples with $\frac{h_i}{h_p} < 2$ exhibited *softening*, therefore the voltage peaks compared to what expected by simulations were shifting towards lower frequen-

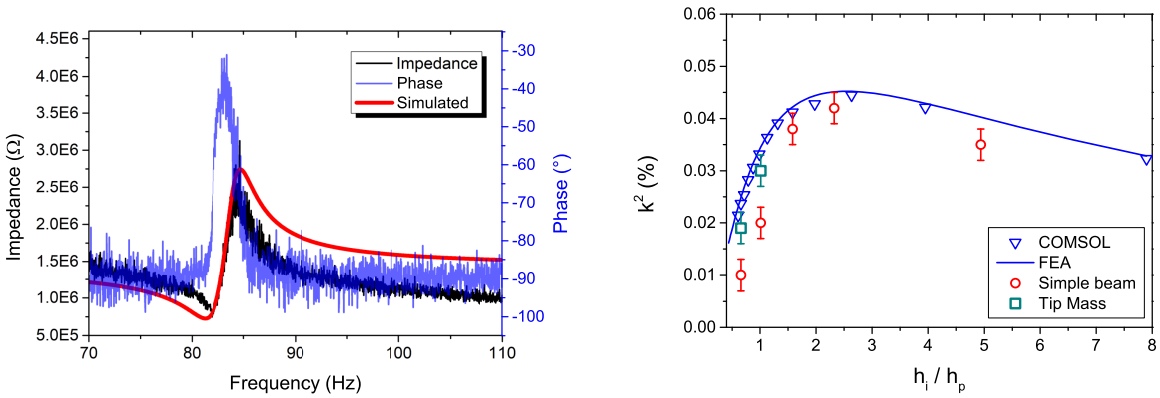

(a) *(b)*

Figure 5.16: (a) Experimental and simulated data impedance and phase of (YXl)/128° $LiNbO_3$ /Brass harvester; (b) electro-mechanical coupling as a function of h_i/h_p for set of fabricated samples on brass.

cies (Fig. 5.17a). Meanwhile, for ratio $\frac{h_i}{h_p} > 2$ the samples exhibited a *hardening* behavior, therefore the resonance was shifting towards higher frequencies (Fig. 5.17b). In both cases we have preformed up and down frequency sweep, in order to see how the nonlinearities were affecting the system. The two phenomena, correspond to precise features of substrate or piezoelectric layer. It is known that softening appears whenever the restoring force decreases with the displacement, so it appears when h_p is smaller that h_i [30]. This effect was observed also in the case of silicon which had a similar configuration. Hardening instead, appears whenever the restoring force is increasing with the displacement, and it occurred whenever around the optimal value of the thickness ratio. Hence, as demonstrated in [17], it exists a critical film thickness for which the hardening or softening behavior is observed if the film thickness is below or above the specific ratio $\frac{h_i}{h_p}$. In our case, especially in the case of softening we saw that this effect can increase the bandwidth of response of the device and also increase the voltage response. For the sample represented in Fig. (5.17a), the frequency bandwidth was increased up to 1 Hz. As for hardening we observed an increase of the displacement levels even for small excitation of the device.

The final step of the characterization was the investigation of the harvesters power response. We have calculated the force factor for the highest coupled device with and without a tip mass. The results are showed in Table (5.6). The force factor for the two devices is similar, even though it is slightly higher for the cantilever with tip mass. The other samples shows higher capacitance due a thinner piezoelectric layer and much higher displacement magnitude, reaching 3.15 mm peak to peak displacement at resonance. We have observed that for the sample with tip mass the quality factor measured at -3dB, was approximately 64 and the product of $k_m Q$, was lower than the simple beam counterpart.

Finally, we characterized the sample with tip mass, which showed the highest volt-

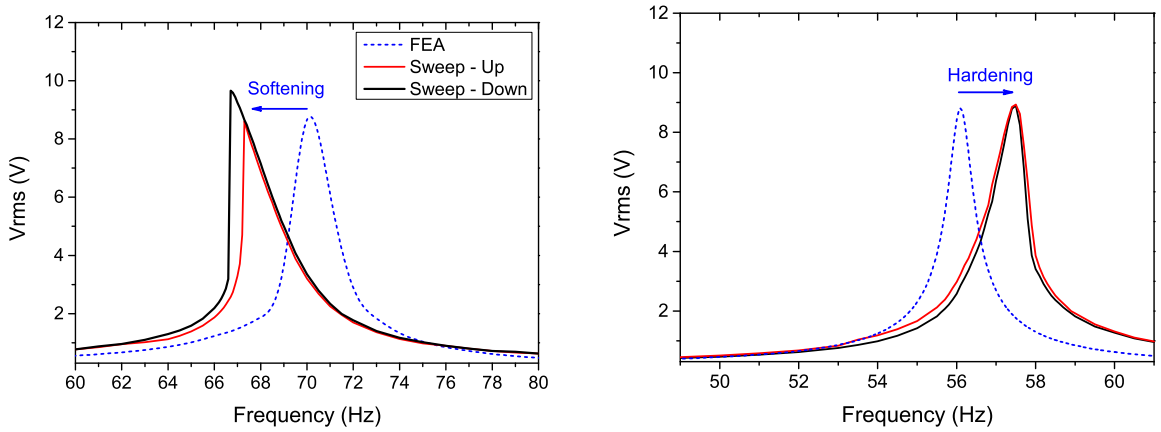

Figure 5.17: Voltage response of the samples: a) softening of sample with thickness ratio $\frac{h_i}{h_p} < 1$. *b) Hardening of sample with* $\frac{h_i}{h_p} > 2$.

Table 5.6: Experimental identifications for (YXl)/128° $LiNbO_3$ /Brass harvester.

C_0(nF)	M(g)	C (mN.s.m^{-1})	K (N.m^{-1})	α (mN.V^{-1})	k_mQ	Tip mass
1.25	0.13	0.24	26.63	0.032	1.92	Yes
2.63	0.03	0.09	3.84	0.021	4.82	No

age levels. Because the beam had lower factor k_mQ it presented only one power peak, being the SC and OC frequencies very close one to another. Moreover, because of the non-linearities, the two distinct peaks were not visible. Thus, we have approximated the device to a piezoelectric generator at resonance. In Fig. (5.17a) we represented the voltage and displacement in open-circuit conditions. The voltage reaches 13 V peak for a displacement of 510 µm peak. We simulated the power output for a full bridge electronic configuration, where we used four Schottky diodes (BAT41) and a smoothing capacitor C_r of 12 µF. We had good agreement between simulations and measured data (Fig. 5.17b), with just a small discrepancy at high load due to the charging time of C_r. The maximum power peak was found around 3 MΩ and for a value of 15.9 µW at the resonance frequency of 66.4 Hz.

5.4.3 Summary

In this last section of the chapter, I have presented our work regarding modeling and characterization of $LiNbO_3$ on metal substrate harvesters. The purpose of this work was to find a suitable micro-fabrication route using Au-Au bonding of high quality $LiNbO_3$ single crystals on metal hosts. We have investigated the properties of such devices with both FEA and Comsol simulation in order to find the best configuration in terms of coupling. The experimental results were in good agreement with the simulations, but the simple model

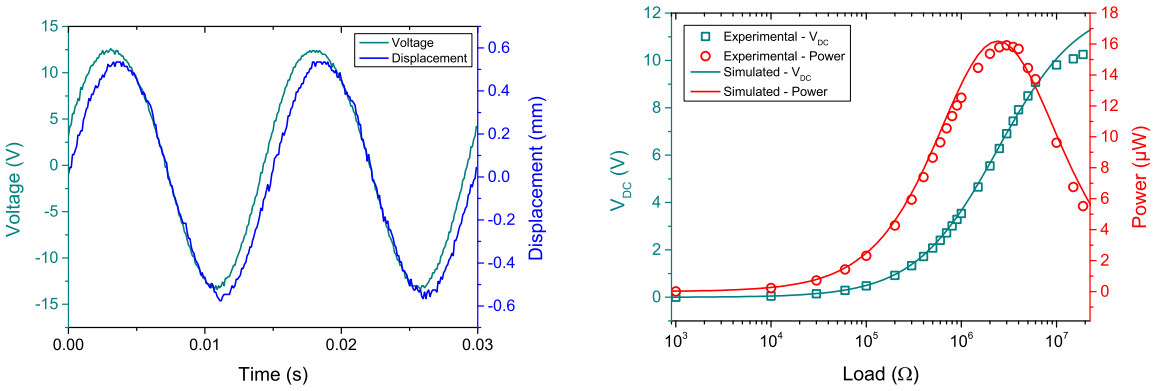

Figure 5.18: Characterization of (YXl)/128° $LiNbO_3$ /Brass harvester with tip mass: (a) voltage and displacement in OC conditions; b) experimental and simulated power output as a function of resistive load.

requires a further optimization, like an additional element in the FEA to refine the predictions, or a study of geometric non-linearity. In fact, the investigation in the frequency domain showed a tendency of the samples to show non-linearities (softening or hardening) which are depending on the thickness ratio between substrate and piezoelectric layer (h_i/h_p). For all the specimens the frequency response was reduced, and the displacement was improved reaching a maximum of 1.57 mm amplitude for the optimized simple beam while providing 12.5 V peak at 0.1 g acceleration amplitude. Finally we have characterized the power output of the sample with tip mass. For an active area of 260 mm^2 and an acceleration of 0.1 g, the power density is equal to 612 $\mu W/cm^2/g^2$. Even though this value is smaller than the silicon counterpart, if we consider the normalized power density, we achieved 9.22 $\mu W/cm^2/g^2/Hz$, which is an improvement compared to previous results.

5.5 Conclusion

In this chapter we have summarized the results regarding the fabrication and characterization of the $LiNbO_3$ harvesters. In particular, in Table 5.7 we present the comparison between the three different generations of $LiNbO_3$ harvesters, in terms of volumetric power density. We started our study from devices working at high frequency and high acceleration levels on silicon. The harvesting capabilities for the first batch of samples, allowed starting an RF sensor node. These high frequency harvesters (LN/Si-HF) have the highest rectified power output, and even if they have the smallest volume, the normalized power density is lower compared to the other devices mostly because high acceleration levels. Therefore, we recommend the use of samples with similar features for application in industrial machinery or aerospace environments. Later on, we have implemented a new design considering samples with tip mass in order to increase the coupling and quality factor of the device. Such structures presented lower resonance frequencies and successfully in-

creased the power density by two order of magnitude. Moreover, we have optimized the fabrication process to produce $LiNbO_3$ harvesters on metal. The specimens were working under similar dynamic conditions, but further reduced resonance frequency and increased robustness. Therefore, low frequency harvesters on silicon (LN/Si-LF) or metal unimorphs (LN/Brass) highly improved the power density. Nevertheless, further optimization is required regarding the coupling of the structures, even though the results obtained are promising both in terms of frequency and power, for automotive applications.

Table 5.7: Experimental normalized power density for $LiNbO_3$ harvesters.

Sample	f_0 (Hz)	Power (µW)	$\overrightarrow{a}$ (g)	Volume (mm^3)	Volumetric NPD ($\mu W.cm^{-3}.g^{-2}.Hz^{-1}$)
LN/Si-HF	1140	380	3.4	39	0.74
LN/Si-LF	105.9	41.5	0.1	262.5	149.3
LN/Brass	66.4	15.9	0.1	64.6	371.2

Finally, in order to compare our devices to the most recent state of the art, we presented their areal power density and frequency response in Fig. (5.19). Where dimensions are limited, hence MEMS scale, thin films are usually employed on thick substrates with large tip masses. They work at high frequency and acceleration levels, therefore the power density is bounded to few μW. LN/Si-HF belongs to this class of devices, even if it does not present a tip mass, has similar performance to other Pb- or Pb-free harvesters. Implementing the proposed MEMS design could theoretically enhance the performance of our device at small scale.

More interesting, at mesoscale the power output is closer to mW scale and frequencies are below 200 Hz. Here, both LN/Si-LF and LN/Brass have significant power density, showing superior performances compared to lead-free materials and comparable results to PZT. Especially in the case of $LiNbO_3$ on brass harvesters, we have obtained a robust and reliable solution for automotive application, having still room for improvements considering higher quality factor substrates or the fabrication of bimorphs. Overall, our devices show good performances and promising outcomes for the implementation of $LiNbO_3$ as energy harvesting transducer and as an affordable alternative to lead-containing materials.

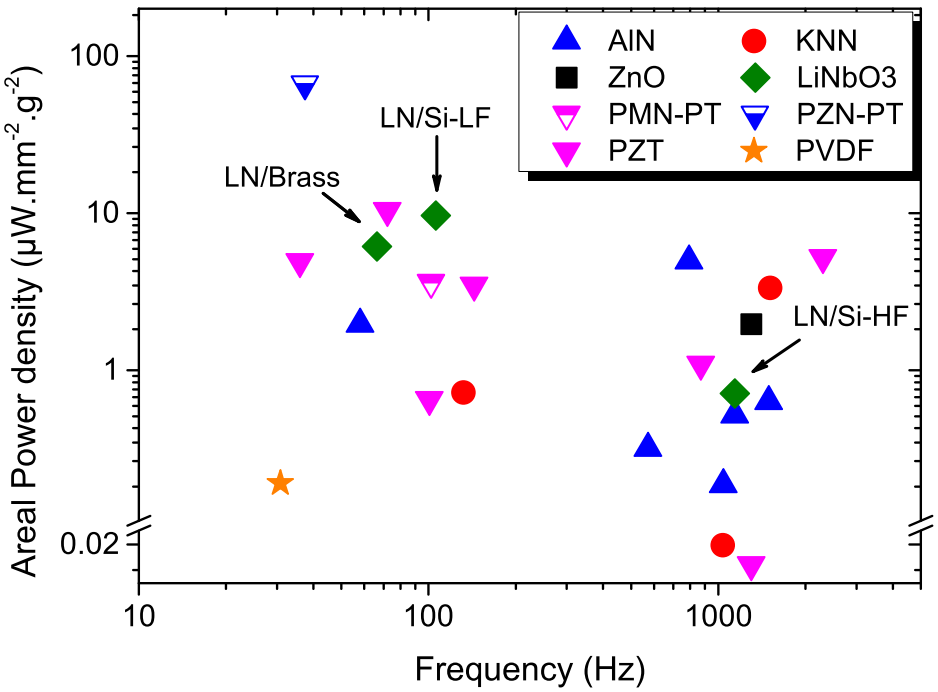

Figure 5.19: Comparison of state of the art harvesters for low and high frequency application. $LiNbO_3$ devices displayed with the following notation: $LiNbO_3$ on silicon device for high frequency application (LN/Si-HF); $LiNbO_3$ on silicon device for low frequency application (LN/Si-LF); $LiNbO_3$ on brass substrate for low frequency application (LN/Brass). All the references are given in the Tables 5.2 and 5.5.

Bibliography

[1] W. Yue and J. Yi-Jian, "Crystal orientation dependence of piezoelectric properties in LiNbO3 and LiTaO3," *Optical Materials*, vol. 23, no. 1-2, pp. 403–408, 2003.

[2] "IEEE Standard on Piezoelectricity: An American National Standard," in *ANSI/IEEE Std 176-1987*, 1988.

[3] Farnell.com, "Transmitter Module PTM 330 / PTM 330C Datasheet," 2011.

[4] P. Muralt, M. Marzencki, B. Belgacem, F. Calame, and S. Basrour, "Vibration Energy Harvesting with PZT Micro Device," *Procedia Chemistry*, vol. 1, no. 1, pp. 1191–1194, 2009.

[5] A. Hajati and S. G. Kim, "Ultra-wide bandwidth piezoelectric energy harvesting," *Applied Physics Letters*, vol. 99, no. 8, pp. 1–4, 2011.

[6] D. Isarakorn, D. Briand, P. Janphuang, A. Sambri, S. Gariglio, J. M. Triscone, F. Guy, J. W. Reiner, C. H. Ahn, and N. F. De Rooij, "The realization and performance of vibration energy harvesting MEMS devices based on an epitaxial piezoelectric thin film," *Smart Materials and Structures*, vol. 20, no. 2, 2011.

[7] I. Kanno, T. Ichida, K. Adachi, H. Kotera, K. Shibata, and T. Mishima, "Power-generation performance of lead-free (K,Na)NbO 3 piezoelectric thin-film energy harvesters," *Sensors and Actuators, A: Physical*, vol. 179, pp. 132–136, 2012.

[8] L. Van Minh, M. Hara, and H. Kuwano, "High Performance Nonlinear Micro Energy Harvester Integrated with (K,Na)NbO3/Si Composite Quad-Cantilever," *The 27TH International Conference on MEMS*, pp. 397–400, 2014.

[9] P. Wang and H. Du, "ZnO thin film piezoelectric MEMS vibration energy harvesters with two piezoelectric elements for higher output performance," *Review of Scientific Instruments*, vol. 86, no. 7, 2015.

[10] M. Marzencki, Y. Ammar, and S. Basrour, "Design, Fabrication and Characterization of a Piezoelectric Microgenerator Including a Power Management Circuit," no. April, pp. 25–27, 2008.

[11] J. Zhang, Z. Cao, and H. Kuwano, "Fabrication of low-residual-stress AIN thin films and their application to microgenerators for vibration energy harvesting," *Japanese Journal of Applied Physics*, vol. 50, no. 9 PART 3, 2011.

[12] A. B. Alamin Dow, A. Bittner, U. Schmid, and N. P. Kherani, "Design, fabrication and testing of a piezoelectric energy microgenerator," *Microsystem Technologies*, vol. 20, no. 4-5, pp. 1035–1040, 2014.

[13] P. M. Mayrhofer, C. Rehlendt, M. Fischeneder, M. Kucera, E. Wistrela, A. Bittner, and U. Schmid, "ScAlN MEMS Cantilevers for Vibrational Energy Harvesting Purposes," *Journal of Microelectromechanical Systems*, vol. 26, no. 1, pp. 102–112, 2017.

[14] W. Tian, Z. Ling, W. Yu, and J. Shi, "A review of MEMS scale piezoelectric energy harvester," *Applied Sciences (Switzerland)*, vol. 8, no. 4, pp. 1–20, 2018.

[15] Y. C. Shu and I. C. Lien, "Analysis of power output for piezoelectric energy harvesting systems," *Smart Materials and Structures*, vol. 15, no. 6, pp. 1499–1512, 2006.

[16] A. Badel and E. Lefeuvre, *Nonlinear Conditioning Circuits for Piezoelectric Energy Harvesters*. 2016.

[17] Y. C. Wang, S. A. Chen, Y. C. Shu, S. C. Lin, C. T. Chen, and W. J. Wu, "Nonlinear analysis of micro piezoelectric energy harvesters," *Active and Passive Smart Structures and Integrated Systems 2017*, vol. 10164, p. 1016418, 2017.

[18] E. Lefeuvre, A. Badel, A. Benayad, L. Lebrun, C. Richard, and D. Guyomar, "A comparison between several approaches of piezoelectric energy harvesting," *Journal De Physique. IV : JP*, vol. 128, pp. 177–186, 2005.

[19] J. V. Vidal, A. V. Turutin, I. V. Kubasov, A. M. Kislyuk, M. D. Malinkovich, Y. N. Parkhomenko, S. P. Kobeleva, O. V. Pakhomov, N. A. Sobolev, and A. L. Kholkin, "Low-Frequency Vibration Energy Harvesting with Bidomain LiNbO3 Single Crystals," *IEEE Transactions on Ultrasonics, Ferroelectrics, and Frequency Control*, vol. 66, no. 9, pp. 1480–1487, 2019.

[20] S. S. Won, J. Lee, V. Venugopal, D. J. Kim, J. Lee, I. W. Kim, A. I. Kingon, and S. H. Kim, "Lead-free Mn-doped (K0.5,Na0.5)NbO3 piezoelectric thin films for MEMS-based vibrational energy harvester applications," *Applied Physics Letters*, vol. 108, no. 23, pp. 0–5, 2016.

[21] H. G. Yeo, T. Xue, S. Roundy, X. Ma, C. Rahn, and S. Trolier-McKinstry, "Strongly (001) Oriented Bimorph PZT Film on Metal Foils Grown by rf-Sputtering for Wrist-Worn Piezoelectric Energy Harvesters," *Advanced Functional Materials*, vol. 28, no. 36, pp. 1–9, 2018.

[22] L. Dhakar, H. Liu, F. E. Tay, and C. Lee, "A new energy harvester design for high power output at low frequencies," *Sensors and Actuators, A: Physical*, vol. 199, pp. 344–352, 2013.

[23] R. Sriramdas, S. Chiplunkar, R. M. Cuduvally, and R. Pratap, "Performance enhancement of piezoelectric energy harvesters using multilayer and multistep beam configurations," *IEEE Sensors Journal*, vol. 15, no. 6, pp. 3338–3348, 2015.

[24] Z. Yang and J. Zu, "Comparison of PZN-PT, PMN-PT single crystals and PZT ceramic for vibration energy harvesting," *Energy Conversion and Management*, vol. 122, pp. 321–329, 2016.

[25] C. L. Kuo, S. C. Lin, and W. J. Wu, "Fabrication and performance evaluation of a metal-based bimorph piezoelectric MEMS generator for vibration energy harvesting," *Smart Materials and Structures*, vol. 25, no. 10, pp. 1–10, 2016.

[26] G. Tang, B. Yang, C. Hou, G. Li, J. Liu, X. Chen, and C. Yang, "A piezoelectric micro generator worked at low frequency and high acceleration based on PZT and phosphor bronze bonding," *Scientific Reports*, vol. 6, no. December, pp. 2–11, 2016.

[27] C. Xu, B. Ren, W. Di, Z. Liang, J. Jiao, L. Li, L. Li, X. Zhao, H. Luo, and D. Wang, "Cantilever driving low frequency piezoelectric energy harvester using single crystal material 0.71Pb(Mg 1/3Nb 2/3)O 3-0.29PbTiO 3," *Applied Physics Letters*, vol. 101, no. 3, pp. 2010–2014, 2012.

[28] R. Andosca, T. G. McDonald, V. Genova, S. Rosenberg, J. Keating, C. Benedixen, and J. Wu, "Experimental and theoretical studies on MEMS piezoelectric vibrational energy harvesters with mass loading," *Sensors and Actuators, A: Physical*, vol. 178, pp. 76–87, 2012.

[29] W. J. Wu, C. T. Chen, S. C. Lin, C. L. Kuo, Y. J. Wang, and S. P. Yeh, "Comparison of the piezoelectric energy harvesters with Si- MEMS and metal-MEMS," *Journal of Physics: Conference Series*, vol. 557, no. 1, 2014.

[30] M. F. Daqaq, R. Masana, A. Erturk, and D. D. Quinn, "On the role of nonlinearities in vibratory energy harvesting: A critical review and discussion," *Applied Mechanics Reviews*, vol. 66, no. 4, 2014.

6 General Conclusion and Perspectives

In the framework of ITN ENHANCE, the work was done in collaboration with several partners and institutions. While the fabrication part was mostly done at FEMTO-ST, other work packages were completed in different institutions. For instance, the electronic interface optimization for the harvesters at INSA Lyon, basic characterization of $LiNbO_3$ at EPFL, CVD and transducer simulations in both AIXTRON and CEDRAT, respectively, while having interesting discussion online with other partners from ST-Microelectronics and IMPERIAL College. This manuscript is the product of many exchanges also with people from other teams and cities around Europe, from whom I have learned interesting new concepts and thought about new ideas to improve the quality of my research. I have presented our work in 8 conferences, and we had many meetings between the partners to update on the state of the works, and then share new information regarding most recent advancements, while contributing in a collective way to the progress of the project through deliverables and work packages. Especially for me and other ESRs which are working on the implementation of materials as energy harvesters, it was particularly important to provide experimental data or devices in order to explore new significant research aspects of the project.

We have started our work on a well known material, $LiNbO_3$, which was barely used in energy harvesting, to explore new interesting possibilities and find an alternative for applications that are efficient, eco-friendly and economically competitive. The EU regulation is banning lead containing materials from the market with few exceptions (biomedical and military applications), so the need of finding new materials is one of the first concerns in this topic. We have accepted the challenge of working with $LiNbO_3$, and we have found interesting ways to introduce it in the vast landscape of energy conversion.

As a first step towards the implementation as energy harvesting material, we have started the study from the orientation aspects, considering its anysotropy and the difference with the other well established materials. We have demonstrated that especially in terms of coupling and figure of merit, $LiNbO_3$ presents very interesting performances which are well suited for energy harvesting applications. Previously the material proper-

ties of $LiNbO_3$ were investigated mostly for acoustic and optic devices, and rarely as a harvester. In terms of electro-mechanical properties, for commercially available (YXl)/128° $LiNbO_3$ the transverse coupling is k_{23}=0.49, hence comparable or even higher than Pb-based materials (k_{31} for PZT-5A and PZT-5H is 0.34 and 0.44, respectively), and generally higher than Pb-free materials (AlN, KNN, ZnO etc.). Also the FOMs, both for strain or stress driven harvesters, are comparable to Pb-based materials, for instance $LiNbO_3$ has FOM^T of 0.61 MJ.cm^{-3} while PZT-5A has 0.51 MJ.cm^{-3}. The following step was the implementation and the fabrication of the piezoelectric films. First we have considered the MOCVD growth of thin films but with limited thickness of the samples (50-500 nm). Therefore we have moved to the integration of single crystal $LiNbO_3$ films with optimized fabrication route, considering thick films (5-100 µm). The thickness, and especially orientation, were considered in this part of the study to match and improve the harvester performances. We have investigated both theoretically and experimentally different $LiNbO_3$ single crystal cuts, and we have identified (YXl)/128° as the best option for piezoelectric transduction (FOM^f=26.6 GJ/m^3). Moreover, we have demonstrated the pyroelectric capabilities of $LiNbO_3$ tilted cuts, but further developments are required for implementation in energy harvesting. On the other hand, we have considered during the design phase, key aspects such as capacitance of the piezoelectric films and electronic interfacing, in order to move towards a global optimization approach.

With the first design proposed of $LiNbO_3$ /Si, we have obtained state of the art results (0.74 µW.cm^{-3}.g^{-2}.Hz^{-1}), but still the prototypes needed further optimization in terms of acceleration levels and frequency response. Consequently, we have introduced other step in micro-fabrication process and changed geometry in order to reduce resonance frequency for matching vibration spectra of cars, and to increase the electro-mechanical coupling of the system, achieving a normalized power density of 149.3 µW.cm^{-3}.g^{-2}.Hz^{-1}. Even though the results at his point were excellent, we have moved towards metal substrates, trying to further increase coupling and to reduce frequency, while having more robust structures. Therefore, we have optimized a new fabrication route implementing metal foils as a substrate, and obtaining $LiNbO_3$ thick films (from 10 µm to 80 µm) on brass in form of unimorph cantilevers. Finally, we have attained the best results in terms of normalized power density (371.2 µW.cm^{-3}.g^{-2}.Hz^{-1}) among the samples fabricated and we have improved system robustness and reliability. If now we consider the state of the art, we can see that the designed and fabricated $LiNbO_3$ prototypes are generally comparable or even better than both Pb-based (like PZT) and Pb-free materials. Some exception still have better performances, but they implement very expensive materials like PZN-PT or are designed as bimorph structures, hence effectively doubling the volume of the piezoelectric layer under strain.

However, we can still elaborate and investigate more aspects of the work so far discussed. For instance, more progress can be achieved in the fabrication of $LiNbO_3$ on

metal substrate. In fact, we have optimized the parameters to implement stainless steel as a host material, and the fabrication of unimorphs is a work in progress. Moreover, we are also working on the implementation of two $LiNbO_3$ wafers Au-Au bonded to the same metal shim, for fabricating a bimorph structure. In virtue of FEA and FEM simulation results, we have confirmation that coupling would increase for such a structure, theoretically improving also the performances. Anyways, we should carefully consider the clamped capacitance of the piezoelectric layers, in order to obtain optimized impedance matching conditions. So particular attention will be given to the thickness optimization of the $LiNbO_3$ thick films. Besides, new exciting opportunities are arising from the first tests on MEMS scale $LiNbO_3$ /Si devices, where we are reducing the scale of $LiNbO_3$ prototypes and exploring new device topologies. Furthermore, *on the field* tests will take place in collaboration with PSA Group using the fabricated $LiNbO_3$ harvesters with optimized electronic interface, to ensure the possibility of final device integration.

Publications

- *$LiNbO_3$ Films – A Low-Cost Alternative Lead-Free Piezoelectric Material for Vibrational Energy Harvesters*, **G. Clementi**, G. Lombardi, S. Margueron, M. A. Suarez, E. Labrasseur, S. Ballandras, J. Imbaud, F. Lardet Vieudrin, L. Gauthier Manuel, B. Dulmet, M. Lallart & A. Bartasyte. Mechanical Systems and Signal Processing 149, February: 107171. https://doi.org/10.1016/j.ymssp.2020.107171. (2021).

- *Piezoelectric and Pyroelectric Energy Harvesting from Lithium Niobate Films*, **G. Clementi**, S. Margueron, M. A. Suarez, T. Baron, B. Dulmet & A. Bartasyte, Journal of Physics: Conference Series. 1407. 012039. 10.1088/1742 6596/1407/1/012039. (2019).

Oral Presentation in International Conferences

- *$LiNbO_3$ films: a Low-Cost Alternative for Vibrational Energy Harvesting*, **Clementi Giacomo**, Ouhabaz Merieme, Lombardi Giulia, Margueron Samuel, Suarez Miguel Angel, Bassignot Florent, Gautier-Manuel Ludovic, Dulmet Bernard, Muralt P., Lallart Mickael, Bartasyte Ausrine. **IWPMA 2020**,19th International Workshop on Piezoelectric Materials and Applications on Actuators 2020, September 2020, PennState University, USA (Online).

- *Characterization of Lead Free $LiNbO_3$ Energy Harvesters*, **Clementi Giacomo**, Lombardi Giulia, Margueron Samuel, Suarez Miguel Angel, Lebrasseur Eric, Ballandras Sylvain, Imbaud Joël, Lardet-Vieudrin Franck, Gautier-Manuel Ludovic, Dulmet Bernard, Muralt Paul, Lallart Mickael, Bartasyte Ausrine. **PowerMEMS 2019**,19th International Conference on Micro and Nanotechnology for Power Generation and Energy Conversion Applications, December 2019, Krakow, Poland.

- *Lead Free $LiNbO_3$ Films for Piezoelectric Energy Harvesting*, **Clementi Giacomo** , Ausrine Bartasyte, Bernard Dulmet and Samuel Margueron. **IWPMA 2019**, International Workshop on Piezoelectric Materials and Applications on Actuators 2019 and Enhance Workshop, October 2019, Lyon, France.

- *Energy Harvesting with Lithium Niobate Films.*, **Clementi Giacomo**, Lombardi Giulia, Margueron Samuel, Suarez, Miguel Angel, Lebrasseur Eric, Ballandras Sylvain, Dulmet Bernard, Lallart Mickael, Bartasyte Ausrine. **ISAF 2019**,IEEE International Symposium on Applications of Ferroelectrics, July 2019, Lausanne, Switzerland.

- *Piezoelectric and Pyroelectric Energy Harvesting from Lithium Niobate Films*, **Clementi Giacomo**, Margueron Samuel, Suarez Miguel Angel, Baron Thomas, Dulmet Bernard, Bartasyte Ausrine. **PowerMEMS 2018**, 18th International Conference on Micro and Nanotechnology for Power Generation and Energy Conversion Applications, December 2018, Daytona Beach, United States.

- *New materials in vibrational energy harvesting,* **Clementi Giacomo**, Bartasyte Ausrine, Dulmet Bernard, Margueron Samuel. **ISEPD 2018**, 19th International Symposuim on Eco-materials Processing and Design, February 2018, Jaipur, India.

Oral Presentation in National Conferences

- *Energy Harvesting with lead free $LiNbO_3$* , **Clementi Giacomo**, Bartasyte Ausrine, Dulmet Bernard, Margueron Samuel. **JNRSE 2018**, Journées Nationales sur la Récupération et le Stockage d'Energie, May 2018, Besançon, France.
- *Modeling new materials for energy harvesting applications*, **Clementi Giacomo**, Margueron Samuel, Dulmet Bernard, Bartasyte Ausrine. **GdR OXYFUN 2018**, March 2018, Piriac sur Mer, France.

Outreach Activities

- Giacomo Clementi, "Science in Society" initiative. "Future of Energy Harvesting and µ-Energies", Highschool Campus Leonardo Da Vinci, Umbertide (Italy). This outreach activity was part of "Science in Society" initiative of ENHANCE project to promote careers in science and technology. The key points of the dissemination event were Renewable Energies, µ-Technology and Internet of Things.
- Giacomo Clementi, European Researchers Night, Besançon (France), September 28, 2019. Presented several harvester and circuit demonstrators of the ENHANCE project to the general public.

Awards

- Association des jeunes chercheurs de Franche-Comté (A'Doc), Photographic Contest "Vis ma Vie de Doctorant.e", 2nd Quality Prize, "Pictures from Europe: MSCA Edition", July 2019, Besançon, France.
- ITN ENHANCE Ambassadors program competition, 2nd Place, Workshop and Symposium "From Molecular Engineering to Advanced Materials", May 2019, Koln, Germany.
- Best poster award, 1st Place, Workshop and Symposium "From Molecular Engineering to Advanced Materials", May 2019, Koln, Germany.

Secondments

- **AIXTRON**, Aachen (Germany), April 2018 (1 month)
- **INSA**, Lyon (France), December 2018 (1 month)
- **EPFL**, Lausanne (Switzerland), February-April 2019 (2 months)
- **EPFL**, Lausanne (Switzerland), May-July 2019 (2 months)
- **CEDRAT**, Grenoble (France), November 2019 (1 month)
- **ST-Microelectronics**, Catania (Italy), July 2020 (1 month, online)
- **Imperial College**, London (UK), August-October 2020 (2 months, online)

Titre: $LiNbO_3$ films: intégration pour la récupération de l'énergie piézoélectrique et pyroélectrique.

Mots clés: Récupération d'énergie, niobate de lithium, piézoélectricité, pyroélectricité

Résumé: Cette thèse fait partie du projet ENHANCE (*Piezoelectric Energy Harvesters for Self-Powered Automotive Sensors : from Advanced Lead-Free Materials to Smart Systems*) du réseau de formation innovant Marie Sklodowska-Curie, qui est lié à la récupération d'énergie pour les applications automobiles, en particulier de l'énergie vibratoire et thermique pour les capteurs autoalimentés. Dans cette thèse, nous avons étudié le matériau piézoélectrique sans plomb $LiNbO_3$ comme transducteur pour les applications de récupération d'énergie, en mettant l'accent sur ses propriétés matérielles optimisées et son interface électronique. Nous avons exploré toutes les voies possibles de micro-fabrication des films $LiNbO_3$, avec des approches top-down ou bottom-up, afin d'obtenir des films $LiNbO_3$ de haute qualité. Nous avons présenté à la fois des films PIMOCVD qui peuvent être développés de manière texturée sur des substrats de silicium, et des films épais de monocristaux $LiNbO_3$ Au-Au colleés au silicium ou au métal. Nous avons optimisé le couplage et les propriétés électro-mécaniques des transducteurs $LiNbO_3$ par des simulations par éléments finis et l'étude de l'orientation. Finalement, nous avons démontré expérimentalement que $LiNbO_3$ (YXl)/128° est la meilleure orientation pour les applications de récupération d'énergie vibratoire. Enfin, nous avons atteint une densité de puissance normalisée de 371,2 $\mu W.cm^{-3}.g^{-2}.Hz^{-1}$ en utilisant la structure composite proposée qui vibre à la fréquence de résonance, ce qui est parmi les meilleures valeurs même par rapport aux matériaux à base de plomb (et autres matériaux sans plomb) disponibles dans le commerce. En outre, nous avons satisfait l'objectif de fournir une tension de sortie redressée dans la gamme 1-3 V à partir de transducteurs sans plomb, obtenant pour des systèmes de dimensions compactes (< 1 cm^3), une figure de mérite piézoélectrique de 26,6 GJ/m^3 avec un facteur de qualité mécanique considérable (> 100), et des fréquences opérationnelles dans la gamme de 10-500 Hz disponibles dans les véhicules.

Title: $LiNbO_3$ films: integration for piezoelectric and pyroelectric energy harvesting.

Keywords: Energy harvesting, lithium niobate, piezoelectricity, pyroelectricity

Abstract: This thesis is a part of the Marie Sklodowska-Curie Innovative Training Network (ITN) ENHANCE project (*Piezoelectric Energy Harvesters for Self-Powered Automotive Sensors: from Advanced Lead-Free Materials to Smart Systems*), which is related to energy harvesting for automotive applications, specifically for vibrational and thermal harvesting for self-powered sensors. In this thesis, we investigated lead-free $LiNbO_3$ piezoelectric material as transducer for energy harvesting applications, with special focus regarding its optimized material properties and electronic interface. We explored all the possible routes of micro-fabrication for $LiNbO_3$ films, with top-down or bottom-up approaches, in order to achieve high quality $LiNbO_3$ films. We presented both PIMOCVD films which can be grown textured on silicon substrates, and thick films from single crystal $LiNbO_3$ Au-Au bonded to silicon or metal. We optimized the coupling and electromechanical properties of the $LiNbO_3$ transducers by finite element simulations and orientation study. Eventually, we demonstrated experimentally that $LiNbO_3$ (YXl)/128° is the best orientation for vibrational energy harvesting applications. Finally, we attained a normalized power density of 371.2 $\mu W.cm^{-3}.g^{-2}.Hz^{-1}$ by using the proposed composite structure vibrating at resonance frequency, that is among best values even compared to lead-based (and other lead-free) materials commercially available. Furthermore, we fulfilled the objective to provide rectified output voltage in 1-3 V range from Pb-free harvesters, achieving for systems of compact dimensions (< 1 cm^3), a piezoelectric figure of merit of 26.6 GJ/m^3 with considerable mechanical quality factor (> 100), and operational frequencies in the range of 10-500 Hz available in vehicles.

UBFC
UNIVERSITÉ
BOURGOGNE FRANCHE-COMTÉ

Université Bourgogne Franche-Comté
32, avenue de l'Observatoire
25000 Besançon